DSE - Unmanned Twin-Lift Rotorcraft for Aid in Disasters

Group 11

M.J. Beuker	4137825	P.F.R. Massart	4161874
M. Bevernaegie	4164245	R.N.J. Rousseau	4147928
J. Büskens	4165314	A.J.G.T. Scholtes	4139011
P.J.H. Deldycke	4175808	T. Van Hemelen	4168534
K. Krieger	4191196		

Final Report

Design Synthesis Excercise

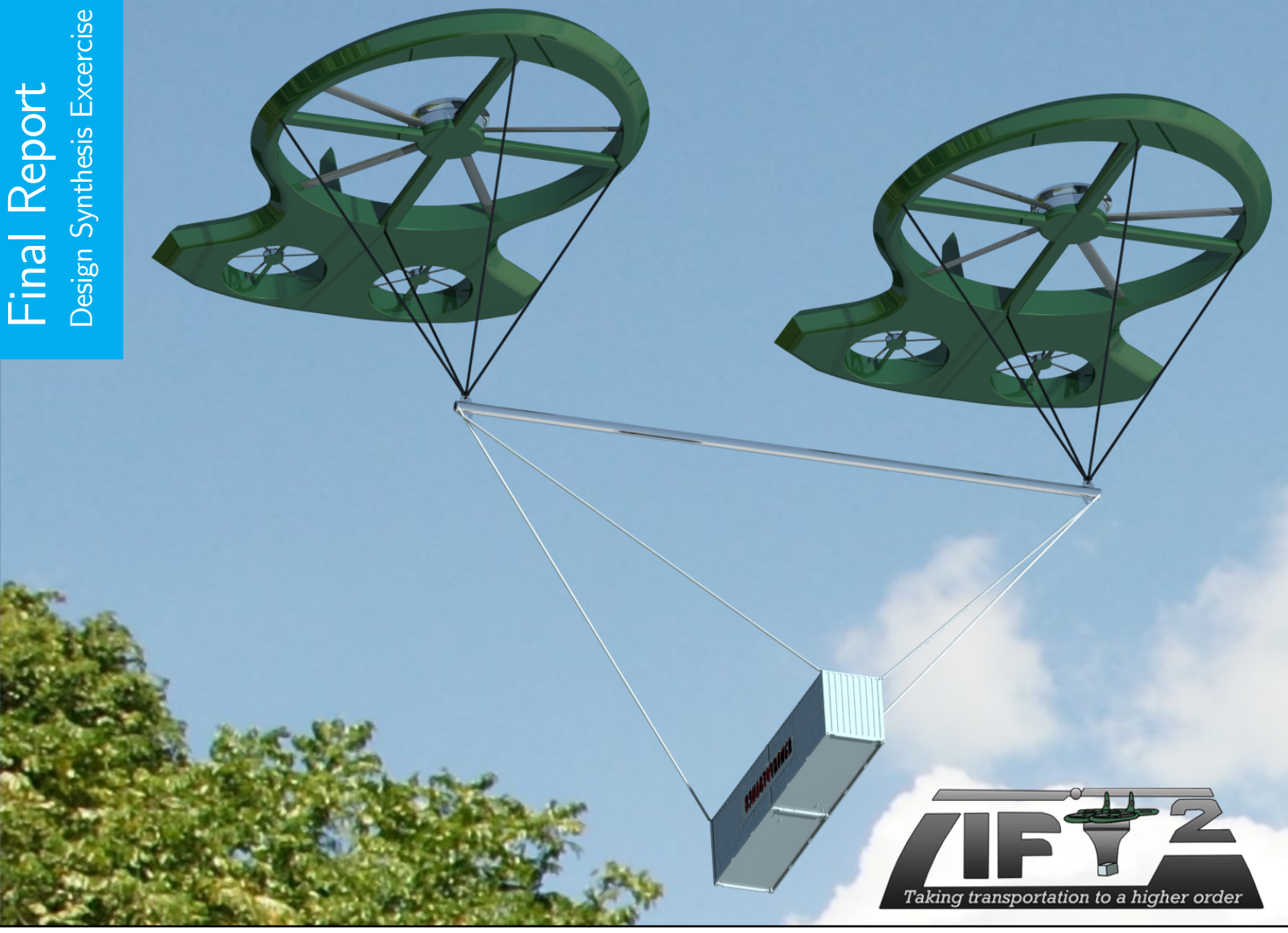

TU Delft Delft University of Technology

Aerospace Engineering

July 1, 2014

Preface

Global warming is the threat of our age. Scientists not only predict an increase of the sea level but also an increase in frequency and severity of natural disasters. Especially poor and developing countries will have hard times dealing with the consequences. Being the guilty party, the industrialised countries have a moral obligation to help those who are not able to help themselves.

The aim of our project is to design a flexible transportation method for a portable hospital. The so called "Hospitainer" is a hospital stored in normal shipping containers. It has proven to be of an indispensable aid for the people affected by the typhoon Haiyan in the Philippines. With our project we want to optimise the transportation of the Hospitainer to provide people in need around the world with fast and easy access to medical care. This report is a follow-up of the baseline and midterm report, in which the requirements of the system have been evaluated and an initial trade-off was made between different aerial vehicles to find the best suiting rotorcraft for the proposed mission. In this report, the preliminary sizing of the ducted fan is presented..

We would like to thank everyone that supports us in our vision. Of course that includes the Hospitainer Container with whom we closely cooperate to understand the transportation needs of their hospital. We also like to express our gratitude to our tutors, M. Pavel, D.Wang and W. Anderson for their guidance and support during the project. Special thanks goes to M. Pavel and J. Stoop, who initiated this project and established the contacts with the associated companies for us.

Delft,
July 1, 2014

List of Symbols

Symbol	Description	Unit
A	Cross sectional area	$[m^2]$
A_e	Exit area of the duct	$[m^2]$
A_h	Area horizontal tail surface	$[ft^2]$
A_{in}	Inlet area of the duct	$[m^2]$
$A_{section}$	Area of a secton	$[m^2]$
A_{swept}	Swept rotor area	$[m^2]$
A_v	Area vertical tail surface	$[ft^2]$
AI	Auto rotation index	$[m^3/kg]$
AR	Aspect ratio	[-]
AR_h	Aspect ratio horizontal tail surface	[-]
AR_v	Aspect ratio vertical tail surface	[-]
b	Width of payload (Chapter 4)	[m]
b	Wing span (Chapter 5)	[m]
b	Section width (Chapter 6)	[m]
b_m	Number of main rotor blades	[-]
C	Rate of climb	[m/s]
C	Labour cost	[US $]
$\bar{C}$	Non dimensional rate of climb	[-]
c_{aero}	Aerodynamic chord	[m]
C_d	Airfoil drag coefficient	[m]
C_D	Drag coefficient	[-]
C_{d_0}	Airfoil zero lift drag coefficient	[-]
C_{D_0}	Zero lift drag coefficient	[-]
C_{D_i}	Induced drag coefficient	[-]
$C_{D,h}$	Horizontal surface drag coefficient	[-]
C_{D_p}	Profile drag coefficient	[-]
$\sum(C_DS)_S$	Flat plate area	$[ft^2]$
$C_{D,v}$	Vertical surface drag coefficient	[-]
cg	cg location	[m]
c_{geo}	Geometric chord	[m]
c_i	Chord length of blade section	[m]
C_l	Airfoil lift coefficient	[-]
C_L	Lift coefficient	[-]
C_{L_α}	Lift gradient	[1/rad]
C_{L_ϵ}	Derivative of lift coefficient w.r.t	[-]
$C_{l_{max}}$	Airfoil maximum lift coefficient	[-]
C_m	Airfoil moment coefficient (Chapter 5)	[-]
c_m	Chord main rotor blades (Subsection 4.4.1)	[ft]
C_M	Moment coefficient	[-]
$Cost_{basic}$	Basic costs	[-]
$Cost_{procured}$	Procured cost	[US $]
c_r	Root chord	[m]
c_t	Tip chord	[m]
C_T	Thrust coefficient	[-]
D	Drag force	[N]
d	Distance between rotorcraft	[m]
D_{blade}	Total drag on a blade	[N]
$D_{h,GF}$	Drag in horizontal direction in the ground frame	[N]
$D_{h,VF}$	Drag force w.r.t the horizontal surface in the vehicle frame	[N]
D_i	Drag on blade section	[N]
DL	Disk loading	$[kg/m^2]$
d_{nose}	Distance from nose	[m]
$D_{payload}$	Payload drag	[N]
D_t	Rotor diameter	[m]
$D_{v,GF}$	Drag in vertical direction in the ground frame	[N]
$D_{v,VF}$	Drag force w.r.t the vertical surface in the vehicle frame	[N]
d_x	Distance to x-axis	[m]
$D_{x,GF}$	Drag force in x direction in the ground frame	[N]
$D_{x,VF}$	Drag force in x direction in the vehicle frame	[N]
$D_{y,GF}$	Drag force in y direction in the ground frame	[N]
$D_{y,VF}$	Drag force in y direction in the vehicle frame	[N]

d_z	Distance to z-axis	[m]
e	Oswald factor	[-]
$EI_{particle}$	Particle emission factor	[-]
F	Force	[N]
F_{cap}	Fuel tank capacity	[gal]
F_{cf}	Centrifugal force	[N]
FoM	Figure of merit	[-]
Fringe	Fringe factor	[-]
F_x	Force in x-direction	[N]
$F_{X,i}$	Force in X direction on a blade section	[N]
F_Y	Total force on a blade in Y direction	[N]
F_y	Force in y-direction	[N]
$F_{Y,i}$	Force in Y direction on a blade section	[N]
$G\&A$	General & Accounting factor	[-]
g	Gravitational constant (Chapter 4.4.1)	$[ft/s^2]$
g	Gravitational constant (Chapter 5)	$[m/s^2]$
h	Height between bar and payload (Chapter 4)	[m]
h	Section height (Chapter 6)	[m]
h_d	Height of the duct	[m]
h_{fus}	Fuselage height	[m]
h_{mr}	Height of main rotor to centre of gravity of ducted fan	[m]
Hr	Amount of labour	[hr]
hp_{rating}	Transmission horse power rating	[Hp]
hp_v	Vertical tail horsepower rating	[Hp]
I	Moment of inertia	[kg m^2]
l_a	Length from nose to end of the duct through the middle of the fuselage	[m]
I_b	Polar moment of inertia of the blades	$[kg\ m^2]$
I_{xx}	Moment of inertia w.r.t the x-axis	$[kg\ m^2]$
I_{xz}	Product of inertia w.r.t xz-plane	$[kg\ m^2]$
I_{zz}	Moment of inertia w.r.t the z-axis	$[kg\ m^2]$
J	Polar moment of inertia main rotor	$[slugft^2]$
k	Flow uniformity coefficient (Chapter 5)	[-]
k	Spring constant (Chapter 7)	[N/m]
k	Non-uniformity factor (Chapter 4)	[-]
K	Kinetic energy (Chapter 7)	[Nm]
k_{dl}	Fuselage download factor	[-]
l	Reference length of geometry	[m]
l_{cg}	Distance to the center of gravity	[m]
l_{cut}	Length from nose to the cut between the main body and tail	[m]
L_d	Diffuser length	[m]
$(L/D)_{max}$	Maximum lift over drag ratio	[-]
$l_{duct,total}$	Total duct length	[m]
l_f	Length of fuselage box	[m]
l_{fans}	Fan arm	[m]
$l_{frontclear}$	Front clearance	[m]
L_h	Lift of horizontal tail surface	[N]
L_i	Lift on blade section	[N]
L_{ls}	Lift of lifing surface	[N]
l_m	Length of nose to centre of main rotor	[m]
l_r	Length from c.g. to main rotor thrust	[m]
$l_{sideclear}$	Side clearance	[m]
l_t	Length from c.g. to horizontal tail rotor thrust	[m]
l_v	Vertical tail arm	[m]
l_v	Vertical tail arm (Subsection 4.1.1)	[ft]
L_v	Lift of vertical tail surface	[N]
m	Take-off mass	[kg]
M	Moment	[Nm]
m_{blade}	Mass of a single blade	[kg]
m_b	Single rotorblade mass	[kg]
M_{drag}	Mach drag divergence number	[-]
M_R	Total moment on the rotor due to blade drag	[Nm]
$m_{section}$	Mass of a section	[kg]
MTOW	Maximum take-off weight (Subsection 4.4.1)	[lbs]
MTOW	Maximum take-off weight	[kg]
M_v	Moment arround vertical tail surface	[Nm]
$M_{x_{cg}}$	Moment arround the x-axis at the center of gravity	[Nm]
$M_{x_{cut}}$	Moment around the x-axis at the cut the between main body and tail	[Nm]
$M_{y_{cg}}$	Moment arround the y-axis at the center of gravity	[Nm]
$M_{y_{cut}}$	Moment around the y-axis at the cut the between main body and tail	[Nm]

$M_{z_{cg}}$	Moment arround the z-axis at the center of gravity	[Nm]
$M_{z_{cut}}$	Moment around the z-axis at the cut between the main body and the tail	[Nm]
n_b	Number of blades	[-]
N_{crit}	Ambient disturbance level of the flow	[-]
No.engines	Number of engines	[-]
no.tailgearboxes	Number of gearboxes in the tail	[-]
No.wheellegs	Number of landing gear wheel legs	[-]
n_z	Flight turn coefficient	[-]
OEW	Operational empty weight	[kg]
Overhead	Overhead factor	[-]
p	Local perpendicular distance to shear center	[m]
P_{actual}	Actual power available	[W]
P_h	Horizontal tail rotor power	[W]
P_{hov}	Power to hover	[W]
$P_{i,hov}$	Ideal hover power	[W]
P_i	Induced power	[W]
P_{inst}	Installed power	[W]
P_{misc}	Miscellaneous power	[W]
P_p	Propeller power	[W]
P_{req}	Power required	[W]
P_s	Parasite power	[W]
P_t	Total power	[W]
P_v	Vertical tail rotor power	[W]
P_x	X component payload factor	[N]
P_y	Y component payload factor	[N]
P_z	Z component payload factor	[N]
q	Pitch velocity	[rad/s]
q_b	Open section shear flow	[N/m]
q_{s0}	Constant shear flow in an open section	[N/m]
$q_{s0_{torque}}$	Shear flow due to pure torque	[N/m]
R	Rotor radius (Chapter 5)	[m]
R	Air specific gass constant (Chapter 8)	[J/kgK]
R	Labour price (Chapter 16)	[US $/hr]
r_0	Hub radius	[m]
r_b	Radius of the bolt	[m]
R_{basic}	Basic labour cost	[US $/hr]
R_c	Radius of the center of mass	[m]
RC	Rate of climb	[m/s]
Re	Reynolds number	[-]
R_H	Hub radius	[m]
r_i	Radial distance blade station	[m]
r_{lip}	Duct lip radius	[m]
r_m	Radius main rotor (Subsection 4.1.1)	[ft]
r_m	Radius main rotor	[m]
r_v	Radius vertical tail rotor	[ft]
rpm_{eng}	Rotational speed engine	[rpm]
S	Surface area	[m^2]
S	Side force of the main rotor (Chapter 6)	[N]
SFC	Specific fuel consumption	[kg/kWhr]
S_h	Horizontal projected frontal surface area	[m^2]
$S_{halfwing}$	Surface area of half of the wing	[m^2]
S_t	Horizontal tail surface	[m^2]
S_v	Vertical projected frontal surface area	[m^2]
$S_{wet_{fus}}$	Wetted fuselage area	[ft^2]
S_{wet_N}	Wetted nacelle area	[ft^2]
S_x	Shear force in x-direction	[N]
S_z	Shear force in z-direction	[N]
t	Thickness	[m]
T	Thrust	[N]
T	Temperature (Chapter 8)	[K]
T_1	Main rotor thrust	[N]
T_2	Left horizontal tail rotor thrust	[N]
T_3	Right horizontal tail rotor thrust	[N]
T_h	Thrust horizontal tails	[N]
T_{hl}	Thrust left horizontal tail	[N]
T_{hr}	Thrust right horizontal tail	[N]
T_m	Thrust main rotor	[N]
$t_{mission}$	Mission time	[hr]
T_v	Anti torque provided by vertical tail surface (Chapter 5)	[Nm]

T_v	Thrust vertical tail (Chapter 4)	[N]
T_{vf}	Thrust of the vertical fenestron	[N]
$T_{x,GF}$	Thrust in x direction in the ground frame	[N]
$T_{Y_{lift}}$	Torque arround the y-axis due to the lift	[Nm]
$T_{y,GF}$	Thrust in y direction in the ground frame	[N]
u	Horizontal component air speed	[m/s]
U	Potential energy	[Nm]
v	Velocity vector (Chapter 5)	[m/s]
V	Air speed (Chapter 7)	[m/s]
V	Flight speed (Chapter 8)	[m/s]
V_0	Free stream velocity	[m/s]
$V_{A,ff}$	Axial velocity forward flight	[m/s]
V_A	Axial velocity	[m/s]
V_{cruise}	Cruise velocity	[m/s]
V_g	Wind gust speed	[m/s]
$V_{h,VF}$	Velocity in horizontal direcion in the vehicle frame	[m/s]
v_i	Induced velocity	[m/s]
$\bar{v}_i$	Non dimensional induced velocity	[-]
$v_{i,hov}$	Induced velocity in hover	[m/s]
V_{max}	Maximum flight speed	[-]
V_{ne}	Never exceed speed	[-]
$V_{R,i}$	Resultant velocity experienced by blade section	[m/s]
V_r	Radial velocity	[m/s]
$V_{swirl,i}$	Swirl velocity at radial station	[m/s]
V_{tip_m}	Main rotor tip speed	[m/s]
$V_{v,VF}$	Velocity in vertical direcion in the vehicle frame	[m/s]
w	Velocity difference between duct inlet and outlet (Chapter 5)	[m/s]
w	Vertical component air speed (Chapter 7)	[m/s]
W	Maximum take-off weight (Chapter 7)	[N]
W	Work (Chapter 6)	[Nm]
$W_{AC\&AI}$	Weight air conditioning and anti-ice	[lbs]
W_{b_m}	Weight main rotor blades	[lbs]
W_{Cables}	Weight of the cables	[N]
$W_{D.S}$	Weight drive train system	[lbs]
W_e	Weight single engine	[lbs]
W_{EL}	Weight electronic systems	[lbs]
W_{eng}	Weight engine installation	[lbs]
W_{FE}	Weight furnising and equipment	[lbs]
$W_{F.S}$	Weight fuel subsystem	[lbs]
W_{fuel}	Fuel weight	[kg]
W_{fus}	Weight fuselage	[lbs]
w_h	Width of between horizontal tails	[m]
W_{h_m}	Weight main rotor hub and hinge	[lbs]
W_{h_s}	Weight horizontal tail surface	[lbs]
W_{hyd}	Weight hydraulic systems	[lbs]
W_{lg}	Weight landing gear	[lbs]
w_m	Width of half the fuselage	[m]
W_{MV}	Weight manufacturing variation	[lbs]
$W_{nacelles}$	Weight nacelles	[lbs]
$W_{particles}$	Weight of particles emitted into the atmosphere	[kg]
W_{pl}	Payload weight	[kg]
$W_{P.SS}$	Weight propulsion subsystem	[lbs]
w_r	Width of fuselage box	[m]
w_s	Section length	[m]
$W_{S.C}$	Weight system controls	[lbs]
$W_{spreader}$	Weight of the spreader bar	[N]
W_{v_r}	Weight vertical tail rotor	[lbs]
W_{v_s}	Weight vertical tail surface	[lbs]
X	Forces in X-direction	[N]
x_v	Vertical tail surface arm	[m]
Z	Forces in Z-direction	[N]
α_{stall}	Airfoil stall angle	[deg]
α_0	Zero lift angle of attack	[deg]
α	Angle of attack	[deg]
β	Mounting angle	[deg]
Δn	Turbulence coefficient	[-]
δ_{tip}	Duct tip clearance	[m]
δ	Duct induced velocity factor	[-]
$\dot{m}_{fuel}$	Fuel mass flow	[kg/s]

ϵ	Angle of attack	[rad]
η_{gen}	Generator efficieny	[-]
η_0	x distance to shear center	[m]
γ	Isentropic expansion factor	[-]
μ_{Vne}	Never exceed advance ratio	[-]
μ	Dynamics viscosity	$[kg/s\ m]$
μ	Advance ratio	[-]
Ω_m	Rotational speed main rotor	[rad/s]
ω_v	Rotational speed vertical tail	[rad/s]
Ω	Rotational velocity	[rad/s]
ω	Induced velocity at far wake (Chapter 5)	[m/s]
ω	Rotational velocity (Chapter 6)	[rad/s]
ϕ	Inflow angle (Chapter 5)	[deg]
ϕ	Bank angle (Chapter 4)	[deg]
ϕ	Payload attachment angle	[deg]
ρ_{cruise}	Cruise density	$[kg/m^3]$
ρ	Density	$[kg/m^3]$
ρ	Air density	[kg/m^3]
σ_d	Duct expansion ratio	[-]
σ_d	Diffuser expansion ratio	[-]
σ_{F_y}	Normal stress due to centrifugal forces	[Pa]
σ_{M_y}	Normal stress due to moments	[Pa]
$\sigma_{vonMises}$	Von Mises stress	[Pa]
σ_v	Von Mises stress	[Pa]
σ_x	Normal stress in x-direction	[Pa]
σ_y	Normal stress in y-direction	[Pa]
σ_z	Normal stress in z-direction	[Pa]
σ	Blade solidity	[-]
τ_{xy}	Shear stress in the xy-plane	[Pa]
τ_{xz}	Shear stress in the xz-plane	[Pa]
τ_{yz}	Shear stress in the yz-plane	[Pa]
τ	Shear stress	[Pa]
θ_d	Diffuser angle	[deg]
θ_f	Pitch angle fuselage	[rad]
θ	Angle at which the cable of the payload is attached	[rad]
ζ_0	y distance to shear center	[m]
$\#_{bolts}$	Number of bolts	[-]

List of Acronyms

Acronym	**Description**
ATC	Air Traffic Control
MMS	Mision Management System
ROI	Return of Investment
SWOT	Strengths Weaknesses Opportunities Treats
UAV	Unmanned Aerial Vehicle
UD	Uni Directional
VMS	Vehicle Management System

List of Figures

List of Tables

Contents

Summary

Natural disasters have increased in frequency and severity in recent years [42]. Due to the climate change this trend is expected to continue. Especially poorer and less developed countries struggle to cope with these problems without help from the international community. In cooperation with the Netherlands Red Cross, the Hospitainer company has developed shipping container based hospitals to provide medical aid for the people affected. Their transportation within the disaster areas where most of the infrastructure is destroyed remains a challenging problem.

This report solves the transportation problem by proposing a design for a twin-lift rotorcraft system capable of deploying the Hospitainer units by air negating the need for roads. The system has been baptised LIFT^2 which is an acronym for Lifting Innovation For Transportation. The mission requires the transportation of a container with a maximum weight of 10 ton over a range of 200 km. After autonomously finding a safe drop-off point for the payload, the rotorcraft should be able to return to its base without refuelling. The rotorcraft cruise at an altitude of 1500 m, with an average speed of 80 kts. One hospital should be placed within 24 hours which corresponds to six missions per day.
The proposed LIFT^2 system complies with all the stakeholder requirements. Ducted fans are chosen as the most suitable rotorcraft type. Therefore, the fuselage width scales with the main rotor radius which are 14.3 m and 6.63 m respectively. For control three tail rotors are chosen, two horizontal ones to provide pitch and roll control and one vertical fenestron to provide anti-torque and yaw control. While the width is determined by the main rotor diameter, the length is set by arms of the tail rotors and is 22.2 m. The height of the fuselage of 1 m is determined by the required value needed for storage and the duct length of the main rotor. Fuselage and leading gear are made of an aluminium alloy while the rotor blades are made of Titanium alloy. This leads to a maximum take-off weight of one rotorcraft of 9324kg.
It has been opted to use ducted fans as they require less power compared with conventional helicopters and have additional benefits with regard to ingestion safety and noise emission. As the design is novel, the development cost of 7.1 billion USD is rather high. A drawback is the inability to perform a safe landing in autoration in case of failure of both engines. It is an inherent characteristic of the ducted fan design that still needs to be overcome. With a power installed of only 2531kW the advantage of the ducted fan becomes evident. In line with the low power consumption, the required fuel per mission is 1710kg and the NOx emission per mission is only slightly above 7 kg.
Being an unmanned system the communication between ground station and aerial vehicles is of uttermost importance for the LIFT^2. For line-of-sight communication the C-band is used, while beyond line-of-sight communication is achieved via satellite relay on the K_u-band. The rotorcraft work in a master-slave configuration. Longitudinal stability of a single rotor has been achieved by applying a PID controller.

It can be concluded that the LIFT^2 system whose design is presented in this report is capable to perform the mission requested by Hospitainer. Due to its versatile nature it is not limited to the mission outlined but can also provide further aid in the disaster area by for instance aiding in search and rescue operations.
The conceptual design presented in this report although capable of performing the mission can be optimised further. Due to time constraints it has not been possible to carry out more than one iteration which should be resolved during future investigations. In addition the high degree of simplification, which has been forced by the time constraint, should be traded for more accuracy.

1. Introduction

Natural disasters have increased in frequency and severity in recent years [42]. Experts see the climate change as the cause and expect the trend to continue [1]. Especially poorer and less developed countries struggle to cope with these problems on their own and require help from the international community. The Red Cross has made it its mission to step in in such cases, providing resources and manpower to help mitigate the consequences for those affected. Supported by the Red Cross the Hospitainer company designs mobile hospitals capable of rapid deployment. One mobile hospital is made of six standard sized shipping containers for smooth transportation by land and sea. As experience has shown this in 2013 after the typhoon Haiyan passed the Philippines, this is still not sufficient to reach an adequate response time. Together with the Netherlands Red Cross, Hospitainer Company issued the request of designing an aerial vehicle configuration capable of transporting containers to the disaster area and hence enabling a faster deployment of medical aid.

Since the infrastructure in the disaster areas is limited, the aerial vehicle should be capable to perform its mission without the use of an airfield. In line with this requirement, a rotorcraft has been chosen as a suitable design option in earlier stages of the project. The mission requires the transportation of a container with a maximum weight of 10 tonnes over a range of 200 km. After autonomously finding a safe drop-off point for the payload, the rotorcraft should be able to return to its base without refuelling. One possible solution to the problem is the design of one rotorcraft carrying the total load. However, this solution is limited when one desires to lift more weight. Therefore a coupling between more aerial vehicles can be designed such that these aerial vehicles will carry the load together. Some theoretical work on the stability and control of a twin-lift system has been published by Schrage [68] and Curtiss [11]. Both authors conclude that the twin-lift system is inherently unstable which gives it unfavourable flight characteristics. In addition to the theoretical work, tests has been performed with two Chinook helicopters. The tests confirmed that flying in twin-lift configuration is possible, but results in a workload too high for the pilots to manage. With the current development in the sector of remote controlled aerial vehicles the twin-lift system becomes a feasible lifting solution for normal operations as the problem with the workload intensity is solved by the use of computers. In the earlier stage of the design a trade-off between different rotorcraft has shown the ducted fan to be the most suitable concept, resulting in lower power consumptions compared with conventional rotorcraft. A detailed description of all requirements and the trade-off can be found in the earlier reports [26] [27]. The complete system has been called *LIFT^2, taking transportation to a higher order*. Here, LIFT is an acronym for Lifting Innovation For Transportation, since the twin-lift system with autonomous ducted fans is an innovative transportation concept. The purpose of this report is to further elaborate on the unmanned ducted fan design and present the conceptual design of LIFT^2.

The mission analysis is revised in Chapter 2. Based on a market analysis (Chapter 3), the initial sizing of the rotorcraft is performed and described in Chapter 4. An aerodynamic, structural and stability analysis are carried out on the initial concept and they are described in Chapter 5, 6 and 7 respectively. Based on the recommendations of these disciplines, the sizes of the rotorcraft are revised and the final lay-out is presented in Chapter 8. A performance analysis on the final concept is discussed in Chapter 9. Based on the final concept, the communication flow and the system architecture are worked out in Chapter 10. The operations and logistics of the twin-lift concept is presented in Chapter 11. In Chapter 12, a risk analysis is performed of the final concept. Afterwards, the Reliability, Availability, Maintenance and Safety of the concept are discussed in Chapter 13. A sustainability analysis is performed in Chapter 14, followed by a cost analysis in Chapter 15. Finally, in Chapter 16, the post design activities and recommendations are discussed after which the report is concluded in Chapter 17.

2. Mission Analysis

This chapter analyses the mission of the unmanned twin-lift system. The mission statement is presented in Section 2.1, followed by the stakeholder requirements set by Hospitainer, which transports containers to disaster areas, in Section 2.2. The mission statement and requirements are combined into the mission profile in Section 2.2.1.

2.1 Mission Statement

This project originates from a request by Hospitainer and TU Delft's scientific interest. Their combined interest is merged into a single mission statement, with which the end product should comply:

> *The system will allow the Red Cross to transport the Hospitainer to a disaster area at a distance of 200 km and return to the initial location, making use of a twin-lift system of aerial vehicles.*

2.2 Stakeholder Requirements

The most important requirements the design has to comply with, which are set by Hospitainer and the TU Delft are summarised here:

- The system shall provide lift using **twin-lift** technology.
- The system shall be able to fly **autonomously**.
- The complete system shall be able to transport a **payload of 10 tonnes** by air while lifting it.
- The system shall have a **cruise velocity of 80 kts**.
- The system shall have a **maximum velocity of 100 kts**.
- The system shall be able to transport its maximum payload over a **range of 200 km and return (200 km)** after the load is dropped, without refuelling.
- The system shall be able to **hover for 30 min.** during the mission.
- The system shall be able to perform **six mission per day**.

2.2.1 Mission Profile

The mission profile can be extracted from the mission statement and stakeholder requirements. This profile is shown in Figure 2.1.

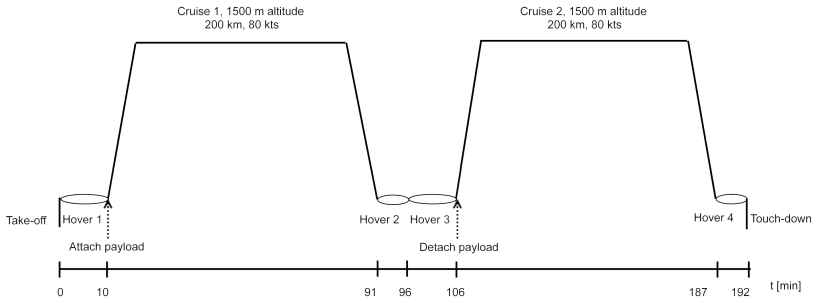

Figure 2.1: Mission profile

The mission consists of six phases; four hover phases and two cruise phases. The rotorcraft take off and hover for ten minutes, while the payload is being attached. After attaching the payload the rotorcraft climb to the cruise altitude of 1500 meter, where the first cruise stage starts. During this cruise the rotorcraft move to the disaster area. After descending, the second hover phase starts, during which the rotorcraft search for a suitable landing spot autonomously. During the third hover stage, which takes ten minutes, the payload is detached from the rotorcraft. After ascending again, the second cruise stage starts, in which the rotorcraft return back to the main base. The final descent is started and during the fourth hover, which takes five minutes, the rotorcraft search for a suitable landing spot.
The total hovering time during the mission is 30 minutes, as required by the stakeholder requirements. The total mission duration is 192 minutes. This should be fast enough to perform six missions per day as was required by Hospitainer. The design discussed in this document will be focussed on performing the mission described in this chapter.

3. Market Analysis

This chapter analyses the market targeted for the LIFT^2 system. In Section 3.1 the current rotorcraft market is analysed. In Section 3.2 competitors of the system are listed and a target cost for the system is determined based on the cost of the competitors. Section 3.3 describes the market trends and provides a forecast of the future market. Finally, Section 3.4 concludes with a SWOT analysis of LIFT^2.

3.1 Current Market

Helicopters are used more every year. Due to their flexibility, helicopters are widely spread throughout the market for aerial vehicles [84]. This section provides a clear picture of the current helicopter market.

The current helicopters market consists of three main customers: the commercial sector, military sector and governments. As can be seen in Figure 3.1, most helicopters are currently used for military purposes.

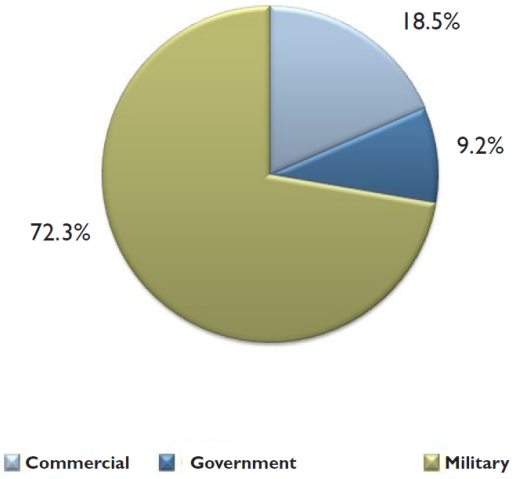

Figure 3.1: Helicopter market segmentation 2012 [54]

Rotorcraft can be used for many different applications because of their high flexibility. Their ability to hover is a characteristic that hardly any other aerial vehicle can perform. The wide range of functions that helicopters offer make it impossible to compete with all helicopters on the market. In the next section, the direct competitors of LIFT^2 are discussed.

3.2 Competitors

The payload weight of rotorcraft has been increasing over the years. This implies that a payload of ten tonnes is not an unusual amount for heavy lift rotorcraft nowadays. Other rotorcraft on the market are able to perform the requested mission from Hospitainer. These rotorcraft can be a threat to the profitability of LIFT^2. For this reason rivalling systems are presented and discussed in this section to identify these threats. The goal is to find the specific market niche for LIFT^2.

An example of a rotorcraft able to carry a load of ten tonnes is the Sikorsky S-64 Skycrane. Well known rotorcraft which are similar in performance are the Chinook and the Mil Mi 46. Although the Sikorsky CH-53K is over designed for the mission requested by Hospitainer since it can carry more than 16 tonnes. Therefore it is expected to be less efficient for the Hospitainer mission but still is a possible solution. Table 3.1 lists rotorcraft operating in the same payload range as LIFT^2 which makes them potential threats.

Table 3.1: Rivalling products on the market

Rotorcraft	**Payload [kg]**	**Range with normal payload [km]**
Sikorsky S-64	10000 [41]	400 [41]
Mil Mi 46	10000-12000 [49]	400 [49]
Chinook CH-47SD	12284 [48]	1205 [48]
Sikorsky CH-53K (Super Stallion)	16329 [46]	840 [46]

The unit price of the Chinook CH-47SD is estimated to be 32 million euro [48]. Having been produced in high numbers this rotorcraft has a relative low purchase price. The low acquisition costs of the Chinook are a potential threat to the system. Since research and development costs for the autonomous twin-lift system are expected to be very high, it might not be comparable to the Chinook with regards to the unit price.
However, LIFT^2 enters completely new parts of the market at the same time. Apart from being just a single heavy-lift rotorcraft, the two rotorcraft in the twin-lift system could be used individually making the system more versatile than its competitors. This twin-lift concept has not entered the market yet, due to the high pilot workload associated with the flight configuration. With the advancement in unmanned aerial vehicle technology the application of the twin-lift concept is possible now.

Besides the conventional piloted helicopters there are now some UAV systems under-development. Among these are the Boeing A160 'Hummingbird' [7], Boeing MD 530 ULB 'Little bird' [43], Northrop Grumman MQ-8 'Fire scout' [45] and the Kaman K-Max UMMH [44]. Out of these only the K-Max is capable of lifting a considerable load at 2721 kg, which is still less than offered by the separate LIFT^2 rotorcraft. Thus existing unmanned rotorcraft should not pose an accountable threat as competitors.

3.3 Future Market

Looking at forecasts for the market development, the share of the three main customers is not expected to shift significantly until 2021, as can be seen in Figure 3.2.

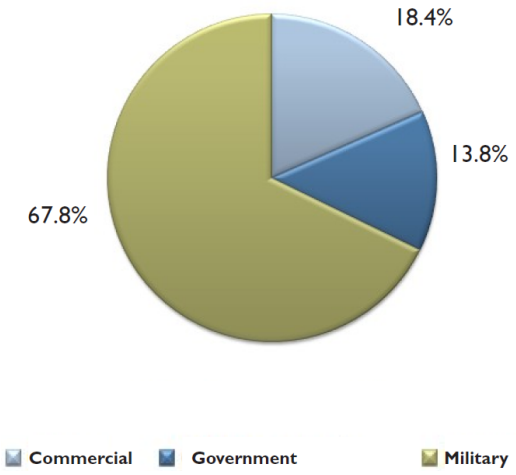

Figure 3.2: Expected helicopter market segmentation 2021 [54]

However, within the different sectors a shift in market shares of different helicopters is expected to take place. The largest expected growth in both civil and military categories is expected for medium helicopters with a growth factor between 58 and 73 percent between 2012 and 2021 as seen in Figure 3.3. The heavy cargo helicopters are expected to experience a rise of approximately 7 to 9.5 percent. LIFT^2 will probably fall somewhere around the border between a medium and heavy rotorcraft.

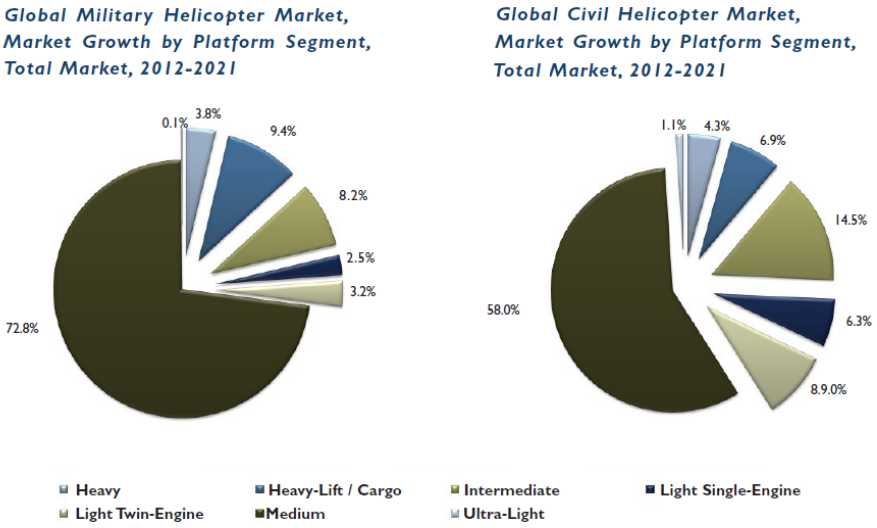

Figure 3.3: Market growth by segment from 2012-2021 [54]

The offshore market is expected to account for the largest rise in demand of rotorcraft in 2014 corresponding to the market growth witnessed in offshore drilling [76]. This market requires medium to heavy-lift rotorcraft for a variety of missions ranging from supplying the drilling rigs, search & rescue and immediate delivery of spare parts. These platforms are located relatively close to the coast as shown in Figure 3.4.

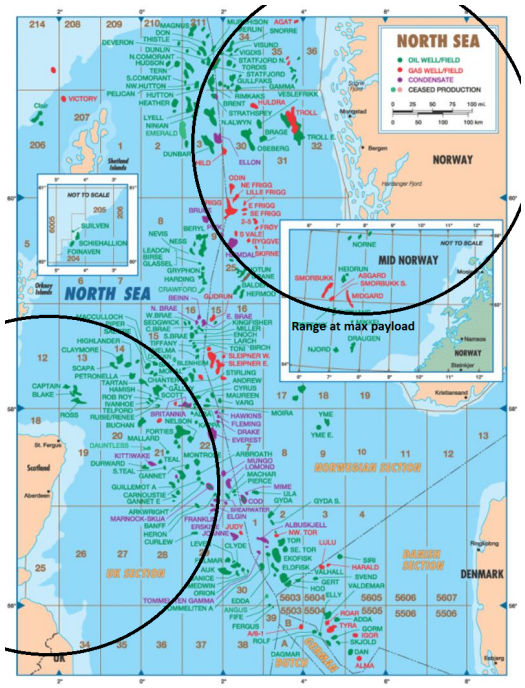

Figure 3.4: Drilling activities in the North Sea

This figure depicts the drilling activities in the North Sea, where the two black circles indicate a distance of two hundred kilometres around the cities Aberdeen and Bergen. The range indicated is considered while LIFT^2 is carrying its maximum payload of 10 tonnes, still allowing for a return flight. However, with a smaller payload this range can be considerably increased such that the whole area shown would be within reach opening up a new market. Companies such as Damen Shipyards are interested in such missions, as they are interested in a twin-lift helicopter system for transporting supplies to locations at sea.
Furthermore, with its payload to range ratio, LIFT^2 is perfectly suited to operate in fire-fighting missions. Global warming is the one of the main hazards of our age so these type of missions will become more and more relevant in the near future. In the helicopter market the general trend is shifting towards more autonomous operations and multi-purpose rotorcraft [54]. More and more manufacturers are developing unmanned and autonomous rotorcraft, eliminating risks for the pilot. The key benefits of LIFT^2 are that it will be capable of performing autonomous supply missions and take up a variety of other tasks. Designing the concept as a modular system would thus certainly allow it to take up multiple roles in distinct markets.

3.4 System SWOT Analysis

The advantages and disadvantages of LIFT^2 are summarised in a SWOT Analysis. SWOT stands for **S**trength, **W**eakness, **O**pportunities and **T**reats and is a common way to analyse a project or process. The SWOT Analysis is summarised in table 3.2 and further elaborated on in the following subsections.

Table 3.2: SWOT Matrix for LIFT^2

Strengths	**Weaknesses**
S1: No pilots at risk S2: Reduced controller workload S3: Autonomous operations S4: Decent range at heavy payload	W1: Crash risk W2: High R&D costs
Opportunities	**Threats**
O1: Multi-purpose operations O2: Heavy-lift with medium helicopters O3: Global warming	T1: People's perception T2: Lack of legislation

3.4.1 Strengths

S1: The unmanned operations of the LIFT^2 eliminate the risk of pilot casualties.
S2: The unmanned on-board control systems reduce the workload induced by the twin-lift configuration. In this case this workload would have fallen to the controller on the ground. Only one controller is needed as opposed to two pilots in a medium to heavy rotorcraft.
S3: The autonomous operations allow LIFT^2 to make basic decisions, further reducing the controller's workload.
S4: LIFT^2 offers a maximum payload of ten tonnes transported over a distance of two hundred kilometres, including return flight without payload afterwards. This is more than the Boeing CH-47 Chinook and the Mi-26 offer [25].

3.4.2 Weaknesses

W1: Two rotorcraft are confined in airspace when trying to carry a load together. This increases the possibility of collisions and increases the workload of the (auto)pilot.
W2: There is no working unmanned twin-lift system. Thus the development cost for the system are high and this might translate to a relatively high unit cost.

3.4.3 Opportunities

O1: LIFT^2 offers the opportunity to perform various missions in different niches in the market, these have been described in Section 3.3 (e.g. off-shore supplying, fire fighting and construction works).
O2: There is a limit to the lifting capacity of current rotorcraft. The relationship between the lifting capacity and the size of the rotorcraft follows the square-cubed law, effectively limiting the payload mass that can be carried by a single rotorcraft. By using twin-lift rotorcraft systems the advantages of rotorcraft transport can also be made available for heavy cargo which currently is restricted to other transportation means.
O3: The cascading effect of global warming will possibly cause an increase in natural disaster and outbreak of tropical diseases [50], resulting in the increasing need for emergency supplies and hospitals.

3.4.4 Threats

T1: On of the biggest threats to the concept is the generally perceived safety issue of UAVs. People tend to be afraid of unmanned vehicles especially if they operate autonomously. This might lead to protest and reputation issues or even flight prohibitions in some countries.
T2: Another threat to the project is the lack of a clearly defined certification process. Currently the legislation is behind on certification regulations for UAVs. This is expected to change soon and the certification regulations might introduce killer requirements. It might also lead to a dragged out certification process and a significant cost overshoot.

4. Sizing

Following from the mission analysis and the requirements stated in Chapter 2, the general sizing of the ducted fan design is explained in this chapter. Two identical rotorcraft have to transport a payload of 10 tonnes for 200 km and return back to base. The mission includes thirty minutes hovering time. The updated mission profile was presented in Chapter 2, which will be used for the initial sizing of the rotorcraft.
The ducted fan concept presented in the mid term report uses two rotorcraft in twin-lift configuration, separated by a spreader bar in between the slings. It has a single main rotor and a fenestron to counteract the torque produced by the main rotor. Pitch, yaw and roll control were assumed to be provided by a swash plate in the main rotor. However, tilting the blades with respect to the duct would lead to a large loss in lift efficiency. Furthermore, for the high number of blades in the design, a swash plate would become too complex. Therefore, the decision was made to omit the swash plate from the design and instead use two horizontal tail rotors at the back of the rotorcraft. These rotors will provide part of the required thrust to lift the payload, and furthermore can be used to trim the rotorcraft and to provide pitch and roll control. The final concept consists of a large main rotor, which is fixed in a duct, two horizontal tail rotors, fixed in a duct and a fenestron as vertical tail rotor.

This chapter starts with a second order weight estimation in Section 4.1. The operational empty weight, fuel weight and payload weight are updated. Section 4.2 discusses the power calculations and the sizing of all main components. During the sizing process, iterations were performed based on the recommendations of the aerodynamics, structures and stability and control disciplines. This chapter states the considerations that influenced the design, focussing on the design of a single rotorcraft that can lift half of the required payload to be transported.

4.1 Second Order Weight Estimation

The initial weight estimation performed in the mid term review report determined the maximum take-off weight of the ducted fan concept to be 10517 kg [27]. This initial calculation was mainly based on statistics. In this section a more refined weight estimation is performed. The maximum take-off weight is divided into operational empty weight, fuel weight and payload weight, which are discussed in the following subsections. An initial power assumption was made and was iterated. The final input parameters for the weight estimation are determined in Section 4.2. Since the entire design procedure is based on iterations, the weight estimation was chosen as a starting point for the discussion of the initial design.

4.1.1 Operational Empty Weight

The operational empty weight is estimated using the method presented in Prouty, Helicopter Performance, Stability and Control [69]. This method is based on statistics of conventional helicopters using the method of multiple linear regression. Therefore, the weight of each subsystem is multiplied with a factor to account for the fact that the current design is an unmanned ducted fan. All equations in this calculation take imperial units as input and return the weight in pounds. Table 4.1 presents the used factors per subsystem and the final weights in kilograms. All inputs used for this weight estimation can be found in Section 4.2, or are presented with the corresponding equation.

The weight of the main rotor blades is calculated using Equation (4.1). Since this weight should not deviate from conventional helicopters a factor of 1 is used.

$$W_{b_m} = 0.026 b_m^{0.66} c_m r_m^{1.3} (\Omega_m r_m)^{0.67} \tag{4.1}$$

Equation (4.2) calculates the weight of the main rotor hub and hinge. The multiplication factor used is 0.9. Since the design does not use a swash plate, the hub will be less complex than for a conventional rotorcraft. The polar moment of inertia of the main rotor is assumed to be 8000 slug ft^2 after investigating helicopters with a similar rotor size and number of blades in Prouty [69].

$$W_{h_m} = 0.0037 b_m^{0.28} r_m^{1.5} (\Omega_m r_m)^{0.43} (0.67 W_{b_m} + \frac{gJ}{r_m^2})^{0.55} \tag{4.2}$$

The horizontal and vertical tail surface weights are calculated using Equations (4.3) and (4.4) respectively. A multiplication factor of 1 is used for both weights, since no inherent difference is expected between the design and a conventional helicopter. The number of tail rotor gearboxes in Equation (4.4) is assumed to be one.

$$W_{h_S} = 0.72 A_h^{1.2} AR_h^{0.32} \tag{4.3}$$

$$W_{v_S} = 1.05 A_v^{0.94} AR_v^{0.32} (No. tail gearboxes)^{0.71} \tag{4.4}$$

Instead of a conventional tail rotor a fenestron is selected for this design. The shroud around this fenestron and the higher blade solidity lead to a higher weight [24]. Therefore, a factor of 1.2 is used on top of Equation (4.5) to determine the vertical tail rotor weight. The transmission horsepower rating is assumed to be equal to the installed power of the engines as described in Section 4.2.5.

$$W_{v_r} = 1.4 r_v^{0.090} \left(\frac{hp_{rating}}{\Omega_m} \right)^{0.90} \tag{4.5}$$

Prouty's method does not include horizontal tail rotors. To determine the weight of these rotors, Equation (4.5) is used again, with the horizontal tail rotor dimensions as input. This result is multiplied by two, since two horizontal tail rotors are used.
The weight of the fuselage is determined using Equation (4.6). Since the equation uses the wetted fuselage area and the length of the fuselage as input, no extra factor is required to account for the unconventional fuselage shape. The wetted fuselage area is the area exposed to the flow and is calculated using Equation (4.7).

$$W_{fus} = 6.9 \left(\frac{MTOW}{1000} \right)^{0.49} l_{fus}^{0.61} (S_{wet_{fus}})^{0.25} \tag{4.6}$$

$$S_{wet_{fus}} = \left(\left(\frac{w_{fus}}{2} \right)^2 - r_m^2 \right) \pi + r_m (l_v - r_v - r_m) \tag{4.7}$$

Equation (4.7) determines the area that is exposed to the flow in two parts: the ring around the main rotor and the tail arm. Since l_v is defined from the main rotor hub until the vertical tail rotor hub, these distances have to be subtracted from l_v as seen in Equation (4.7). A graphical representation is given in Figure 4.1. These values are determined in Section 4.2.7.

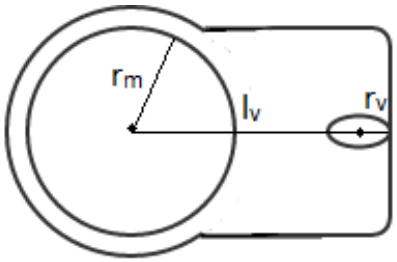

Figure 4.1: Wetted fuselage area

The landing gear weight is found using Equation (4.8). In this equation the number of wheel legs is assumed to be three, in order to avoid tipping over after landing. The weight is increased by 10% to account for a retractable landing gear.

$$W_{\text{lg}} = 40 \left(\frac{MTOW}{1000} \right)^{0.67} (No.wheellegs)^{0.54} \tag{4.8}$$

The weight of the nacelles is found using Equation (4.9). The number of engines and their weight is determined in Subsection 4.2.5. The wetted area of the nacelles is assumed to be zero, since they are embedded in the fuselage.

$$W_{nacelles} = 0.041 (W_e)^{1.1} (No.engines)^{0.24} + 0.33 (S_{wet_N})^{1.3} \tag{4.9}$$

Equation (4.10) determines the weight of the engine installation. A factor of 1.2 is used to account for the complex installation of the engines, since the drive train has to run along support struts underneath the main rotor.

$$W_{eng} = (W_e)(No.engines) \tag{4.10}$$

The weight of the propulsion subsystem of the design, which consists of pumps and valves, is determined using Equation (4.11). No extra factor is used with respect to conventional helicopters.

$$W_{P.SS} = 2 W_{eng}^{0.59} (No.engines)^{0.2} \tag{4.11}$$

Equation (4.12) calculates the weight of the fuel systems, which mainly consists of the fuel tanks. To calculate the capacity of the fuel, the density of jet A-1 fuel (0.804 kg/L [5]) was used together with the fuel weight calculated in Subsection 4.1.2. The number of fuel tanks is assumed to be four, so the fuel can be divided in the ring around the main rotor.

$$W_{F.S} = 0.43 (F_{cap})^{0.77} (No.tanks)^{0.59} \tag{4.12}$$

To determine the weight of the drive train system, Equation (4.13) is used. The rpm of the engine selected in Section 4.2.5 is 21000. The tail rotor horsepower is assumed equal to the maximum power required by the tail rotor (Section 4.2.2). The number of gearboxes is still assumed to be one.

$$W_{D.S} = 13.6(hp_{rating})^{0.82}\left(\frac{rpm_{eng}}{1000}\right)^{0.037}\left[\left(\frac{hp_v}{hp_{rating}}\right)\left(\frac{\Omega_m}{\Omega_v}\right)\right]^{0.068}\frac{(No.gearboxes)^{0.066}}{\Omega_m^{0.64}} \tag{4.13}$$

The weight of the system controls is computed using Equation (4.14). Equation (4.15) is used to calculate the weight of the hydraulic system of the concept.

$$W_{S.C} = 36b_m c_m^{2.2}\left(\frac{\Omega_m r_m}{1000}\right)^{3.2} \tag{4.14}$$

$$W_{hyd} = 37b_m^{0.63}c_m^{1.3}\left(\frac{\Omega_m r_m}{1000}\right)^{2.1} \tag{4.15}$$

The weight of the electrical systems in the rotorcraft are computed using Equation (4.16). Afterwards a factor 1.2 is applied, since the design uses more electronic components than a conventional helicopter in the form of cameras and other sensing equipment, since it is unmanned. For the furnishing and equipment Prouty gives a low, medium and high weight. Since this concept is unmanned little furnishing is required. The equipment aimed at a crew can also be omitted. Therefore the lowest value is chosen and a factor of 0.5 is applied. Equation (4.17) applies to this case.

$$W_{EL} = \frac{9.6(hp_{rating})^{0.65}}{\left(\frac{MTOW}{1000}\right)^{0.40}} - W_{hyd} \tag{4.16}$$

$$W_{FE} = 6\left(\frac{MTOW}{1000}\right)^{1.3} \tag{4.17}$$

Since the ducted fan design is flying unmanned, no air conditioning is required. Therefore, the weight of the air conditioning and anti-ice system are multiplied with a factor 0.5. Equation (4.18) calculates the weight of the system. The manufacturing variation in Prouty is calculated using Equation (4.19). The ducted fan concept is unconventional and not proven at such a large scale. Therefore, a factor of 1.2 is applied to the extra weight caused by manufacturing variation.

$$W_{AC\&AI} = 8\left(\frac{MTOW}{1000}\right) \tag{4.18}$$

$$W_{MV} = 4\left(\frac{MTOW}{1000}\right) \tag{4.19}$$

For the auxiliary power plant a weight of 150 lbs is assumed [69]. For the avionics system Prouty gives four options for a high, low or medium weight. Since the detection system with all its cameras and sensors is seen as part of avionics, the highest weight is taken. This leads to a weight of 400 lbs for the avionics system [69].
Two systems were completely omitted from the weight estimation proposed by Prouty: the cockpit controls and the pilot instruments. Both systems are unnecessary in the unmanned design of the ducted fan rotorcraft.

All resulting component weights and the operational empty weight are summarised in Table 4.1. The resulting operational empty weight of the concept is concluded to be 3258 kg. This value is used in the determination of the maximum take-off weight in Section 4.1.4.

Table 4.1: Second order weight estimation of components

Subsystem	*Factor*	*Weight [kg]*
Main rotor blades	1	233.4
Main rotor hub	0.9	157.7
Horizontal stabiliser	1	17.2
Vertical stabiliser	1	13.7
Vertical tail rotor	1.2	40.9
Horizontal tail rotors	1	74.6
Fuselage	1	741.0
Landing gear	1.1	273.8
Nacelles	1	17.7
Engine installation	1.2	476.8
Propulsion subsystem	1	56.8
Fuel system	1	33.7
Drive system	1	391.4
System controls	1	70.8
Hydraulics	1	39.6
Electrical	1.2	206.4
Furnishing & equipment	0.5	69.3
Air conditioning & anti-ice	0.5	37.3
Manufacturing variation	1.2	44.8
Auxiliary power plant	1	68.0
Avionics	1	181.4
Operational empty weight		**3258**

4.1.2 Fuel Weight

The second contribution to the maximum take-off weight comes from the fuel weight. The fuel weight of a specific mission segment is calculated using Equation (4.20).

$$W_{fuel} = SFC \cdot P_{req} \cdot t_{mission} \tag{4.20}$$

The specific fuel consumption depends on the engines, which are selected in Section 4.2.5. For the chosen engines it is 0.282 kg/kW·h. The mission time per segment was determined in Chapter 2. The power required for each part of the mission is determined in Section 4.2.4. The required power, mission time and required fuel weight are summarised in Table 4.2. To determine the total fuel weight 5% reserve fuel is taken into account.

Table 4.2: Fuel weight estimation

Mission segment	$t_{mission}$ [h]	P_{req} [kW]	W_f [kg]
Hover 1	0.167	515	24.22
Cruise 1	1.35	1271	484.2
Hover 2	0.083	1652	38.87
Hover 3	0.167	1652	77.73
Cruise 2	1.35	478	177.16
Hover 4	0.167	515	12.11
Total			**855**

The total fuel weight necessary for the mission is 855 kg, which will be used in the determination of the maximum take-off weight in Section 4.1.4.

4.1.3 Payload Weight

The payload weight of an individual rotorcraft consists of two contributions: half of the weight of the container to be transported and half the weight of the spreader bar, which is used to keep the rotorcraft apart. A schematic overview of the lifting configuration is presented in Figure 4.2. The maximum container weight is 10 tonnes as determined by the stakeholder requirements, presented in Chapter 2.

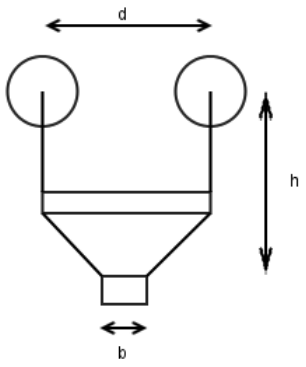

Figure 4.2: Lifting configuration with spreader bar

The initial sizing of the spreader bar is necessary to compute the actual payload weight. An initial structural analysis performed in the the initial investigation determined the weight of the spreader bar as a function of the distance between the rotorcraft d and between the bar and payload h. To allow for sufficient safety in flight, the rotorcraft will fly four main rotor radii apart [68]. The distance to the payload is assumed to be twice the main rotor radius. This main rotor radius is determined in Section 4.2.1. The spreader bar is sized to ensure that no buckling occurs in the material. The resulting weight of the cylindrical spreader bar, which is assumed to be made from aluminium, was found to be 421 kg in the mid term review report [27]. If this weight is distributed over the two rotorcraft, the resulting maximum payload weight of a single rotorcraft is 5211 kg.

4.1.4 Maximum Take-Off Weight

In the previous subsections the revised operational empty weight, fuel weight and payload weight were calculated. These values can be added to compute the maximum take-off weight. The operational empty weight is found to be 3258 kg, the total fuel weight 855 kg and the payload weight 5211 kg. Therefore, the maximum take-off weight of a single rotorcraft is equal to 9324 kg. This second order estimation is lower than the value of 10517 kg found in the mid term report. This difference is caused by the more accurate fuel weight estimation and the revised operational empty weight.

The weight of the rotorcraft when cruising back to base after payload delivery can be used to accurately calculate the required power for the second cruise of the mission. It is calculated as the maximum take-off weight minus the payload weight and the fuel required for the mission segments until the second cruise. Computing this leads to a weight of 3487 kg on the cruise back to the base.

4.1.5 Centre of Gravity

To determine the thrust needed by the horizontal tail rotors to keep the rotorcraft longitudinally trimmed, the distance from the rotors to the centre of gravity was computed. To determine the centre of gravity the three types of weight discussed in the previous subsections are considered. In this chapter the location of every subsystem is discussed. To determine the centre of gravity the following equation is used.

$$cg = \frac{\sum W_i \cdot d_{nose_i}}{\sum W_i} \tag{4.21}$$

The weight of all separate contributions have been calculated in the previous subsections. The distance from the nose of the rotorcraft to each subsystem is shown in Table 4.3. The position of the centre of gravity with respect to the nose is calculated for three different loading cases and shown in Table 4.4.

In order to trim the rotorcraft, the horizontal tail rotors have to counteract the moment produced by the main rotor. To allow the horizontal tail rotors to provide a lifting force upwards, the centre of gravity should be positioned between the main rotor hub and the control rotors as displayed in Figure 4.3. Since one would like to design the horizontal tails as small as possible to limit the drag, the centre of gravity should be positioned as closely behind the main rotor hub as possible.

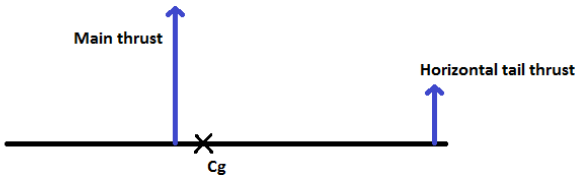

Figure 4.3: Longitudinal equilibrium around centre of gravity

The center of gravity can be actively controlled by changing the location of various subsystems. To calculate the center of gravity, all systems that have a fixed position are placed first. Afterwards, the other subsystems are shifted to get the centre of gravity as close behind the main rotor as possible, since this results in the smallest possible horizontal tail rotors due to the larger tail arm. All dimensions used to calculate the distance from the nose to a subsystem are determined in Section 4.2.

The main rotor blades are located at the centre of the main rotor, which is equal to the front clearance plus the radius of the rotor. The hub of the main rotor is then located at the same position. The position of the horizontal and vertical stabilisers is found by adding the horizontal or vertical tail arm (l_h and l_v) to the position of the main rotor hub. The vertical and horizontal tail rotors are located at the position of respectively the vertical and horizontal stabiliser.

The weight of the fuselage, landing gear, hydraulics, electronics, anti-ice, furnishing, equipment and manufacturing variation are assumed to be positioned at half the total fuselage length l_{fus}, assuming that their weight is evenly distributed throughout the fuselage. The nacelles and engine installation are positioned at the location of the engines. Since the engines have to reach both the main rotor and all three tail rotors, they are positioned behind the main rotor. To keep the centre of gravity from shifting too far backwards they are positioned directly after the main rotor. The largest part of the drive train runs from the engines to the centre of the main rotor. Therefore the position of the drive train is assumed to be exactly in between these two. The propulsion subsystem is located at the same position, since its centre of gravity is positioned in between the fuel system and the engines. The weight of the fuel is assumed to act at the centre of the main rotor, since it is located in the ring surrounding the main rotor. The payload weight is also assumed to act at the centre of the main rotor, since the four attachment points are located around the main rotor as will be explained in Section 6.5.

The last two components that have to be added are the auxiliary power plant and the avionics. Before adding these into the calculation the centre of gravity was positioned too far aft. Therefore both the avionics subsystem and the auxiliary power plant are installed in front of the main rotor. All locations in meters are summarised in Table 4.3.

Table 4.3: Location of components measured from nose

Subsystem	*Location [m]*	*Weight [kg]*
Main rotor blades	7.95	233.4
Main rotor hub	7.95	157.7
Horizontal stabiliser	18.95	17.2
Vertical stabiliser	19.95	13.7
Vertical tail rotor	19.95	40.9
Horizontal tail rotors	18.95	74.6
Fuselage	10.33	741.0
Landing gear	10.33	273.8
Nacelles	14.91	17.7
Engine installation	14.91	476.8
Propulsion subsystem	11.43	56.8
Fuel system	7.95	33.7
Drive system	11.43	391.4
System controls	10.33	70.8
Hydraulics	10.33	39.6
Electrical	10.33	206.4
Furnishing & equipment	10.33	69.3
Air conditioning & anti-ice	10.33	37.3
Manufacturing variation	10.33	44.8
Auxiliary power plant	0.5	68.0
Avionics	0.5	181.4
Fuel	7.95	855
Payload	7.95	5211

The centre of gravity with respect to the nose is computed for two cases: the empty and the fully loaded rotorcraft. The results are summarised in Table 4.4.

Table 4.4: Location of centre of gravity with respect to nose

Case	*cg [m]*
Empty	9.85
Full	8.48

For the fully loaded rotorcraft, this means that the centre of gravity is located 0.53 m behind the main rotor centre. This is acceptable in terms of stability and control as will be shown in Chapter 7.

4.2 Power Calculations and Sizing

This section evaluates the sizing of all parts of the rotorcraft starting with the main rotor sizing in Section 4.2.1, followed by the horizontal and vertical tail rotor sizing in Sections 4.2.3 and 4.2.2 respectively. Determining the sizes allows for power calculations and an engine selection in Section 4.2.5. The final fuselage sizing is explained in Section 4.2.7. Since all decisions are made in an iterative process, this is elaborated on in Section 4.2.8, followed by a verification and validation of the design tool.

Since no comprehensive tool exists for the design of a ducted fan with the rotors not directly facing the incoming flow, Prouty's method used for helicopters has been altered to create a new sizing tool [69]. After the initial design steps have been taken, the aerodynamics, structures, stability and control of the system are evaluated in Chapters 5, 6 and 7. Considerations and design flaws discovered there are iterated in the main design tool and explained in this section.

4.2.1 Main Rotor Sizing

The main design steps that have to be taken while sizing the main rotor of the design are shown in Figure 4.4. These steps are elaborated on in this section.

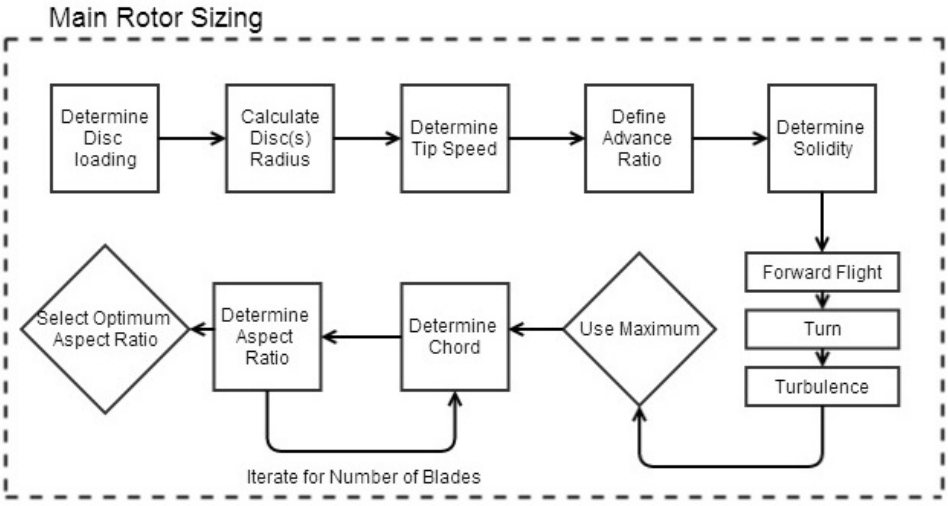

Figure 4.4: Flow of main rotor sizing

Ducted fan designs generally have a higher disc loading than conventional helicopters, which is why a deviation from Prouty's approach is necessary [16]. An initial value for the disc loading of the main rotor is found using Equation (4.22), which is based on small scale ducted fan designs [22].

$$DL = \left(\frac{25 \cdot P_{inst}}{MTOW}\right)^2 \tag{4.22}$$

Since the disc loading is a sensitive parameter that determines the main rotor size and general dimensions, this parameter will later be used to tune the design to an optimal design. This iteration is explained in Subsection 4.2.8. The radius of the main rotor is calculated using Equation (4.23) [69].

$$r_m = \sqrt{\frac{MTOW}{\pi DL}} \tag{4.23}$$

The tip speed of the main rotor is determined using a regression line based on conventional helicopters as shown in Figure 4.5.

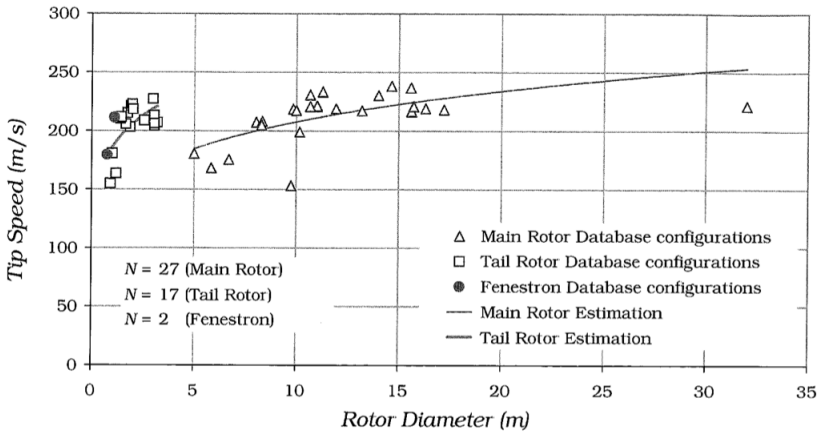

Figure 4.5: Rotor tip speed vs rotor radius [70]

The regression line based on the main rotor database (triangles) is used, since those resemble the main rotor tip speeds. The corresponding regression line is given by Equation (4.24).

$$V_{tip_m} = 140(2r_m)^{0.171} \tag{4.24}$$

The rotational speed of the rotor can be defined using Equation (4.25).

$$\Omega = \frac{V_{tip}}{r} \tag{4.25}$$

The advance ratio is defined as the ratio between the never exceed speed and the tip speed, where the never exceed speed is equal to 1.1 times the maximum flight speed. From the requirements the maximum speed was found to be a 100 kts [26].

$$\mu_{Vne} = \frac{1.1V_{\max}}{V_{tip_m}} = \frac{1.1V_{\max}}{\Omega_m r_m} \tag{4.26}$$

The blade solidity σ is defined as the ratio of the total area of the blades divided by the total disc area and is an important parameter in the design of the main rotor blades. Equation (4.27) will be used to determine the chord of the rotor blades.

$$\sigma = \frac{bcr}{\pi r^2} \tag{4.27}$$

From FAR regulations follows that σ has to be calculated for three different lift conditions [65] [27]:

- **FAR 29.175(b)** Forward flight at $1.1V_{ne}$
- **FAR 29.251** Turns with a roll angle of 30° at V_{ne} and continuous power
- **FAR29.341** Horizontal gusts of 30 ft/sec horizontal and vertical at $1.1V_{ne}$

The relationship between the advance ratio and the ratio between the thrust coefficient C_T and the blade solidity is shown in Figure 4.6.

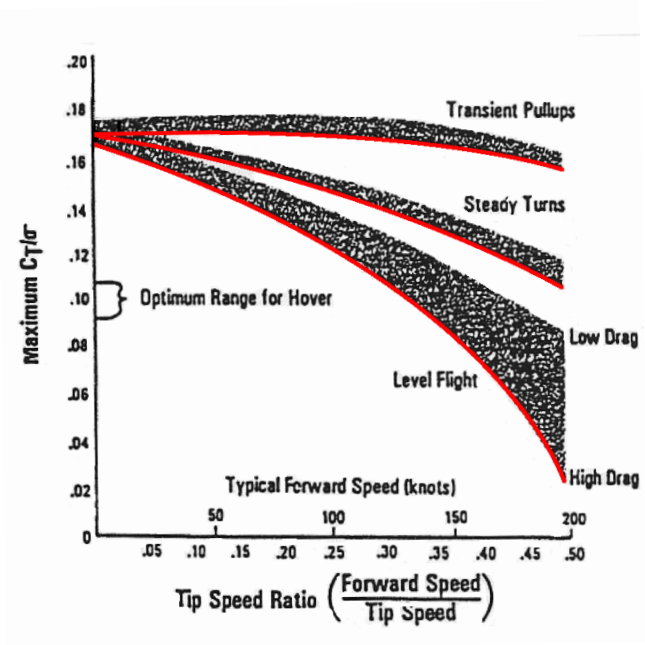

Figure 4.6: C_T/σ vs advance ratio μ (modified after [65])

From Figure 4.6 it can be seen that the ratio C_T/σ decreases for higher advance ratios. The smaller this ratio, the higher σ, which would result in a larger number of blades. Therefore, for each mode, the critical relation is the lower border of each area, indicated by the red lines. In order to maintain an efficient iteration process, coefficients of a fourth order polynomial have been derived to represent this border. The polynomials for transient pull ups (turbulence), steady turns and level flight are shown in Equations (4.28), (4.29) and (4.30) respectively.

$$\frac{C_T}{\sigma} = 0.90\mu^4 - 0.97\mu^3 + 0.24\mu^2 - 1.63 \cdot 10^{-2}\mu + 0.17 \tag{4.28}$$

$$\frac{C_T}{\sigma} = 1.27\mu^4 - 1.04\mu^3 + 3.51 \cdot 10^{-2}\mu^2 - 4.95 \cdot 10^{-2}\mu + 0.17 \tag{4.29}$$

$$\frac{C_T}{\sigma} = -1.90\mu^4 + 1.41\mu^3 - 0.75\mu^2 - 0.04\mu + 0.16 \tag{4.30}$$

As stated by the FAR requirements listed above, for level flight and transient pull-ups V_{ne} has to be multiplied by 1.1, when calculating the advance ratio. The last step to obtain the blade solidity is evaluating the thrust coefficient. Thrust in level forward flight is defined as a factor k_{dl} times the weight. This factor accounts for the download of the vertical drag on the fuselage since for a conventional helicopter the air propelled by the rotors is directed at the fuselage. The download factor is assumed to be 1, since the ducted fan in this design is embedded into the fuselage and no air is pushed

down on the fuselage. Equation (4.31) shows two other factors, firstly $n_z = 1/\cos(\phi)$. This factor applies during steady turns or when turbulence occurs. In this case ϕ is the maximum roll angle (30°) defined by the FAR requirements listed above. Secondly, the factor Δn, only applicable for the turbulent case, which is calculated using equation (4.32). The calculation of the ratio between the thrust of the horizontal tail rotors and main rotor is used as a factor, since the horizontal tail rotors provide part of the required lift. The computation of this factor depends on the centre of gravity and is explained in Section 4.2.3.

$$T_m = (1 + \Delta n - \frac{T_h}{T_m}) n_z k_{dl} MTOW \tag{4.31}$$

$$\Delta n = \frac{1}{4} C_{l_\alpha} \frac{V_g}{\Omega_m r_m} \tag{4.32}$$

The gust speed in this equation is 30 ft/s as found in the FAR29.341 requirement. The $C_{l\alpha}$ of the main rotor airfoil during the initial sizing is assumed to be 2π from thin airfoil theory [4]. In Chapter 5 this parameter will be further elaborated on.

The thrust can be expressed as a non-dimensional thrust coefficient C_T by dividing the thrust by the air density, disc area and tip speed as in Equation (4.33). Now the blade solidity can be evaluated for each mode and the highest value will be taken for further rotor dimensioning representing the most critical case.

$$C_{T_m} = \frac{T_m}{\rho \pi r_m^2 {V_{tip_m}}^2} \tag{4.33}$$

Remember that Equation (4.27) describes σ as a function of the number of blades b and the chord of the blade c. This equation can be rearranged to calculate the blade chord for a given integer number of blades. Furthermore the aspect ratio of the blades (Equation (4.34)) follows from the radius and the blade chord.

$$AR = \frac{r^2}{cr} = \frac{r}{c} \tag{4.34}$$

The aspect ratio should be high to perform aerodynamically well, but should be low for structural purposes. As a rule: $14 < AR < 20$ [65]. If the aspect ratio is lower than 14, the induced drag on the blades will be too high to be efficient, but if the aspect ratio is higher than 20 the blade is so slender that it cannot be built with enough stiffness to account for torsion. The number of blades should be iterated such that the aspect ratio falls in this range. For the ducted fan design the blades should be stiffer than usual rotorcraft blades, to maintain an efficient position in the duct. Therefore, the lowest number of blades that still results in an aspect ratio above 14 is selected. A lower number of blades also allows for a decrease in hub weight and cost [65]. The initial main rotor dimensions are summarised in Table 4.5. Further considerations on the main rotor design (i.e. twist and taper) are elaborated on in Section 5.1.

Table 4.5: Initial main rotor dimensions

Parameter	*Value*
DL	67.5 kg/m^2
r_m	6.63 m
σ_m	0.0118
Ω_m	32.85 rad/s
b_m	5
c_m	0.47 m
AR_m	14.24

4.2.2 Vertical Tail Sizing

The vertical tail of the rotorcraft serves two purposes, to counteract torque and to ensure yaw stability and control. A tail rotor is used for this purpose which is aided by a vertical fin in cruise. In the mid term report a fenestron is selected, in which the tail rotor is embedded in a shroud that protects the blades. The main advantage of a fenestron is the lower induced power required to provide the same thrust. The difference can be seen in Equation (4.35) where σ_d is calculated using Equation (4.36) [16].

$$\frac{(P_i)_{open}}{(P_i)_{ducted}} = \sqrt{2 \cdot \sigma_d} \tag{4.35}$$

$$\sigma_d = \frac{A_e}{\pi r^2} \tag{4.36}$$

For the expansion ratio of the duct 1.1 is assumed. This is the ratio between the rotor area and the exit area of the duct. A higher expansion ratio would lead to a thicker duct and therefore more drag while it also increases propulsive efficiency. The thrust required to overcome the torque produced by the main rotor is given by Equation (4.37).

$$T_v = \frac{P_{hov}}{\Omega_m l_v} \tag{4.37}$$

The power to hover that is necessary to compute the vertical tail thrust depends on the ideal power to hover and the Figure of Merit of the main rotor as described by Equation (4.38).

$$P_{hov} = FoM_m \sqrt{\frac{W^3}{2\rho\pi {r_m}^2}} \tag{4.38}$$

An initial assumption for the Figure of Merit of the main rotor of 0.7 has been made [65]. After the first iteration it is calculated using Equation (4.39). The required parameters for this equation are elaborated on in Section 4.2.4.

$$FoM_m = \frac{1}{k + 0.82 \frac{C_{D_P}}{C_L} \left(\frac{V_{tip}}{v_i}\right)} \tag{4.39}$$

The final Figure of Merit of the main rotor at sea level is 0.755 and 0.716 at cruise altitude, which is close to the initial assumption.

The required thrust for the vertical tail rotor can thus be computed using Equation (4.37). After aerodynamic analysis of the main rotor, as will be discussed in Chapter 5, the torque produced by the main rotor seemed to be underestimated. Therefore, a higher thrust should be produced by the vertical tail rotor. The adaptations to the method are described in Chapter 5.

The power required by the vertical tail rotor can be computed using Equation (4.40) [65]. Since the fenestron design is also a ducted fan, the factor described in Equation (4.35) has to be taken into account for the expansion ratio of 1.1, as described before.

$$P_v = \frac{1}{FoM_v} \sqrt{\frac{{T_v}^3}{2\rho\pi {r_v}^2}} \frac{1}{\sqrt{2\sigma_{d_v}}} \tag{4.40}$$

The Figure of Merit of the vertical tail rotor, which is a fenestron, is assumed to be 0.7 [16].

Two values remain open for iterations during the tail rotor dimensioning. The arm between the main rotor and the tail rotor and the radius of the tail rotor. Using these values the required power for the vertical tail can be computed and used in later sections. The process behind these iterations is elaborated on in Section 4.2.8.

An initial blade dimensioning for the vertical tail rotor blades is also performed. Equations (4.27) and (4.34) are used to size the rotor blades just like for the main rotor. Fenestron however, have a higher blade solidity. For this design the blade solidity of the vertical tail is assumed to be 0.5 [24]. The aspect ratio of a fenestron is also generally lower than for a regular tail rotor. Aspect ratios in the range from 6 to 9 are common [24]. Using ten blades in the fenestron leads to an aspect ratio of 6.37. Since this already is a large number of blades, no higher number is considered to avoid an even more complex vertical tail rotor.

The main dimensions of the vertical tail rotor are summarised in Table 4.6.

Table 4.6: Initial vertical tail rotor dimensions

Parameter	*Value*
r_v	0.7 m
l_v	12 m
σ_v	0.5
b_v	10
c_v	0.11 m
AR_v	6.37

The design of a vertical fin that takes over part of the work of the vertical tail rotor in forward flight is described in Chapter 5.

4.2.3 Horizontal Tail Sizing

The two horizontal tail rotors are used for stability and control in pitch and roll direction. However, they also provide part of the lift required to keep the rotorcraft in the air. They are sized to counteract the moment produced by the main rotor around the centre of gravity. Based on Figure 4.3, the following Equation holds:

$$T_h = \frac{1}{2} T_m \frac{x_{cg} - x_m}{x_h - x_{cg}} \tag{4.41}$$

Here, the distances x are measured with respect to the nose and calculated in Section 4.1.5. The factor 0.5 comes from the fact that two tail rotors are used to overcome the moment produced by the main rotor.

The thrust required from the horizontal tail rotors is calculated for four cases: fully loaded at sea level and cruise altitude and empty at sea level and cruise altitude. Although the main rotor thrust is larger in the fully loaded case, the centre of gravity is located further behind the main rotor for the empty case. Investigating all four options the empty rotorcraft at cruise altitude has been found to be the most critical case, in which the horizontal tail rotors need to generate 2817 N of thrust each. The vertical tail arm in this case is 11 meters, measured between the horizontal tail rotor centre and the centre of the main rotor. This value is found after the iteration described in Section 4.2.8 has been performed.

The power required by the horizontal tail rotors is computed using Equation (4.40). Where the expansion ratio of the duct is also assumed to be 1.1. The Figure of Merit of the horizontal tail is assumed to be 0.7 [16]. The radius and arm of the horizontal tail can still be iterated. This iteration process is described in Section 4.2.8. To obtain the total power required by the horizontal tails P_h the result should be doubled, since two horizontal tail rotors are used.

The chord of the horizontal tail rotors is determined in the same way as for the main rotor and vertical tail rotor using Equations (4.27) and (4.34). The blade solidity of the horizontal tail rotor is assumed to be 0.12 [65]. The number of blades is iterated until an aspect ratio higher than 14 is found as described during the sizing of the main rotor. The lowest number of blades that results in a ratio higher than 14 is chosen.

The dimensions of the horizontal tail rotors are summarised in Table 4.7. The design of the horizontal fin that takes over part of the work of the horizontal tail rotor in forward flight is described in Chapter 5.

Table 4.7: Initial horizontal tail rotor dimensions

Parameter	*Value*
r_h	1.9 m
l_h	11 m
σ_h	0.12
b_h	6
c_h	0.11 m
AR_h	17.08

4.2.4 Power calculations

The rotorcraft weight and dimensions of the main and tail rotors have been determined in previous sections. These are used to determine the required operational power. The flowchart in Figure 4.7 shows the design steps that this section will elaborate on.

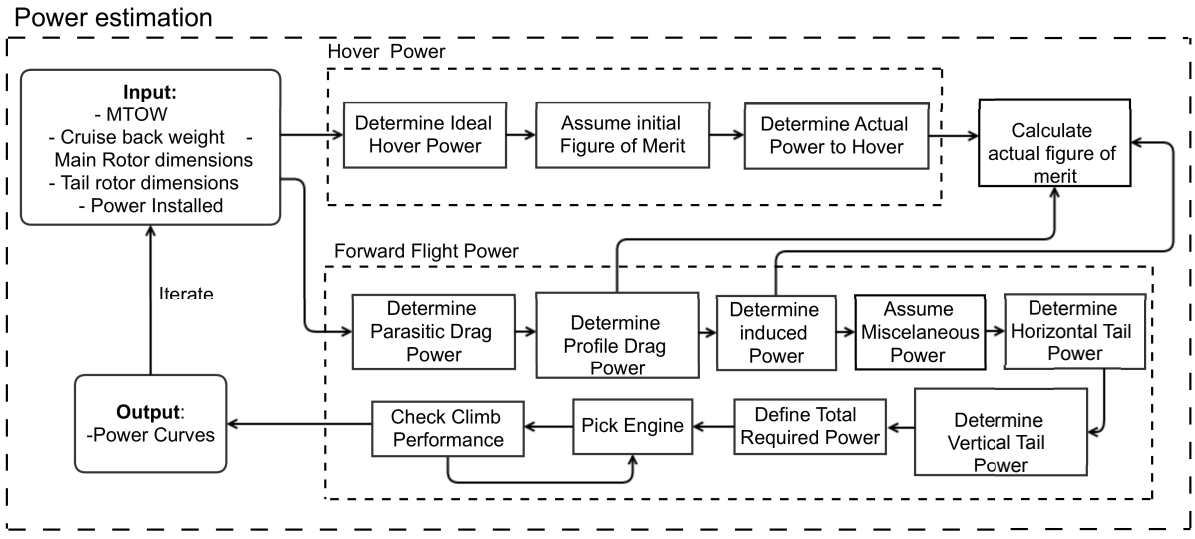

Figure 4.7: Global block flow diagram of power estimation

In forward flight the engines have to overcome several forms of drag. The total required power is the sum of the power required to overcome each form of drag plus the power the horizontal and vertical tails require. All powers will be calculated for four cases: sea level with full weight, sea level at cruise back-weight, cruise altitude with full weight and cruise altitude at cruise-back weight. This will lead to four different power curves in Section 4.2.6, which can be used to calculate the required power at each point in the mission.

$$P_{req} = P_s + P_d + P_p + P_i + P_h + P_v + P_{misc} \tag{4.42}$$

In this equation P_d and P_p can be combined as being the profile drag.

Parasite Drag Power

The parasite drag power is the power necessary to overcome the rotorcraft drag in forward flight and increases with flight speed. This drag is dependent on the projected frontal area of the helicopter and is estimated by the equivalent flat plate area. The equivalent flat plate area $\sum (C_D S)_S$ is also obtained from statistics, making use of the MTOW again. Figure 4.8 shows these statistics for a collection of reference rotorcraft. The figure shows two relationships: one for *utility helicopters* and one for *clean helicopters*. Since a transport rotorcraft is generally considered to be a utility helicopter, this regression line is used. As the ducted fan design has a larger projected frontal area than a conventional helicopter the flat plate area is increased by 20 %. This value is found to be appropriate after comparing the frontal area of the design to that of the EC 725 helicopter [47].

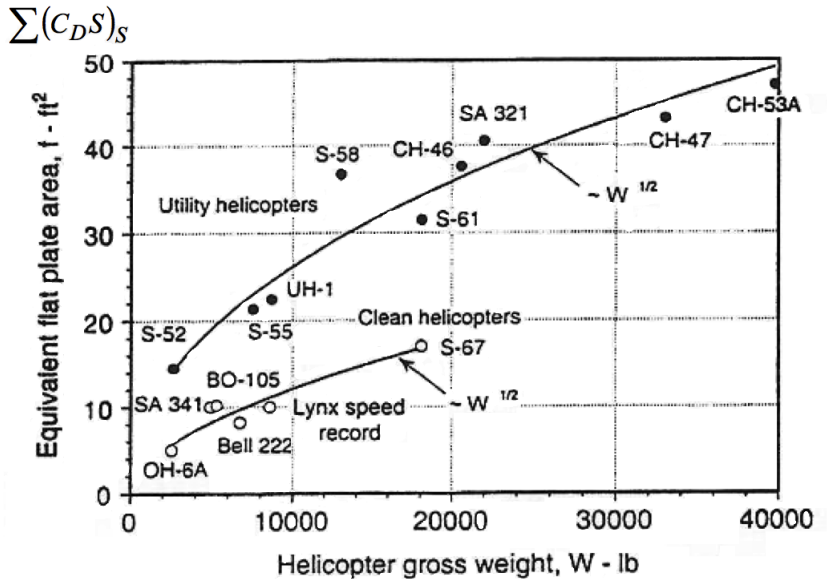

Figure 4.8: Equivalent flat plate area vs MTOW (modified after [65])

For the utility aircraft category, an equation of the trend line has been constructed to speed up the iteration process (Equation (4.43)).

$$\sum (C_D S)_S = -7.70 \cdot 10^{-18} MTOW^4 + 1.14 \cdot 10^{-12} MTOW^3 - 62.74 \cdot 10^{-9} MTOW^2 + 2.16 \cdot 10^{-3} MTOW + 10.01 \tag{4.43}$$

Consecutively, the parasite drag power is calculated by means of Equation (4.44).

$$P_S = DV = \sum (C_{Deq} S) \frac{1}{2} \rho V^3 \tag{4.44}$$

Profile Drag Power

The profile drag power in forward flight consists of two terms: P_d and P_p. The first term is the power required to counter the drag on the rotorblades, whereas the second term accounts for the difference in profile drag on the left and right side of the hub. Van Holten et al suggests Equation 4.45 to compute the profile drag power [79].

$$P_p + P_d = \frac{\sigma \bar{C}_{D_p}}{8} \rho \left(V_{tip_m}\right)^3 \pi r_m^2 \left(1 + 4.65\mu^2\right) \tag{4.45}$$

All terms in Equation (4.45) have been defined before, except for $\bar{C}_{D_p}$. This is the average profile drag coefficient and it is estimated using the lift coefficient and the rotor tip speed[65]. Figure 4.9 shows this relation and is used to derive $\bar{C}_{D_p}$. In addition, the lift coefficient comes from:

$$\bar{C}_L = \frac{6.6}{\sigma_m} \frac{W}{\rho \pi r_m^2 {V_{tip_m}}^3} \tag{4.46}$$

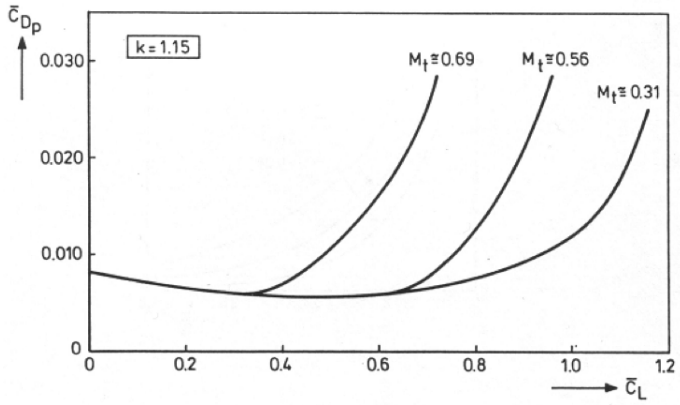

Figure 4.9: Profile drag coefficient vs lift coefficient as function of the tip Mach number [65]

The weight in Equation (4.46) is the actual weight of the helicopter at that point. For the first phases of the mission it is equal to the maximum take-off weight. Later the cruise back weight should be used. This allows for different power curves per mission segment as explained before.

Induced Power

As the rotor turns, the air flows over the rotor blades. Each blade always operates partially in the wake of the other blades and experiences the induced velocity v_i caused by the preceding blade. The induced velocity is a result of the vortices present on and behind the blades. Figure 4.10 shows two types of vortices: *bound vortices*, which are attached to the blade and cause lift and *free vortices*, which have separated from the blade and move with the wake.[79] These vortices result in drag and have to be overcome by the *induced power* (Equation (4.47)). [65]

$$P_i = kT_m V_i \sqrt{2\sigma_{d_m}} \tag{4.47}$$

The factor k accounts for the non-uniformity of the inflow of the air through the rotor and is usually in the range of 1.1 to 1.2. For this design an average factor of 1.15 has been chosen. The expansion ratio of the duct is assumed to be 1.1, to allow for a more efficient design, without increasing the fuselage height too much as will be described in Section 4.2.7.

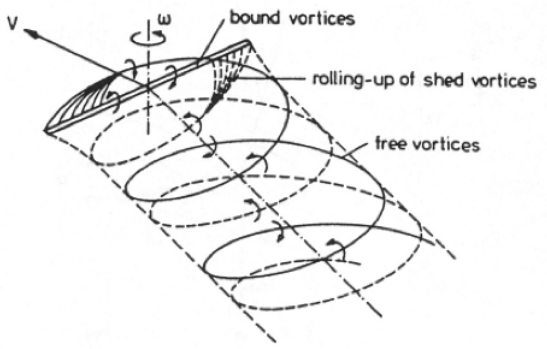

Figure 4.10: Rotor vortex system in forward flight [65]

To accurately describe the flow through a rotor system one needs complex simulation models. However, by applying simplifications, relations can be obtained which are still valid for simple performance calculations and can be used for first order approximations. Van Holten et al [79] derived these relations based on Glauert's hypothesis on momentum theory describing the mass flow through a rotor. The result is presented below from Equation (4.48) to Equation (4.51) and is valid for low speed non-climbing flight. During low speed flight the parasite drag is small with respect to the weight of the helicopter and the flight path angle γ is assumed zero. Therefore also the angle of attack is approximately equal to zero. Equation (4.48) shows the induced velocity during hover. During hover, at zero flight speed, the induced velocity is at its highest because the blade-vortex interference is maximal. This theory is also supported by Figure 4.10: at higher speed the free vortices move along with the wake and the consecutive blades experience less induced velocity.

$$v_{ih} = \sqrt{\frac{W}{2\rho\pi r^2}} \tag{4.48}$$

Equations (4.49) and (4.50) describe the normalisation of the flight velocity V and the induced velocity v_i with respect to the induced velocity in hover. These normalisations are used to relate the induced velocity to the flight speed, shown

by Equation (4.51).

$$\bar{V} = \frac{V}{v_{ih}} \tag{4.49}$$

$$\bar{v}_i = \frac{v_i}{v_{i_h}} \tag{4.50}$$

$$\bar{v}_i = \sqrt{-\frac{\bar{V}^2}{2} + \sqrt{\frac{\bar{V}^4}{4} + 1}} \tag{4.51}$$

By combining Equation (4.47) to (4.51) and rearranging, the induced power can be expressed directly as a function of the flight speed (Equation (4.52)).

$$P_i = kT_m \sqrt{-\frac{V^2}{2} + \frac{1}{2}\sqrt{V^4 + \frac{W^2}{4\rho^2\pi^2 r^4}}} \tag{4.52}$$

Tail rotors

The power required by the horizontal and vertical tail rotors was determined in Subsection 4.2.2 and 4.2.3 respectively. As explained, the horizontal and vertical surfaces will take over part of required thrust in cruise. To account for this both horizontal and vertical tail rotors are assumed to perform at 50% of the power in hover during cruise. This assumption is validated in Chapter 5.

Miscellaneous Power

The miscellaneous power is used for all other remaining systems such as the stability and control system, navigation system and the communication system. For large UAVs a value of 20 kW can be assumed [35]. The contribution of P_{misc} is very small with respect to the power required for the other systems and is assumed to be independent of flight speed.

Required Power

The required power at different altitudes and for different mission segments is summarised in Table 4.8.

Table 4.8: Maximum power in kW required for different mission segments and altitudes

	Sea level	1500 m
MTOW	1652.4	1900.7
Cruise-back weight	514.9	505.5

The maximum required power was computed in the last section to be 1900.7 kW at an altitude of 1500 meters for the fully loaded rotorcraft. The engine to be selected should at least be able to provide this power.

4.2.5 Engine Selection

The power an engine can deliver is often determined at sea level conditions. The gas turbine engines used in rotorcraft lose approximately 30 % of their performance at an altitude of 2000 meters [65]. Furthermore, a generator efficiency has to taken into account. This leads to the following equation for actual power the engine can deliver at altitude.

$$P_{actual} = \eta_{gen} P_{inst} \frac{\rho^{1.25}}{\rho_0} \tag{4.53}$$

The coefficient of 1.25 in this equation was iterated until the 70% efficiency at an altitude of 2000 meters was ensured. The ρ in this equation represents the air density at altitude and ρ_0 the density at sea level. The generator efficiency for this design is assumed to be 0.9 [2].

With Equation (4.53) and the maximum required power of 1900.7 kW at 1500 meter, the necessary installed power at sea level can be computed. When selecting an engine, a small amount of extra power should be taken into account, to allow for climb performance at altitude.

A database with rotorcraft engines is consulted in order to pick an engine [77]. All engines in this database that are able to deliver the computed installed power are compared by looking at their specific fuel consumption and dry weight. Finally a configuration with two T700-GE-701 engines was selected. These engines have the lowest specific fuel consumption and are the least heavy. At sea level the two engines together produce 2532 kW of power. They weigh 198.7 kg each, have a specific fuel consumption of 0.464 $\frac{kg}{kWhr}$ and spin at 21,000 rpm [77]. These values can be used to calculate the fuel and operational empty weight in Section 4.1.2. A picture of the engine is provided in Figure 4.11.

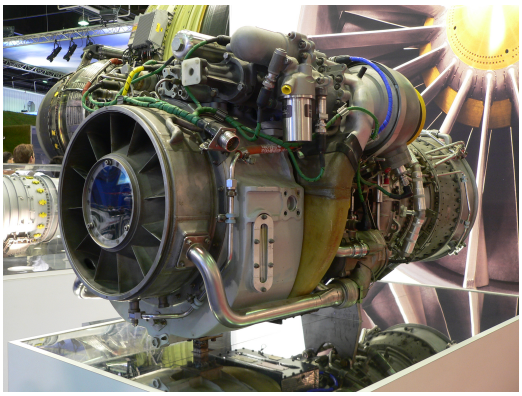

Figure 4.11: T700-GE-701 Engine [2]

4.2.6 Power Curves

In Sections 4.2.3 and 4.2.2 the required power for the horizontal and vertical tail rotors has been estimated. Together with the power calculations and the engine selection, the power curves of the design can be constructed. These curves show the maximum available power by the engines and the total required power at different flight velocities. The difference between these two can be used for climbing.

The rate of climb can be expressed using Equation [65]:

$$RC = \frac{P_{available} - P_{req}}{W} \tag{4.54}$$

Iterations are performed until the rate of climb with a fully loaded rotorcraft at 1500 m altitude is still at least 1 m/s with no forward speed, which was found to be the most critical case. If this is not the case a different engine has to be selected.

The plots are constructed for four different cases: fully loaded at sea level and 1500 meter altitude and for the cruise-back weight at sea level and 1500 meter altitude. From this data the power required for each mission segment can be computed, which is used to calculate the total fuel weight in Section 4.1.2.

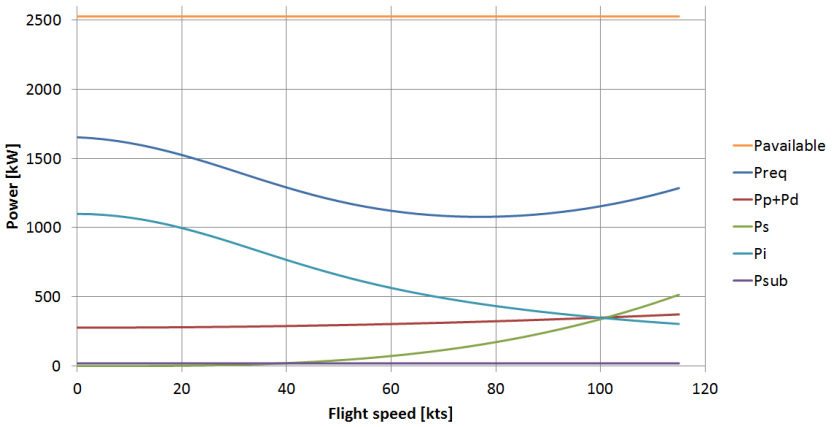

Figure 4.12: Power curve for fully loaded rotorcraft at sea level

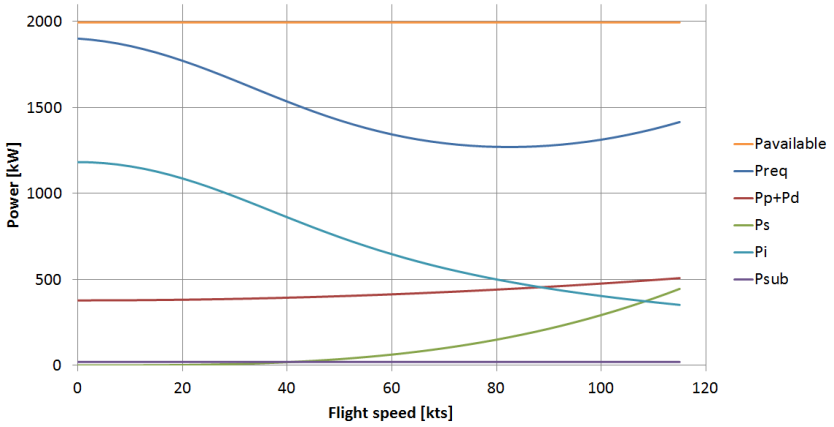

Figure 4.13: Power curve for fully loaded rotorcraft at 1500 m

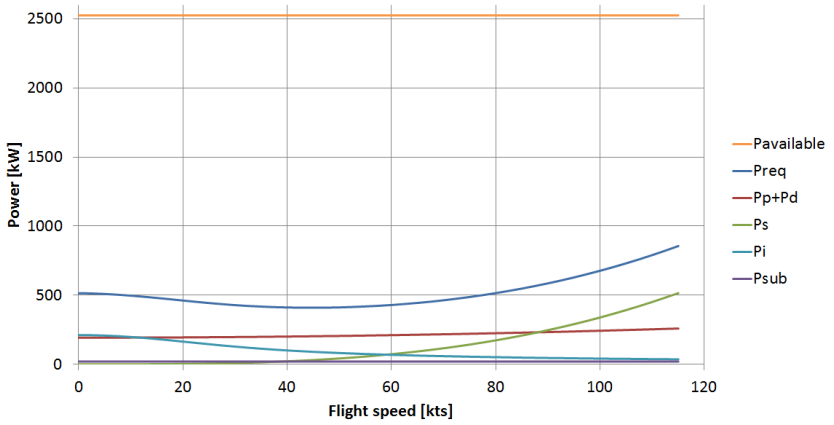

Figure 4.14: Power curve for cruise-back weight at sea level

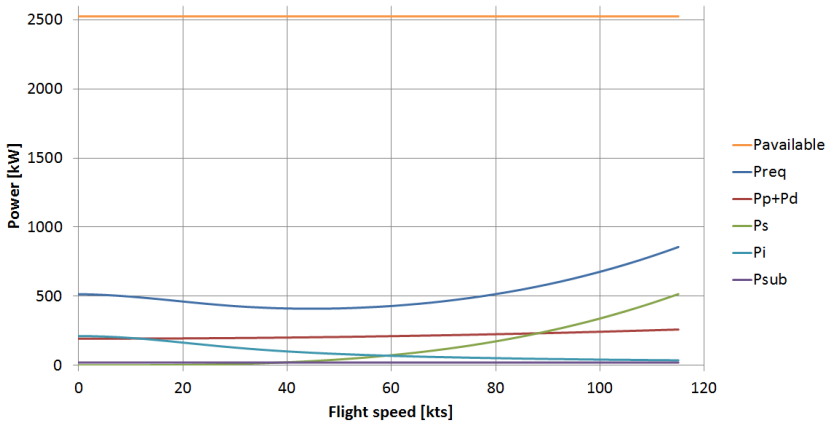

Figure 4.15: Power curve for cruise-back weight at 1500 m

The figures show that the critical condition for power required is with payload and operating at cruise altitude. It also becomes clear that flying at a lower altitude leads to better climb performance, since more power is available by the engines (Equation 4.53). Furthermore, a large difference is found between the fully loaded and cruise-back case, which is to be expected. After dropping the payload and having burned most of the fuel, the rotorcraft has lost about two-third of its initial weight as described in Section 4.1.4.

4.2.7 Fuselage Sizing

The size of the fuselage can be determined by the size of the main rotor and the distance between the main rotor, the centre of gravity and the tail rotors. Since the main rotor duct has an expansion ratio of 1.1, the exit radius of the duct

can be calculated using Equation (4.36). The main rotor radius was calculated to be 6.63 m in Subsection 4.2.1. The exit radius of the main duct is thus found to be 6.95 m.

Since the main rotor is shrouded in the fuselage the ring around the rotor can be sized. The ring around the rotor mainly houses the fuel. In the nose of the rotorcraft the auxiliary power unit and the avionics are located as described in Section 4.1.5. To allow these components to be stored at the front a front clearance ($l_{frontclear}$) of 1 meter is necessary. The clearance at the sides of the rotor ($l_{frontclear}$) can be less, since only the fuel is stored there. For this a clearance of 0.5 meter is assumed.

Behind the ring the fuselage has to extend until the tail rotors. The horizontal fins have to be in the direct airflow and are therefore positioned sidewards. This also allows for a higher effectiveness of the horizontal tail rotors in roll control due to the increased arm. With the computed tail arms (Section 4.2.8) measured from the main rotor centre, the total length of the fuselage can be estimated. The total length is the addition of the front clearance, the main duct exit radius, the longest tail arm (vertical or horizontal) and the corresponding tail rotor radius. The total length of the fuselage is found to be 20.65 meters. The total width of the ring is 14.91 meters.

The height of the fuselage depends of two factors. Firstly, all systems, fuel and engine have to fit into the fuselage. Furthermore, the expansion ratio of the duct should be taken into account. For a better efficiency an expansion ratio of 1.1 is preferred as determined in Subsection 4.2.1. To keep the incoming airflow from separating when entering the duct at a corner, the angle of the duct should not be too large. This will be considered in the duct sizing in Chapter 5. To calculate the capacity of the fuel the density of jet A-1 fuel (0.804 kg/L [5]) has been used together with the fuel weight calculated in Section 4.1.2. Furthermore, the thickness of the engines has been found to be 0.40 meter [2]. Considering all other subsystems, a fuselage with a height of 1.0 meter is chosen. Further aerodynamic considerations on the sizing of the duct and possible thickness alterations are presented in Chapter 5.

4.2.8 Iteration Process

During all design stages described in previous section mutual dependencies can be identified. Figure 4.16 shows an N2-chart with all main design steps. The arrows identify the inputs and outputs for each design step. Note that during later stages of the design process, after the aerodynamics, structures and the stability and control are investigated, new input can be used in the design process shown in Figure 4.16. Loops can be identified in the design process. For example, increasing the size of the main rotor leads to a heavier operational empty weight, which in turn leads to a larger main rotor. To get to the final conceptual design, iterations have to be performed.
During the design process six variables were left open for iteration: the disc loading of the main rotor, the horizontal and vertical tail arms, the radii of the horizontal and vertical tail rotors and the engine to be selected.

The disc loading is the most sensitive parameter in this design tool. A larger disc loading leads to a larger main rotor. This decreases the power required for the main rotor, but does increase the size of the entire rotorcraft. This increase in size, increases the empty weight and therefore the power required.

The same can be said for the tail rotors. Increasing their distance from the main rotor decreases the direct thrust and power required. However, the size and weight of the rotorcraft increase, again increasing the required power. The radius of the rotors is also sized in an iterative process.

Finally, the engine selection has to be iterated if the power required has changed. A lower required powered allows for a smaller, lighter and more fuel efficient engine.

These six parameters have been iterated and adjusted by trial and error, until the lowest possible required power has been found. The final values for the iteration parameters are displayed in Table 4.9. The final engine that has been selected is described in Subsection 4.2.5.

Table 4.9: Final values of iteration parameters

Parameter	*Value*	*Unit*
DL	67.5	[kg/m^2]
r_h	1.9	[m]
l_h	11	[m]
r_v	0.7	[m]
l_v	12	[m]

4.2.9 Initial Sizing Results

The initial results after the described iterations are presented in Table 4.10. These values will also be used to verify and validate the sizing tool in the next section.

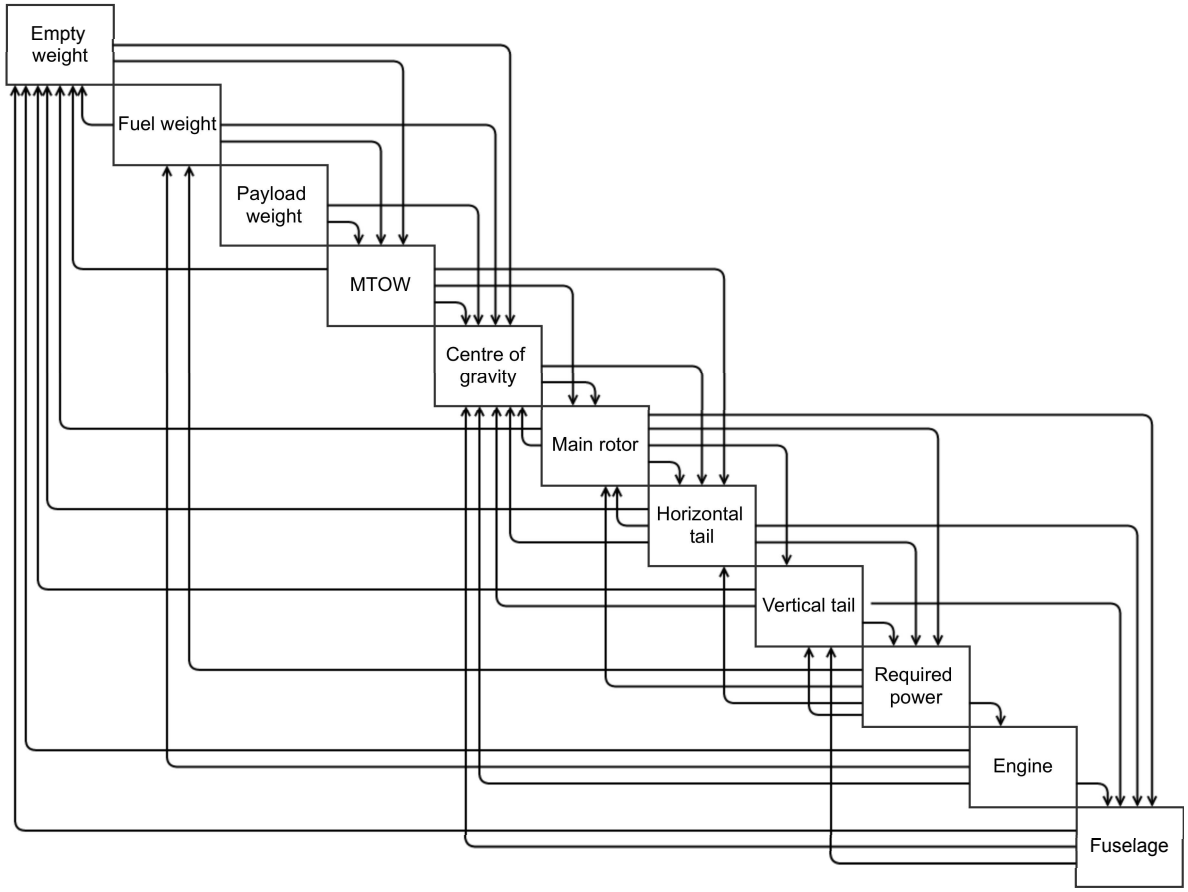

Figure 4.16: Dependencies during design process

Table 4.10: Initial sizing results

Parameter	*Value*	*Unit*
OEW	3258	[kg]
W_{fuel}	855	[kg]
W_{pl}	5211	[kg]
$MTOW$	9324	[kg]
r_m	6.63	[m]
b_m	5	[m]
c_m	0.47 [m]	
AR_m	14.24	[-]
σ_{d_m}	1.1	[-]
l_v	12	[m]
r_v	0.7	[m]
b_v	10	[-]
c_v	0,11	[m]
AR_v	6.37	[-]
σ_{d_v}	1.1	[-]
l_h	11	[m]
b_h	6	[m]
c_h	0.11	[m]
AR_h	17.08	[-]
σ_{d_h}	1.1	[-]
P_{inst}	2532 kW	[kW]
SFC	0.2822	[kg/kWhr]
l_{fus}	20.65	[m]
w_{fus}	14.91	[m]
$l_{frontclear}$	1	[m]
$l_{sideclear}$	0.5	[m]
h_{fus}	1	[m]

4.2.10 Verification and Validation

To verify the sizing tool presented in this chapter, Figure 4.16 is used. As explained in the previous subsection, the figure shows the relationship between design parameters. Unit checks are performed on the tool by altering de-

sign parameters and checking the influence on the design. This check is performed for every parameter in the sizing process.

An increase in vertical tail arm resulted in an increased weight, a backward shift in the centre of gravity and a decrease in the required thrust and power of the vertical tail. This is exactly as expected, so this part of the tool is verified. The process is repeated for all other parameters.

The validation of the design tool requires the output to be compared to existing rotorcraft. Since no large scale, unmanned, ducted fan design exist a more qualitative approach is selected. The design is compared to the Eurocopter EC725. This rotorcraft is selected because of the comparable payload capacity. It can transport a load of 5000 kg [47], which is equal to the requirements of a single designed rotorcraft. Some main design parameters are compared in Table 4.11.

Table 4.11: Comparison of main dimensions to EC 725 [47]

	EC 725	*Initial design*
P_{inst} [kW]	2604	2532
MTOW [kg]	1100	9324
r_m [m]	8.10	6.63
r_v [m]	1.56	0.7
l_{fus} [m]	19.5	20.65
h_{fus}	4.97	1

The maximum take-off weight of the EC725 is heavier than for the current ducted fan design. This can mainly be contributed to the fact that the ducted fan is unmanned, which allows for weight saving in the operational empty weight. The radius of the main rotor is smaller for the ducted fan. The increased efficiency due to the duct and the focus on a small rotor size in the design process are the main contributors.

The lengths of the fuselages are comparable, while the heights differ significantly. The difference is a result of the different concepts. The ducted fan is much wider, so all necessary equipment can be stored without the use of a high fuselage. Furthermore, the unmanned concept does not require a conventional fuselage that is used to accommodate a pilot.

The radius of the vertical tail rotor for the ducted fan design is half of the radius for the EC 725. Since the EC 725 uses a conventional tail rotor, which have higher radii, this difference is expected. The compact fenestron however, uses almost 14 % of the required power in hover, which is more than for conventional tail rotors [65]. However, the increased efficiency of the main rotor compared to a conventional rotor decreases the total required power. Therefore the installed power of the ducted fan design is slightly lower than that of the EC 725.

All validation parameters differ from the conventional rotorcraft in a way that has been expected. Therefore, the tool is verified and validated and the output can be used in further design stages explained in Chapters 5, 6 and 7.

5. Aerodynamics

This chapter discusses the aerodynamic aspects of the rotorcraft design. As stated before designing is an iterative process, Chapter 4 mainly delivers the input for this chapter. In turn this chapter returns the obtained values to the performance group. First Section 5.1 presents the theory used to design the fan blades of the four rotors. In Section 5.2 the horizontal and vertical tail surfaces are sized. Section 5.3 considers the dimensioning of the duct of the main rotor. Finally, Section 5.4 investigates the drag on the fuselage, payload and the required thrust and Section 5.5 elaborates on the autorotation capabilities of the rotorcraft.

5.1 Rotor Sizing

This section outlines the methods used to size the rotors. The blades, airfoil and twist distribution of the main rotor, two horizontal fenestrons and the vertical fenestrons are designed. The input values for the sizing of the rotors come from the preliminary sizing discussed in Chapter 4. These inputs are used in the evaluation of rotor dimensions and have to be iterated together with the preliminary sizing:

- Thrust
- Power
- Fan radius
- Rotational speed
- Number of blades
- Blade chord

The sizing method is generally the same for all four fans, yet their dimensions are different. First the sizing method is discussed in Subsection 5.1.1 after which the airfoil options are presented in Subsection 5.1.2. Finally, the result of the calculations for each rotor type is presented seperately in Subsections 5.1.3 to 5.1.5.

5.1.1 Rotor Sizing Theory

The method of sections is applied to size the rotor blades, as suggested in Wright and De Piolenc [34]. The blades are not discretised into sections of equal span but rather such that the area of the annuli is constant. The reasoning behind this is that equal ring area corresponds to equal power. Experience has shown that the most accurate results are obtained with this approach. The division of a blade into sections for the computation of the aerodynamic forces is generally referred to as the blade element theory. As the structural sizing of the blade is dependent on the input aerodynamic forces computed in this analysis, the number of sections is equal to the number utilised in the structural analysis to achieve similar accuracy. In order to evaluate each blade section, the so called swept area (disk area) is defined, which is the total area the blades sweep while rotating. Furthermore Wright and De Piolenc [34] state that the radius of the hub should be at least 20% of the tip radius (distance from center to blade tip), mostly for aerodynamic reasons. Therefore the hub radius of each fan is set at 20% tip radius. Now the radial distance of each blade station is determined by Equation (5.1). A blade station marks the boundary between two blade sections.

$$r_i = \sqrt{\frac{A_{swept}}{\pi n} + {r_{i-1}}^2} \quad \text{for} \quad i = 0 : n \tag{5.1}$$

Where r_0 is the hub radius and n the number of sections. Figure 5.1 aids to illustrate the division. Please note that the rings get thinner, because the radial distance becomes larger but the swept area of each section, and thus each ring (A1=A2=A3), is the same.

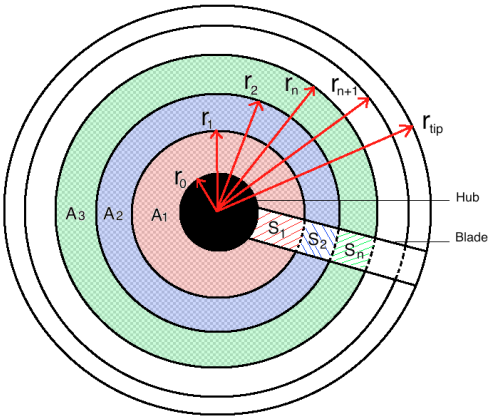

Figure 5.1: Radial blade sectioning

Each rotor blade is in the wake of its predecessor and thus the prediction of the free stream velocity experienced by the blade is rather complex. As the interference is difficult to quantify with mathematical models, commonly windtunnel tests are performed to obtain a basis for the rotor sizing. When cutting a ring section from a fan and straightening it out, it will look like a cut through a shutter. This arrangement of airfoils is generally referred to as an airfoil cascade. Such cascades are used for windtunnel testing.

The magnitude of the interference between the blades depends on the inter blade gap. If the gap is large enough the effect of the interference diminishes. As such, sufficiently accurate results are obtained by simply modelling several independent blades. A value for the inter blade gap, which renders it necessary to use one or the other approach, is difficult to specify as it depends on the chosen airfoil and the accuracy required. However Eck [20] as well as Wright and De Piolenc [34] suggest to neglect the interference unless the fan has an unusual high number of blades. Considering in addition that only conceptual design is performed in this report, the assumption of an isolated airfoil is deemed appropriate and is adopted.

According to Weir [81] a blade section experiences a resultant velocity V_R that consists of three components: swirl induced velocity, radial velocity and axial velocity. This is illustrated in Figure 5.2.

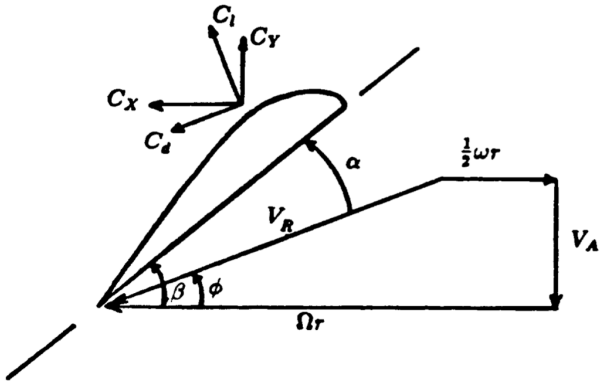

Figure 5.2: Propeller blade section geometry [81]

The tangential velocity is thus given as the subtraction of the radial velocity and the swirl induced velocity. The first is given by Equation (5.2) and the latter is estimated with Equation (5.3) [81].

$$V_r = \Omega r \tag{5.2}$$

$$V_{swirl,i} = \frac{P}{2r_i \Omega \rho V_A A_{swept}} \text{for} i = 0 : n \tag{5.3}$$

Whereas the tangential velocity is independent of the flight velocity, the axial velocity is heavily dependent on it. In hover, the free stream velocity is zero which is obviously not the case in forward flight. Weir [81] suggests different approaches for determining the axial velocity for the different flight conditions. To determine the axial velocity a blade element experiences, the momentum theory is used. For a more elaborate derivation and explanation of the momentum theory as used for rotorcraft the reader is referred to a general book on rotary wing aerodynamics such as Stepniewski [80]. Here only a brief explanation is provided.

A major assumption made is that the axial flow velocity is constant over the entire fan disc. In addition the flow is assumed to be inviscid, incompressible, steady and quasi-one-dimensional. Furthermore it is stipulated that the pressure is expanded back to ambient at the duct exit. Conservation of linear momentum then yields Equation (5.4).

$$T = \dot{m}w \tag{5.4}$$

From the conservation of mass Equation (5.5) follows.

$$\dot{m} = \rho A_{in} V_A = \rho A_e w \tag{5.5}$$

Combining Equation (5.5) and Equation (5.4) and defining the diffuser ratio as $\sigma = \frac{A_e}{A_{in}}$ results in Equation (5.6). As an initial input, σ is assumed to be equal to 1.1. With this value the duct still fits in the fuselage.

$$V_A = \sqrt{\frac{T\sigma}{\rho\pi(R^2 - R_H^2)}} \tag{5.6}$$

For forward flight Weir, [81] suggests a different estimation method for the axial velocity which is dependent on the flight velocity V_0. In Equation (5.7) ω refers to the increase in velocity due to the fan and δ is a factor to account for the duct induced velocity in forward flight.

$$V_A = V_0 + \frac{w}{2} + V_0\delta \tag{5.7}$$

The fully developed induced velocity ω is also proportional to the free stream velocity rendering the axial velocity proportional to the free stream velocity. In contrast to the ducted fan discussed in Weir [81], which turns its axis of rotation approximately parallel to the flight path in forward flight, the design under consideration is supposed to remain nearly horizontal. As a common helicopter, it tilts slightly downward for forward flight. In this way the thrust vector is tilted given a forward component in addition to the lift component and the total required thrust will increase. Therefore, Weirs method is not used, but rather the vertical component of the free stream due to pitching down will be added to the axial velocity as in Equation (5.8). In accordance with experiences for conventional helicopters the pitch angle is assumed to be 8 degrees downward in cruise condition with payload. Since the mission mostly concerns the cruising stage, the blades will be designed according to forward flight conditions and checked with the hover configuration afterwards.

$$V_{A,ff} = V_A + V_0 \sin(\theta) \tag{5.8}$$

In addition to the velocity components, Figure 5.2 also defines three angles: β, ϕ and α, which are respectively the mounting angle, the sum of the inflow angle ϕ and the blade angle of attack. The mounting angle is different for each section and results in a twist distribution over the blade. The inflow angle results from the velocities and the angle of attack of the blade is set at the maximum lift to drag ratio $(L/D)_{max}$ of the airfoil. The angle of attack is a result of an iterative airfoil selection, where the airfoil is chosen such that the sum of the thrust contributions of each section equals the predefined required thrust. Now the lift contribution of each section is determined by Equation (5.9):

$$L_i = 0.5\rho {V_{R,i}}^2 c_i (r_i - r_{i-1}) C_L \tag{5.9}$$

Where c_i is the local root chord [m] and $r_i - r_{i-1}$ the distance between two radial stations. Note that a capital L is used in the description of the lift coefficient. Since the propeller is shrouded the assumption of infinite blades is adopted and as such the lift coefficient of the airfoil equals the coefficient of the blades ($C_L = C_l$) and tip vortices can be neglected. Furthermore, the lift coefficient does not have an index. Although one could use different airfoils for different blade sections, it makes structural analysis and blade production more complicated and therefore each blade element uses the same type of airfoil. The lift coefficient depends on the angle of attack and is evaluated at the angle of $(L/D)_{max}$. Note that the blade chord can be changed as to achieve the required lift.

A similar approach is used for the drag and moment torque of the blade element:

$$D_i = 0.5\rho {V_{R,i}}^2 c_i (r_i - r_{i-1}) C_D \tag{5.10}$$

$$T_{b,i} = 0.5\rho {V_{R,i}}^2 {c_i}^2 (r_i - r_{i-1}) C_M \tag{5.11}$$

And the total drag on each blade:

$$D_{blade} = \sum D_i \tag{5.12}$$

In which both coefficients are also evaluated at $(L/D)_{max}$. The moment torque $T_{b,i}$ will serve as an input for the structural analysis of the blade. The lift and drag can now be transformed to the vertical and horizontal force on a blade section as defined in Figure 5.2 by the inflow angle ϕ:

$$\begin{aligned} F_{X,i} &= L_i \sin(\phi) + D_i \cos(\phi) \\ F_{Y,i} &= L_i \cos(\phi) - D_i \cos(\phi) \end{aligned} \tag{5.13}$$

The resultant vertical force of the rotor is simply the sum of the forces on the blade sections times the number of blades n_b (Equation (5.14)). In addition, the moment the rotor exerts on the fuselage is the sum of the horizontal force times the average radial station distance. This is the moment that the vertical fenestron and fin have to counter during both cruise and hover (Equation (5.15).

$$F_Y = n_b \sum F_{Y,i} \tag{5.14}$$

$$M_R = n_b \sum 0.5\,(r_n + r_{n-1}) F_{X,i} \tag{5.15}$$

The obtained vertical force has to be checked against the input thrust from sizing calculations that was initially used in Equation (5.6). The blade airfoil is selected such that its lift and drag coefficient evaluated at the angle of $(L/D)_{max}$ results in the required thrust. As a safety factor, an excess thrust of 2% to 3% is included in this thrust. This safety factor accounts for imperfections of the blade and other thrust losses. Note that tapering of the blades is not considered here. In general, high taper results in a good hover performance while low taper is structurally easier [65]. Taper has been implemented in the tool, yet it is not required to obtain the lift characteristics. An improved investigation in helicopter blade taper design criteria should be done in a further design stage to optimize the blades.

5.1.2 Airfoil Candidates

This subsection presents the airfoil candidates for the rotor blades. Five different airfoils are considered and are analysed making use of airfoil data obtained from CFD tools [3]. This airfoils are selected based on simulations ran on a large variety of airfoils and the data is presented in Table 5.1. Each airfoil is evaluated at a Reynolds number of 10^6 and an N_{crit} value of 9. The actual Reynolds number of the blades differ from root to tip, since the resultant velocity changes. The minimum Reynolds number on the blade is $1.6 \cdot 10^6$ at the root and the maximum Reynolds number is $6.5 \cdot 10^6$ at the tip. There is no airfoil data available for Reynolds numbers higher than 10^6 and since the orders of magnitude correspond the use of the data is justified. N_{crit} depends on the ambient disturbance level of the flow and relates to the corresponding effects of transition [75]. A flow with a low disturbance value (4 to 8) corresponds to 'dirty' wind tunnels and will be more prone to separation bubbles on the surface. N_{crit} values in the range of 12-15 are applicable to sail planes and for an average wind tunnel N_{crit} is smaller than or equal to 9. In actual atmosphere, this value ranges from low to high. Therefore, a value of 9 is chosen as best approximation.

The five airfoils are chosen based on a range of lift coefficients. If the lift coefficient of a specific airfoil is too low to generate the required vertical force, another airfoil with a higher lift coefficient will have to be chosen. The Onera OA212 is the airfoil that was originally chosen during preliminary sizing and is therefore compared to other airfoils. The selection of the RAF 6 and Clark Y is based on a proposition of Wright & de Piolenc [34] who claim that these airfoils are popular in the use of ducted fans. Furthermore, the selection also includes the Sikorsky SSC-A07, which is used on Sikorsky helicopters. This airfoil contributes to the range of lift coefficients since it has a somewhat lower C_L at $(L/D)_{max}$. Finally the Onera OAF095 is an airfoil which is often used for fenestrons and therefore included.

Table 5.1: Airfoil data of five different airfoils

		Airfoil				
Description	**Symbol**	**Clark Y**	**RAF 6**	**OA-212**	**SSC-A07**	**OAF095**
Reynolds number [-]	Re	1,000,000	1,000,000	1,000,000	1,000,000	1,000,000
Max lift to drag ratio [-]	$(L/D)_{max}$	119.6	104.8	96.6	76.1	131.2
Angle of Attack at $(L/D)_{max}$ [deg]	α	3.00	7.50	7.75	5.25	3,50
Lift coefficient at $(L/D)_{max}$ [-]	C_l	0.80	1.23	0.98	0.64	0,93
Drag coefficient at $(L/D)_{max}$ [-]	C_d	0.0067	0.0117	0.0101	0.0085	0.0071
Moment coefficient at $(L/D)_{max}$ [-]	C_m	-0.0965	-0.0731	-0.0074	-0.0080	-0.0776
Maximum lift coefficient [-]	$C_{l_{max}}$	1.57	1.61	1.50	1.29	1,72
Stall angle [deg]	α_{stall}	16.5	14.25	15.25	12.50	15

5.1.3 Main Rotor

This subsection describes the result of the application of the theory described above for the largest of the four rotors: the main rotor. The input, as a result from sizing calculations, is presented in Table 5.2. Furthermore, the flight velocity is included as a cruise condition requirement.

Table 5.2: Input from sizing calculations for hover and forward flight

Sizing input	**Hover**	**Forward Flight**	**Unit**
Thrust	86214	87061	[N]
Power	1110	1452	[kW]
Flight velocity	0	41.16	[m/s]
Fan radius	6.61		[m]
Rotational speed	32.93		[rad/s]
Number of blades	5		[-]
Blade chord	0.47		[m]

As stated in Subsection 5.1.1 a differentiation is made between hover and forward flight. The assumption of flying at a vehicle angle of $-8°$ is adapted, which results in a higher thrust during forward flight compared to hover. The results of Equations (5.8), (5.12), (5.14) and (5.15) are presented in Table 5.3 and are based on the Sikorsky SSC-A07. By making use of this airfoil, the variation of the chord with respect to the initial chord obtained from sizing stays minimal while delivering the required thrust, i.e. using another airfoil from the selection would change the chord more, in absolute sense.

Table 5.3: Calculation results for forward flight

Description	Result	Unit
Axial velocity	31.94	[m/s]
Airfoil	Sikorsky SSC-A07	[-]
Chord	0.5	[m]
Required thrust	87061	[N]
Delivered thrust	89060	[N]
Extra thrust	2.3	[%]
Drag per blade	243	[N]
Total torque	92804	[Nm]

The results in the table show an excess of thrust of 2.3% and the chord has been increased from 0.47 m as sizing input to 0.50 m. Since the blade chord has to be increased to obtain the required lift, another airfoil could be used with a higher lift coefficient at $(L/D)_{max}$. However, the Clark Y airfoil, with a lift coefficient of 0.80, results in an excess thrust of 20%. Therefore, the other airfoil types are not feasible since they would be over designed and only result in a higher blade drag and thus main rotor torque (which has to be countered by the tail, etcetera). Later iterations might substitute minor adaptions of the SSC-A07 for optimization. The drag per blade is used as an input for structural analysis. Defining a total blade drag does not make sense, since the drag force of each blade is in another direction. The resulting mounting angle distribution, or in other words, twist distribution as a function of radial position is presented in Figure 5.3.

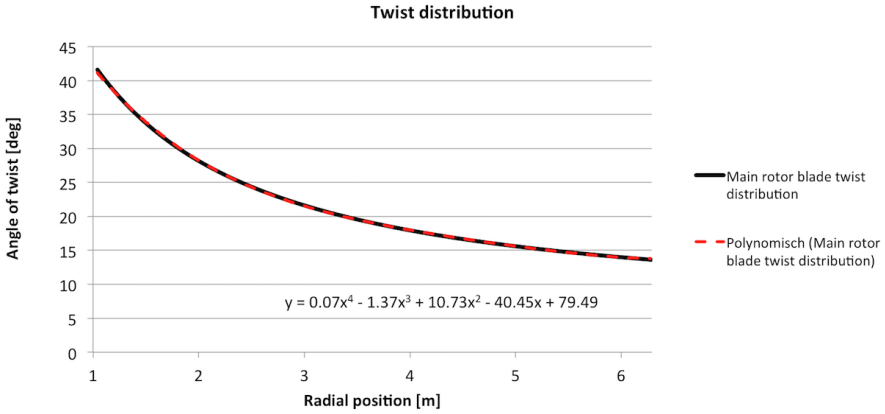

Figure 5.3: Twist distribution as function of radial position optimised for forward flight

The twist distribution has been optimised for cruise conditions, but is not ideal for hovering conditions. Applying the twist distribution to hover conditions and adapting the collective pitch angle of the blades such to have a 2% to 3% safety factor in delivered thrust once more yields the results shown in Table 5.4. It shows that the collective pitch has to be decreased by 1.25° in order to get closer to the angle of $(L/D)_{max}$. The collective pitch could be decreased even further to make the absolute change minimal, but that will reduce the safety factor. Later design iterations will allow the safety factor to reduce to be able to fly at $(L/D)_{max}$ conditions. Included in the table is the angle offset with respect to the optimal twist angle for hover. The collective pitch change has been applied for these angles. In addition to the table, Figure 5.4 shows both optimal lift distributions. In this Figure, the collective pitch deduction is not applied.

Table 5.4: Calculation results for hovering flight based on the twist distribution optimised for forward flight

Description	Result	Unit
Axial velocity	26.08	[m/s]
Required thrust	86214	[N]
Delivered thrust	88267	[N]
Extra thrust	2.4	[%]
Drag per blade	247	[N]
Total torque	76610	[Nm]
Collective change w.r.t. Forward flight	-1.25	[deg]
Max mount angle change w.r.t. Optimal	1.59	[deg]
Min mount angle change w.r.t optimal	-0.21	[deg]

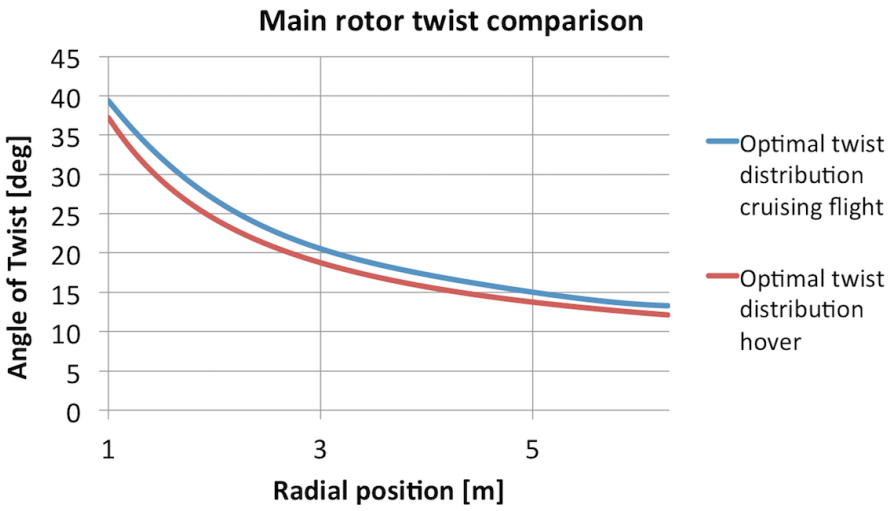

Figure 5.4: Optimal lift distributions of forward flight and hover

5.1.4 Horizontal Fenestrons

The two horizontal fenestrons have to account for a portion of the required thrust in forward flight. Blade forces and dimensions are based on the input from sizing shown in Table 5.5. The thrust and power in the table are for a single fenestron. Since the horizontal fenestrons are symmetric with respect to each other, their properties are the same.

Table 5.5: Input from sizing calculations for

Sizing input	Hover	Forward Flight	Unit
Thrust	2629	2659	[N]
Power	26.50	26.57	[kW]
Fan radius	1.9	1.9	[m]
Rotational speed	72.20	72.20	[rad/s]
Blade chord	0.111	0.111	[m]
Number of blades	6.00	6.00	[-]

The calculation results for the horizontal fenestrons are presented in Table 5.6 using the Sikorsky SSC-A07 airfoil once more.

Table 5.6: Calculation results for one horizontal fenestron in forward flight

Description	Result	Unit
Axial velocity	21.66	[m/s]
Airfoil	Sikorsky SSC-A07	[-]
Chord	0.111	[m]
Required thrust	2659	[N]
Delivered thrust	2716	[N]
Extra thrust	2.2	[%]
Drag per blade	6.2	[N]
Total torque	872	[Nm]

As can be deduced from the table, the Sikorsky airfoil is quite a good fit. The chord remains the same as estimated in sizing and an excess thrust of 2.2% is produced as a safety factor. Choosing the other types of airfoils would increase the thrust, which is not required. Using this chord in hover configuration and running calculations yields the results in Table 5.7.

Table 5.7: Calculation results for one horizontal fenestron during hover

Description	Result	Unit
Axial velocity	15.84	[m/s]
Required thrust	2629	[N]
Delivered thrust	2693	[N]
Extra thrust	2.4	[%]
Drag per blade	6.4	[N]
Total torque	647	[Nm]
Collective change w.r.t. Forward flight	-3.23	[deg]
Max mount angle change w.r.t. Optimal	4.74	[deg]
Min mount angle change w.r.t optimal	-0.74	[deg]

The resulting optimal twist distribution of both flight conditions is shown in Figure 5.5. The displayed equation corresponds to the blue line, since it is optimised for cruising flight. The optimum twist during hover shown in the figure is without the adaption of collective pitch. For the mount angle changes in the table, the collective change is included.

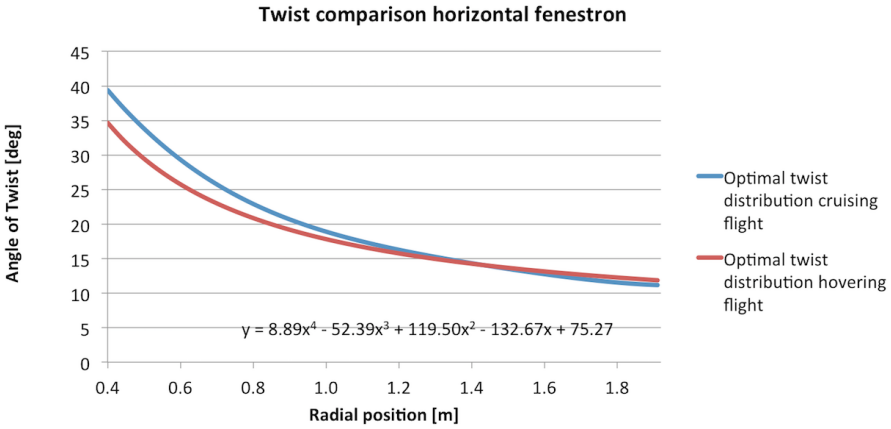

Figure 5.5: Optimal lift distributions of the horizontal fenestrons for cruising flight and hover

5.1.5 Vertical Fenestron

This subsection describes the sizing of the vertical fenestron based on the sizing methods presented in Subsection 5.1.1 with some minor adaptions. The thrust the vertical fenestron is required to produce is considered only during hover. Although the moment induced on the fuselage is higher during cruise conditions, as comparison between Tables 5.3 and 5.4 shows, the vertical fin will counteract a portion of the moment during cruise and therefore the actual thrust the fenestron has to produce is lower compared with hover. Inputs resulting from sizing in Chapter 4 are presented in Table 5.8.

Table 5.8: Input resulting from sizing calculations for the vertical fenestron

Sizing input	Value	Unit
Power	271	[kW]
Fan radius	0.70	[m]
Rotational speed	304.80	[rad/s]
Number of blades	10	[-]
Chord	0.130	[m]
Fan arm	12	[m]

In which the fan arm is the horizontal distance between the center of the main rotor and the center of the vertical fenestron. Now the required thrust is not adapted from sizing, but based on the torque that has to be countered during hover:

$$M_R = T_{vf} l_{fans} \rightarrow T_{vf} = \frac{M_R}{l_{fans}} \tag{5.16}$$

Where the subindex vf stands for vertical fenestron. As presented in Table 5.4 the total moment to be countered is equal to 76610 Nm and with a fan arm of 12 m this results in a required thrust T_{vf} of 6384 N. The calculation results are presented in Table 5.9 using the Onera OAF95 as airfoil. This airfoil proves to be the best fit corresponding to the input from sizing with the least required change in chord length. The chord length is decreased by 2 mm, to fall in the range of 2% to 3% excess thrust. The resulting twist distribution is presented in Figure 5.6.

Table 5.9: Calculation results of the vertical fenestron under hover conditions

Description	Result	Unit
Axial velocity	67.02	[m/s]
Airfoil	Onera OAF95	[-]
Chord	0.128	[m]
Required thrust	6384	[N]
Delivered thrust	6545	[N]
Extra thrust	2.52	[%]
Drag per blade	8.1	[N]
Total torque	1593	[Nm]

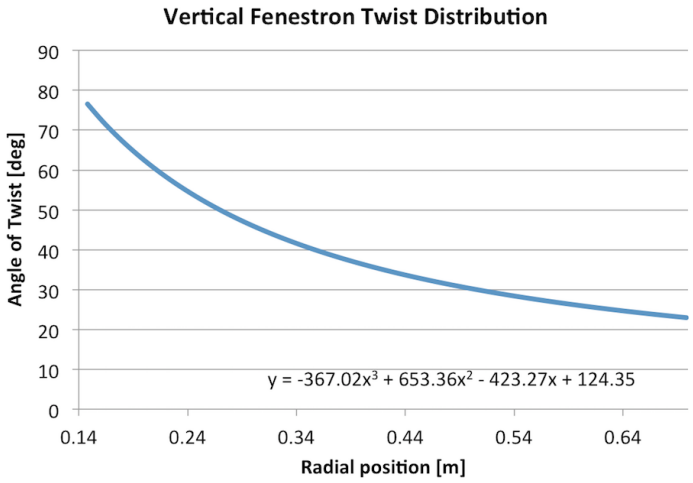

Figure 5.6: Twist distribution of the vertical fenestron

5.2 Tail Surfaces

As the main rotor cannot be tilted with respect to the fuselage, a tail has been designed to allow for controlled flight. The tail rotors have already been sized in Section 5.1 and they are able to provide the required control forces. In forward flight though it is possible to unload these rotors and decrease the total power consumption by the lifting surfaces. This section explains the sizing method adopted for the tail surfaces and then sizes the horizontal and vertical tail accordingly.

5.2.1 Tail Fin Sizing Method

The power and performance group has determined the necessary forces for stability and given a suggestion on the percentage to be provided by the tail surfaces in cruise. For the generation of a force by a lifting surface Equation (5.17) holds.

$$L = 0.5\rho V^2 S C_L \tag{5.17}$$

Attention should be paid to the definition of span and wing surface area. Wing span and wing area are defined as including both wing sides. The tail surfaces under design though can be modelled as one half wing. Therefore the surface area used in Equation (5.19) should reflect that, in mathematical terms this means:

$$L_{ls} = 0.5\rho_{cruise} V^2_{cruise} S_{halfwing} C_L \tag{5.18}$$

As the design condition is cruise, the density is the ISA density at the cruise altitude of 1500m. Determining the velocity the horizontal tail experiences is more complex. The fuselage, main rotor wake and the wake caused by the three tail rotors create a flow field around the tail surfaces that requires high computational effort to predict. Most likely even the accuracy of those prediction models is not sufficient and they need to be tuned after more insight has been gained by windtunnel experiments. As this is beyond the scope of this project the velocity the tail experiences is assumed equal to the free stream velocity, which in the absence of wind is equal to the flight velocity. The cruise velocity is a customer requirement. All the known input parameters are shown in Table 5.10.

Table 5.10: Known parameters for the lift calculation of the horizontal tail surface

Parameter	Symbol	Value	Unit
Density at cruise altitude (1500m)	ρ	1.058	[kg/m^3]
Cruise velocity	V_{cruise}	41.16	[m/s]

The lift required for each tail surface is also known from power and performance calculations. As it varies for the lifting surfaces under consideration its value is discussed in the corresponding sizing section. Rearranging Equation (5.17) and inputting the value of Table 5.10 the product of tail surface area and lift coefficient is known to be as is given in (5.19).

$$S C_L = \frac{L}{1792.4} \tag{5.19}$$

The horizontal tail surface area and the lift coefficient need to be chosen to satisfy Equation (5.19). Although seemingly independent, both parameters are indirectly related via the stabiliser planform and thus can only be chosen within certain constraints.

In contrast to the rotor blades the horizontal tail surface can not be assumed to be infinite and the airfoil lift polar requires adjustment for this case. Mainly due to the tip vortices the gradient of the lift curve decreases with respect to the infinite case (see Equation (5.20)). With the zero lift angle of attack remaining the same for finite and infinite wings, the linear regime of the finite case is completely determined with Equation (5.20).

$$C_{L_\alpha} = \frac{C_{l_\alpha}}{1 + \frac{C_{l_\alpha}}{\pi e AR}} \tag{5.20}$$

Thus to determine the lift coefficient for the horizontal tail surface the airfoil used (C_{l_α}), the lift distribution (Oswald factor e) and the aspect ratio (AR) need to be determined. The Oswald factor is set equal to one, thus assuming elliptical lift distribution. For this assumption to be valid either an elliptical or optimal tapered planform is necessary. With ease of manufacturing as an argument the option of a tapered planform is selected. Optimum taper is a function of sweep angle as shown in Figure 5.7.

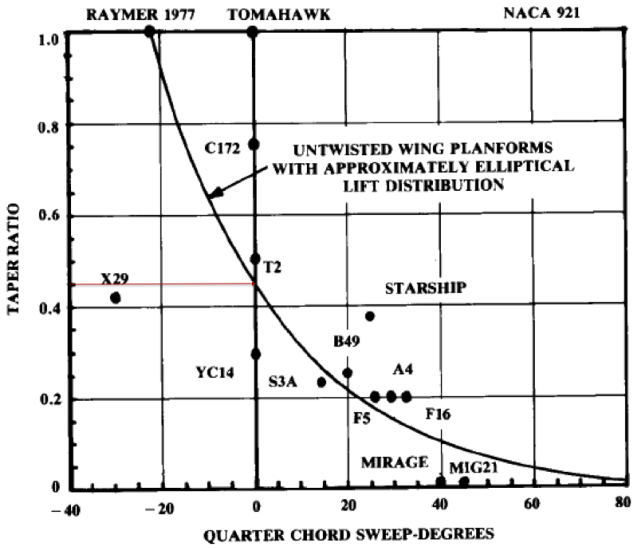

Figure 5.7: Relation of sweep angle and taper for elliptical lift distribution [71]

Sweep is generally used to delay the critical Mach number. For the ducted fan designed, the maximum flight velocity is limited by the tip speed of the rotor blades and is determined in Section 9.3 to be about 72 m/s. This velocity does not warrant a sweep angle to delay the critical Mach number. Consequently the sweep angle is set to zero. Consulting Figure 5.7 the taper ratio is chosen to be $\lambda = 0.45$.

$$\lambda = \frac{c_t}{c_r} \tag{5.21}$$

With the taper ratio set, root and tip chord become interdependent parameters (see Equation (5.21)). For this iteration process the root chord is selected as the independent parameter and the tip chord as the dependent one. The root chord is set as the diameter of the corresponding control rotor plus 70 cm. It is desired to have a smooth transition from the structure surrounding the control rotor to the tail surface to avoid stress concentrations and ensure a smooth flow over the surface. Whereas the 70 cm (35cm on each side) is selected to ensure enough room for structure and electronics. With a chosen root chord also the average geometric chord is known by using Equation (5.22)

$$c_{geo} = \frac{c_t + c_r}{2} \tag{5.22}$$

To fix the planform the only remaining parameter to be chosen is the span of the horizontal tail surface. This in turn sets the surface area (see Equation (5.23)) and the aspect ratio (see Equation (5.24)).

$$S = c_{geo} b \tag{5.23}$$

$$AR = \frac{b^2}{S} \tag{5.24}$$

Considering all the assumptions explained in this section there are only two parameters that can be chosen: the airfoil (thus C_{l_α}) and the span. The remaining parameters are calculated based on these two parameters.

Three airfoils are selected based on the criterion that the maximum $\frac{L}{D}$ ratio is obtained at relatively low angles of attack (below 5 degrees). The airfoil of the horizontal tail should preferably operate at maximum $\frac{L}{D}$ in design condition

(cruise with payload) as it is the most "efficient" operating condition. As the stabiliser is mounted directly adjacent to the tail rotor it should be fitted onto the rotor support structure without major twist angle for the ease of structural design and smoother flow over the aerial vehicle. The tail rotors themselves can not be mounted under an angle with respect to the vehicle's principal axis due to control considerations. Following from the combination of those two constraints is the angle of incidence constraint for the horizontal tail surface. This in turn demands the optimum operating condition of the airfoil to be located at small angles of attack. The chosen airfoils and their characteristics are summarised in Table 5.11.

Table 5.11: Airfoil characteristics

Airfoil [-]	$(L/D)_{max}$ [-]	α **at** $(L/D)_{max}$ [**deg**]	C_{l_α} [-]	α_0 [**deg**]	C_{d_0} [-]	C_m **at** $(L/D)_{max}$ [-]
Goe 693	115.5	3.0	5.9	-3.15	0.00825	-0.088
Clark Y smoothed	119.6	3.0	5.42	-3.98	0.008	-0.0965
Goe 796	122.7	3.5	5.6	-3.5	0.0084	-0.0893

Furthermore it is assumed that the maximum (L/D) occurs at the same angle of attack for the case of a finite and an infinite wing. This is to ease the computational efforts as the angle for the infinite case is available in literature (lift drag polar) but would need to be constructed for the finite case. As lift and drag coefficients change with the aspect ratio for the finite case the angle at maximum (L/D) changes too, requiring an additional loop in the iteration.

With the given values in Table 5.11 and the approach outline in this section an optimum tail surface design is made for each airfoil by adjusting the span. These are then compared and the most favourable one is chosen. To perform a final trade-off for the airfoil, three parameters are selected: tail surface size, moment and drag generated. The tail surface size should preferably be small to have a low structural weight. As an indicator the total tail surface area is utilised. With increasing size the structural weight increases but the effect is smaller than for an increase in load. Therefore the tail surface area is given the lowest weight of 2.

The moment is not adjusted to the finite case and therefore can be determined according to Equation (5.25).

$$M = 0.5\rho_{cruise}V_{cruise}^2 S_{halfwing}c_m c_{aero} \tag{5.25}$$

An increase in moment requires the tail structure to sustain a larger torque and thus increases the structural weight. Therefore it is preferred to have a small moment. A load increase is expected to have more effect on the structural weight than the size increase. Thus the moment is assigned a weight factor of 4 which is higher compared with the weighting criteria for the tail size.

Drag, similar to lift, needs to be adjusted to the case of a finite wing. The total drag is given as the sum of the induced drag and the zero lift drag. Equations (5.26) and (5.27) can be used for the calculations.

$$C_{D_i} = \frac{C_L^2}{\pi e AR} \tag{5.26}$$

$$C_D = C_{D_0} + C_{D_i} \tag{5.27}$$

Obviously a low drag is preferred in order to lower the thrust required and with it the fuel consumption. The drag is assumed to have the highest effect on the fuel consumption and is thus given the highest weight. In addition this section is devoted to the sizing based on aerodynamics which adds to the arguments for giving the drag the highest weight of 5.

The different airfoils are given a score 1 to 3 for each category, with 3 being the best and 1 being the worst. Then the weighted average gives an indication of which design is best suited for the task.

5.2.2 Vertical Tail

In contrast to the vertical tail rotor the vertical tail fin is sized for cruise flight with payload. As can be seen by Equation (5.17) a vertical tail fin is not able to unload the vertical tail rotor in the critical hover condition as by definition the forward velocity is zero in this flight condition. The condition with payload is critical as it requires the highest lift generation of the main rotor and thus the largest torque is generated. As outlined in Section 5.1.5 it is assumed that 50% of the required anti torque is provided by the fenestron and the other 50% by the vertical tail fin.

Based on the blade element theory and the momentum theory the torque generated by the main rotor in the described condition has been determined to be $T = 92804Nm$. Following the suggestion of the propulsion and power group the anti torque generated by the vertical tail fin should be $T_v = 46402Nm$. Iterations have shown that this leads to a rather large surface of the vertical fin. Therefore the torque counteracted by the vertical fin is reduced to 25%. To keep the report more concise these iterations are not shown but the reader is encouraged to reflect on the tail sizes obtained with the reduced torque.

In contrast to the horizontal tail the vertical tail is solemnly sized for torque. The moment generated around the tail as well as product of lift and tail arm provide anti torque (see Equation (5.28)).

$$T_v = M_v + x_v L_v \tag{5.28}$$

Thus the lift required from the vertical fin is reduced by the moment acting around the tail. The process explained in Section 5.2.1 can then be applied in an iterative way to find the optimum design for each airfoil under consideration. For convenience the input variables are summarized in Table 5.12.

Table 5.12: Input parameter for vertical fin sizing

Parameter	Symbol	Value	Unit
Required anti torque	T_v	23201	[Nm]
Vertical tail arm	x_v	12	[m]
Cruise velocity	V_{cruise}	41.16	[m/s]
Density at cruise altitude	ρ_{cruise}	1.058	[kg/m^3]

Performing the sizing leads to the three design options for the vertical tail that are outlined in Table 5.13.

Table 5.13: Characteristics of possible vertical tail designs

Airfoil	Geo 639	Clark Y smoothed	Goe 796	Unit
Aspect ratio	7.86	7.49	7.32	[-]
Semi span (span)	2.85 (5.7)	2.72 (5.43)	2.66 (5.31)	[m]
Vertical tail area	4.13	3.94	3.85	[m^2]
Mean aerodynamic chord	1.52	1.52	1.52	[m]
Geometric average chord	1.45	1.45	1.45	[m]
Root chord	2	2	2	[m]
Tip chord	0.9	0.9	0.9	[m]
Lift gradient	4.76	4.41	4.51	[1/rad]
Zero lift angle of attack	-3.15	-3.98	-3.5	[deg]
Lift coefficient	0.51	0.54	0.55	[-]
Zero lift drag coefficient	0.0083	0.008	0.0084	[-]
Induced drag coefficient	0.011	0.012	0.013	[-]
Drag coefficient	0.019	0.020	0.022	[-]
Total drag	69.8	71.4	74.4	[N]
Total moment	-495	-517	-468	[Nm]

The design trade-off, as outlined earlier, is based on total moment, total drag and size and is visualised in Table 5.14.

Table 5.14: Trade-off table for vertical tail design

	Goe 693		Clark Y smoothed		Goe 796		
Parameter	**Value**	**Score**	**Value**	**Score**	**Value**	**Score**	**Criteria Weight**
Total drag [N]	69.8	3	71.4	2	74.4	1	5
Total moment [Nm]	-495	2	-517	1	-468	3	4
Vertical tail area [m^2]	4.13	1	3.94	2	3.85	3	2
Weighted average score	2.27		1.64		2.09		

Scoring the highest the Goe 693 is selected as airfoil and the tail is sized accordingly (see Table 5.13 first column).

It might be worth to add that the zero sweep assumption is debatable for the vertical tail. In practice it can be seen that most vertical tails mounted on a fenestron have at least a small sweep angle (see for example the EC135 or the SA 341). For helicopters with conventional tail the vertical fin often has a sweep angle of around 40 degrees [85]. The reason for these sweep angles is not the delay of the critical Mach number (as common for aircraft) but to minimise structural weight and moment due to the empenage [85]. Therefore the sweep angle is kept at zero for now but it might be changed if deemed beneficial.

5.2.3 Horizontal Tail

Similarly to the horizontal tail rotors the horizontal tail surfaces are sized for cruise condition without payload. The same line of arguments can be followed as for horizontal tail rotors. The surfaces are used to unload the horizontal tail rotors decreasing the power required in cruise. As outlined in Section 4.2.3 it is assumed that 50% of the required horizontal tail lift is provided by the rotors and the other 50% by the horizontal tail surfaces.

To allow for lateral stability and roll control the design has two tail rotors. An axissymmetrical tail is necessary to avoid the introduction of a rolling moment in forward flight. The choice is made to split the horizontal tail into two surfaces that are mounted adjacent to the horizontal tail rotors. During the sizing process the complete horizontal

tail is considered (so both horizontal tail surfaces). The dimensions for one of the surfaces is then half of the values computed.

The power and performance group determined the required total lift of the horizontal tail to be $L_{h,total} = 5320N$ in order to counteract gravity. In addition the horizontal tail is required to generate a negative pitching moment of $M_{h,total} = 55730Nm$. Half of each is to be generated by the horizontal tail surfaces, thus $L_{h,ls} = 2659$ and $M_{h,ls} = 27865$. The tail arm is set by the propulsion and power group to be $x_h = 10.48$ (see Section 4.2.3). Consequently the moment does not account for the moment generated by the horizontal tail surface about its own axis. For now it is assumed that this moment is negligible and the tail is sized based on the lift criterion. At the end of the section it shall then be investigated if the assumption is valid and what its impact is.

The input parameters for the horizontal tail sizing are summarised for the reader's convenience in Table 5.15.

Table 5.15: Input parameters for horizontal tail sizing

Parameter	Symbol	Value	Unit
Required lift	L_h	2659	N
Cruise velocity	V_{cruise}	41.16	$\frac{m}{s}$
Density at cruise altitude	ρ_{cruise}	1.058	$\frac{kg}{m^3}$

Following the design steps outlined in Section 5.2.1 three possible designs are established whose characteristics can be seen in Table 5.16.

Table 5.16: Characteristics of possible vertical tail designs

Airfoil	Geo 639	Clark Y smoothed	Goe 796	Unit
Aspect ratio	1.16	1.09	1.08	[-]
Span (semi span)	3.77 (1.89)	3.56 (1.78)	3.53 (1.77)	[m]
Horizontal tail area	12.30	11.61	11.52	[m^2]
Mean aerodynamic chord	3.42	3.42	3.42	[m]
Geometric average chord	3.26	3.26	3.26	[m]
Root chord	4.5	4.5	4.5	[m]
Tip chord	2.03	2.03	2.03	[m]
Lift gradient	2.25	2.10	2.21	[1/rad]
Zero lift angle of attack	-3.15	-3.98	-3.5	[deg]
Lift coefficient	0.24	0.26	0.26	[-]
Zero lift drag coefficient	0.0083	0.008	0.0084	[-]
Induced drag coefficient	0.016	0.019	0.020	[-]
Drag coefficient	0.024	0.027	0.028	[-]
Total drag	267.7	281.9	289.5	[N]
Total moment	-3316	-3433	-2945	[Nm]

Then the trade-off is performed based on the criteria outlined. It is visualised in Table 5.17.

Table 5.17: Trade-off table horizontal tail designs

	Goe 693		Clark Y smoothed		Goe 796		
Parameter	**Value**	**Score**	**Value**	**Score**	**Value**	**Score**	**Criteria Weight**
Total drag [N]	267.7	3	281.9	2	289.5	1	5
Total moment [Nm]	-3316	2	-3433	1	-3151	3	4
Vertical tail area [m^2]	12.3	1	11.61	2	11.52	3	2
Weighted average score	2.27		1.64		2.09		

Scoring the highest the Goe 693 is selected as airfoil and the horizontal tail is sized accordingly (see Table 5.13 first column). The readers attention is again directed to the fact that the dimensions are for the complete horizontal tail (and not for only one tail fin).

As mentioned before the horizontal tail has two objectives: provide the necessary pitching moment and provide required lift. With the given values the tail can only be sized for one. Table 5.18 outlines the resultant horizontal tail designs for the Goe 693 airfoil for both cases based on the approach of Section 5.2.1.

Table 5.18: Comparison of lift and moment based sizing for the Goe 693

Horizontal tail parameters	Lift based sizing	Moment based sizing	Difference %
Span (semi span) [-]	3.77 (1.89)	3.51 (1.80)	7.4
Horizontal tail area (both) [m^2]	12.3	11.5	7.0
Total lift [N]	2659	2367	12.3
Total drag [N]	267.7	246.2	8.7
Total moment [Nm]	-3316	-3087	7.4

All values compared in Table 5.18 have a difference lower than 13 percent. The assumption made earlier is that the moment about the horizontal tail can be neglected and the sizing can therefore be performed based solely on the lift. As outlined, the difference is minor and the engineering assumption is considered valid. If more accurate results are required the main rotor thrust needs to be taken into the loop. The requirements then are that the total moment about the center of gravity has to equal zero and the total lift produced has to equal the weight.

5.3 Duct Sizing

For the calculations so far a simplified form of a duct has been considered which is essentially a cylinder of changing cross-sectional area. This is sufficient to establish models based on momentum theory to calculate the necessary aerodynamics and performance parameters.

In reality not only the cross-sectional area but also other parameter such as inlet radius or the gap between rotorblade and duct will have an influence on the performance of the ducted fan. This is due to effects (e.g. viscosity) that are not considered in the momentum theory.

There are numerous parameters that can be adjusted during the duct sizing. The four most influential ones are [67]:

- Lip radius r_{lip}
- Tip clearance δ_{tip}
- diffuser expansion ratio σ_d
- diffuser angle θ_d

Figure 5.8 shows a schematic build up of a duct. With the rotor radius and the expansion ratio determined from the power sizing and the above mentioned sizing parameter known, the dimensions of the duct can be determined by simply geometric considerations.

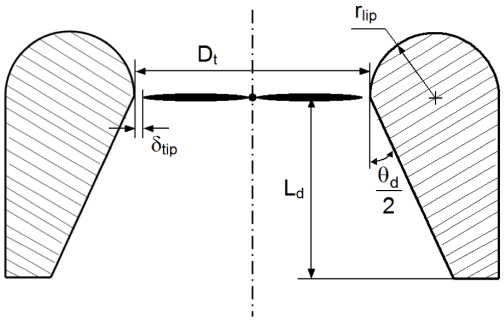

Figure 5.8: Scheme of a duct with general sizing parameters indicated [67]

In the following sections these four parameters and their influence on the performance of a ducted fan are discussed. Furthermore suggestions are given on how to estimate those parameters. The last section then summarizes the sizing results for all three rotors types: the main rotor, the horizontal tail rotors and the vertical tail rotor.

Attention needs to be paid at the methods, though that the sizing methods used are based on the work of authors, who have worked with micro-aerial vehicle in axial flight. The range of Reynold's numbers as well as the flow distribution through the rotor is thus different. If their observations hold for the case under consideration remains to be seen. But as this project has limited resources the necessary CFD simulations or even windtunnel test are beyond the scope.

5.3.1 Lip Radius

The lip radius is the radius of the tip of the airfoil that constitutes the duct. It also determines the distance between the duct inlet and the propeller location (see Figure 5.8). A small lip radius forces the incoming flow to perform more turning. This increases the suction pressure at the duct inlet, which generally increases the thrust efficiency [67] at the same time, though the area upon which this suction acts decreases. Therefore the exact effect is to be determined for each individual case. An obvious disadvantage of a large tip radius is the increased size of the duct that in turn increases the drag.

Hovey [39] suggest a lip radius of 5 % -15 % of the propeller diameter. This is for axial flight. In nearly horizontal flight, which is what this ducted fan is designed for, the flow needs to turn over a large angle due to rotor attitude with respect to flow direction. It is also assumed that the flow in edgewise flight is more turbulent when compared to the axial flight case, as the flow is accelerated nearly perpendicular to the flight axis. Whereas the acceleration is nearly in parallel to the

flow for axial flying condition. Turbulent boundary layers can withstand stronger adverse pressure gradients. Due to the significant increase in Reynold's number from micro aerial vehicle to the size of the design under consideration, the separation resistance of a turbulent boundary layer increases. The combination of these factors is assumed to allow for a smaller lip radius without the danger of flow separation. A value of 25% of the radius is chosen for the ducted fan under design. It might be beneficial to change this at a later stage of the design process or it might even prove to be an unacceptable sharp turn, which leads to inlet flow separation.

Additionally it could be beneficial to decouple the rotor location within the duct from the lip radius (currently it is located at one times the lip radius from the duct inlet). This would allow the flow more time to straighten after the turn while keep the turning angle the same. These thoughts are kept for a later design stage.

5.3.2 Tip Clearance

Tip clearance is defined as the gap between the tip of the rotor blades and the shroud. Small clearance decreases the vortex structure and increases thrust [58]. On the other hand the clearance is required to be large enough to prevent the blades from scratching against the duct in case of vibrations. Hovey [39] suggests to use a tip clearance in the range of 0.1-0.2 % of the rotor radius. For this design, the lower boundary value of 0.1% of the radius was chosen for all rotors.

$$\delta_{tip} = 0.001 * r \tag{5.29}$$

In order to prevent problems with the blades scraping the duct, the blade tips are made of an easily abrasive material. So even if the rotors scratch the shroud, it remains undamaged. The blade tips can be replaced during maintenance with a minimum of extra costs and the abrasion residue can be cleaned from the shroud.

5.3.3 Diffuser Expansion Ratio

The diffuser expansion ratio is defined in Equation (5.30).

$$\sigma_d = \frac{A_e}{A} \tag{5.30}$$

Generally speaking the task of the shroud is to constrain the contraction of the flow after it has passed through the propeller [67]. This lowers the induced power which results in the performance benefits the ducted fan is known for.

The thrust of a propeller is generally given as

$$T = 2mv_i \tag{5.31}$$

Whereas the induced power is given by the following relation

$$P_i = 0.5T\omega \tag{5.32}$$

These formulas originate from the momentum theory. For a conventional rotor the induced velocity at the rotor disk v_i and the induced velocity in the far wake ω are related by $\omega = 2v_i$. In case of the ducted fan this relation is not valid as the duct restraints the natural contraction of the flow [67]. Considering the conservation of mass of a incompressible flow it can easily be derived that a high diffuser expansion ratio lowers the induced velocity in the far wake and thus improves performance.

$$\dot{m} = \rho v_1 A_1 = v_2 A_2 \tag{5.33}$$

Assuming station 1 is at the fan and station 2 at the duct exit and using the definition of the diffuser ratio the equation can be rearranged to yield

$$\sigma_d = \frac{v_1}{v_2} \tag{5.34}$$

Theoretically the higher the diffuser ratio the lower the velocity at the duct exit if the velocity at the propeller remains constant. This in return means that increasing the diffuser ratio decreases the induced power while the thrust remains constant. In theory this performance improvement has no boundaries whereas in reality there are boundaries originating from viscosity which is not accounted for in the momentum theory.

If the diffuser ratio is too high the flow is no longer able to fight the adverse pressure gradient and separates from the diffuser wall which is not desirable. Another limit for the diffuser expansion ratio is the duct size and with it the drag. For the design a diffuser expansion ratio of $\sigma_d = 1.1$ has been chosen by the power group (see Section 4.2.4).

5.3.4 Diffuser Angle

Besides the limit to the expansion ratio there is also a limit on the diffuser angle. The change of cross-sectional area needs to be gradual enough in order to avoid flow separation. If now the diffuser ratio is increased at constant diffuser angle the thickness of the shroud increases with diffuser expansion ratio. Pereira determined in his experiments a diffuser angle of 10 degrees to be optimal [67] and this value is adopted for a first estimation of the duct design.

5.3.5 Overall Duct Sizing

Based on the suggestions outlined in previous sections the duct dimensions in Table 5.19 are obtained. The radii have been determined by power calculations in Section 4.2.3, 5.3 and 4.2.1.

Table 5.19: Duct size parameter suggestions based on literature

Duct parameters	Main Duct	Vertical tail duct	Horizontal tail duct
Rotor radius [m]	6.61	0.7	1.9
Tip clearance δ_{tip} [mm]	6.6	0.7	1.9
Expansion ratio [-]	1.1	1.1	1.1
Expansion angle θ_d [deg]	10	10	10
diffuser length L_d [m]	3.61	0.38	1.04
Tip lip radius r_{lip} [m]	0.33	0.07	0.19
Total duct length [m]	3.94	0.45	1.23

As outlined in section 4.2.7 a fuselage height of 1m would be sufficient to provide enough storage room for all systems and the fuel and thus this value has been assumed for further sizing. This assumption clearly clashes with the calculation results shown in Table 5.19 as it was also assumed that the fuselage height in a later stage will be determined by the duct size of the main rotor. To solve this issue a closer look at the calculation of the total duct length is taken. The total duct length is the sum of the lip radius and the diffuser length.

$$l_{duct,total} = r_{tip} + L_d \tag{5.35}$$

While the diffuser length can be determined by geometric considerations (see Figure 5.8). To simplify the formula which is mainly used to illustrate the relation of the duct length and the diffuser expansion ratio the tip clearance is neglected. The duct area at the rotor should be adapted to account for the gap, while in the formula presented, it only takes into account the area of the rotor. For the calculations of the final values this adaption has been made.

$$L_d = \frac{\sqrt{\frac{\sigma_d * A - A}{\pi}} - r}{tan(\frac{\theta}{2})} \tag{5.36}$$

So a trade-off is required between thrust efficiency, which increases with increasing diffuser ratio and drag, which also increases with increasing diffuser ratio. The overall drag of the system is relatively large already due to the under slung container that has a rather high drag coefficient caused by its form. This in combination with the fact that the fuselage volume is sufficient with a height of 1m the decision has been made to adapt the diffuser expansion ratio of the main rotor in order to obtain a total duct length of 1m. To improve performance again, which deteriorates with this adaption of the diffuser expansion ratio, flow straighteners can be inserted into the duct. This is left for a second iteration step. For the vertical tail duct the size is reasonable and the values in Table 5.19 are used.

In the case of the horizontal tail ducts, it seems beneficial to adapt the diffuser expansion ratio to again decrease the frontal area of the design. The value of $\sigma_d = 1.05$ is chosen as a compromise between aerodynamics and thrust performance. The final values for the duct which incorporate the discussed changes are summarised in Table 5.20. For the main rotor and the horizontal tail rotor the changed diffuser expansion ratio needs to be fed back into the power sizing for a second iteration.

Table 5.20: Final duct size parameters

Duct parameters	Main Duct	Vertical tail duct	Horizontal tail duct
Rotor radius [m]	6.61	0.7	1.9
Tip clearance δ_{tip} [mm]	6.6	0.7	1.9
Expansion ratio [-]	1.02	1.1	1.05
Expansion angle θ_d [deg]	10	10	10
diffuser length L_d [m]	0.68	0.38	0.51
Tip lip radius r_{lip} [m]	0.33	0.04	0.10
Total duct length [m]	1.00	0.42	0.61

5.4 Balance of Forces

In order to determine the optimum angle of attack in cruise condition one rotorcraft is modelled as a point mass and the force balance is considered. Figure 5.9 illustrates the relevant forces.

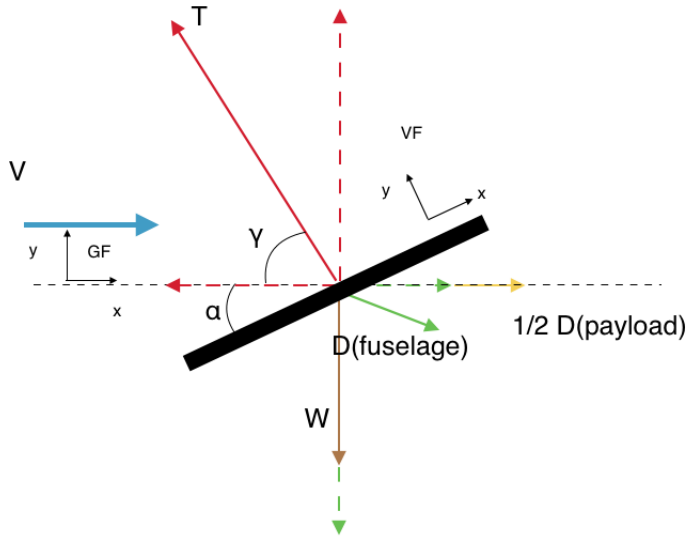

Figure 5.9: Balance of forces during steady cruise flight

Regarding the payload it is assumed that half the drag and half the weight is carried by one rotorcraft. As the equivalent weight of one rotorcraft (so with a contribution of the payload) has already been determined in Section 4.1.4, it is not subdivided into the different constituents but shown as one force.

For all other forces the derivation of the numerical values is outlined in the following sections. With the magnitude of all forces determined, the optimum angle of attack can be derived.

5.4.1 Fuselage Drag

The fuselage drag is a function of angle of attack of the ducted fan. In order to determine a mathematical relation the principle of superposition is applied. It is assumed that the total drag can be decomposed in a part in x-direction and a part in y-direction in the vehicle reference frame. The vectorial sum of both gives the magnitude and direction of the total drag. Furthermore the force in y-direction is caused by the velocity increment along the y-axis while the force in x-direction is due to the x-component of the velocity only. See Figure 5.10 for a graphical illustration.

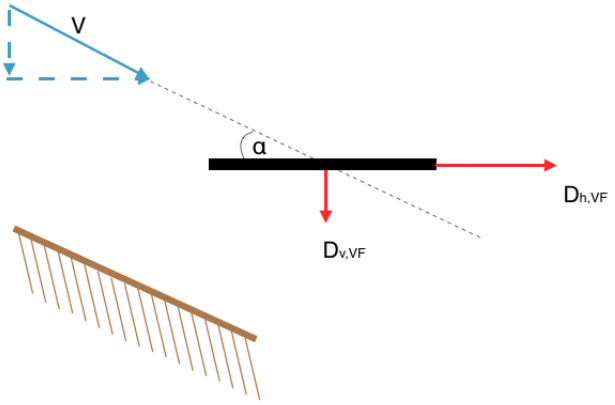

Figure 5.10: Drag components for angled flight at cruise

With this assumption the drag force in each direction can be determined with Equations (5.37) and (5.38).

$$D_{x,VF} = 0.5\rho V_{h,VF}^2 S_h C_{D.h} \tag{5.37}$$

$$D_{y,VF} = 0.5\rho V_{v,VF}^2 S_v C_{D,v} \tag{5.38}$$

The free stream velocity is decomposed into its two components according to Equations (5.39) and (5.40).

$$V_{x,VF} = cos(\alpha)V \tag{5.39}$$

$$V_{y,VF} = sin(\alpha)V \tag{5.40}$$

In each principal direction the fuselage has a specific drag coefficient that is independent of angle of attack. Their respective values are determined by a flow simulation over a model using CFD. The modelling does not account for the rotation of the fans. A verification of the tool used is presented in Appendix C. Refer to Table 5.21 for the values of the drag coefficient.

Table 5.21: Fuselage drag coefficient for different orientations

	Drag coefficient [-]
horizontal (yz-plane)	0.695
vertical (xz-plane)	0.898

Table 5.22: Frontal area of the ducted fan for different orientations

	Frontal area $[m^2]$
horizontal (yz-plane)	15
vertical (xz-plane)	120

With these values given and the ISA, which stipulated a density of $\rho = 1.058 kg/m^3$ for the cruise altitude of 1500m, the drag in the vehicle frame can be written as a function of angle of attack only. Finally the drag is transformed from the vehicle frame to the ground frame with Equations (5.41) and (5.42).

$$D_{x,GF} = cos(\alpha)D_{v,VF} - sin(\alpha)D_{h,VF} \tag{5.41}$$

$$D_{y,GF} = -sin(\alpha)D_{v,VF} + cos(\alpha)D_{h,VF} \tag{5.42}$$

5.4.2 Payload Drag

The payload as specified by Hospitainer is a standard size 40 ft shipping container. Its dimensions are given in Table 5.23.

Table 5.23: Dimension of a 40ft container

	Dimensions [m]
Width	2.438
Height	2.891
Length	12.192

Due to its rectangular shape the container will experience a significant amount of drag. Besides the container orientation the drag also depends on the flight altitude and the flight velocity. As mentioned earlier force equilibrium in cruise condition is to be analysed and thus this is the condition the drag is calculated for. One needs to keep in mind that this might not be the condition with the highest drag during the mission. The payload drag can be computed according to Equation (5.43).

$$D_{payload} = 0.5\rho V_{cruise} S C_D \tag{5.43}$$

Hoerner [37] states a drag coefficient of 2.05 for a cubic body. It is the form that most accurately resembles a rectangular shape and thus this drag coefficient is utilised for the drag calculations. The value for the density at cruise altitude is $\rho_{cruise} = 1.058 \frac{kg}{m^3}$ and the cruise speed is required to be $V_{cruise} = 41.16 \frac{m}{s}$. Depending on the container orientation the frontal area S changes. There are essentially three different options, which are illustrated in Figure 5.11 and the corresponding values of frontal area and drag are given in Table 5.24.

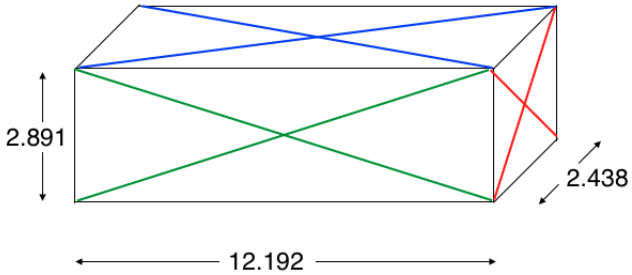

Figure 5.11: Sketch of a 40ft container with dimensions

Table 5.24: Payload cruise drag for different container orientations

	Frontal area [m^2]	**Drag [N]**
Option 1 (red)	7.05	12949
Option 2 (blue)	29.72	64756
Option 3 (green)	35.24	54610

In order to keep the drag as low as possible the container is oriented such that the surface indicated in red faces the free stream. Then the total drag due to the container is around 13 kN. Each rotorcraft thus needs to be capable of producing an extra forward oriented thrust of around 7.5 kN to be able to tow the container at cruise speed.

5.4.3 Thrust

As the ducted fan has no swash plate the thrust is always perpendicular to the xz-plane of the vehicle reference frame. The decomposition into components in the ground reference frame is shown in Figure 5.12.

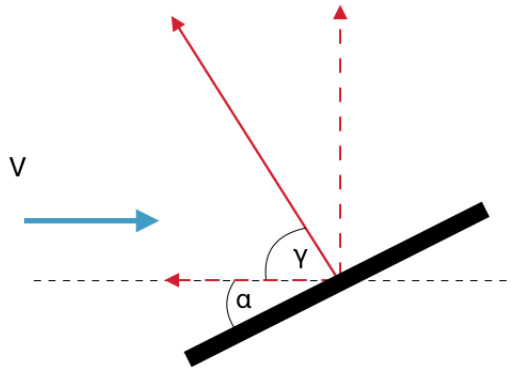

Figure 5.12: Decomposition of the thrust

The transformation from the vehicle reference frame to the ground frame is given by Equations (5.44) and (5.45).

$$T_{y,GF} = cos(\alpha)T \tag{5.44}$$

$$T_{x,GF} = sin(\alpha)T \tag{5.45}$$

Note that two thrust components have a fixed ratio when the angle of attack is set.

5.4.4 Optimum Flight Angle and Thrust Required

In steady horizontal flight the sum of forces in x and y-direction has to be zero. Or rephrased: the thrust needs to be equal in magnitude and opposite in direction to the vectorial sum of the drag forces and the weight.

Thus summation of the drag and weight forces determines the thrust. All considered forces are constant with angle of attack except for the fuselage drag. For every possible angle of attack (0-90 degrees) the vectorial sum of drag and weight has been determined. The angle for which the magnitude is the smallest is the optimum angle of attack for cruise flight with payload. This angle is about 2.8 degrees and the corresponding forces are given in Table 5.25.

Table 5.25: Forces at optimum angle of attack

Angle of attack [deg]	$D_{h,GF}$ **[N]**	$D_{v,GF}$**[N]**	**Weight [N]**	$0.5D_{payload}$ **[N]**	**Total force to overcome [N]**
2.8	9331	225	91468	6475	92602

The issue with this solution is though that the vertical and horizontal component of the trust are not independent but can only be applied at a ratio which is dependent on the angle of attack. Thus an angle of attack needs to be found where the required ratio of the horizontal and vertical force is equal to the one that can be provided. At cruise speed this is the case for 9.74 degrees and the corresponding forces are given in Table 5.26.

Table 5.26: Force at actual angle of attack

Angle of attack [deg]	$D_{h,GF}$ **[N]**	$D_{v,GF}$ **[N]**	**Weight [N]**	$0.5D_{payload}$ **[N]**	**Total force to overcome [N]**
9.74	9424	1193	91468	6475	94015

Currently the total thrust available is the sum of the horizontal fenestrons and the main rotor, which in total is $T = 92379N$ (see Section 4.2.1 and 4.2.3) for optimum collective pitch. The collective pitch can be increased to give the required thrust but the blades then do not operate at optimum L/D and the rotor torque increases.

The values for the required thrust and the actual angle of attack can be fed back to the aerodynamic and power calculations for a second iteration. Additionally it might be beneficial to consider either a standard inclination of the rotor with respect to the fuselage or even the use of a swash plate to allow cruise operation at optimum angle of attack.

5.5 Autorotation

Since a ducted fan with the flying configuration as proposed is not common, hardly any literature is available on the assessment of its autorotation capabilities. It is expected though that ducted fans will not be capable of performing controlled landing in autorotation as the shroud shields the rotor blades form the oncoming flow. This section aims at providing proof of this assumption by analysing the autorotation coefficient and showing what the rate of descent would be for the unshrouded case.

5.5.1 Autorotative Index

Usually in preliminary sizing, the autorotation capabilities of a helicopter are expressed in terms of the so-called autorotative index (AI). Note that this index is based on helicopters and is not proven to be valid for ducted fans. However, it will be used as an indication of the rotorcraft's autorotation capabilities. A variety of autorotative indices have been defined, but basically it is a stored energy factor. Sikorsky uses a form of the AI that is weighted by Disk Loading as in Equation (5.46) and is proposed by Fradenburgh [31].

$$AI = \frac{I_R \Omega^2}{2WDL} \tag{5.46}$$

In order to determine the auto rotative index of the rotorcraft, the blade polar moment of inertia has to be calculated. Filippone [29] derives an estimation with Equation (5.47) as result in which m_b is the mass of a single blade.

$$I_b = \frac{1}{3} m_b (R - R_i)^2 \tag{5.47}$$

The angular velocity of the main rotor as it is used throughout this chapter $\Omega = 32.93$. The rotorcraft weight with payload equals 9324 kg and without payload 4113 kg. The total mass of the blades has been estimated in Subsection 4.1.1 to be 233.4 kg, so one blade weighs 46.48 kg. F rom sizing results a blade radius of 6.61 m with a hub radius of 1.32 m. The disk loading of the rotorcraft is equal to its weight divided by the disk area:

$$DL = \frac{W}{\pi R^2} \tag{5.48}$$

Combining Equations (5.49), (5.47) and (5.48) yields:

$$AI = \frac{I_R \Omega^2}{2WDL} = \frac{\frac{1}{3} m_b (R - R_i)^2 \Omega^2}{2W \cdot \frac{W}{\pi R^2}} = \frac{m_b (R - R_i)^2 \Omega^2}{6 \frac{W^2}{\pi R^2}} \tag{5.49}$$

Evaluating Equation (5.49) for the rotorcraft with and without payload yields autorotative coefficients of $AI_{payoad} = 0.37 m^3/kg$ and $AI_{nopayload} = 1.92 m^3/kg$. Note that these values are only of use for comparison, and not in absolute sense. Leishman [55] states that the autorotation coefficient of a normal helicopter is about 20 and multi engine helicopters can have a somewhat lower index and are still able to land safely. The calculated indices are much lower than 20 though and as such the rotorcraft is not really able to autorotate. The reason for this values mainly comes from the high disk loading of the rotorcraft. During initial sizing the disk loading of a ducted fan was assumed to be higher due to higher efficiency. Another approach is the investigation of the rate of descent after engine failure, which is discussed below.

5.5.2 Rate of Descent

From actuator disk theory and the assumption that weight equals thrust the rate of decent can be derived. For the detailed derivation please refer to van Holten et al. [79]. With the figure of merit $FoM = 0.716 - 0.75$ (varying for different flight conditions) and the flow uniformity coefficient $k = 1.15$ the rate of descent can be estimated. The highest figure of merit of $FoM = 0.75$ is used as it is the most critical case.

$$C = -97 m/s \tag{5.50}$$

The calculated decent velocity of nearly 100 m/s is too high for the vehicle to withstand the forces upon impact and it will disintegrate. For comparison, CS25 stipulates for an aircraft in steep approach landing a maximum vertical descent velocity of 6 ft/s (1.8 m/s) [18] at touch down. The calculated decent velocity is even higher than the terminal velocity of

the rotorcraft and would thus not be reached in reality. Drag would lower the decent rate.

One might argue that the aerodynamics of a ducted fan are different than for a conventional helicopter and thus the outlined calculations do not represent reality. The classical actuator disk theory does not hold for a ducted fan as the duct constrains the contraction of the flow. Due to this the classical ratio of 2 between the induced velocity at the rotor disk and the completely develop induced velocity at the wake does not hold. It is assumed though, that this difference is not large enough to change the assessment of the autorotation capability. In addition the assumption has been made that the total weight of the ducted fan is carried by the main rotor while in reality the horizontal tail rotors aid in it. However, compared to the previous assumption this one is minor.

In conclusion the ducted fan under consideration is not capable of sufficient autorotation to ensure a safe and controlled landing after the failure of both engines. This result has been expected as conventional helicopters generally need some forward velocity component to successfully enter autorotation. The rotors of a ducted fan however are shielded from the forward velocity component which ultimately is the reason for the inability to perform a proper landing in autorotation.

6. Structures

This chapter evaluates the structural sizing of the ducted fan rotorcraft. It is of crucial importance that the structure of the ducted fan rotorcraft is able to withstand the large forces and moments that act on it during flight. Failure of the load bearing structure would be catastrophic. As the rotorcraft operate unmanned no cabin pressurisation is required. This will decrease the loads acting on the fuselage from the inside. Also as structural failure will not endanger pilot life, the safety factor can be decreased.
The center of gravity location is important to determine force arms which in turn influence the magnitude of the moments. On a normal manned helicopter the pilot has to sit in the front to have sufficient visibility. This introduces a front located point load which is not necessarily beneficial for the location of the centre of gravity. In the unmanned case of the ducted fan rotorcraft, the control computers can be placed without a location constraint.

The ducted fan rotorcraft is assumed to have six critical structural members, which are the main rotor system, blades, fuselage, the load carrying cross inside the duct, the attachment points of load carrying structure to the fuselage and the undercarriage. The main rotor system is discussed in Section 6.1, consecutively the blades design is specified in Section 6.2. Section 6.3 expands on the methodology and sizing of the fuselage and its connection to the main rotor system is elaborated in Section 6.4. The attachments and undercarriage are considered in Section 6.5 and 6.6 respectively. The values obtained in this chapter are fed back to the aerodynamics group and the performance group in order to allow further iterations.

6.1 Main Rotor Sizing

The lifting capabilities of a helicopter are generated by the main rotor system. This system mainly consists of two parts: the hub and the rotor blades. At this preliminary sizing stage, the blades are sized for the load case of forward flight while only a qualitative analysis is performed to determine the optimum hub type. This section expands on the hub design, while section 6.2 specifies the rotor blade sizing.

6.1.1 Hub Design

This section elaborates on the main rotor hub which connects the blades to the rotor shaft. This connection should ensure the transfer of thrust and moments of the blades to the fuselage. It should be noted that the moments acting on the blade root are large and introduce design complications. Originally these moments could only be accounted for by using rigid connections, however these resulted in unstable motions in forward flight [79]. Currently, four attachment methods are commonly used, which are classified according to their mechanical attachment method [73]. These methods are shown in Figure 6.1.

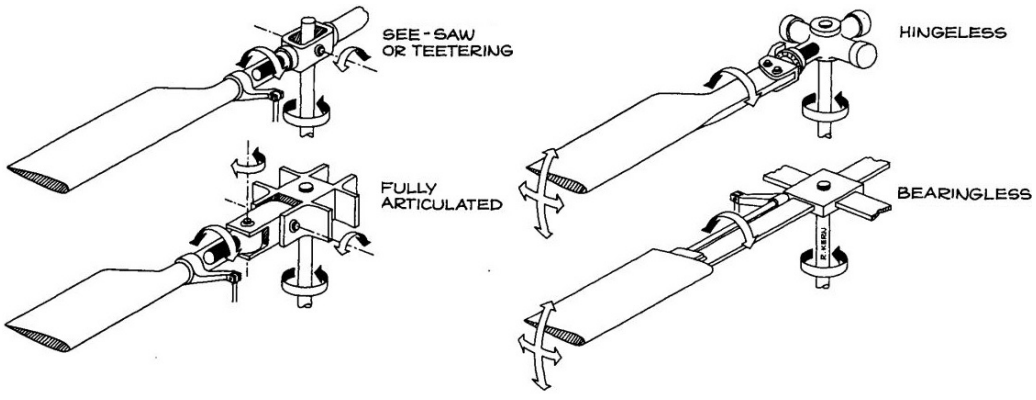

Figure 6.1: Different rotor hub systems [73]

The teetering method considers a semi-rigid connection only applicable to two bladed designs and thus, is not applicable to the five blades ducted fan design in consideration. This teetering method is actually a simplified version of the fully articulated hub [63]. This fully articulated hub design was introduced as a solution on the unstable rigid connections [73]. This resulted in a complex design consisting of three hinges at the blade root allowing flapping, lead-lag and feathering movements (i.e over all axis). Schindler's study on rotor hub designs indicated that the completely hinged concept results in low blade stress, relatively low vibrations and good stability and control characteristics. Yet, the complicated hinge system is accompanied by high maintenance cost and relatively high aerodynamic drag at the hub. [73][63]

The development of the hingeless hub was focused on decreasing these high maintenance cost by decreasing the number of hinges. This is achieved by returning to a rigid connection of the blade roots to the hub, while the blades

accommodate the flapping and lead-lag motion by elastic deformation. Note that the feathering (i.e. pitch) movement of the blade is still performed by a hinge in the hingeless concept, while the bearingless hub design also replaces this feathering hinge by elastic deforming material. The removal of these hinges decreases the mechanical complexity and aerodynamic drag, while complexity of the structural components is increased. The structure is required to have sufficient elasticity and fatigue characteristics [73]. Because of the reduction in maintenance cost and the technological capabilities of current composite materials, the bearingless rotor hub is considered the best design principle. [73][32]
The bearingless hub consist of two main parts, the flex beam and control cuff. The flex beam is rigidly connected to both the main rotor shaft as the remainder of the blade and is considered to be the main load carrying member of the hub, while the control cuff enclosed the flex beam and allows pitch control[28]. The control cuff is considered to be a secondary load carrying member. The flex beam assures bending and twisting due the flapping moment and blade torsion. These motions are established in different regions of the beam. The in-board portion of the beam is designed to be torsionally stiff, while allowing bending. In contrast to the out-board portion of the hub, which allows twisting of the blade. [32]
A hub design similar to the Bell Helicopter Trexton Model 680 is chosen in the preliminary sizing. The in-board part has a rectangular, closed cross section, specified for torsion. The outer part consist of a triple H cross section, resulting in a flapping stiff design. The transition of the inner and outer parts is considered to be stiff in torsion aswell as in bending [28]. The proposed hub design in shown in Figure 6.2.

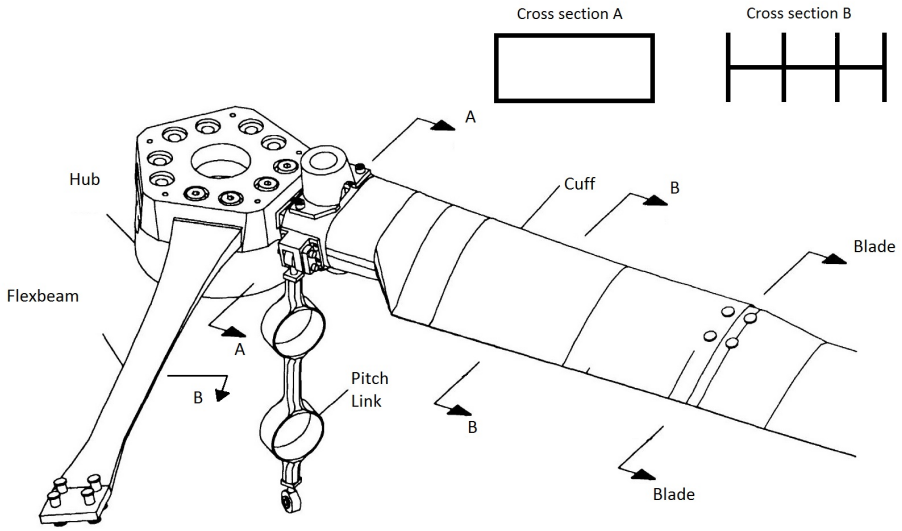

Figure 6.2: Proposed hub design [28][32]

6.2 Blade Design

This section elaborates on the preliminary structural sizing of the main rotor blades. The structural sizing of the main rotor blades expands on the design specified by the aerodynamic optimization of the rotor blades as described in Section 5.1.1. The input variables are summarized in Table 6.1. The forward flight load case is considered as this is the most critical case. The methodology used is described in Subsection 6.2.1. Consecutively the corresponding loads and stress computations are described in Subsections 6.2.1 and 6.2.1, after which the results of the sizing method are presented in Subsection 6.2.2.

Table 6.1: Structural blade input variable

Loads		**Dimensions**	
Lift per blade $[N]$	18331	Radius [m]	6.63
Drag per blade $[N]$	244	Hub radius [m]	1.32
Torque per blade $[Nm]$	114.59	root chord [m]	0.5
Mass per blade $[kg]$	46.8	tip chord [m]	0.5

6.2.1 Blade Sizing Methodology

This section describes the methodology used in the preliminary structural sizing of the rotor blades. First the simplified model is described and consecutively the assumptions related to the model are specified.

The section to be sized is the part of the blade outside the main rotor hub. The three-dimensional blade, as specified in Section 5.1.1, is modelled as an equivalent closed-section beam. The load carrying element of the airfoil cross section is

assumed to be a rectangular box having four load carrying plates, as shown in Figure 6.3a. This beam is assumed to be rigidly connected to the hub (i.e. cantilevered beam model). Moreover, in this first order estimation the beam is assumed to be a rigid structure, therefore no internal deformations are considered.

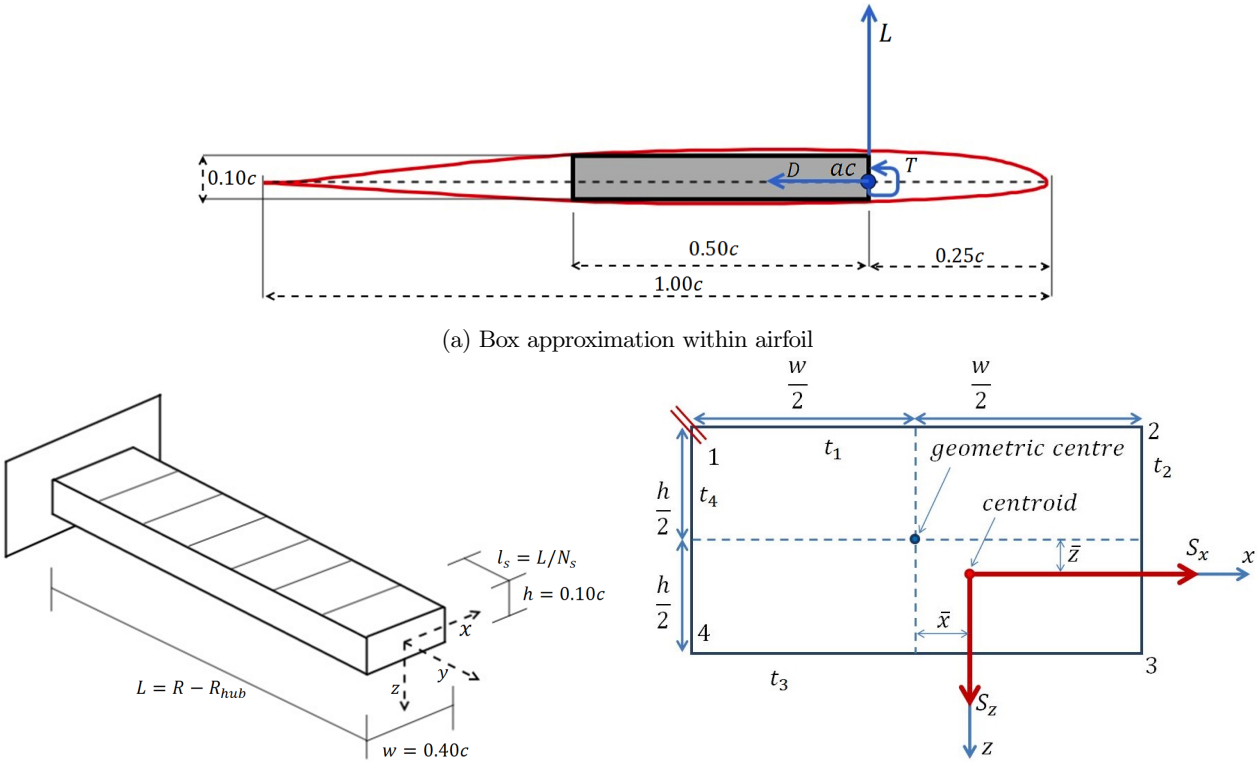

(a) Box approximation within airfoil

(b) Cantilever beam approximation of blade

(c) Box cross sectional dimensions

Figure 6.3: Rotorcraft blade simplification to a load carrying box in a cantilever system, including axis systems

This reduces the rotor blade problem to a cantilever beam, as shown in Figure 6.3b. The critical stresses are determined by consecutively defining the geometrical properties over the blade span, applying the applicable loads as specified in Section 5.1 and computing the associated stresses. These are approximated numerically by discretizing the beam in n-elements (N_s) of equal length. The geometric properties, as well as the loads over a single element are considered constant and are determined at the middle of the section. This means that a distributed force (i.e lift & drag) and corresponding moment are replaced by equivalent point loads and constant moments at the middle of each section. These discritizing effects and steps are further described in the respective subsections of geometric properties, applied loads and stresses.

Geometric properties

The geometric properties of the beam can be reduced to three main parts, namely the cross-sectional dimensions, corresponding neutral axis and moment of inertias of each element. The cross sectional dimensions are based on the chord distribution as defined by the aerodynamic optimization. The width and height of each beam element are assumed to be 50% and 10% of the local blade chord respectively , while the individual thicknesses of the four plates are initially assumed constant over the entire blade span. The geometric center line of the box is considered to be located on 50% of the chord, thus the box ranges from 25% to 75% of the chord. As the thickness of the plates is allowed to vary within the design optimization process, the neutral axis needs to be determined using Equations (6.1) and (6.2). The reference coordinate system in consideration is located at the geometric center of the beam, as indicated in Figure 6.3c.

$$\bar{x} = \frac{\sum x_i A_i}{\sum A_i} \tag{6.1}$$

$$\bar{z} = \frac{\sum z A_i}{\sum A_i} \tag{6.2}$$

Consecutively both moment of inertias (I_{xx} & I_{zz}) over the x and z neutral axis, as well as the product of inertia (I_{xz}) of each section are determined. These are obtained by considering each plate individually as a rectangular shape using Equations (6.3), (6.4) and (6.5), in which b and h refer to the width and height of an individual plate. These individual contributions are added together to obtain the total moments and product of inertias of each section. Note that these inertias are taken with respect to the neutral axis of a section (i.e d_z and d_x refer to the distance between the individual

plate centroids with respect to the neutral axis in respectively z and x direction).

$$I_{xx} = \frac{1}{12}bh^3 + bhd_z^2 \tag{6.3}$$

$$I_{zz} = \frac{1}{12}hb^3 + bhd_x^2 \tag{6.4}$$

$$I_{xz} = bhd_x d_z \tag{6.5}$$

Applied loads

The resulting stresses are greatly influenced by the applied forces over the beam cross section. The applied loads should be considered in three steps. First of all, the type of forces and moment and their corresponding location of application are set. These loads are moved to the neutral point, introducing a moment. Finally the applied load distributions are analysed and converted to the equivalent loads over each section. These loads are used to determine the internal forces and moment over the beam cross section, required to determine the stresses. The applied loads under consideration are:

- Lift
- Drag
- Centrifugal force
- Torque

The aerodynamic forces act through the aerodynamic center of the airfoil cross section, which is conventionally assumed to be located on the x axis at approximately the quarter chord length [4]. While the centrifugal force acts through the neutral axis (Figure 6.3a). As both the drag and the centrifugal force already act through the neutral axis, only the lift forces have to be moved. This introduces an additional torque component of each section, which can be determined using Equation (6.6).

$$T_{lift_y} = L_i \cdot 0.25c_i \tag{6.6}$$

The lift, drag and moment distributions over the blade are determined in Section 5.1.1. At that point the continuous distributions are replaced with equivalent point loads over the middle of the respective sections. These distributions/point loads are based on the principle of equal power over equal disk area for each blade segment. This results in sections of varying length in contrast to the constant length sections in this structural model. These distributions are converted to the current model, as is illustrated in Figure 6.4. The equivalent point loads over the varying length sections are converted to a distributed load over the respective sections. Consecutively these distributed loads are integrated over the boundaries of the sections of the beam in consideration. This conversion is verified by the fact that at any span wise location the resultant force should be equal for both equivalent load distributions. This resultant force is obtained by summing the individual contributions. The comparison of the equivalent load conversion for the lift case and the corresponding sanity check are shown in Figure 6.5. Note in the comparison of the equivalent section load forces that the varying section curve has an increasing density of data points, while the other has a constant spacing of data point. This directly relates to the varying section length, as the length of sections near the tip decrease the number of data points increase. The verification clearly indicates that both equivalent loads correspond to the same lift distribution. The same method and verification are used to discretise the drag and torque distribution over the blade. Note that these sectional airfoil induced torques should be combined with the individual torque components introduced by the translation of the lift loads (Equation (6.6)). Moreover, each section has a individual moment component around z and x due to respectively the drag and lift loads, which are determined using Equation (6.7).

$$M_{x_i} = \frac{F_{z_{i-1}} + F_{z_i}}{2} w_s \qquad M_{z_i} = \frac{F_{x_{i-1}} + F_{x_i}}{2} w_s \tag{6.7}$$

Lastly, the centrifugal force of the blades is determined using Equation (6.9). The m_{blade} refers to the mass of a single blade, of which a preliminary estimation is given in Section 4.1.1, and the ω and R_c respectively refer to rotational velocity and radius of the center of mass. Similar as for the aerodynamic loads, the centrifugal force has individual component for each section. These components are determined by using the mass and center of mass radius of the individual sections in Equation (6.9). The mass of an individual section is determined assuming the mass is proportional with the cross sectional area (Equation (6.8)).

$$m_{section_i} = m_{blade} \frac{A_{sections_i}}{\sum_{j=1}^{N_s} A_{sections_j}} \tag{6.8}$$

$$F_{cf} = m_{blade}\omega^2 R_c \tag{6.9}$$

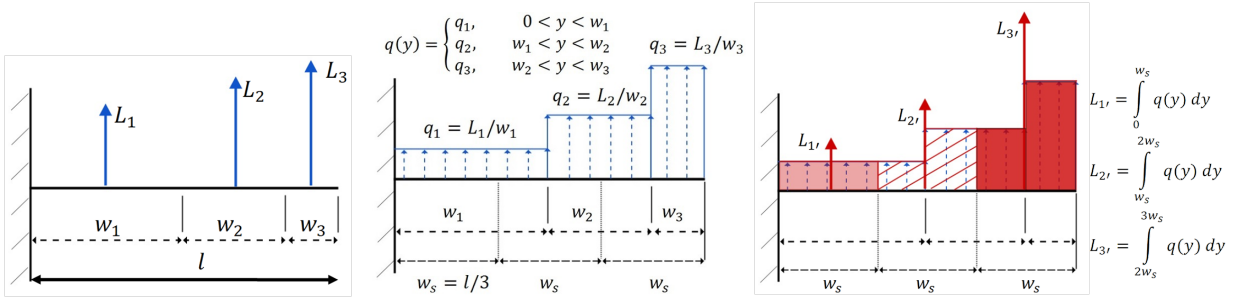

(a) Point loads of constant length sections

(b) Converted distributed loads

(c) Equivalent point load determination of constant length sections

Figure 6.4: Ilustration of conversion of point loads of varying to constant length sections

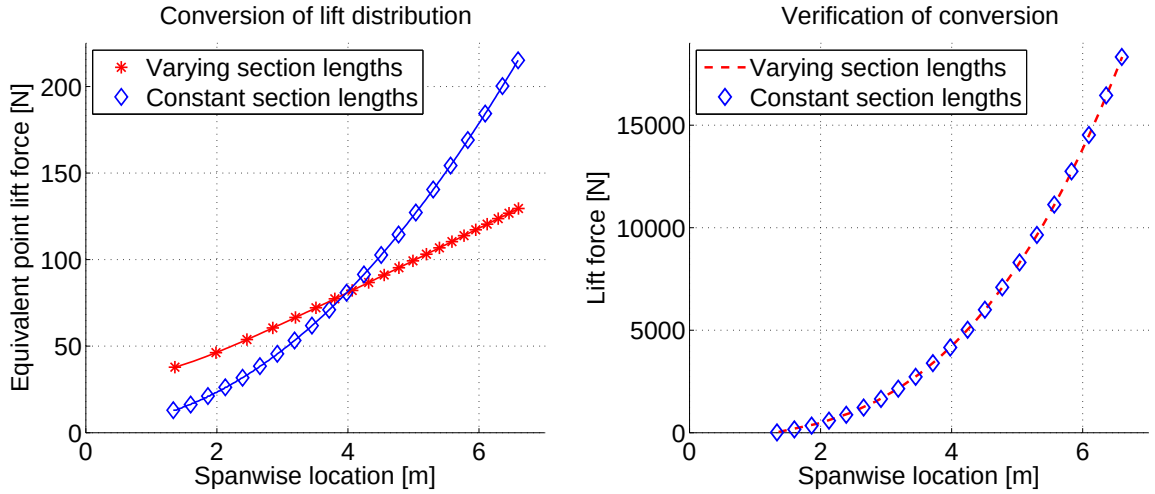

Figure 6.5: Converted lift distribution and verification

The span wise internal force and moment diagrams, as shown in Figure 6.6, are obtained by adding the individual components from tip to root. It can clearly be seen that the force in x direction (i.e the drag) is significantly smaller than both the z and y forces. This difference relates to ratio of lift and drag and the large centrifugal forces. The moment around z is also significantly lower compared to the others moments. This is due to the direct relationship with the drag force, as both the moments around y and x are dependent on the lift force. Note that the magnitude of F_x and F_z at the root is equal to the total lift and drag per blade (Table 6.1). Regulations dictate that the structure should be able to withstand a load factor of 3.5, therefore the obtained internal forces and moments are multiplied by a factor 3.5. These are used in the stress calculations of the blades [19].

Stresses

The internal forces and moments described above result in stresses over the individual cross sections. The stresses in considerations are the normal, shear and Von Mises stresses. Note that these stresses vary within a single cross section, as they are dependent on the location within such a cross section. Regulations dictate that a safety factor of 1.5 should be considered [19]. The resulting stresses are therefore increased by this factor.

The normal stress is determined by superimposing the contributions of the normal force and both moments over the z and x axis (i.e F_y, M_z and M_x). Both stress contributions are obtained for each section by using respectively Equations (6.10) and (6.11). The variables refer to the local section variables. The normal force introduces a constant normal stress over a cross section, while the moments contribute to a varying stress over the cross section. Note that x and z refer to the coordinates over the box plates with respect to the neutral axis of a cross section.

$$\sigma_{F_y} = \frac{F_y}{A} \tag{6.10}$$

$$\sigma_{M_y} = \frac{I_{xx}M_z - I_{xz}M_x}{I_{xx}I_z z - I_{xz}^2}x + \frac{I_{zz}M_x - I_{xz}M_z}{I_{xx}I_{zz} - I_{xz}^2}z \tag{6.11}$$

The shear stress is obtained by first evaluating the shear flow distribution over the beam and consecutively dividing the shear flow by the plate thickness. The derivation of the shear flow distribution over the blade cross section consist out of two parts. First the torque T_y results in a constant shear flow (Equation (6.12)), while F_z and F_x act as shear forces.

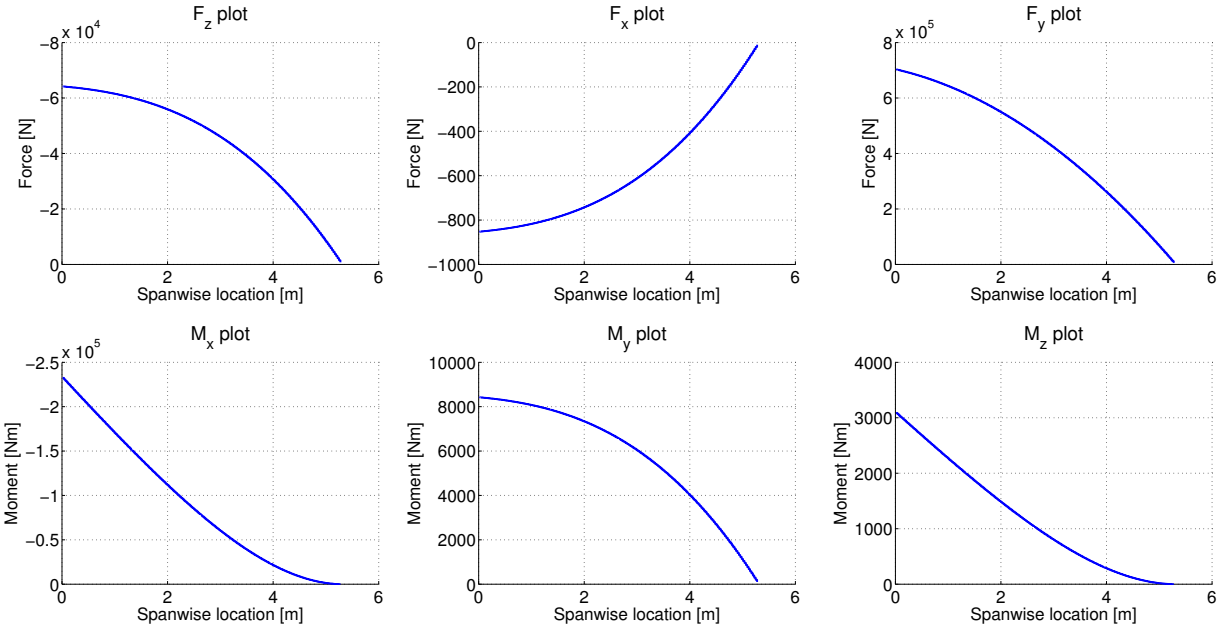

Figure 6.6: Internal forces and moments over the blade

These shear forces are incorporated in two steps. First the open section shear flow is determined using Equation (6.13) by introducing a cut at the top left corner, which is illustrated in Figure 6.3c. Additionally, moment equivalence is applied to compensate for this open section shear flow with respect to the actual closed section flow (Equation (6.14)).

$$q_{s0_{torque}} = \frac{T_y}{2A} \tag{6.12}$$

$$q_b = -\frac{I_{xx}S_x - I_{xz}S_z}{I_{xx}I_{zz} - I_{xz}^2}\int_0^s txds - \frac{I_{zz}S_z - I_{xz}S_x}{I_{xx}I_{zz} - I_{xz}^2}\int_0^s tzds \tag{6.13}$$

$$S_x\eta_0 - S_z\zeta_0 = \oint_s pq_b ds + 2Aq_{s0} \tag{6.14}$$

Finally, the Von Mises Stress is computed using these normal and shear stress distributions. The Von Mises stress is by definition determined by Equation (6.15).

$$\sigma_{vonMises} = \sqrt{\frac{1}{2}\left[(\sigma_x - \sigma_y)^2 + (\sigma_y - \sigma_z)^2 + (\sigma_z - \sigma_x)^2\right] + 3\tau_{xy}^2 + 3\tau_{yz}^2 + 3\tau_{xz}^2} \tag{6.15}$$

However, as the span wise length of the plates is much larger than the thickness, the Von Mises definition can be reduced to:

$$\sigma_{vonMises} = \sqrt{{\sigma_y}^2 + 3\tau^2} \tag{6.16}$$

6.2.2 Results Structural Blade Sizing

The structural sizing of the blade results in an iterative process in order to find the optimum thickness variation over the total blade span. This thickness is determined by the normal, shear and Von Mises criteria of materials.
The stress variation over the blade is closely related to the internal force and moment variation over the blade. The moment M_x and the forces F_z and F_y are significantly larger than the remaining loads, as can be seen in Figure 6.6. As these have the largest influence on the stress distribution in the blade, the thickness distribution should be taken in accordance with these loads. Moreover, the blade is loaded significantly higher at the root compared to the tip. Therefore a lower skin thickness is required at the tip. As the loads are significantly larger in the first meter of the blade, a constant thickness is selected within this range, while it decreases linearly in the remainder of the blade. The variation of the maximum shear and normal stress distribution over the blade span is shown for a number of thickness combinations of the first iteration in Figure 6.7. All combinations start with a constant root thickness and linearly decreases till the tip thickness.

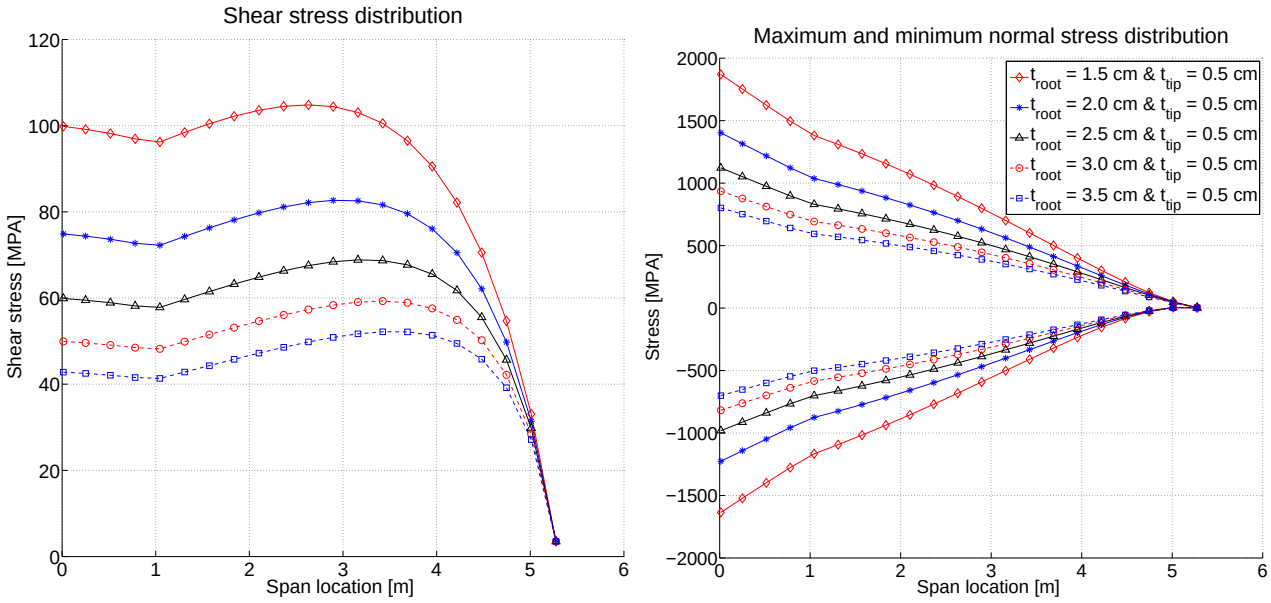

(a) Maximum shear stress distribution over blade span for varying plate thickness distributions

(b) Maximum normal stress distribution over blade span for varying plate thickness distributions

Figure 6.7: Maximum stress distribution over blade span of the blade box - iteration 1

Note that these stresses include a required safety factor of 1.5, while a load factor of 3.5 is incorporated in the applied loads. Additionally the negative normal stresses correspond to a compression strength. The Von Mises and normal stress distribution are approximately equal as the shear is significantly smaller than the normal stresses.

The first iteration of the blade sizing and material selection only considers metal alloys. A list of possible metal alloys is shown in Table 6.2. The normal stress strength in combination with the density are the critical sizing criteria for these alloys, as the shear stresses are clearly within the shear strengths limits of the possible materials. The steel alloy (17-7PH) is discarded, due to the high weight compared to the titanium alternative. While the low normal strength of the aluminium option requires an increase in thickness of approximately 200% compared to the titanium solution, resulting in a higher total blade weight. Therefore aluminium is also discarded and leaving titanium as main blade material. However a complete titanium blade results in a overdesigned outer part of the blade, as the normal stress decreases significantly over the blade span. Therefore the outer part of the blade is replaced by aluminium, as its lower normal strength complies with the local strength requirement and decreases the total weight. A list of possible design combinations and corresponding properties are shown in Table 6.3, of which option 4 is the most optimal design corresponding with the material properties.

Table 6.2: Mechanical material properties of metal alloys [83]

		Metal alloys		
Properties	**Units**	**17-7PH**	**Ti-6Al-4V**	**Al-7075**
Density	g/cm^3	7.65	4.43	2.80
Ultimate Stress (ten/comp)	MPa	1380/1210	1180/1100	570/505
Ultimate Shear Stress	MPa		550	331

In current trends within aerospace industry has shown an increase in the use of composite materials. Particularly in the development of rotorcraft blades is mainly focused on implementing composite designs [32]. Therefore the second iteration of the blade sizing involves an composite light weight alternative for the described titanium/aluminium design.

Table 6.3: List of possible design combinations for the first iteration - metal alloys considered only

Option	*Design layout*			*Maximum stresses†*				*Weight*		
	Root Thickness	**Tip Thickness [m]**	**Inner blade length [m]**	**Titanium**		**Aluminium**		**Ti [kg]**	**Al [kg]**	**Total [kg]**
				Shear [MPa]	**Normal ten/com [MPa]**	**Shear [MPa]**	**Normal ten/com [MPa]**			
1	0.035	0.005	1.39	42.8	700/800	43.8	479/568	126.4	108.0	234.3
2	0.030	0.005	2.29	49.9	818/935	58.8	448/569	166.5	56.3	222.8
3	0.0275	0.005	2.68	54.5	890/1020	68.0	431/567	172.0	39.7	211.7
4	0.025	0.005	3.00	59.9	981/1122	78.02	417/569	168.9	28.5	197.3
5	0.0225	0.005	3.32	66.6	1090/1246	89.9	395/567	162.0	19.7	181.6

† Computed stresses include a load and safety factor of respectively 3.5 and 1.5[19]

The current methodology, which assumes constant mechanical material properties over an cross section, is implemented as a first order estimation to evaluate composite design options. Although composite laminate plates are characterised by having varying properties over the plate cross section, as the plies normally have varying orientations. The first order composite estimation only involves unidirectional orientated fibers to comply with the constant material properties of the methodology. The affect of this assumption is shortly discussed after the second design iteration.

Table 6.4 shows a selection of possible carbon fiber composites and the corresponding properties.The metal alloys are with respect to these materials clearly not viable options due to their high density and relatively low strengths. Additionally, the HMCF, Kevlar, E-glass options are discarded, due their lower strengths, while having densities in the same order of magnitude. Note that the normal stress still decreases significantly over the blade span, while the shear stress increases over the blade span. This shear stress distribution becomes the critical sizing condition with respect to the composite materials, since only Boron as an ultimate shear strength complying with the applied stresses, while having a higher density. The shear stress distribution over the blade is optimized by decreasing the thickness in two linear steps. This results in an approximately constant shear stress over the initial part of the blade span, such that the shear stress is maximum at the root. The stress variations of both the normal as the shear stress distributions resulting from the second iteration are shown in Figure 6.8.

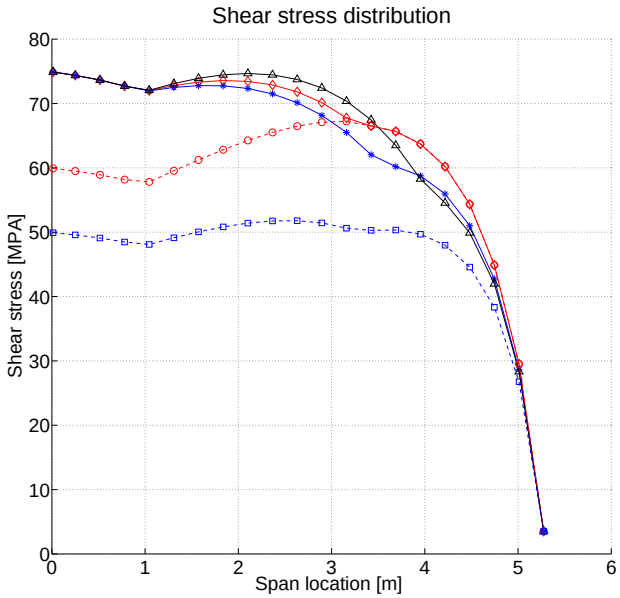

(a) Maximum shear stress distribution over blade span for varying plate thickness distributions

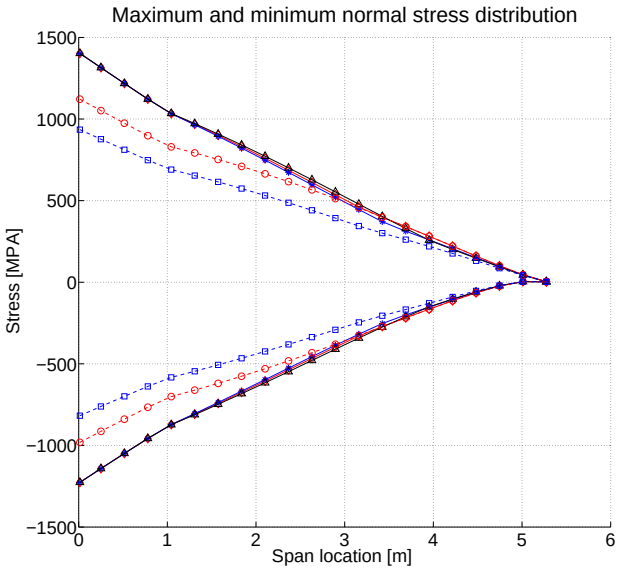

(b) Maximum Normal stress distribution over blade span for varying plate thickness distributions

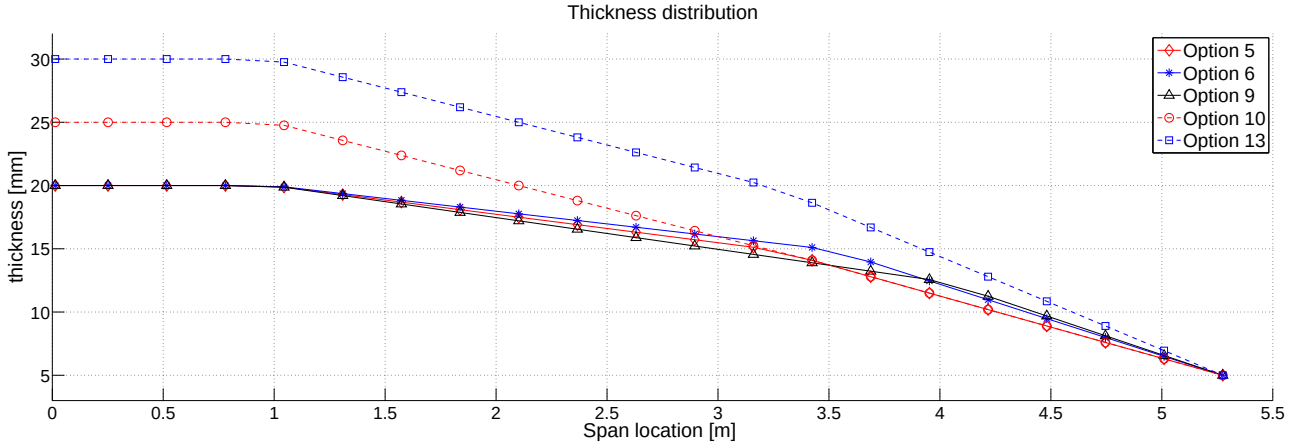

(c) Plate thickness distribution over blade span

Figure 6.8: Maximum stress distribution and thickness combination over blade span of the blade box - iteration 2

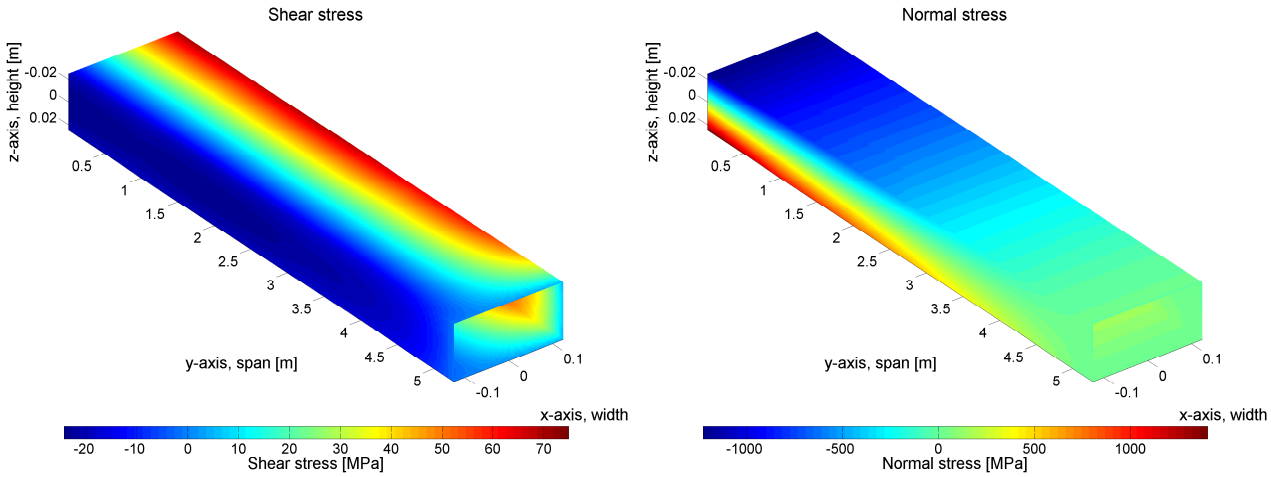

(a) Shear stress distribution over entire blade surface

(b) Normal stress distribution over entire blade surface

Figure 6.9: Stress distribution over entire blade surface of the final blade design

A list of design combinations originating from the second iteration is shown in Table 6.5. A root thickness of 20 mm results in the most optimal normal stress distribution with respect to the possible materials. The shear strengths of the remaining materials requires maximum shear stress to be lower than either 70 or 75 MPa. only options 5, 6 and 9 correspond to these criteria using M55 UD as material, while maintaining the optimal root thickness with respect to the normal stress distribution. Of these option five results in the lowest blade weight and is therefore selected. The final stress variation over the entire blade is shown in Figure 6.9.

Table 6.4: Mechanical material properties of carbon fiber composite and metal alloys and required design sizes [10][83]

		Carbon Fiber Composite Materials *Fiber/Epoxy resin (120°C Cure)*					
Properties	**Units**	**Std CF UD**	**HMCF UD**	**E glass UD**	**Kevlar UD**	**Boron UD**	**M55 UD**
Density	g/cm^3	1.6	1.6	1.9	1.4	2.0	1.65
Ultimate Stress (ten/comp)	MPa	1500/1200	1000/850	1000/600	1300/280	1400/2800	1600/1300
Ultimate Shear Stress	MPa	70	60	40	60	140	75

This blade blade design, consisting out of unidirectional composite carbon fiber material, result in an overestimation of the structural performance, as solely using unidirectional fibers is not implemented in common designs. This design is optimised for the described primarily load paths, while in reality structures are also affected by secondary load paths. Additionally having too many plies orientated in a single direction increases the likelihood of delamination. For this reason, best practices rules of designing composites suggest that laminate plates should have atleast one layer in the $0°/90°/\pm45°$ directions[14]. The current methodology should be adjusted to incorporate such composite designs. The main change relate to the varying young's modulus over the cross section[56]. Consecutively the analysis of failure of a laminate plate is less straight forward as that of a homogeneous material[51]. Failure of each individual ply should be considered by consecutively evaluating, the laminate mid plain strains and curvatures, the individual ply strains and finally the corresponding ply stresses. These individual ply stresses are checked on failure.

Table 6.5: List of possible design combinations for the second iteration - composite materials considered only

	Design				***Stresses†***		***Weight***		
Option	**Root Thickness [m]**	**Intermediate Thickness [m]**	**Location [m]**	**Tip Thickness [m]**	**Shear [MPa]**	**Normal ten/com [MPa]**	**Std CF UD**	**M55 UD**	**Boron UD**
1	0.015	-	-	0.015	99.8	1870/1635	76.1	78.5	95.2
2		-	-	0.005	104.8		55.5	57.2	69.3
3	0.020	-	-	0.020	74.9	1402/1227	101.5	104.7	126.9
4		-	-	0.005	82.7		70.5	72.7	88.1
5		0.015	3.25	0.005	74.9		76.3	78.7	95.4
6			3.50	0.005	74.9		78.2	80.9	97.8
7		0.0125	3.50	0.005	77.8		73.1	75.4	91.3
8			3.75	0.005	75.9		74.8	77.1	93.5
9			4.00	0.005	74.9		76.7	79.1	95.9
10	0.025	0.015	3.25	0.005	67.2	1122/981	86.4	89.1	108.0
11			3.75	0.005	61.8		91.25	94.1	114.1
12	0.030	-	-	0.030	49.9	935/818	152.29	157.1	190.37
13		0.020	3.25	0.005	51.8		106.86	110.2	133.57
14	0.035	-	-	0.005	42.8	800/700	177.7	183.2	222.1

† Computed stresses include a load and safety factor of respectively 3.5 and 1.5[19]

6.2.3 Recommendations

A preliminary sizing of the blade is presented in Subsection 6.2.2. The methodology considers an equivalent beam having four load carrying plates of equal thickness, which varies over the blade span. A single material was used over the entire blade span. The current sizing could be further optimized in future design phases. This optimization could consider the use of different material over the blade span, as the blade tip is currently over designed. Shear capabilities of the material should be increased for material further from the root, while the tensile and compressive strength can be decreased. This could be achieved by changing the ply direction of the current material or even considering different materials. Moreover the deflections and deformations should be further analysed. Rotor blades do deform during the flight and it should be investigated if the current design remains within certain deflection limits. Finally a more optimal cross section could be considered, as the dimensions of the current box do not correspond with the selected airfoil.

6.3 Fuselage

This section will elaborate on the structural design of the fuselage. Assumptions have been made to simplify the model in such a way that critical loads can be calculated. With these critical loads the stresses are calculated throughout the load carrying part of the fuselage. Then the process of iterating the thicknesses and material of the box followed of which only one iteration was performed due to time constraints. Since the conceptual design of the ducted fan has a time limit, only the load case of hover will be calculated in this section. Since the same tool that was made for hover can be used for other load cases, hover was the first case to be analysed because this was more efficient. Also, hover was important to analyse since the torque is higher during this load case. As a recommendation, other load cases for cruise, landing and transitional flight can be calculated in the detailed design of the ducted fan.

6.3.1 Total Equilibrium

As can be seen in Figure 6.10, the final design resembles a disc with a tail attached to it. Inside the disc a cross is placed which attaches the shaft of the blades to the fuselage. This cross has four attachment points to the fuselage. At these points the payload is also attached. In that way the force pointing downward due to the payload, counteracts the force pointing upwards due to the thrust, which is stress relieving for the structure. An amount of four attachments points is chosen because in that way the circle can be analysed in quarters and the thrust and weight is still symmetrically distributed, which is desirable because it simplifies the calculations. The choice for four attachment points was not optimised by calculations but motivated by the reasons given in this section. An amount of only one attachment point was not possible because in that case the attachment of the payload to the fuselage and the attachment of the cross to the fuselage cannot coincide. Also, the cross would be too highly loaded at only one point. This would make the structure unnecessarily large and heavy. Two attachment points would mean high stress concentrations at two points on the fuselage which is not desirable because these attachment points would have to be made heavier. Also a very large bending moment would be created halfway of these attachments points which would cause for too high normal stresses. Three attachment points does not give a symmetrical distribution which is therefore not chosen as option. Four attachments points does give a symmetrical distribution and also distributes the loads on the circle in such a way that loads are equally distributed over the entire structure.

To be able to calculate forces and moments in the structure itself, the external forces and moments will have to be determined. As can be seen there are thrust vectors defined at all rotor systems. So there is a large thrust vector at the main rotor T_m, two equal but smaller thrust vectors at the horizontal tails T_ht and a horizontal thrust vector to counteract the torque at the vertical tail T_{vt}. The torque created by the main rotor is acting at the center of the cross where the main rotor is attached to the structure. A drag force D is present when the $LIFT^2$ is in forward flight. The side force S acting at the centre of the cross is created by the blades and is also counteracted by T_{vt}. Since the payload is attached at four points to the fuselage, these force vectors are applied at an angle depending on the size of the cable underneath the ducted fan rotorcraft. The force vector P represents the payload and is split in P_z, P_y and P_z at the attachment points. Figure 6.10 shows all external forces and moments on one ducted fan when it is in hover. Since the ducted fan rotorcraft is in hover, there is no drag force present. It is shown in the figure however where it would be acting and in what direction if it would have a value.

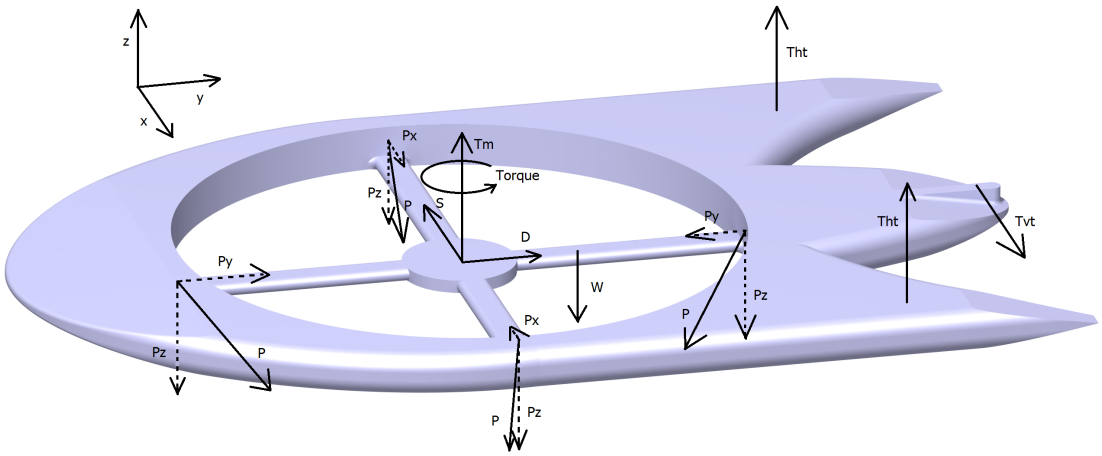

Figure 6.10: All external forces and moments of one ducted fan in hover

To calculate the forces and moments of the entire system, equilibrium has been used as shown in Equation (6.17) to (6.22).

$$\sum F_x = 0 \; P_x - P_x - S + T_{vt} = 0 \tag{6.17}$$

$$\sum F_y = 0 \; P_y - P_y + D = 0 \tag{6.18}$$

$$\sum F_z = 0 \; T_m - 4 \cdot P_z - W + T_{hr} + T_{hl} = 0 \tag{6.19}$$

$$\sum M_{x_{cg}} = 0 \; P_z \cdot (l_{cg} - l_f) + 2 \cdot P_z \cdot (l_{cg} - l_m) - P_z \cdot (l_a - l_{cg}) + (T_{hr} + T_{hl}) \cdot (l_{ht} - l_{cg}) - D \cdot h_{mr} = 0 \tag{6.20}$$

$$\sum M_{y_{cg}} = 0 \; -S \cdot h_{mr} + T_{vt} \cdot h_{vt} + P_z \cdot R - P_z \cdot R + T_{hr} \cdot \frac{1}{2} \cdot w_h = 0 \tag{6.21}$$

$$\sum M_{z_{cg}} = 0 \; -S \cdot (l_{cg} - l_m) - T_{vt} \cdot (l_{vt} - l_{cg}) + Torque = 0 \tag{6.22}$$

6.3.2 Internal Forces at Cut

Now all external forces and moments are known, the internal forces and moments can be calculated. Since the fuselage has a complex design a simplified model is used to analyse the structure. The load carrying part of the fuselage is modelled as a circular box illustrated in Figure 6.11.

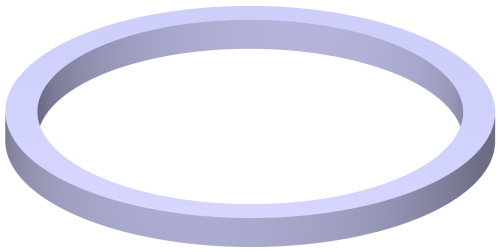

Figure 6.11: Schematic drawing of structural model of the fuselage

The loads generated by the blades are transferred by the shaft to the center of the cross which is shown as the rectangular cross section in Figure 6.12. So the side force created by the blades and counteracted by the tail acts here, as well as the thrust generated by the blades. The loads are then transferred through the beams of the cross to the point where the cross is attached to the fuselage. The circular shape is chosen because the duct is a perfect circle, so a circular box resembles the original shape of the fuselage best.

To analyse the structure, a starting point has to be chosen in the circular box. This starting point is chosen at the most aft attachment of the cross to the fuselage seen from the nose. To analyse every force and moment at this position on

both the left side and the right side of the cross section, a cut has been made at the attachment of the ring and the tail. At this location the internal forces and moments are calculated. In this way, the internal forces and moments on the right side of the fuselage box' cross section are known. This is shown in Figure 6.12.

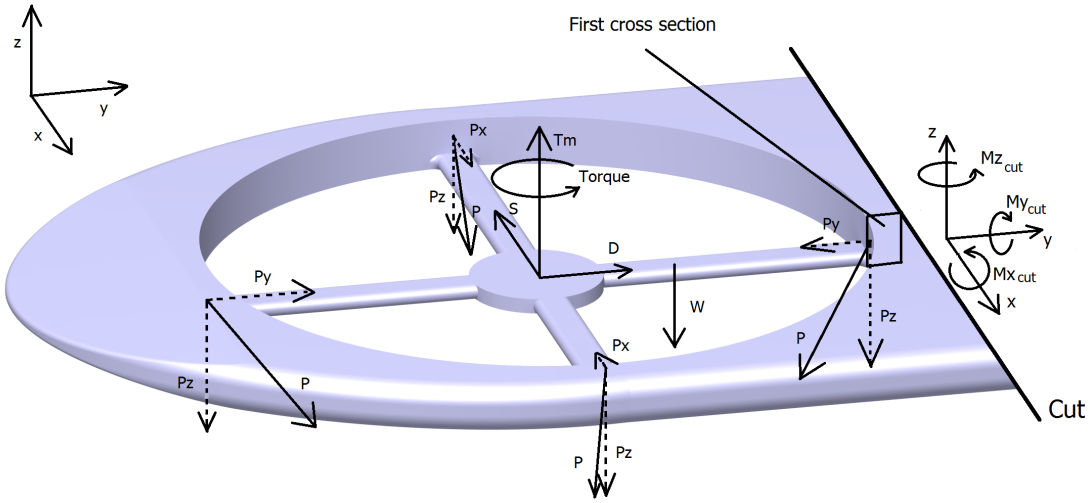

Figure 6.12: All internal forces and moments of the right side of the cross section of the circular box

To give the structural analysis of the fuselage, the fuselage is divided in four quarters. Each quarter is then analysed separately. The first quarter to be analysed is the quarter starting at the most aft point on the circle. Since the cut of the starting point of the first cross section is made exactly at the attachment of the cross and the fuselage, the loads at that point are divided by two. This is because half of the loads acting at an attachment acts to the right of the attachment, and the other half acts at the left. This means that an eighth of the total thrust by the main rotor is acting at the cross section, which has an influence when analysing a quarter of the circle. The same holds for the forces acting at the other attachment of the quarter. This can be seen in Figure 6.13. What can also be seen from Figure 6.13 is that the axis system of the cross section is rotating with the curvature of the beam. This will be important during the transformation of the forces and moments inside the beam.

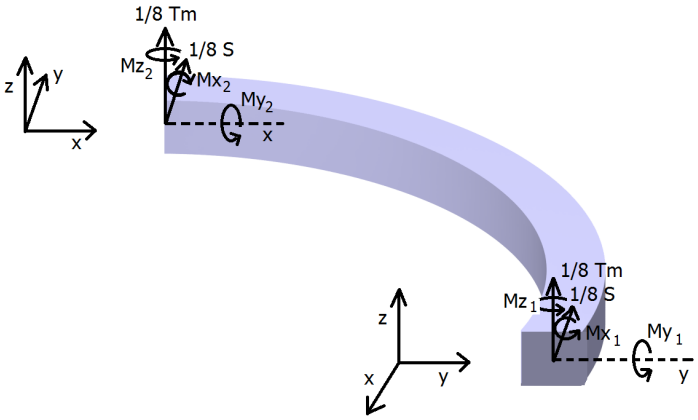

Figure 6.13: Forces and moments acting at the ends of a quarter of the fuselage circular box

The forces and moments at the cut now can be calculated. The equations are shown below in Equations (6.23), (6.24) and (6.25).

$$M_{x_{cut}} = -P_z{\cdot}(l_{cut}{-}l_f{+}y){-}2{*}P_z{\cdot}(l_{cut}{-}l_m{+}y){-}W{\cdot}(l_{cut}{-}l_{cg}{+}y){-}P_z{\cdot}(l_{cut}{-}l_a{+}y){+}T_m{\cdot}(l_{cut}{-}l_m{+}y){+}D{\cdot}(0.5{\cdot}h_d{+}h_{mr}{*}z); \quad (6.23)$$

$$M_{y_{cut}} = S \cdot (h_{mr} - z) - 2 \cdot P_z \cdot x - P_z \cdot (w_m - w_r + x) + P_z \cdot (w_m - w_r - x) - W \cdot x + T_m \cdot x; \quad (6.24)$$

$$M_{z_{cut}} = S \cdot (l_a + y) - D \cdot x + Torque; \quad (6.25)$$

In equations (6.23), (6.24) and (6.25) x, y and z represent the coordinates of the center of gravity of the fuselage box taken from the left bottom corner of the first cross section. This is done because when calculating the normal stresses the

moments are required around the center of gravity. Since the local axis system of the sections rotate at the same angle as the section itself does, the y and z coordinates will never change. The x-coordinate does change with every loop however.

6.3.3 Internal Forces at Cross Attachment to the Fuselage

At this point the forces and moments at one side of the fuselage box have been determined. To analyse the stress distribution over the entire box, the forces and moments at the other side of the fuselage box are also needed. This is done by analysing the forces and moments which are transferred from the attachment of the cross to the fuselage. The forces and moments on the cross are shown in Figure 6.14. The red forces and moments vectors indicate the internal forces and moments. For clarity, only the value of the forces and no value of the moments are shown in the figure.

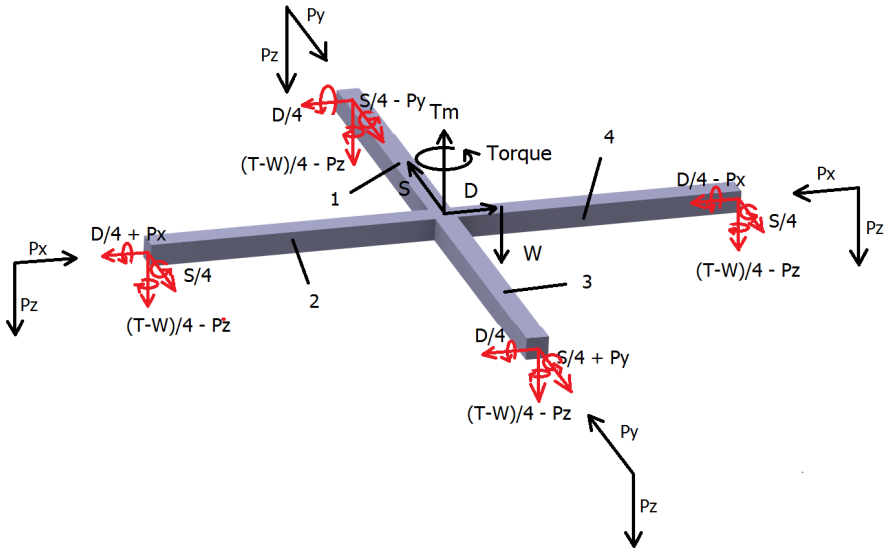

Figure 6.14: Forces and moments acting at the cross inside the main rotor

To determine the forces and moments at the attachment points, the forces and moments are shifted to the main center of the cross which is where the shaft is connected. The weight of the ducted fan which acts at the center of gravity therefore introduces a new moment. Next, every force and moment is equally distributed over the four attachment points. In this way multiple moments are created which are kept dependent on their arm which is kept variable. In this way when going through the structure, the moments keep changing which they should. Figure 6.15 shows one beam of the cross, now with the forces and moments shifted to the attachment points. As can be seen, the torque which is generated by the blades of the main rotor is modelled in Figure 6.15 as forces at the attachments of which the example of beam 2 is given in 6.15. Again the red vectors are the internal forces and moments.

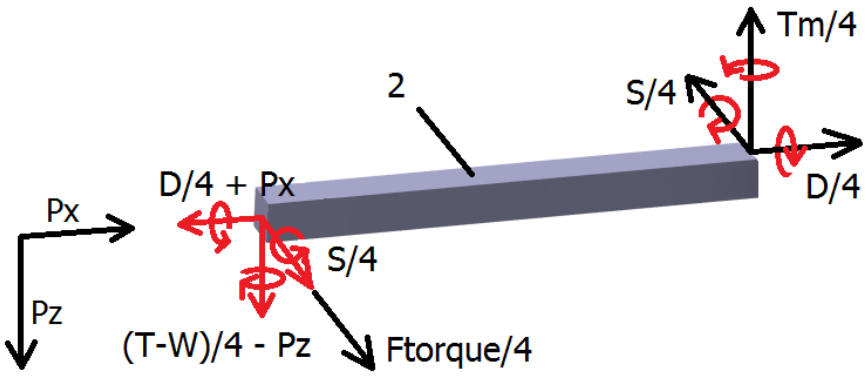

Figure 6.15: Internal and external forces and moments acting at the attachment points of the cross to the fuselage

With these as input, the forces and moments throughout the entire box can be computed. The ring is modelled as several straight beams as illustrated in Figure 6.16. With the cross section where all forces and moments are known as starting point, the forces and moments at the end of this section can be calculated by using equilibrium. The next section is rotated at an angle dependent on the number of sections used to model the quarter circle. All forces and moments at the end of the section are analysed in an axis system which is rotated at the same angle to give the forces and moments at the starting point of the next section. When many sections are used, the circle is modelled as almost an continuous

circular beam but more than 20 section is not necessary because the result already converges at 20 sections. Therefore 20 sections are used with an achievement of satisfactory accuracy and high computational efficiency.

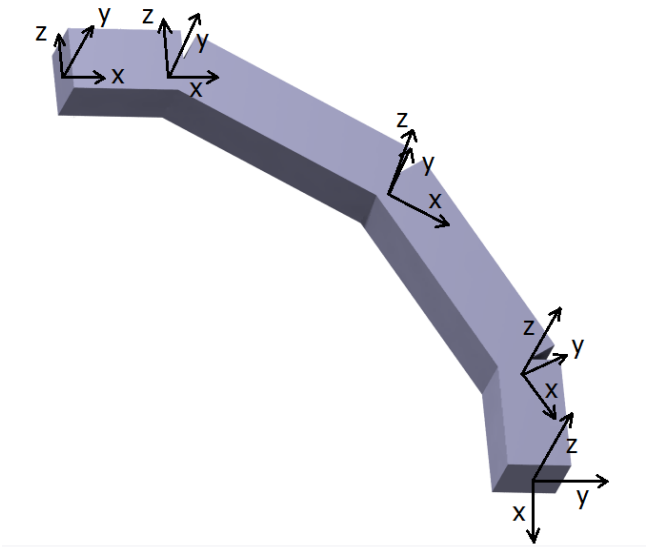

Figure 6.16: Different elements of a quarter of the circular box

When analysing different quarters of the circular box, the forces and moments are acting at different axes than they were for the first quarter. Since in this report only hover is analysed, the drag force will be zero. This makes the forces symmetrically distributed over the x-axis with the exception of the force due to the torque of the main rotor. However, in this report only two quarters of the circle will be analysed. Since the other quarters of the fuselage circle will have loads acting on it with an opposite sign, the force combinations will not give a more critical load case. When one half of the fuselage will therefore be analysed, the most critical case of that analysis will be used to determine the thickness and the material of the structure. The other half of the fuselage will then be able to resist the loads acting on it as well. In a further design stage, this assumption will have to be verified.

6.3.4 Stresses

With the forces and moments known over the entire fuselage, the corresponding stresses can be calculated. Since the fuselage is modelled as multiple straight beams, the same program can be used to calculate the stresses as was done for the beams in the rotor blades in Section 6.2. Using this program, the normal stress and shear stresses in the fuselage section is obtained. Since a combination of these stresses can be more critical, the Von Mises stresses are shown as well. The result is shown below in Figures 6.17a, 6.17a and 6.17c. In all calculations, a load factor of 3.5 and a safety factor of 1.5 have been applied which the certification stated. The input values of the forces and moments defined in Figure 6.10 are stated in Table 6.6. These values are used in the calculations for the fuselage as well as the cross and the undercarriage.

Table 6.6: Table of input values of main forces and moments

Loads	**Symbol**	**Value**	**Unit**
Thrust main rotor	T_m	$8.4 \cdot 10^4$	N
Side force	S	$5.8 \cdot 10^4$	N
Payload weight vector at one attachment point	P	$1.4 \cdot 10^4$	N
Maximum weight ducted fan without payload	W	$4.04 \cdot 10^4$	N
Torque due to main rotor	Torque	$1.01 \cdot 10^5$	Nm
Thrust vertical tail	T_{vt}	$5.8 \cdot 10^4$	N

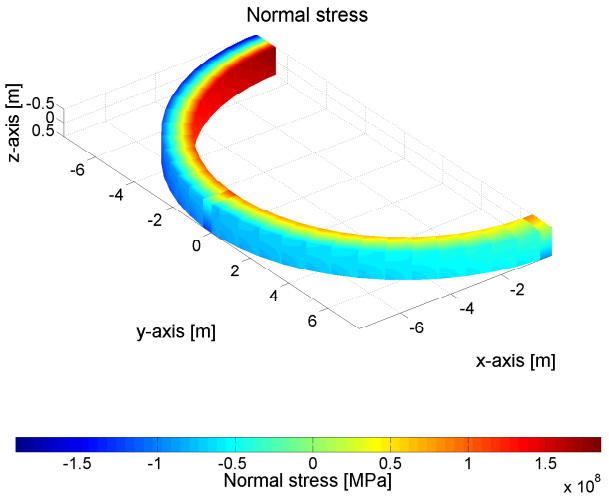

(a) Normal stresses of half of the fuselage circular box

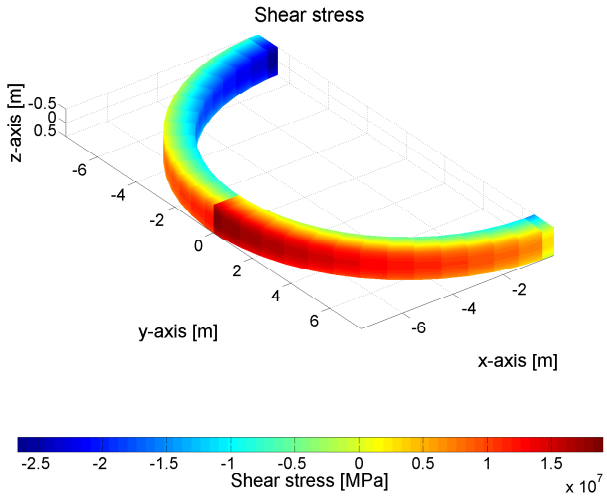

(b) Shear stresses of half of the fuselage circular box

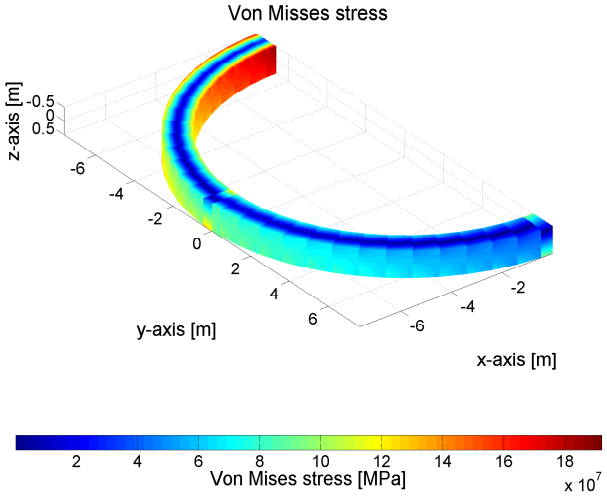

(c) Von Mises stresses of half of the fuselage circular box

Figure 6.17: Stress distributions of half of the fuselage circular box

As can be seen from Figures 6.17a, 6.17a and 6.17c, the different separate straight beams are visible. Because the forces and moments that are calculated at each beginning and end of a section are rotated over a certain angle, and the local axis system rotates with it, the forces and moments acting at the different axes will change. The absolute forces and moments will of course be the same because they are still in equilibrium but the stresses will differ a bit because forces and moments are rotated. The overall flow of the stresses are still well visible though. From the shear stress from Figure 6.17b it can be seen that the stresses are not symmetrical over the length of the sections. This can be expected since there are unsymmetrical shear forces acting on the structure. Furthermore, the maximum and minimum stresses are also rotating around the surface over the sections, which can also be expected since both a horizontal as a vertical shear force are present. However there is a discontinuity at the connection of both quarters. This stress flow should be continuous so it is expected improvements are still possible in the computation of the stresses.

From Figure 6.17a it can be seen that the normal stress distribution changes over the entire fuselage box. This was expected since there are many moments working on the structure, all of which were changing. At the connection of both quarters, the stress is lower. This can be due to the fact that there is less bending because the side force cannot contribute to a bending moment at that location. At one end of the fuselage box, the normal stress is at a maximum, on the other end however the stress is lower. It was expected that at both ends, the normal stress would be maximum because at these locations both forces introduce a bending moment. Since at one side the normal stress is lower, it is expected that there are mistakes present in the computation of the stresses.

The Von Mises stress distribution seen in Figure 6.17c is a combination of the normal and shear stresses. Its validity therefore depends on both the shear and normal stresses. Since an error is expected in the normal stress, this can also be expected in the Von Mises stress. However, the overall order of stresses is expected to give a realistic overview.

6.3.5 Verification & Validation

Since a program has been written to calculate the forces, moments and stresses in the beams, the model has to be verified and validated. This is done by comparing the method with the well-known finite elements method. The finite elements method also makes use of the fact that a structure can be divided into several smaller elements. Of each element the stresses can then be calculated after which all elements together approximate the real structure in a very accurate way. This was then analysed by using finite elements analysis, the result is shown in the Figures 6.18a, 6.18b and 6.18c.

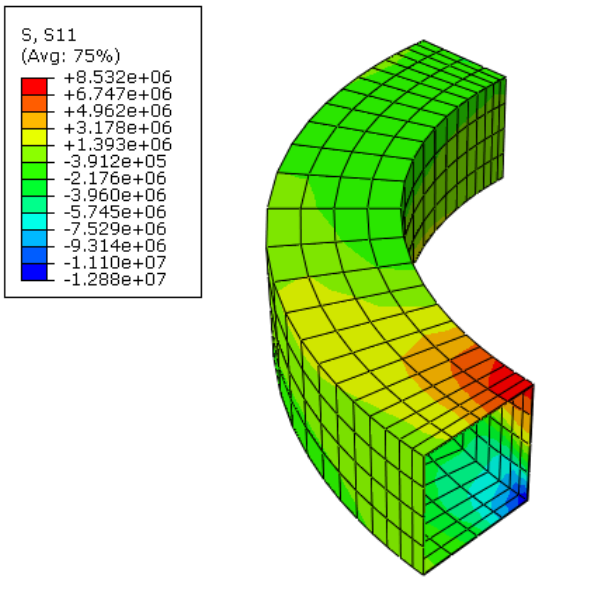

(a) Normal stresses on a quarter beam.

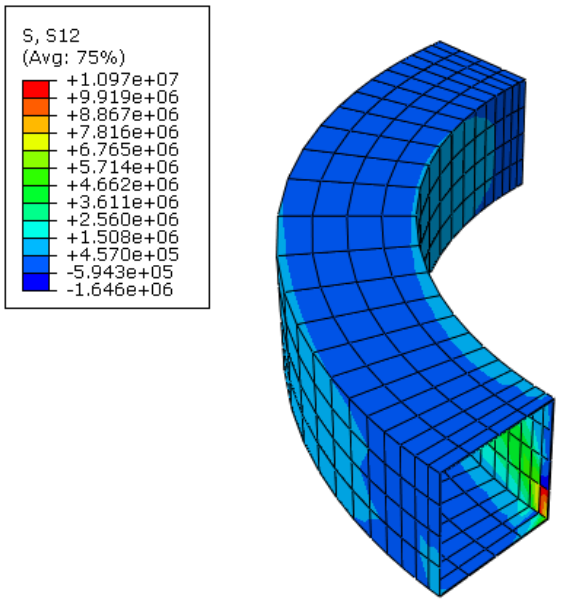

(b) Shear stresses on a quarter beam.

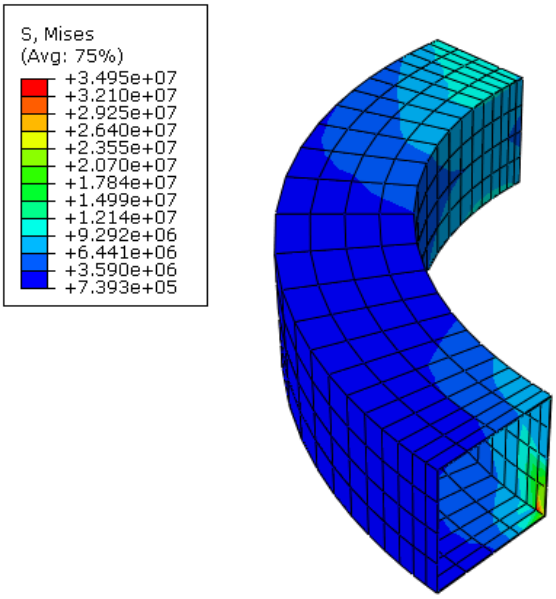

(c) Von Mises stresses on a quarter beam.

Figure 6.18: Stresses on a quarter beam.

What can be seen is that the order of magnitude of the stresses are the same as the for the stresses calculated with the method before. However there are some magnitude differences, these can be explained by the fact that a larger thickness has been used in the analysis model. The model of the method explained before uses a thickness of 5 mm, whereas the analysis model uses a thickness of 10 mm. This difference is there because the method explained before has been iterated to get a more accurate stress distribution but due to a time constraint this could not be changed in the analysis. Although the analysis model cannot be used to verify the exact values of the stresses, the overall flow of the stresses can be checked. Only one quarter has been analysed because this will serve as enough verification, so only the lower quarter from Figures 6.17a, 6.17a and 6.17c can be compared. The normal stress is similar for both methods in the sense that the outer side of the quarter has less stress and the inner part at the start has more. The shear stress is similar in the sense

that the shear stress in both cases is not symmetric over the length of the section. However, there are large differences here. Therefore the method has to be checked during the detailed design of the ducted fan rotorcraft. Because the Von Mises stress are dependent on the other stresses, and the shear stress had some dissimilarities, the Von Mises stress also differs for both methods. Since a safety factor has been used in the method, it is still valid to use for the conceptual design. However, the method needs checking during the detailed design.

6.3.6 Material Selection

The maximum stress of all three stresses of the structure is around $190MPa$. Materials often used for structural components in helicopters are aluminium, steel and titanium [21]. Table 6.7 shows the material properties of these materials. Since all three materials have a higher yield stress than $190MPa$, all three of them can be used. Steel is discarder, since it is very heavy and weight should be minimised. Titanium is discarded because of the cost. Therefore aluminium will be used in the design of the fuselage of the ducted fan.

Table 6.7: List of material properties of three materials possible for the fuselage design [83]

Material	**Density [kg/m^3]**	**[$ US/m^3]**	**Yield Strength [MPa]**
Steel Alloy A36	7850	0.9-1.5	220-250
Aluminium Alloy 7075 T6	2800	11.30-14.70	505
Titanium Alloy Ti-5 AL-2.5Sn	4480	110-120	760

6.4 Connection Rotor-Fuselage

As was explained in Section 6.3, the forces and moments of the main rotor are transferred to the fuselage by a large cross which is attached to the fuselage at four attachment points. Naturally this cross has to cope with large forces and moments. Therefore this section analyses the stresses in this structure to make sure it will not fail. Again only hover will be analysed for the same reason as given in Section 6.3.

To calculate the forces and moments on the cross, again the total equilibrium of the ducted fan can be used as was shown in Section 6.3. Figure 6.15 shows the free body diagram of this structure. Figure 6.15 is used so the cross can be divided in four different beams which can be analysed separately and shows beam 2. The initial dimensions of the beams were a thickness of 5 mm, a width of 0.5 m and a height of 0.3 m.

Since hover is again analysed the drag force is zero because there is no forward speed. As can be seen in Figure 6.15 there is one beam with more critical loads. This is because the force due to the torque of the main rotor is acting in the same direction as the side force is at beam 2 which results in a more critical load. Therefore beam 2 has a more critical load case than beam 4. Beam 1 and 3 actually have similar load cases except for the fact that the side force is working in compression at beam 1 and in tension at beam 3. The material is assumed to have the same yield strength in both tension and compression. Since beam 1 is also under pure compression, this beam is checked for column buckling as well the same way as will be done in Section 6.6. This turned out not to be critical however. Therefore only the beam under tension will be analysed. To analyse the beam they are then modelled as being clamped at both sides of which the reaction forces are once more calculated.

The forces and moments acting on the cross were already defined when the structure of the fuselage was analysed. Again the same method is used to calculate the stresses in the structure as was used in Section 6.2. With this method, the shear stresses, normal stresses and the Von Mises stresses are calculated. The plots are shown below. Figure 6.19a shows the normal stress of beam 2. Figure 6.19b shows the normal stress of beam 3, which has a tensional force acting on it. Figure 6.19d shows the Von Mises stress of the beam which turned out to be most critical. What can be seen from Figure 6.19b is that the normal stress is not zero (although it is very small) at the beginning. This is because the tensional force gives a constant normal stress. However, the normal stress of beam 2 is much higher and is therefore critical.

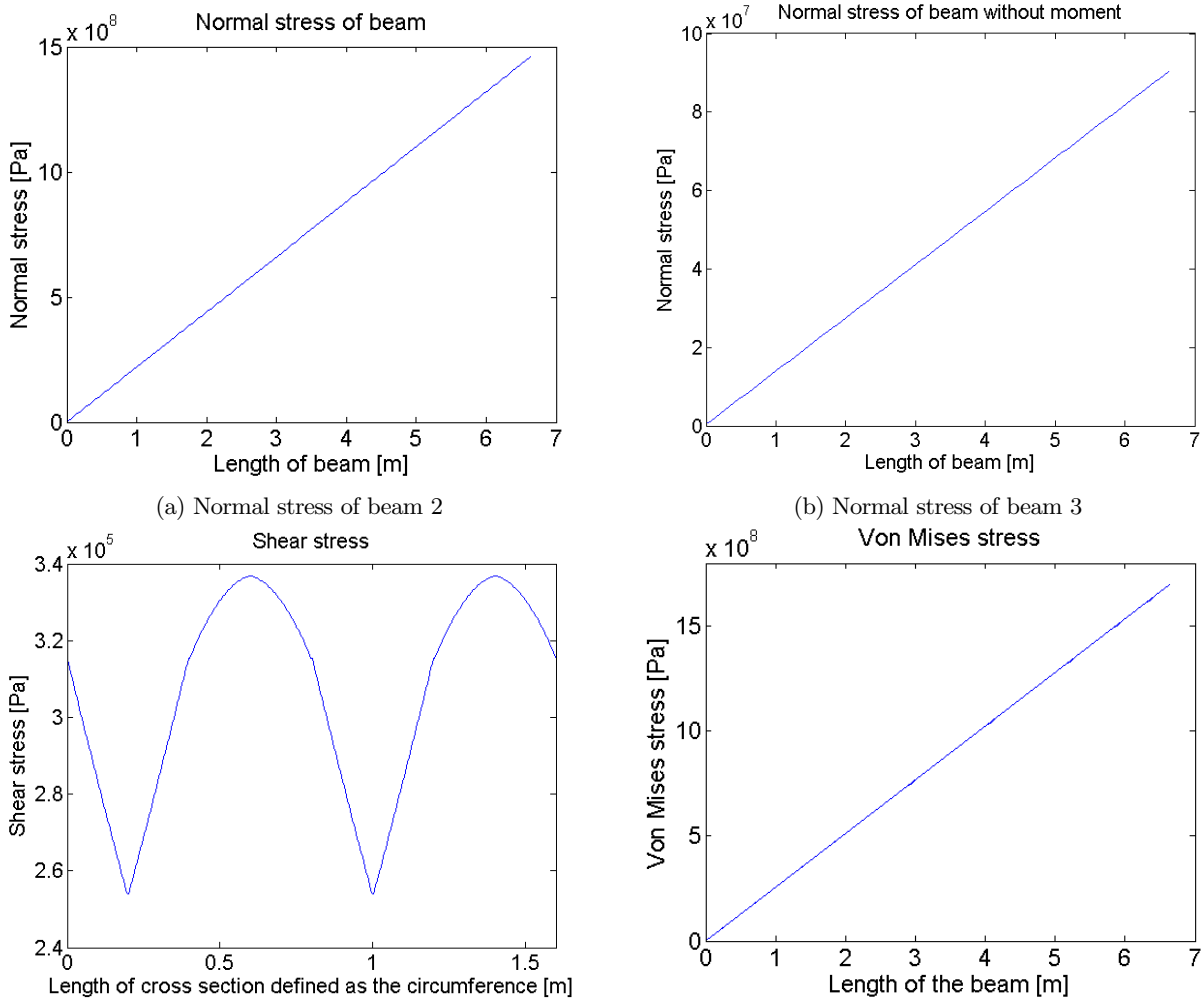

(a) Normal stress of beam 2

(b) Normal stress of beam 3

(c) Shear stress of beam 2

(d) Von Mises stress of beam 2

Figure 6.19: **Shear, normal and Von Mises stresses of beams of the connection rotorcraft to fuselage**

The shear stress is given around the entire circumference of the cross section of the beam. This means it starts at the bottom of the cross section, then proceeds on the right side after which the top is shown to end with the left side of the beam. In this way the entire circumference is given starting at the bottom and proceeding in a counter clockwise direction. The shear force on the top and bottom appear linear, which is caused by the vertical force. Since the vertical force is a factor 10 larger than the horizontal force, the contribution of the horizontal force is less apparent. However it should be noted that the stress distribution is not linear due to the horizontal shear force although its contribution is very small. The same reasoning holds for the sides, which has a primary contribution of the vertical force which causes the quadratic stress distribution. The horizontal force also has a linear contribution on the stress distribution on the sides. Compared to the normal stress distribution, the shear stress is not at all critical.

The normal stress of both beams is increasing linearly throughout the length of the section. This is because the moment increases linearly as well. Since the vertical force and horizontal force both create a bending moment in the structure, only the most critical stress distribution is shown. The normal stress in beam 4 however is much higher because the bending moment is larger. This is because the side force and the force due to the torque act in the same direction.

Since beam 4 turned out to be most critical, the material and thickness will be based on those stresses. The maximum Von Mises stress of beam 4 is around 1570 MPa. This is far too high for most materials. After an iterative process the thickness is therefore increased to 1.4 cm which causes the Von Mises stress to drop to $480MPa$. This makes aluminium a good material to use as can be seen in Section 6.3.

6.5 Attachment Point Sizing

The payload attachment points introduce the load of the payload weight into the rotorcraft structure. Their sizing and location is an important aspect of the structural design. Subsection 6.5.1 introduces the location and basics of the attachment points followed by Subsection 6.5.2 in which the bolts of the attachment points are sized. Recommendations for the design of a hook supporting the underslung payload is given in Subsection 6.5.3. The main focus of this section is

the sizing of the bolts used to link the attachment point to the fuselage.

6.5.1 Location & Fixture

The location of the hard points for the payload are shown in Figure 6.20 as red dots. These locations were chosen as they simplify the introduction of forces into the fuselage being on four symmetrical points. The attachment points will be fixed where the rotor support beams meet the outer fuselage ring.

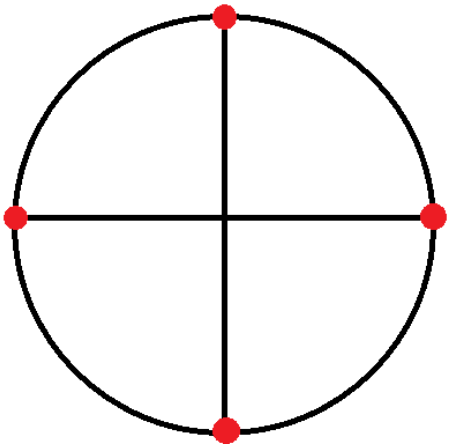

Figure 6.20: The location of the payload attachment points on the simplified structure (indicated by the red dots)

The payload will be attached to a sort of bearing similar to the one shown in Figure 6.21. A hook would be attached to the bearing to support the underslung payload. The bearing is bolted to the fuselage structure, these bolts are sized in Subsection 6.5.2. The design of the bearing plate is considered out of the scope of this design stage and hence, tear-out, a failure mode in which the holes of the plate plastically deform such that the bolts fall through, is not considered.

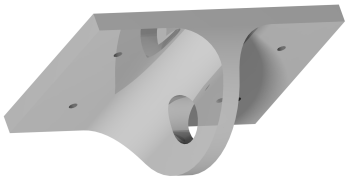

Figure 6.21: Concept drawing of the attachment bearing

6.5.2 Bolt Sizing

The payload weight is supported vertically up to a certain point at which the cable is divided into four parts each going to an attachment point. This introduces a reaction force in each point as shown in Figure 6.22, where $F_{payload}$ is the part of the weight applied at that point, b is the distance from the rotor centre to the attachment and h is the height between the plane of the attachment points and the point at which the cable is divided into four. $F_{payload}$ is half the weight of the payload plus half the weight of the spreader bar and cables, divided across the four attachment points. On top of this there is the drag caused by the container, assumed to be acting in the x-axis and carried by all four attachment points. This drag was determined in Chapter 5.

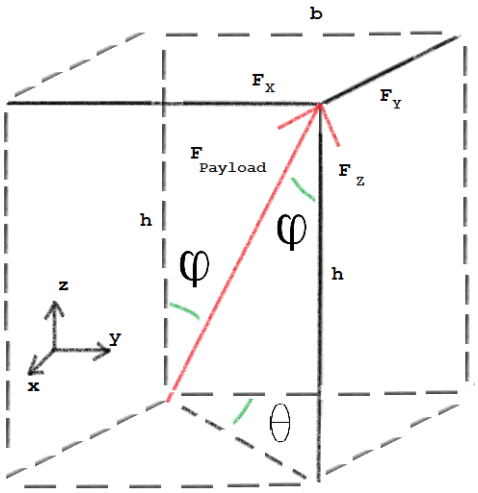

Figure 6.22: Breakdown of the reaction force at the attachment into axial components

Note that during steady horizontal flight there is only an x- and z-component acting on the bolt. However, they are sized for the worst case, which would occur in a turn. During this manoeuvre both an x- and y-component act in shear on the bolt. It is assumed that θ equals $\frac{\pi}{4}$, such that the x- and y-component are equal. Resulting in the equations for the axial components of $F_{Payload}$:

$$\phi = arctan(\frac{b}{hcos(\theta)}) \tag{6.26}$$

$$F_z = \frac{W_{Payload} + W_{Spreader} + W_{Cables}}{2} \cdot \frac{1}{4} \tag{6.27}$$

$$F_x = \frac{F_z sin(\phi)}{cos(\phi)} \cdot cos(\theta) + \frac{D_{Payload}}{4} \tag{6.28}$$

$$F_y = \frac{F_z sin(\phi)}{cos(\phi)} \cdot sin(\theta) \tag{6.29}$$

The x and y components of the force will enforce a shear stress on the bolts while the z-component will act as tension upon the bolt. The way these forces act on the bolts is shown in Figure 6.23. A load factor of 3.5 is applied on these forces to account for in-flight manoeuvres. This is done in accordance to the CS29.337 regulation [19].

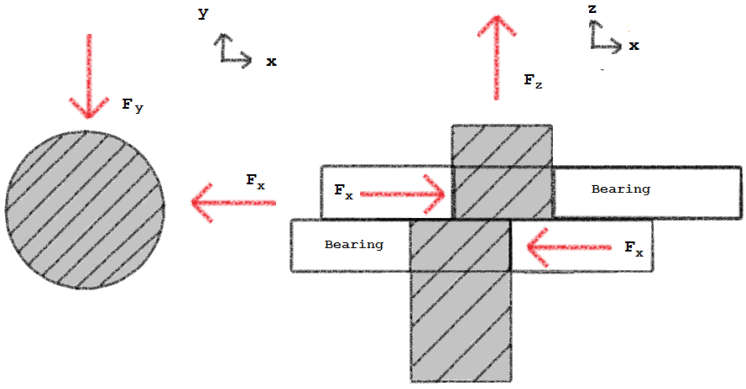

Figure 6.23: The component forces acting on a single bolt.

The stresses caused by these forces are given by the following equations:

$$\sigma_x = \frac{F_x}{\pi r_b^2 \cdot \#_{bolts}} \tag{6.30}$$

$$\sigma_y = \frac{F_y}{\pi r_b^2 \cdot \#_{bolts}} \tag{6.31}$$

$$\sigma_z = \frac{F_z}{\pi r_b^2 \cdot \#_{bolts}} \tag{6.32}$$

Where the x- and y-stresses from Equation (6.30) and (6.31), respectively act as shear stresses and the z-stress given by Equation (6.32) is a normal stress in the bolt. As can be seen from these equations the number of bolts ($\#_{bolts}$) reduces the overall stress in each bolt. A safety factor of 1.5 is used in accordance with the CS 29.303 requirements. The yielding state of the bolt is defined using the Von Mises yield criterion:

$$\sigma_v = \sqrt{\frac{1}{2}((\sigma_{11}-\sigma_{22})^2 + (\sigma_{22}-\sigma_{33})^2(\sigma_{33}-\sigma_{11})^2 + 6(\sigma_{12}^2+\sigma_{23}^2+\sigma_{31}^2))} \tag{6.33}$$

The principal stresses in Equation (6.33) in this case are:

$$\sigma_{11} = \sigma_x \tag{6.34}$$

$$\sigma_{22} = \sigma_y \tag{6.35}$$

$$\sigma_{33} = \sigma_z \tag{6.36}$$

$$\sigma_{12} = \frac{\sigma_I - \sigma_{II}}{2} = \frac{\sigma_x - \sigma y}{2} \tag{6.37}$$

$$\sigma_{23} = \frac{\sigma_{II} - \sigma_{III}}{2} = \frac{\sigma_y - \sigma z}{2} \tag{6.38}$$

$$\sigma_{31} = \frac{\sigma_{III} - \sigma_I}{2} = \frac{\sigma_z - \sigma x}{2} \tag{6.39}$$

This stress, along with the normal and shear stress, is plotted against the radius of the bolts. Horizontal lines representing the yield stress of different materials is plotted amongst them. The intersection of the stresses giving the largest radius is the critical condition for which the bolt will be sized. Table 6.8 gives the input used in the calculation of stresses. The stress curves are plotted in Figure 6.24.

Table 6.8: Input values of the stress calculations

Parameter	**Value**
b	6.75 m
h	12 m
ϕ	$\arctan(\frac{6.75}{12}) = 0.512$ rad
θ	$\frac{\pi}{4}$ rad
$\#_{bolts}$	3
r_b	0.001-0.01 m
$W_{Payload}$	98100 N
$W_{Spreader}$	4139.82 N
W_{Cables}	0 N
$D_{Payload}$	12949 N

The results given by this input are shown in Figure 6.24 along with the yield stresses of the selected materials. From this it can be seen that the shear stress in x-direction is the critical condition. For three bolts the required radius will be larger than 5.9 mm, if the bolts were shaped out of ASTM A36 steel. Which is a common used steel alloy. If Ti6Al4V were to be used, the radius would drop down to 3.3 mm. However, the ASTM A36 steel is a more favourable choice with respect to production costs.

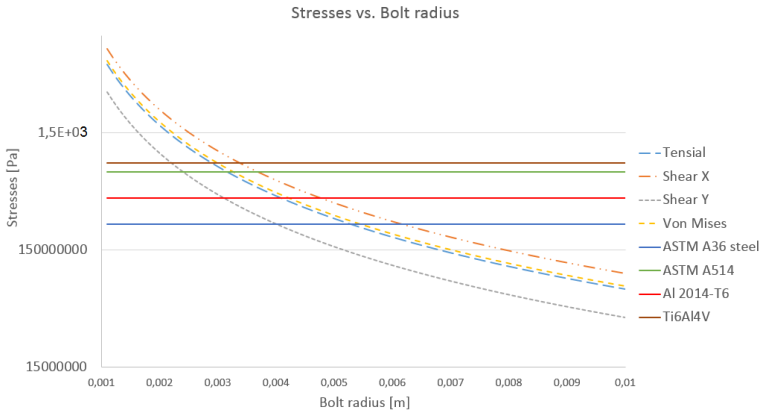

Figure 6.24: The stresses in the bolts compared to the radius of the bolts for three bolts.

With these results, a set of three bolts with a radius of 5.9 are selected. The bolts are made out of ASTM A36 steel and are sized such that one bolt can fail without the attachment failing (e.g. if there are four bolts and one fails, the other three can carry the full load without failure). The result is summed up in Table 6.9. An upper limit on the bolts is provided by the maximum spacing of the bolts in the bearing plate, however this is outside of the conceptual design scope. Therefore the number of bolts is chose to be four.

Table 6.9: Resulting bolt requirements

Parameter	Value
$\#_{bolts}$	4
r_b	0.0059 m
Material	ASTM A36 steel
Yield stress	250 MPA

It might be considered to select a standard ISO metric bolt to ease the production process and slightly reduce the production costs. An example of this is an M4x250 bolt, having a nominal outer diameter of four millimetre and a length of 250 mm. A bolt which would be able to support the loads would be an M6xXXX bolt made out of ASTM A36 steel, where the XXX denominates the length of the bolt which will be equivalent to the bearing thickness. The design of this thickness however is not in the scope of this design stage.

6.5.3 Loading Hook

To connect the payload slings to the rotorcraft, some sort of hook must be provided. A concept drawing of this is shown in Figure 6.25, in this figure three different parts are indicated by the numbers one to three. The payload slings are kept by part one and two forming the hook. Part one is rigidly connected to part three and can not rotate or move. The second part can rotate such that the hook can be opened and is kept closed by a strong spring. This spring system prevents the slings from slipping out of the hook. Part three is held in place by the bearing given by Figure 6.21, providing the connection with the rotorcraft. This concept is chosen because it still offers a rotational degree of freedom to the slings compared to a rigid hook. If, for example, a rigid hook was used, the movement of the payload would be more easily transferred to the rotorcraft. It is to be noted that a commercially available hook can be used such as the one applied on the CH-47 'Chinook'.

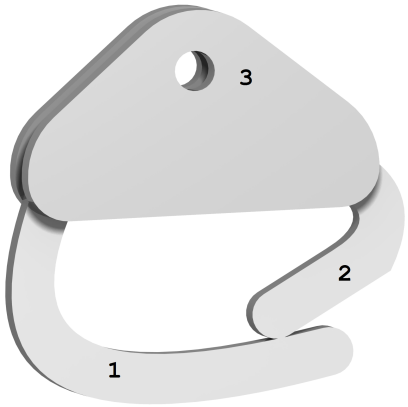

Figure 6.25: Concept drawing of the loading hook.

6.6 Undercarriage

A structural analysis has been given on the blades, hub, fuselage and the cross of the ducted fan presented in this report. Finally, it is important to design an undercarriage that can withstand the loads that are acting on it during landing, take off or when the ducted fan is on the ground when not in a mission.

6.6.1 Types of Undercarriages

There are two kinds of undercarriages that can be used on helicopters and ducted fans. One type is skids and the other one is wheels. An advantage of skids is that they weigh less than wheels. These are therefore often used on smaller helicopters because it is important to save weight. On larger helicopters however, utility and convenience on the ground is more important than saving weight, so wheels are used often. Wheels are naturally more convenient because the helicopter with wheels can taxi. When skids are used, ground wheels have to be attached to the skids in order to move the helicopters. On

the other hand, using skids allow you to lift more payload because weight is saved on the undercarriage and less maintenance is needed compared to wheels. However since the ducted fan design in this report has a MTOW of around 10 tonnes, wheels are necessary to move it around on the ground. Therefore the ducted fan in this report will use wheels as undercarriage. [12]

When using wheels as undercarriage, the design decision of retractable or fixed wheels can be made. An advantage of using retractable wheels is a larger aerodynamic efficiency due to less disturbance of the flow around the body. Retractable wheels also add complexity though, which can therefore be a reason to choose fixed wheels. Since the mission $LIFT^2$ has to perform contains a cruise segment of 400 km, it will be much more fuel efficient to use retractable wheels. This is an important factor in the decision because the fuel is an important contribution to the total weight of the ducted fan. The ducted fan will therefore use retractable wheels.

Next, the amount of landing gears has to be determined. Since the payload and the cross are already attached at four point in the fuselage there is no space left at these point to attach also a landing gear. The ducted fan will therefore have three landing gears. This is done because the center of gravity of the ducted fan is placed more aft than the main rotor. Therefore two landing gears will be placed behind the main rotor and one at the nose so the ducted fan will not tip over.

Another aspect important in the design of the undercarriage of the ducted fan is the height of the undercarriage. Unlike a helicopter, the ducted fan has its blades lower to the ground than a normal helicopter since there is no fuselage underneath it. A problem occurring because of this, is that the ducted fan has more ground effect during landing and take off. Therefore the undercarriage can have a larger height so the ducted fan is positioned higher above the ground when landing or taking off. Since detailed research of the ground effect is not within the scope of the conceptual design, the height of the landing gear is based on reference ducted fans. The Project Zero [82] has a landing gear which is approximately half a meter high. This means that it is possible for a landing gear to take off when close to the ground. Since the ducted fan presented in this report is larger, it was chosen to take a landing gear of 1.0 m to make sure ground effect is not a large problem.

Now the height of the landing gear is known, the landing gear can be tested for column buckling. Since there is a pure vertical force on the landing gear when the ducted fan is landing or before take off, column buckling is a critical load case. The landing gear is assumed to be clamped to the rest of the structure of the ducted fan, because the end of the landing gear which is attached to the fuselage is not able to pivot or move away from the fuselage. When the landing gear is on the ground however, the landing gear is assumed to be pinned because the landing gear is able to pivot around the wheel. The equation for column buckling is given below [13].

$$P_{crit} = \frac{\pi^2 \cdot EI}{L^2} \tag{6.40}$$

In this equation, the landing gear was assumed pinned. The landing gear of the ducted fan rotorcraft however, will buckle in a different mode than in Equation (6.40). This is because in Equation (6.40) the beam, which is calculated for buckling, is assumed to be able to pivot around both ends. Since this is not the case for the landing gear of the ducted fan rotorcraft, the effective length of the beam has to be changed. The effective length of the column is defined as the distance between points where the moment is zero [13]. The effective length of the landing gear of the ducted fan is $0.7L$. The buckling equation becomes:

$$P_{crit} = \frac{\pi^2 \cdot EI}{(0.7L)^2} \tag{6.41}$$

Since the ducted fan may not be landing on all three landing gears at once. The critical load will be the entire weight of the ducted fan with a load factor because the landing gear should also resist shocks during landing. Because these shocks can be rather large, a load factor of 3.5 has been chosen. The safety factor of 1.5 is already taken into account in the forces. Also since column buckling is not the only failure mode of a beam under compression another factor has to be taken into account. The other failure mode is plate buckling but this is detailed research and therefore is again not part of the conceptual design phase. Instead, a safety factor of 10 has been used to make sure the landing gear will not fail. This results in a critical load of $P_{crit} = 40348.53 \cdot 3.5 \cdot 10 = 1.41 \cdot 10^6 N$. The length of the landing gear was already chosen to be 1.0 m. The moment of inertia is then calculated by defining the dimensions of the landing gear. As initial dimensions, the landing gear is assumed as a solid cylinder with radius of $R = 0.15$ m. This results in a moment of inertia of $I = \frac{1}{4}\pi R^4 = 3.47 \cdot 10^{-}4$ m^4. The Youngs modulus required to resist the critical load is 0.36 GPa. Determining these dimensions are an iterative process because both the moment of inertia and the Young's Modulus can change. Therefore, different Young's moduli of materials that can be used are listed in Table 6.12.

When the ducted fan is landing vertically, there will only be a vertical force acting on the landing gear, which was why buckling was the critical load case. When the ducted fan is not landing entirely vertically, one landing gear will have to withstand the entire weight, but also a large bending moment will be introduced, which will cause normal stress. This also has to be taken into account. The bending moment will be defined as:

$$M = (MTOW - PLW) \cdot arm \tag{6.42}$$

The arm used in equation (6.42) is the distance between the center of gravity of the entire ducted fan and the landing gear. This distance will be the same for the two aft landing gears, but will be different for the front landing gear. Therefore both will be calculated. The moments are listed in Table 6.10.

Table 6.10: Arms and bending moments around the landing gear

Landing gear	Arm [m]	Bending moment [Nm]
Front	9.99	$1.21 \cdot 10^6$
Aft	7.22	$8.74 \cdot 10^5$

With these bending moments, the normal stresses were calculated when an initial radius of 0.14 has been assumed. These are listed in Table 6.11.

Table 6.11: Normal stresses of landing gear during landing on seperate landing gear

Landing gear	Normal stress [MPa]
Front	656
Aft	473

Materials most used in structural components are listed below in Table 6.12 with their Youngs moduli and yield stresses.

Table 6.12: List of material properties of three materials possible for the undercarriage design [83]

Material	Youngs Modulus [GPa]	Density [kg/m^3]	Cost [$US/$m^3$]	Yield Strength [MPa]
Steel Alloy A36	207	7850	0.9-1.5	220-250
Aluminium Alloy 7075 T6	71	2800	11.30-14.70	505
Titanium Alloy Ti-5 AL-2.5Sn	110	4480	110-120	760

It appears that every Young's modulus of all three materials is high enough for the initial dimension. Therefore steel shall not be used because it is by far the heaviest. Since the titanium alloy is that much more expensive than the aluminium alloy and the aluminium alloy already is capable of handling the loads, aluminium alloy will be used on the landing gear. Now aluminium has been chosen as material, the dimensions can be iterated to the optimised values. The total normal stress is then the sum of the normal bending stress and the normal stress caused by compression. The final radius of the landing gear will therefore be 0.1546 m.

The landing gear will look like something such as Figure 6.26 is showing except for the fact that the column supporting the wheel will be higher. Three of these landing gears are used as was explained before. The locations of these landing gears (the green circles) are shown in Figure 6.27.

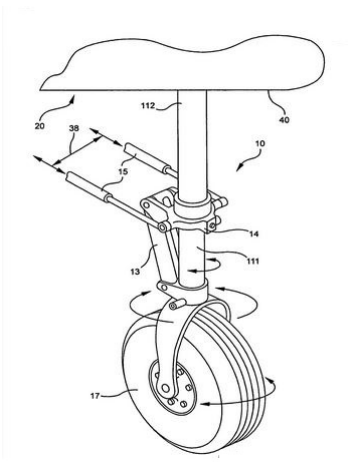

Figure 6.26: Technical drawing of the landing gear [36]

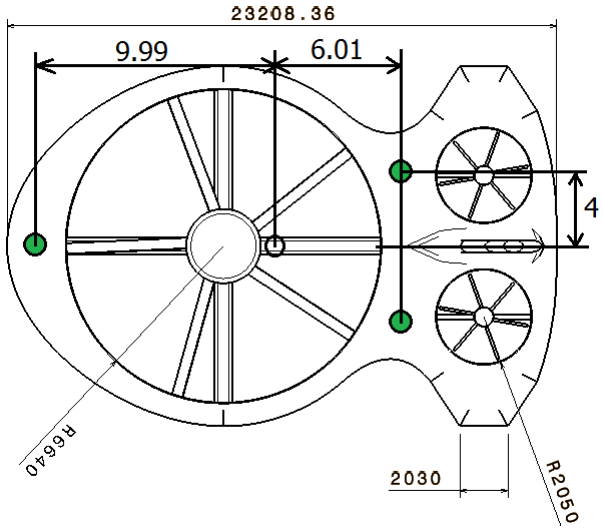

Figure 6.27: Technical drawing of the locations of the landing gear

7. Stability and Control

After establishing the aerodynamics, structural design and the initial sizing the system needs to be stable and controllable. These vital subjects are highlighted in this chapter. As explained in Chapter 4 the design requires three fenestrons in the tail to enable control about all three axes. By simultaneously increasing or decreasing their thrust, the horizontal fenestrons are used to induce a pitching moment. A rolling motion can be initiated when their thrust is varied separately. Finally, the yawing motion can be induced by changing the thrust of the vertical fenestron. Section 7.1 further investigates the stability and control of a single rotorcraft while Section 7.2 deals with the stability of the complete LIFT^2 system.

7.1 Single Rotorcraft

In order to design a stable system, first the stability of the separate rotorcraft should be ensured. The control mechanisms of the rotorcraft are discussed in Section 7.1.1. In Section 7.1.2 the static stability is discussed. Static stability does not ensure dynamic stability of the system. A linear model of the rotorcraft was made to investigate the longitudinal dynamic stability of the rotorcraft, as presented in Section 7.1.3. As it was found that the ducted fan design is not inherently stable, a control loop is designed to ensure dynamic stability. This is discussed in Subsection 7.1.4. Finally, a simulation model of the longitudinal movement of a single rotorcraft is presented in Section 7.1.5.

7.1.1 Control Mechanism

Conventional helicopters use a swash plate to provide both cyclic and collective pitch of the rotor. This principle is illustrated in Figure 7.1. By raising the collective control, the swash plate slides up and all rotorblades pitch with a constant amount. By controlling the cyclic control the swashplate tilts, resulting in a change in the angle of attack per blade.

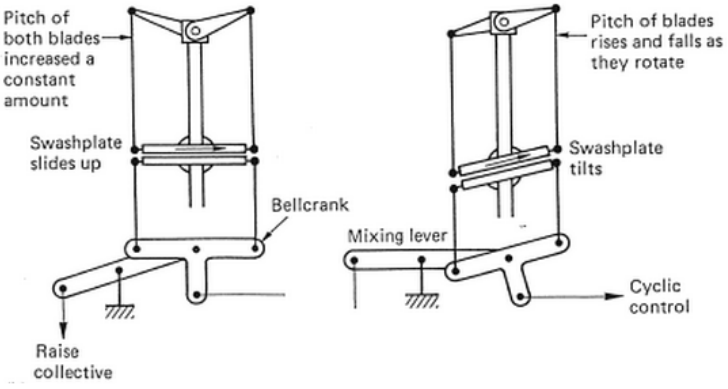

Figure 7.1: Swashplate conventional rotorcraft

The current design is unable to use a tilting swash plate for cyclic pitch. A tilting swash plate would change the clearance between the tip of the rotor and the duct. This would lead to aerodynamic inefficiencies or contact between the blade and the duct. Therefore, the two horizontal tail rotors were designed, to provide pitch and roll control. However, to be able to change the thrust coefficient of the rotors, collective pitch is still required.

The type of swash plate used in the design of the ducted fan rotorcraft can be much simpler compared with a conventional helicopter, since no tilting of the swash plate is necessary. This system is displayed in Figure 7.2. Raising the collective also raises the swashplate, which in turn increases the angle of attack of all blades. The larger angle of attack leads to more produced lift and thrust. The same type of control is used in every rotor. The control input used in the next sections are the thrust coefficients of all rotors. The underlying principle in changing these coefficients is the collective control of all rotors as displayed in Figure 7.2.

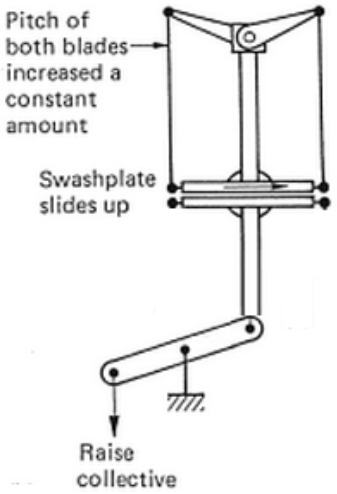

Figure 7.2: Collective pitch control ducted fan

Controlling the rotorcraft

The rotorcraft should be controllable around all three axis. Pitch, roll and yaw control should be achieved by alternating the collective pitch of the three rotors as explained in the previous section.

To longitudinally trim the rotorcraft, the moments generated around the centre of gravity by the main rotor and horizontal tails should cancel out. To pitch the rotorcraft nose up, the main rotor collective is raised, which increases the thrust and rotates the rotorcraft around the centre of gravity. The collective of the horizontal tail rotors is lowered, to keep the same total lift produced and ensure that the rotorcraft will not climb or descent.

The roll control of the rotorcraft is ensured by the horizontal tail rotors. Increasing the collective on one of them and lowering it on the other leads to a rolling moment around the centre of gravity. Since the thrust on one tail rotor is lowered, the total lift remains equal and the rotorcraft will not gain or lose altitude.

The vertical tail rotor counters the torque produced by the main rotor. Increasing or decreasing the collective pitch and tail rotor thrust creates a yawing moment around the centre of gravity.
R

7.1.2 Static Stability

Static stabillity is required for the rotorcraft to keep the same attitude during flight. This means that the rotorcraft returns to its original angle of attack after a perturbation.

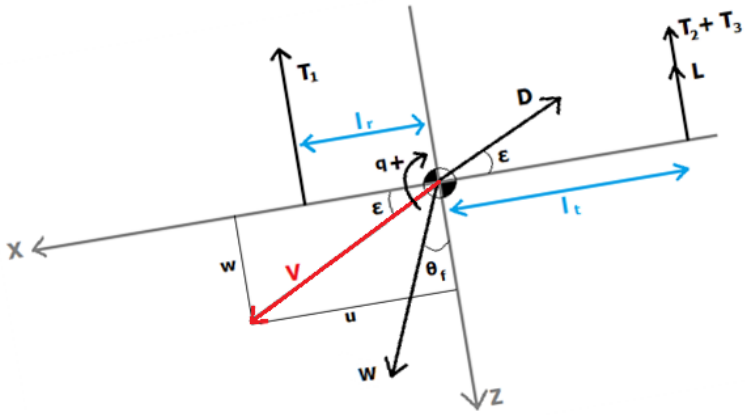

Figure 7.3: Free Body Diagram of ducted fan concept

The Free Body Diagram in Figure 7.3 shows the forces acting on the rotorcraft. For static stability the moment about the center of gravity of the rotorcraft should be zero to be in equilibrium. ($\Sigma M = 0$). A change in angle of attack α ($\alpha = -\varepsilon$) should then generate a moment to return the rotorcraft to its original position ($\frac{\partial M}{\partial \alpha} < 0$). Neglecting the

moment generated by the fuselage itself, the moment about the center of gravity is equal to:

$$+\circlearrowleft \Sigma M = T_1 \cdot l_r - (T_2 + T_3 + L) \cdot l_t = 0 \tag{7.1}$$

To account for the changes with angle of attack, the lift of the horizontal stabilisers is expressed as a function of the angle of attack.

$$(C_L + C_{L_\alpha}\alpha)\,\frac{1}{2}\rho V^2 S_h \tag{7.2}$$

In order to remain flying at constant angle of attack, it is necessary to trim the rotorcraft at that angle for a certain airspeed. In Figure 7.4 the moment M is plotted against the angle of attack for different velocities and a trim angle α of -9.74° (see Section 5.4.4). This means that when flying exactly at an angle of -9.74° the rotorcraft is statically stable. Because the slope of the curves are negative, $\frac{\partial M}{\partial \alpha}$ is negative, perturbations of the rotorcraft will be counteracted by a moment and the rotorcraft will return to its trim angle.

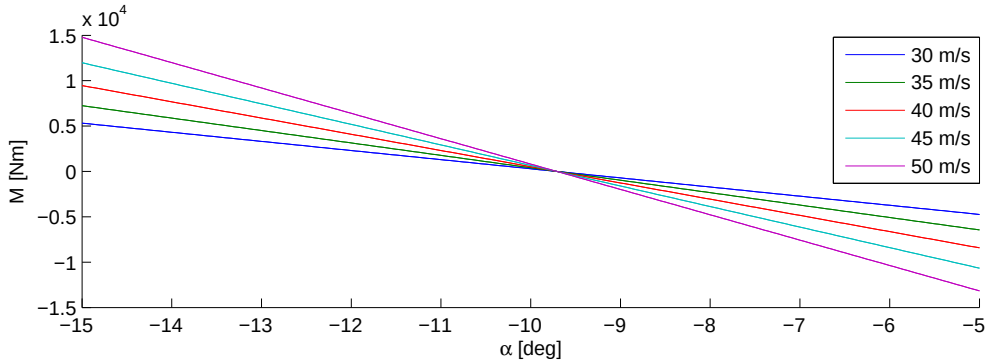

Figure 7.4: Moment vs angle of attack (trim angle = −9.74°)

7.1.3 Longitudinal Dynamic Stability

In this section the linearised set of equation of motions for a single rotorcraft is discussed. Since the model for a conventional helicopter is not valid for the proposed ducted fan design, the equations of motions are derived based on the Free Body Diagram of the system in Figure 7.3. From the figure, the aerodynamic forces and moments for longitudinal symmetric motions can be derived as follows:

$$\begin{aligned} &X : W\sin(\theta_f) - D\cos(\varepsilon) \\ &Z : W\cos(\theta_f) - D\sin(\varepsilon) - T_1 - (T_2 + T_3) - L \\ &M : T_1 \cdot l_r - (T_2 + T_3 + L) \cdot l_t \end{aligned} \tag{7.3}$$

Assuming small angles for ϵ [79], the following system of differential equations is formed:

$$\begin{aligned} &W\sin(\theta_f) - D\tfrac{u}{V} = m(\dot{u} + qw) \\ &W\cos(\theta_f) - D\tfrac{w}{V} - T_1 - (T_2 + T_3) - L = m(\dot{w} - qu) \\ &T_1 \cdot l_r - (T_2 + T_3 + L) \cdot l_t = I_y \dot{q} \end{aligned} \tag{7.4}$$

In contrast to a conventional helicopter, the ducted fan concept only makes use of a change in collective pitch on the different rotors. This means that the control inputs differ from a conventional helicopter. Instead of the collective and cyclic pitch of the main rotor, the thrust coefficients of the main rotor and the two horizontal fenestrons have been chosen as longitudinal control variables. The state variables of the system are comparable to the system of a conventional helicopter. Therefore, the state vector consists of u, w, q and θ_f. Rearranging the system of differential equations in Equation (7.4), results in the following set of equations:

$$\dot{u} = g\sin(\theta_f) - \frac{D}{m} \cdot \frac{u}{V} - qw \tag{7.5}$$

$$\dot{w} = g\cos(\theta_f) - \frac{T_1}{m} - \frac{D}{m} \cdot \frac{w}{V} - \frac{T_2 + T_3 + L}{m} \tag{7.6}$$

$$\dot{q} = \frac{T_1}{I_y} \cdot l_r - \frac{T_2 + T_3 + L}{I_y} \cdot l_t \tag{7.7}$$

$$\dot{\theta}_f = q \tag{7.8}$$

The complete set of equations can be linearised to yield:

$$\begin{aligned}\dot{u} &= X_u u + X_w w + X_q q + X_{\theta_f}\theta_f + X_{C_{T_1}}C_{T_1} + X_{C_{T_2}}C_{T_2} + X_{C_{T_3}}C_{T_3}\\ \dot{w} &= Z_u u + Z_w w + Z_q q + Z_{\theta_f}\theta_f + Z_{C_{T_1}}C_{T_1} + Z_{C_{T_2}}C_{T_2} + Z_{C_{T_3}}C_{T_3}\\ \dot{q} &= M_u u + M_w w + M_q q + M_{\theta_f}\theta_f + M_{C_{T_1}}C_{T_1} + M_{C_{T_2}}C_{T_2} + M_{C_{T_3}}C_{T_3}\end{aligned} \tag{7.9}$$

Here, X_u is the derivative of $\dot{u}$ with respect to the variable in the subscript, u. Similarly, Z_u is the derivative of $\dot{w}$ with respect to u and M_u is the derivative of $\dot{q}$ with respect to u.
Equation (7.5) can be rewritten as Equation (7.10), where V is $\sqrt{u^2+w^2}$. All the derivatives of $\dot{u}$ can now be computed analytically, resulting in Equations (7.11) to (7.17).

$$\dot{u} = g\sin(\theta_f) - \frac{C_D\rho V^2}{2m}\frac{u}{V} - qw \tag{7.10}$$

$$X_u = \left.\frac{d\dot{u}}{du}\right|_{t=0} = -\frac{C_{D_0}\rho_0 S_{ref}(2u_0^2+w_0^2)}{2m_0\sqrt{u_0^2+w_0^2}} \tag{7.11}$$

$$X_w = \left.\frac{d\dot{u}}{dw}\right|_{t=0} = -\frac{C_{D_0}\rho_0 S_{ref}u_0 w_0}{2m_0\sqrt{u_0^2+w_0^2}} - q_0 \tag{7.12}$$

$$X_q = \left.\frac{d\dot{u}}{dq}\right|_{t=0} = -w_0 \tag{7.13}$$

$$X_{\theta_f} = \left.\frac{d\dot{u}}{d\theta_f}\right|_{t=0} = g_0\cos(\theta_{f_0}) \tag{7.14}$$

$$X_{C_{T_1}} = \left.\frac{d\dot{u}}{dC_{T_1}}\right|_{t=0} = 0 \tag{7.15}$$

$$X_{C_{T_2}} = \left.\frac{d\dot{u}}{dC_{T_2}}\right|_{t=0} = 0 \tag{7.16}$$

$$X_{C_{T_3}} = \left.\frac{d\dot{u}}{dC_{T_3}}\right|_{t=0} = 0 \tag{7.17}$$

In the same way, Equation (7.6) can be rewritten as Equation (7.18). The derivatives are analytically computed in Equation (7.19) to (7.25)

$$\dot{w} = -\frac{C_{T_1}\rho(\Omega_1 R_1)^2\pi R_1^2}{m} + g\cos(\theta_f) - \frac{C_D\rho V^2 S}{2m}\frac{w}{V} - \frac{(C_{T_1}+C_{T_2})\rho(\Omega_t R_t)^2\pi R_t^2}{m} + qu - \frac{C_L\rho V^2 S}{2m} \tag{7.18}$$

$$Z_u = \left.\frac{d\dot{w}}{du}\right|_{t=0} = q_0 - \frac{C_{D_0}\rho_0 S_{ref}u_0 w_0}{2m_0\sqrt{u_0^2+w_0^2}} - \frac{C_{L_0}u_0\rho_0 S_t}{m_0\sqrt{u_0^2+w_0^2}} \tag{7.19}$$

$$Z_w = \left.\frac{d\dot{w}}{dw}\right|_{t=0} = -\frac{C_{D_0}\rho_0 S_{ref}(2u_0^2+w_0^2)}{2m_0\sqrt{u_0^2+w_0^2}} - \frac{C_{L_0}w_0\rho_0 S_t}{m_0\sqrt{u_0^2+w_0^2}} \tag{7.20}$$

$$Z_q = \left.\frac{d\dot{w}}{dq}\right|_{t=0} = u_0 \tag{7.21}$$

$$Z_{\theta_f} = \left.\frac{d\dot{w}}{d\theta_f}\right|_{t=0} = -g_0\sin(\theta_{f_0}) \tag{7.22}$$

$$Z_{C_{T_1}} = \left.\frac{d\dot{w}}{dC_{T_1}}\right|_{t=0} = -\frac{\rho_0(\Omega_1 R_1)^2\pi R_1^2}{m_0} \tag{7.23}$$

$$Z_{C_{T_2}} = \left.\frac{d\dot{w}}{dC_{T_2}}\right|_{t=0} = -\frac{\rho_0(\Omega_2 R_2)^2\pi R_2^2}{m_0} \tag{7.24}$$

$$Z_{C_{T_3}} = \left.\frac{d\dot{w}}{dC_{T_3}}\right|_{t=0} = -\frac{\rho_0(\Omega_3 R_3)^2\pi R_3^2}{m_0} \tag{7.25}$$

Finally, only the moment derivatives need to be computed. Equation (7.7) can again be rewritten as Equation (7.26). Then, the derivatives are calculated as stated in Equation (7.27) to (7.33).

$$\dot{q} = \frac{C_{T_1}\rho(\Omega_1 R_1)^2\pi R_1^2 l_r}{I_y} - \frac{(C_{T_2}+C_{T_3})\rho(\Omega_t R_t)^2\pi R_t^2 l_t}{I_y} - \frac{C_L\rho V^2 S_t l_t}{2I_y} \tag{7.26}$$

$$M_u = \left.\frac{d\dot{q}}{du}\right|_{t=0} = -\frac{C_L \rho S_t u_0 l_t}{I_y \sqrt{u_0^2 + w_0^2}} \tag{7.27}$$

$$M_w = \left.\frac{d\dot{q}}{dw}\right|_{t=0} = -\frac{C_L \rho S_t w_0 l_t}{I_y \sqrt{u_0^2 + w_0^2}} \tag{7.28}$$

$$M_q = \left.\frac{d\dot{q}}{dq}\right|_{t=0} = 0 \tag{7.29}$$

$$M_{\theta_f} = \left.\frac{d\dot{q}}{d\theta_f}\right|_{t=0} = 0 \tag{7.30}$$

$$M_{C_{T_1}} = \left.\frac{d\dot{q}}{dC_{T_1}}\right|_{t=0} = \frac{\rho_0 (\Omega_1 R_1)^2 \pi R_1^2 l_r}{I_y} \tag{7.31}$$

$$M_{C_{T_2}} = \left.\frac{d\dot{q}}{dC_{T_2}}\right|_{t=0} = -\frac{\rho_0 (\Omega_2 R_2)^2 \pi R_2^2 l_t}{I_y} \tag{7.32}$$

$$M_{C_{T_3}} = \left.\frac{d\dot{q}}{dC_{T_3}}\right|_{t=0} = -\frac{\rho_0 (\Omega_3 R_3)^2 \pi R_3^2 l_t}{I_y} \tag{7.33}$$

Now that all the derivatives have been computed, the following state space system can be set up:

$$\begin{bmatrix} \dot{u} \\ \dot{w} \\ \dot{q} \\ \dot{\theta}_f \end{bmatrix} = \begin{bmatrix} X_u & X_w & X_q & X_{\theta_f} \\ Z_u & Z_w & Z_q & Z_{\theta_f} \\ M_u & M_w & M_q & M_{\theta_f} \\ 0 & 0 & 1 & 0 \end{bmatrix} \begin{bmatrix} u \\ w \\ q \\ \theta_f \end{bmatrix} + \begin{bmatrix} X_{C_{T_1}} & X_{C_{T_2}} & X_{C_{T_3}} \\ Z_{C_{T_1}} & Z_{C_{T_2}} & Z_{C_{T_3}} \\ M_{C_{T_1}} & M_{C_{T_2}} & M_{C_{T_3}} \\ 0 & 0 & 0 \end{bmatrix} \begin{bmatrix} C_{T_1} \\ C_{T_2} \\ C_{T_3} \end{bmatrix} \tag{7.34}$$

The state space system can be used to model the dynamic stability of the system. Applying an impulse input at the horizontal tail rotors results in an unstable response of the rotorcraft. The results for the open loop system are presented in Figure 7.5. Figure 7.6 gives the open loop block diagram [60].

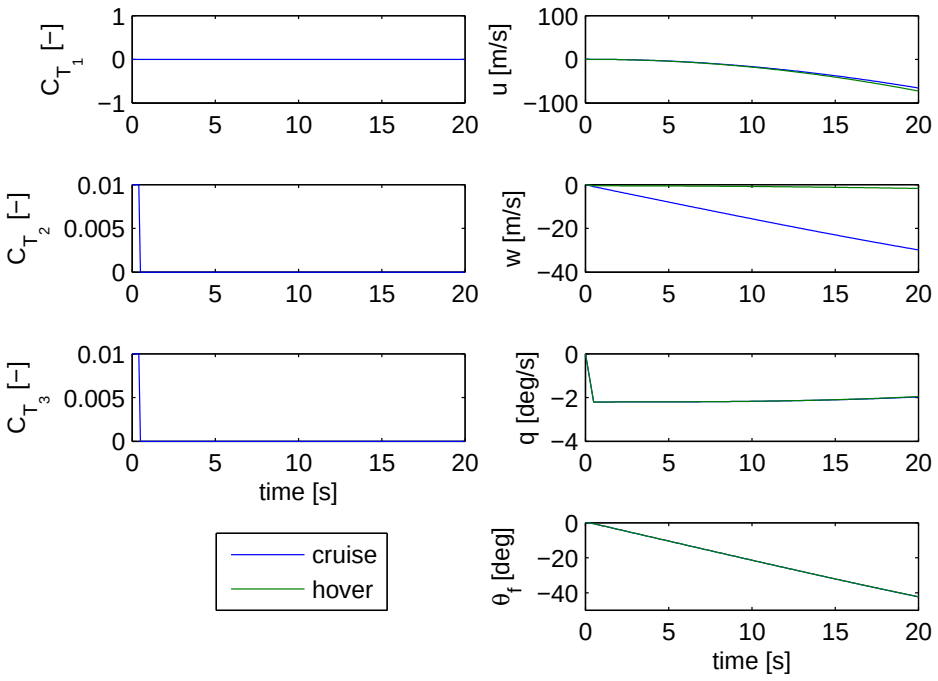

Figure 7.5: Open loop response plots for a single rotorcraft

The resulting poles of the system are shown in Figure 7.7 and 7.8.This plot is further discussed in Section 7.1.4.

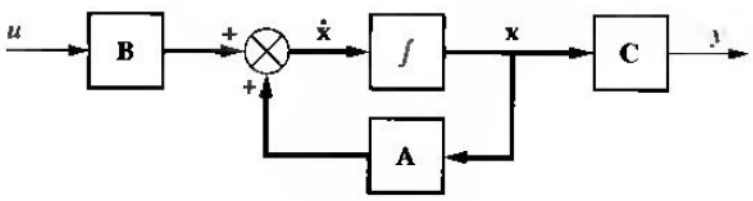

Figure 7.6: Open loop block diagram [60]

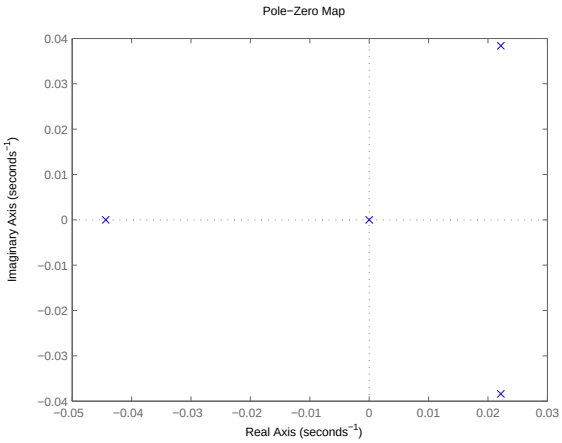

Figure 7.7: Poles of the open system of a single rotorcraft (hover)

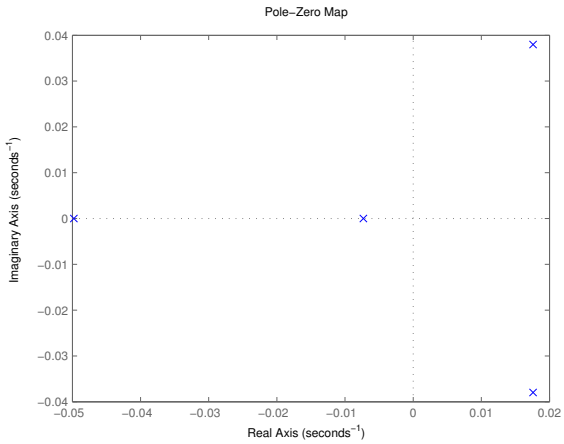

Figure 7.8: Poles of the open system of a single rotorcraft (cruise)

By giving different inputs to the system, the eigenmotions corresponding to the eigenvalues of the system can be analysed.

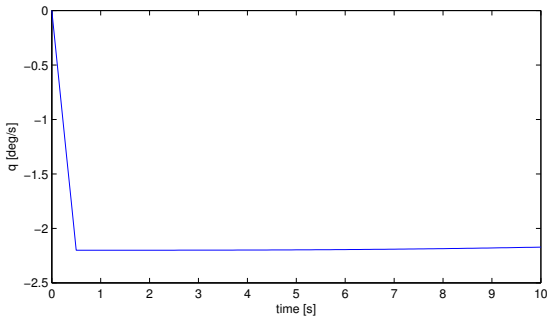

Figure 7.9: First seconds after an impulse input

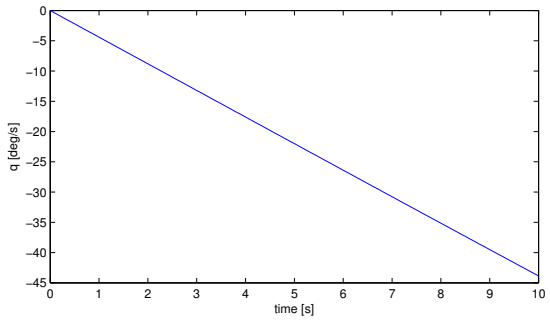

Figure 7.10: First seconds after a step input

Impulse Input Applying an input of $C_{T_2} = C_{T_3} = 0.01$ for 0.5 seconds starts a phugoid. This input models an impulse input which can not be achieved in reality. When looking at Figure 7.9 it seems that the motion is only slightly damped if at all. However, looking at the result for 600 seconds in Figure 7.11, the oscillatory motion of the phugoid is clearly visible. The motion is unstable as the amplitude is increasing.

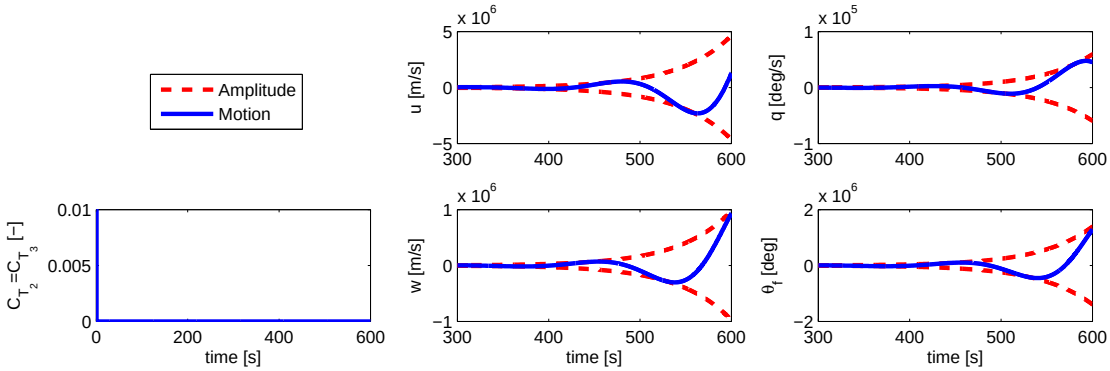

Figure 7.11: Impulse input

Step Input When applying a step input of $C_{T_2} = C_{T_3} = 0.01$ a similar motion as for an impulse input can be observed. However, it can be seen immediately in Figure 7.10 that the motion is unstable. When looking at Figure 7.12, the divergent amplitude of the unstable oscillatory motion is again clearly visible.

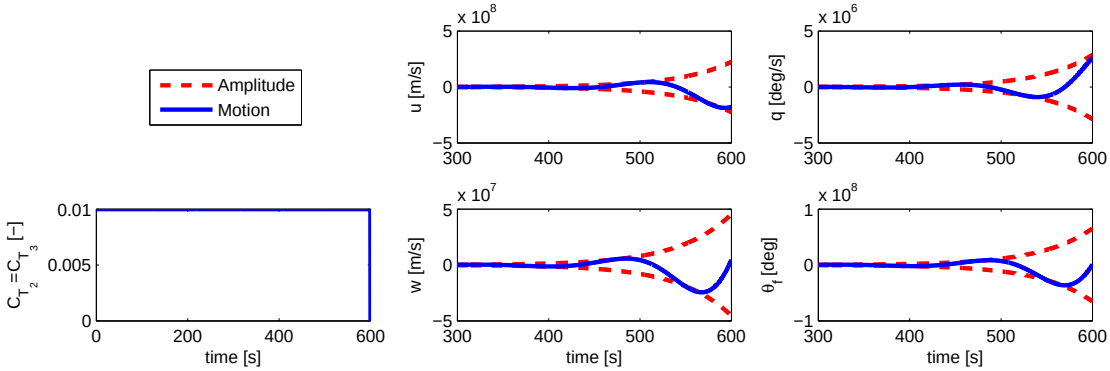

Figure 7.12: Step input

Eigenvalues The four eigenvalues of the system are: -0.00730, 0.0176 ± 0.0380i and -0.0498. The eigenvalues corresponding to the motions above can be found by comparing the plots to the properties of the eigenvalues. These properties can be determined by using the relation between the real part ξ_c, the imaginary part η_c, the period and the time to double amplitude.

$$T_{2A_{m0}} = \frac{\ln 2}{\xi_c} \tag{7.35}$$

$$P = \frac{2\pi}{\eta_c} \tag{7.36}$$

$A_m = A_{m0}e^{-\zeta\omega_n t}$ has been used to plot the amplitude with $\omega_n = \frac{2\pi}{P}$. Because the motion is unstable, the time to double amplitude $T_{2A_{m0}}$ can be calculated. Table 7.1 summarises the calculated properties of the eigenmotion. It can be seen that both inputs result in the same eigenmotion with the same eigenvalues.

Table 7.1: Properties of the eigenmotions

	P [s]	ω_n [s^{-1}]	ζ [-]	$T_{2A_{m0}}$ [s]	ξ_c [s^{-1}]	η_c [s^{-1}]	eigenvalues
Impulse input	165.3	0.0380	-0.420	39.3834	0.0176	0.0380	0.0176±0.0380i
Step input	165.3	0.0380	-0.420	39.3834	0.0176	0.0380	0.0176±0.0380i

Lateral Dynamic Stability Further analysis of the dynamic stability of the single rotorcraft can be done by performing the entire process again for the lateral stability.

7.1.4 Control

The rotorcraft is inherently unstable without a feedback controller. This can be seen by looking at the poles of the open loop system in Figure 7.7 and 7.8. The plot shows that some poles are located on the positive real axis (i.e. there are eigenvalues with a positive real part). A PID controller is necessary to shift the poles to the negative real part of the complex plane and hence make the ducted fan stable. When simulating around the hover condition only a PI controller is used in order to make the rotorcraft stable. The advantage of a proportional integral derivative (PID) controller is the fact that it improves the transient response (i.e. improve settling time and percentage overshoot) and it reduces the steady state

error. The proportional controller feeds the error to the plant, the integral controller feeds the integral error to the plant and the derivative controller feeds the derivative of the error to the plant [61]. Figure 7.17 illustrates the closed loop system [60].

For a first order analysis, a check is made in order to determine if the vehicle is controllable or not. A balance between the response time and phase margin is found by calculating the right gain of the feedback loop. For now, the main rotor and both the horizontal tail rotors are used in order to control the longitudinal stability of the rotorcraft. After applying the controller the responses presented in Figure 7.15 are obtained for an impulse input on the horizontal tail rotors. On the left hand side of the figure the inputs are shown and on the right hand side the response of the states is given. As can be seen the rotorcraft will decrease in angle of attack and gain altitude. Figure 7.16 gives the response when additionally an impulse input is applied on the main rotor. As can be seen the forward velocity now increases. A control algorithm is required to keep a constant altitude. The PID controller matrix G used in the feedback loop is given in Table 7.2. As can be seen the outputs are linked to the inputs via transfer functions. The rows of the matrix contain the inputs and the columns contain the outputs (i.e. the states).

In the detailed design phase, further tuning can be done in order to reduce the rise time and overshoot by making use of nyquist plots. With these plots the poles can be chosen to be such that a suitable gain is obtained.

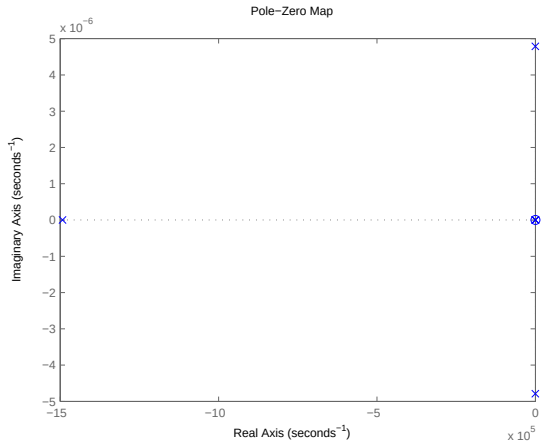

Figure 7.13: Poles of the closed loop system (hover).

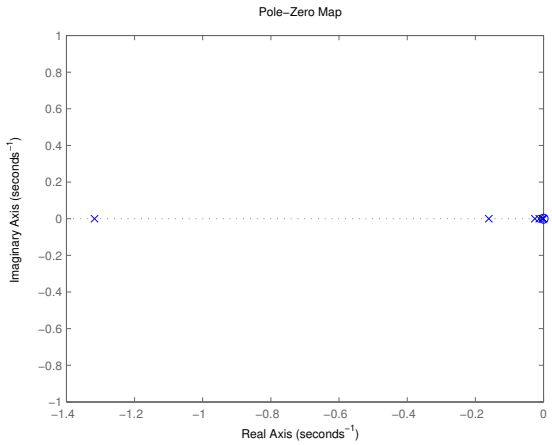

Figure 7.14: Poles of the closed loop system (cruise).

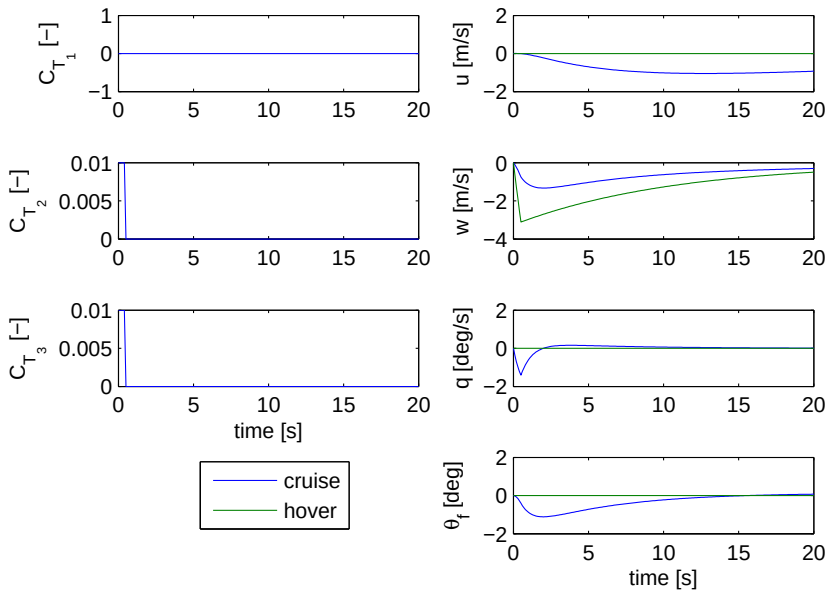

Figure 7.15: Closed loop response.

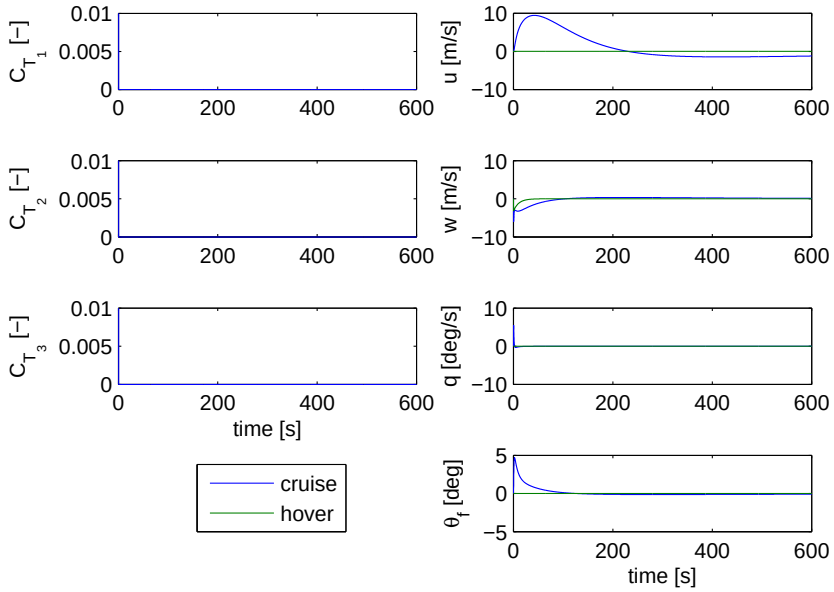

Figure 7.16: Closed loop response with impulse input main rotor.

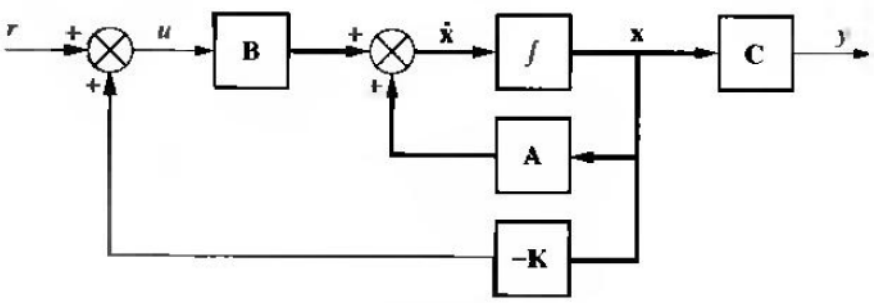

Figure 7.17: Closed loop block diagram [60]

Table 7.2: PID controller matrix G

	u	w
Main rotor	$\frac{1.362e{-}05s^2+2.695e{-}08s+1.333e{-}11}{s}$	$\frac{-7.467e{-}05s^2-7.365e{-}08s-1.816e{-}11}{s}$
Horizontal tail rotor	$\frac{-8.695e{-}05s^2-1.721e{-}07s-8.511e{-}11}{s}$	$\frac{-0.001135s^2-0.0001674s-6.166e{-}07}{s}$
Horizontal tail rotor	$\frac{-8.695e{-}05s^2-1.721e{-}07s-8.511e{-}11}{s}$	$\frac{-0.001135s^2-0.0001674s-6.166e{-}07}{s}$

	q	θ
Main rotor	$\frac{0.007889s+0.0009947}{s}$	$\frac{0.008058s^2+0.001019s+3.888e{-}06}{s}$
Horizontal tail rotor	$\frac{-0.05036s-0.00635}{s}$	$\frac{-0.05143s^2-0.006503s-2.482e{-}05}{s}$
Horizontal tail rotor	$\frac{-0.05036s-0.00635}{s}$	$\frac{-0.05143s^2-0.006503s-2.482e{-}05}{s}$

7.1.5 Simulation

To visualise the dynamic stability of the rotorcraft, a 3D simulation is made. The simulation shows the longitudinal motion of the rotorcraft at cruise speed for given inputs on the main rotor or the horizontal tail rotors. A manual for downloading the software required to run the simulation is shown in Appendix A.

When launching the simulation, the rotorcraft is shown from the left side view. By pressing 'V' the rotorcraft

will fly at cruise velocity. By pressing the buttons in Table 7.3 an input can be given to the rotorcraft. When applying for example a positive step input on the horizontal tail rotors (by pressing 'I' for a few seconds) it can clearly be seen that the rotorcraft is pitching down and gets an upward velocity. Both movements damp out fast with unnoticable overshoot. This shows how well the PID-controller functions. The motion is shown in Figure 7.18.

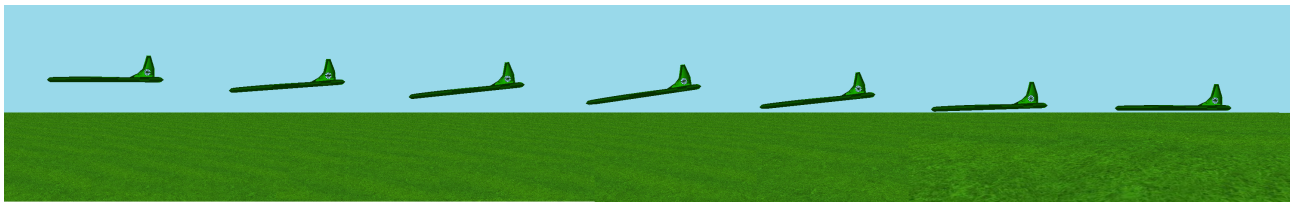

Figure 7.18: Rotorcraft motion for a step input on the horizontal tail rotors (flying from right to left)

The simulation has several controls in 2 different modes. In the flight mode (default) you move along with the rotorcraft, in the fixed mode you are at a fixed position looking at the rotorcraft. All controls are listed in Table 7.3.

Table 7.3: Simulation controls

Button	**Action**
Control inputs	
I	Positive input on horizontal tail rotors ($C_{T_2} = C_{T_3} = 0.02$)
K	Negative input on horizontal tail rotors ($C_{T_2} = C_{T_3} = -0.02$)
U	Positive input on main rotor (C_{T_1} =0.01)
J	Negative input on main rotor ($C_{T_1} = -0.01$)
Flight mode	
W	Rotate upwards about rotorcraft
A	Rotate leftwards about rotorcraft
S	Rotate downwards about rotorcraft
D	Rotate rightwards about rotorcraft
Z	Zoom in
X	Zoom out
Drag mouse	Rotate about rotorcraft
Fixed mode	
W	Move forward
A	Move left
S	Move backward
D	Move right
Z	Move up
X	Move down
Drag mouse	Look around
Other controls	
C	Change mode
V	Switch cruise velocity on/off
B	Switch clouds on/off

Any state space system can be put into the simulation to visualise the motion of the rotorcraft. The simulation uses the state space of the rotorcraft including the PID controller. Because Java is not able to solve state space systems, a numerical algorithm has been used to solve the state space system using the Runge-Kutta method [15] [23]. The algorithm is shown in Appendix B.

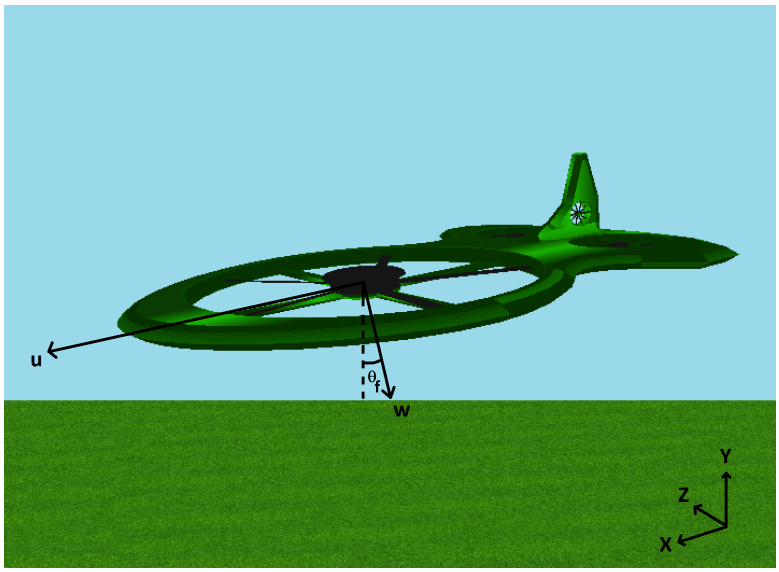

Figure 7.19: Coordinate systems of the simulation

The accurate geometry model was included into the simulation. The attitude of the rotorcraft is updated every Δt of ± 20 ms. The rotorcraft pitches by using a rotation about its center of gravity, while its location in the coordinate system of Java is calculated using Equation (7.37), derived from Figure 7.19.

$$\begin{aligned} Xlocation_{new} &= Xlocation + u \cdot \Delta t \cdot \cos(\theta_f + \theta_{f_0}) + w \cdot \Delta t \cdot \sin(\theta_f + \theta_{f_0}) + V_{cruise} \cdot \Delta t \\ Ylocation_{new} &= Ylocation - u \cdot \Delta t \cdot \sin(\theta_f + \theta_{f_0}) - w \cdot \Delta t \cdot \cos(\theta_f + \theta_{f_0}) \end{aligned} \tag{7.37}$$

7.2 System

Now that a stable rotorcraft is ensured, it is important to investigate the dynamic stability of the complete system. Section 7.2.1 describes the stability calculations of the system. Section 7.2.2 describes the required control loop to ensure a stable system.

7.2.1 Dynamic Stability

Figure 7.20 displays a side view of the complete system. The attachment points are modelled as rotational springs, each with a different spring constant k. The system consists of eight degrees of freedom, marked in red in Figure 7.20. Furthermore, the constant variables are marked in blue and the non-conservative forces acting on the different masses are marked in purple. It is assumed that every mass experiences horizontal and vertical perturbations.

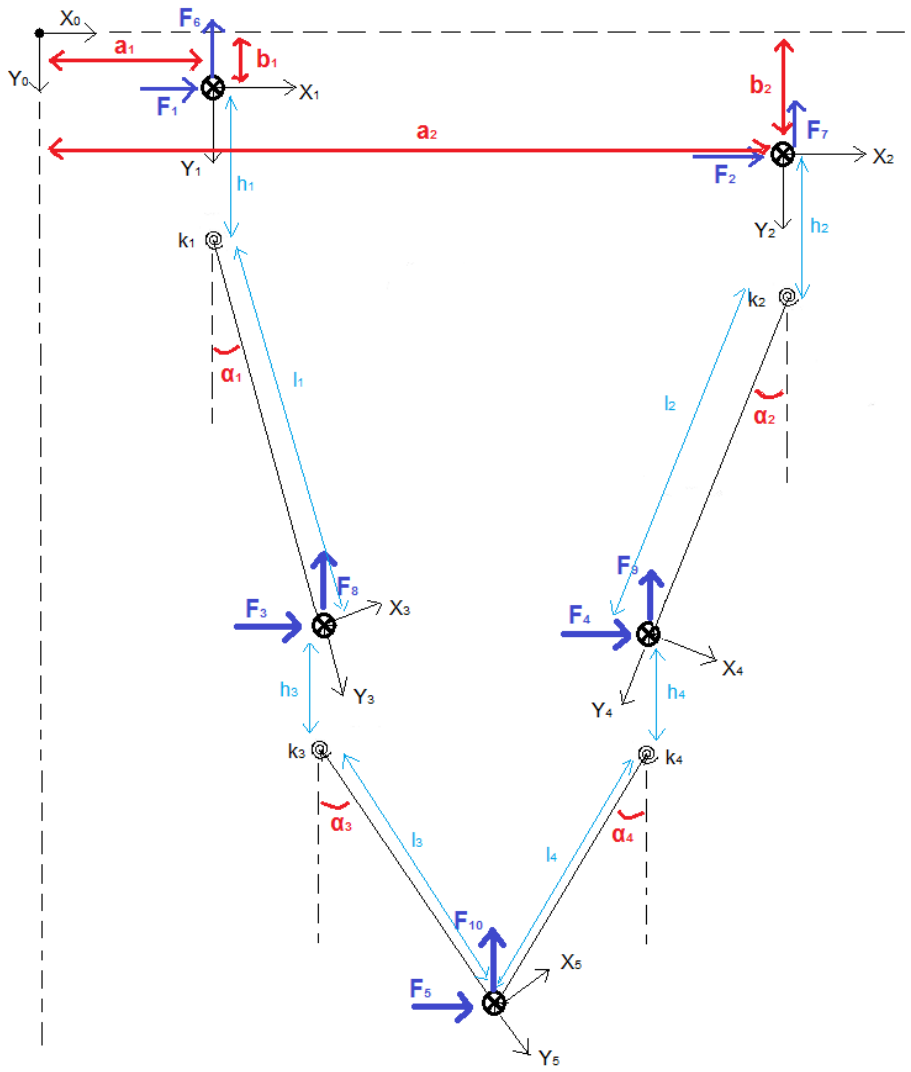

Figure 7.20: Side view of complete system

The different attachment points on the corners of the payload are located much closer to each other than the attachment points of the spreader bar. The red dots in Figure 7.21 display the attachment points. Since the distance between the attachment points of the spreader bar is much bigger than for the payload, it is assumed this can not be modelled as a point mass. By modelling the spreader bar as two point masses, the possibility of a rotation around the y-axis is incorporated. This rotation would result in a different x-position of the two ends of the spreader bar. In further calculations, the weight of both point masses is assumed to be half of the total spreader bar mass. Since the attachment points of the payload are closer together, it is assumed that the load can be modelled as a point mass.

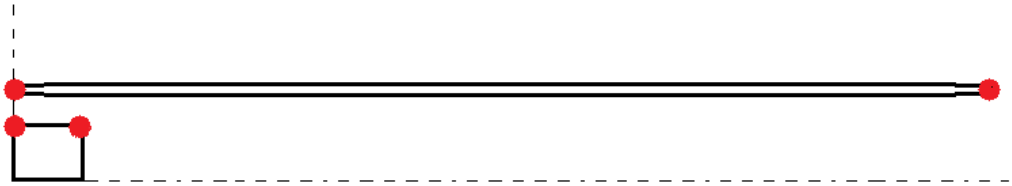

Figure 7.21: Front view comparison spreader bar and load width

To find the different equations of motions, the method of Lagrange is used. The Lagrange equation has to be solved with respect to all generalised coordinates, units that completely determine the attitude of the system [66]. For the system in Figure 7.20, the generalised coordinates are chosen to be a_1, a_2, b_1, b_2, α_1, α_2, α_3, α_4. Lagrange uses the energy from conservative and non-conservative forces to determine the motion. Conservative forces are forces for which the work is independent of its path (i.e. the forces that cause kinetic and potential energy). Non-conservative forces are forces for which the work depends on the path (i.e. the forces caused by the moving helicopter, aerodynamic forces and

perturbations from wind). For a generalised coordinate q_i in a non-conservative force field, Equation (7.38) is used [66]. Here, K is the kinetic energy, U the potential energy and W is the work done by the non-conservative forces.

$$\frac{d}{dt}\frac{\delta K}{\delta \dot{q}_i} - \frac{\delta K}{\delta q_i} + \frac{\delta U}{\delta q_i} = \frac{\delta W}{\delta q_i} \tag{7.38}$$

In order to find an expression for the kinetic and potential energy, the position vectors of the different masses have been expressed in the X_0Y_0-plane. Making use of transformation matrices to switch between the different axis systems in Figure 7.20, this results in Equations (7.39) to (7.43).

$$\begin{bmatrix} x_{10} \\ y_{10} \\ z_{10} \end{bmatrix} = \begin{bmatrix} a_1 \\ 0 \\ b_1 \end{bmatrix} \tag{7.39}$$

$$\begin{bmatrix} x_{20} \\ y_{20} \\ z_{20} \end{bmatrix} = \begin{bmatrix} a_2 \\ 0 \\ b_2 \end{bmatrix} \tag{7.40}$$

$$\begin{bmatrix} x_{30} \\ y_{30} \\ z_{30} \end{bmatrix} = \begin{bmatrix} a_1 \\ 0 \\ b_1 \end{bmatrix} + \begin{bmatrix} 0 \\ 0 \\ h_1 \end{bmatrix} + \begin{bmatrix} \cos\alpha_1 & 0 & \sin\alpha_1 \\ 0 & 1 & 0 \\ -\sin\alpha_1 & 0 & \cos\alpha_1 \end{bmatrix} \begin{bmatrix} 0 \\ 0 \\ l_1 \end{bmatrix} = \begin{bmatrix} a_1 + l_1\sin\alpha_1 \\ 0 \\ b_1 + h_1 + l_1\cos\alpha_1 \end{bmatrix} \tag{7.41}$$

$$\begin{bmatrix} x_{40} \\ y_{40} \\ z_{40} \end{bmatrix} = \begin{bmatrix} a_2 \\ 0 \\ b_2 \end{bmatrix} + \begin{bmatrix} 0 \\ 0 \\ h_2 \end{bmatrix} + \begin{bmatrix} \cos\alpha_2 & 0 & -\sin\alpha_2 \\ 0 & 1 & 0 \\ \sin\alpha_2 & 0 & \cos\alpha_2 \end{bmatrix} \begin{bmatrix} 0 \\ 0 \\ l_2 \end{bmatrix} = \begin{bmatrix} a_1 - l_1\sin\alpha_2 \\ 0 \\ b_2 + h_2 + l_2\cos\alpha_2 \end{bmatrix} \tag{7.42}$$

$$\begin{bmatrix} x_{50} \\ y_{50} \\ z_{50} \end{bmatrix} = \begin{bmatrix} x_{30} \\ y_{30} \\ z_{30} \end{bmatrix} + \begin{bmatrix} 0 \\ 0 \\ h_2 \end{bmatrix} + \begin{bmatrix} \cos\alpha_3 & 0 & \sin\alpha_3 \\ 0 & 1 & 0 \\ -\sin\alpha_3 & 0 & \cos\alpha_3 \end{bmatrix} \begin{bmatrix} 0 \\ 0 \\ l_3 \end{bmatrix} = \begin{bmatrix} a_1 + l_1\sin\alpha_1 + l_3\sin\alpha_3 \\ 0 \\ b_1 + h_1 + h_3 + l_1\cos\alpha_1 + l_3\cos\alpha_3 \end{bmatrix} \tag{7.43}$$

The velocity vectors of the different point masses are computed by taking the derivative of the position vectors with respect to time. Next, the kinetic energy and potential energy of the system can be computed by means of Equation (7.44) and (7.45) respectively. In the potential energy equation, gravitational as well as spring forces are included.

$$K = \sum_{i=1}^{5} \frac{1}{2} m_i v_i^2 \tag{7.44}$$

$$\begin{aligned} U = {} & m_H g b_1 + \tfrac{1}{2}k_1\alpha_1^2 + m_H g b_2 + \tfrac{1}{2}k_2\alpha_2^2 + \tfrac{1}{2}m_{sb}\left(b_1 + h_1 + l_1\cos\alpha_1 + b_2 + h_2 + l_2\cos\alpha_2\right) + \\ & \tfrac{1}{2}k_3\alpha_3^2 + \tfrac{1}{2}k_4\alpha_4^2 + m_L g\left(b_1 + h_1 + l_1\cos\alpha_1 + l_3\cos\alpha_3\right) \end{aligned} \tag{7.45}$$

Now that the conservative forces are accounted for, the non-conservative forces have to be included. The virtual work δW is determined with respect to a small change δq_i of the generalised coordinates. Starting at the bottom of the system and working up, this results in the following terms for the virtual work:

$$\frac{\delta W}{\delta \alpha_4} = -F_5 l_4 \cos\alpha_4 \tag{7.46}$$

$$\frac{\delta W}{\delta \alpha_3} = F_5 l_3 \cos\alpha_3 \tag{7.47}$$

$$\frac{\delta W}{\delta \alpha_1} = \left(F_3 + F_5\right) l_1 \cos\alpha_1 \tag{7.48}$$

$$\frac{\delta W}{\delta \alpha_2} = -\left(F_4 + F_5\right) l_2 \cos\alpha_2 \tag{7.49}$$

$$\frac{\delta W}{\delta a_1} = F_1 + F_3 + F_5 \tag{7.50}$$

$$\frac{\delta W}{\delta b_1} = -F_6 - F_8 - F_{10} \tag{7.51}$$

$$\frac{\delta W}{\delta a_2} = F_2 + F + 4 + F_5 \tag{7.52}$$

$$\frac{\delta W}{\delta b_2} = -F_7 - F_9 - F_{10} \tag{7.53}$$

The signs of the work are determined in coherence with the positive y-axis direction. In Equations (7.46) up until (7.49), only the component of the horizontal force that acts in the direction of the pendulum motion is used to determine the work ($Fcos(\alpha) \cdot l$). Furthermore, in Equation (7.48) and (7.49), it is assumed that the payload experiences the same displacement as the spreader bar when a small displacement of α_1 and α_2 is considered. This idea is demonstrated in Figure 7.22. Subsequently, the movement of the load with respect to the spreader bar is accounted for in the α_3 and α_4 terms (Equation (7.47) and (7.46)).

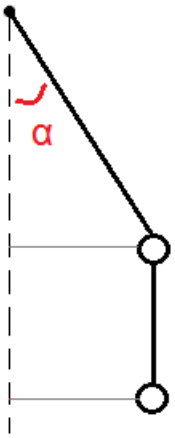

Figure 7.22: Mass displacement caused by $\delta\alpha_1$ and $\delta\alpha_2$

Now that the non-conservative and conservative forces have been accounted for, the Lagrange equation (Equation (7.38)) can be derived with respect to all eight generalised coordinates. These non-linear equations are shown in Appendix F. Next, the equations need some simplifications to enable numerical modelling of the stability. The first step in simplifying the model is to assume small angles for α_1, α_2, α_3 and α_4. This results in the sine and cosine terms dropping out since they are replaced by α and 1 respectively.

One of the problems that remains after the small angle approach is that the system consists of second derivatives of the generalised equations. To solve this problem, 8 new variables are introduced in the system. The way in which a_{11} up until α_{41} are introduced in the system is demonstrated in Table 7.4. The equations in this table are also used as remaining equations in the state space matrix later on.

Table 7.4: New variables

$\dot{a}_1 = a_{11}$	$\dot{b}_1 = b_{11}$	$\dot{\alpha}_1 = a_{11}$	$\dot{\alpha}_1 = a_{11}$
$\ddot{a}_1 = \dot{a}_{11}$	$\dot{b}_1 = \dot{b}_{11}$	$\ddot{\alpha}_1 = \dot{\alpha}_{11}$	$\ddot{\alpha}_3 = \dot{\alpha}_{31}$
$\dot{a}_2 = a_{21}$	$\dot{b}_2 = b_{21}$	$\dot{\alpha}_2 = \alpha_{21}$	$\dot{\alpha}_4 = \alpha_{41}$
$\ddot{a}_2 = \dot{a}_{21}$	$\dot{b}_2 = \dot{b}_{21}$	$\ddot{\alpha}_2 = \dot{\alpha}_{21}$	$\ddot{\alpha}_4 = \dot{\alpha}_{41}$

After all first and second derivatives are substituted by the new variables according to Table 7.4. After linearising the equations of motion, the accompanying state space matrices can be set up. The state vector x is presented in Equation (7.54). Since the first and second derivatives of α_4 do not occur in the last equation, this variable does not occur in the state space vector.

$$x = \begin{bmatrix} a_1 & a_2 & b_1 & b_2 & \alpha_1 & \alpha_2 & \alpha_3 & a_{11} & a_{21} & b_{11} & b_{21} & \alpha_{11} & \alpha_{21} & \alpha_{31} \end{bmatrix}^T \tag{7.54}$$

The input vector u is presented in Equation (7.55). Section 7.2.2 will discuss what inputs are used to control the system.

$$u = \begin{bmatrix} F_1 & F_2 & F_3 & F_4 & F_5 & F_6 & F_7 & F_8 & F_9 & F_{10} \end{bmatrix}^T \tag{7.55}$$

With the state vector and the input vector, the state space system of Equation (7.56) is formed.

$$\begin{aligned} E\dot{x} &= Ax + Bu \\ \dot{x} &= E^{-1}Ax + E^{-1}Bu \end{aligned} \tag{7.56}$$

The resulting state space system is shown in Appendix F and was used to plot the response curves presented in Figure 7.23 after applying a forward horizontal force on both rotorcraft ($F_1 = F_2 = 20$N).

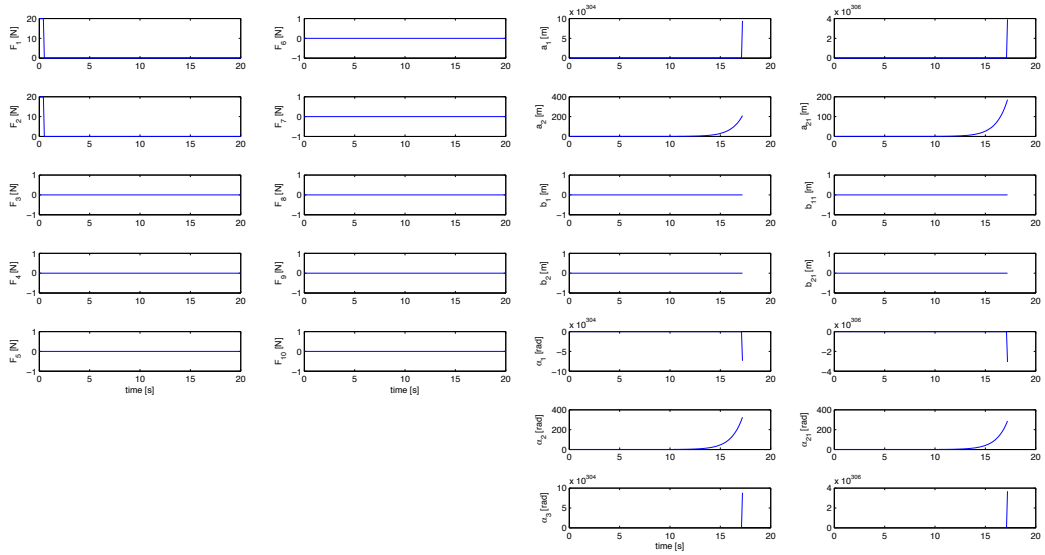

Figure 7.23: Open loop response plots complete system

The plots in Figure 7.23 show very unstable behaviour of the system. Although the system is known to be inherently unstable from earlier studies [68], this level of instability is too high. The developed state space system should be evaluated to see what the consequences of the simplifications are. In the future, the accuracy of the tool could be increased by considering a non-linear system.
Furthermore, the tool does not include any lateral stability. To be able to model the pendulum motion in both directions, the lateral and longitudinal stability would need to be simulated simultaneously. This will result in an increase of degrees of freedom of the system, increasing the complexity but at the same time also increasing the accuracy of the tool. In the detailed design, the stability of the system should be investigated in more detail.

7.2.2 Control

The development of a complete control loop for the entire system does not fall within the scope of this project. From the ten entries of the input vector in Equation (7.55), only four forces are real control variables of the system. The forces on the two helicopters, F_1, F_6, F_2 and F_7 are considered control variables. By increasing or decreasing the vertical and horizontal components of the thrust, the movement of the helicopters can be controlled. If a detailed model needs to be obtained the attitude and dynamics of the single rotorcraft need to be implemented together with the attitude and dynamics of the system. After this a control algorithm needs to be written in order to ensure sufficient stability of the system while allowing agility at the same time. This will be done for the longitudinal and for the lateral control.

In the future, a complete control system needs to be developed. Thinking about a controllable system, it can be convenient to have the vertical position of the spreader bar and load coupled back to the rotorcraft. In this way, the rotorcraft would be able to react to the movements of the load and to counteract destabilising payload movements before the system response diverges.

8. Configuration

In Chapter 4 the initial lay-out of the design was presented. The individual disciplines investigated the aerodynamics, structures and stability of the design. The final concept after these adaptations is presented in this chapter. A concept image of the system in action is shown in Section 8.1. Section 8.2 contains the technical drawings of the design detailing the most important dimensions with a brief discussion.

8.1 Concept

The LIFT^2 system is designed to transport heavy payloads. Specifically, Hospitainer requested a vehicle capable of transporting their mobile hospitals by air. Figure 8.1 gives an impression of what this will look like if the system were to be produced.

Figure 8.1: The Lift^2 system deploying a Hospitainer.

8.2 Technical Drawings

The final concept is shown in Figure 8.2 along with the appropriate dimensions. The twin-lift configuration forming the LIFT^2 system is shown in Figure 8.3.

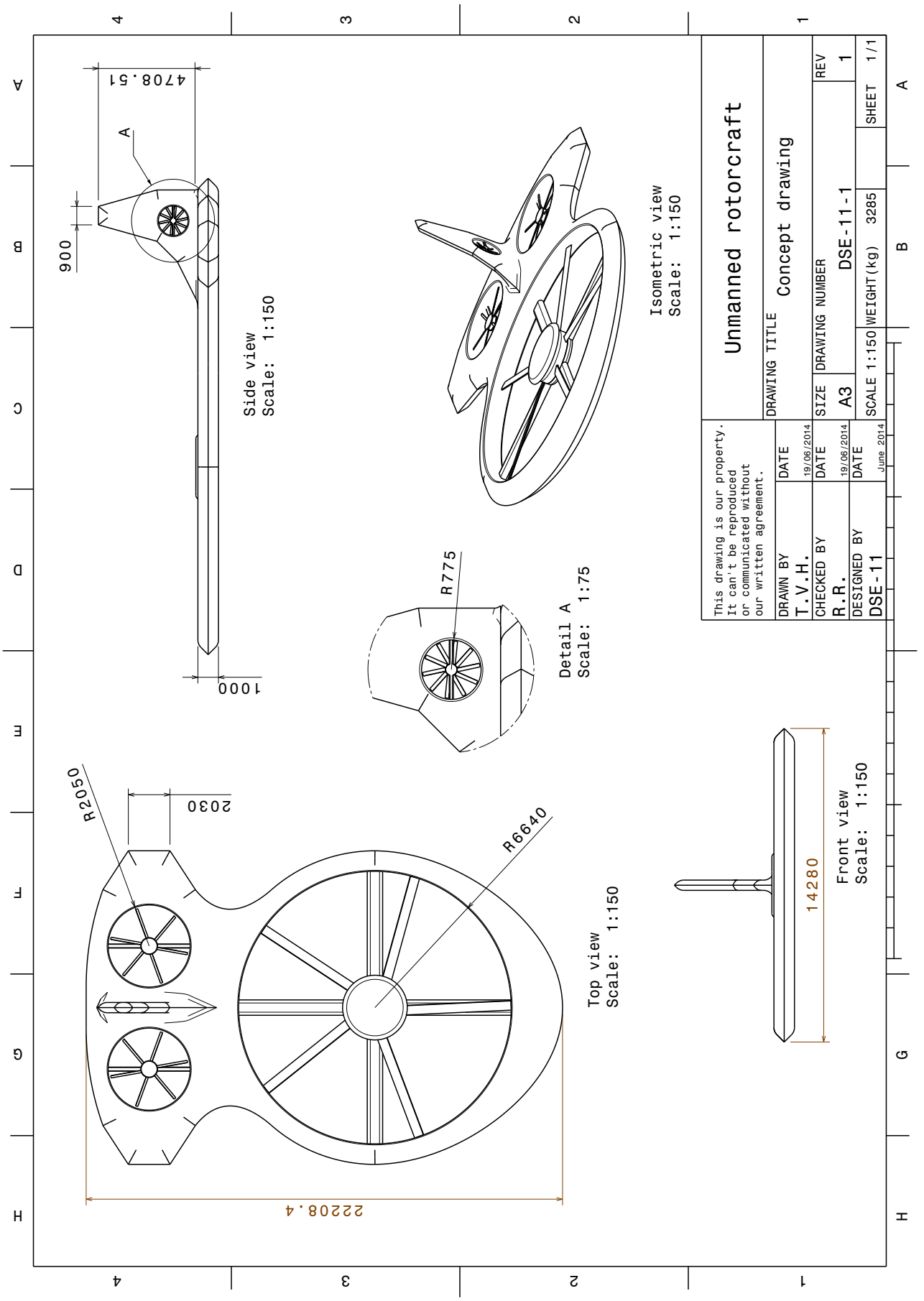

Figure 8.2: Technical drawing of proposed concept.

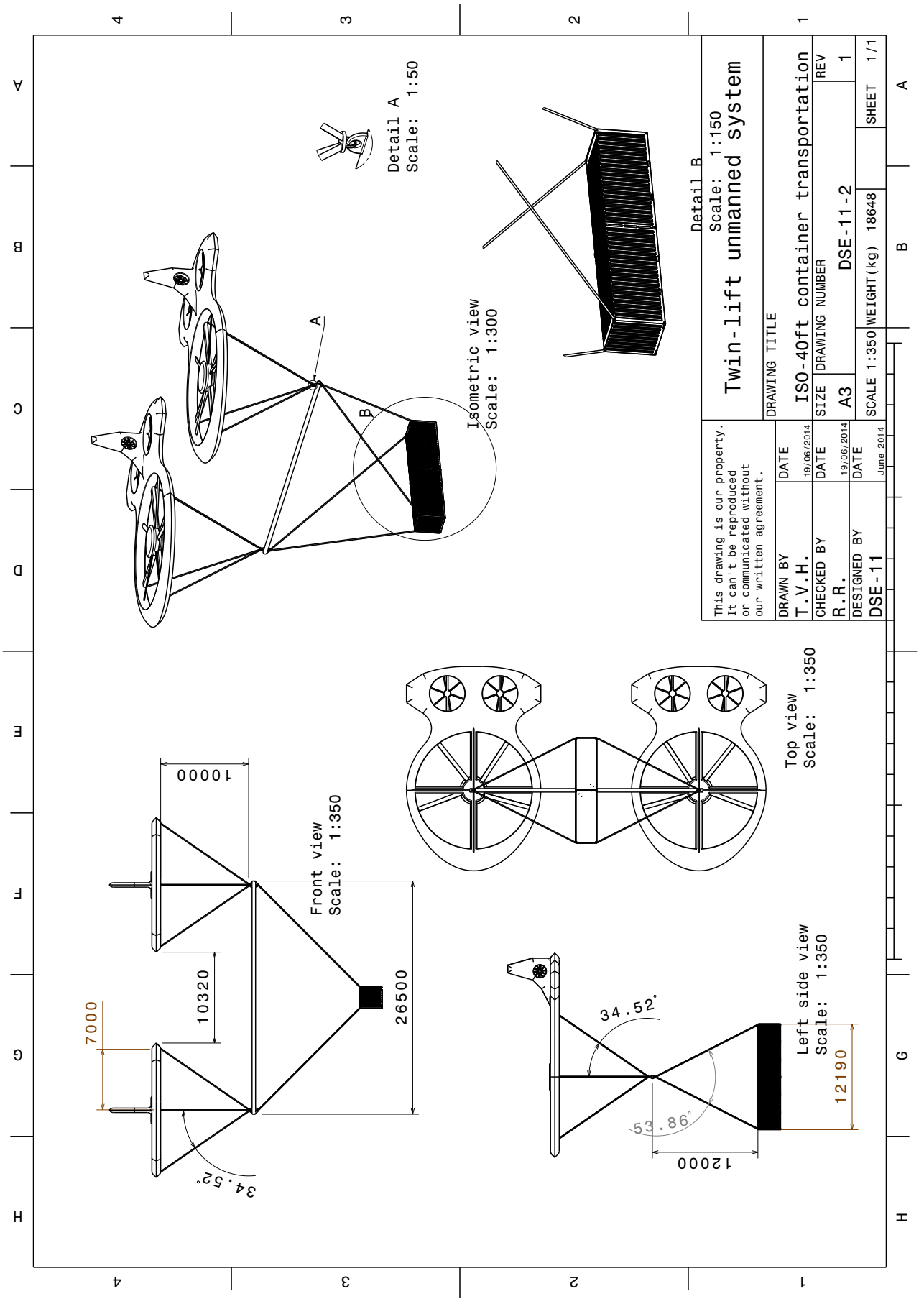

Figure 8.3: Technical drawing showing the twin-lift configuration.

9. Performance

This chapters evaluates on the performance of conceptual design, as presented in Chapter 8. The conceptual design resulted from an initial sizing as described in Chapter 4, on which consecutively an aerodynamic and structural analysis were performed. The performance is evaluated by firstly considering the payload range diagram in Section 9.1. Subsequently the climb performance and the flight envelope are elaborated respectively in Sections 9.2 and 9.3.

9.1 Payload Range Diagram

In Chapter 2 the revised mission profile was determined. The rotorcraft should be able to fly 200 km to an emergency area and return to the base. The fuel weight was determined to fulfil this mission requirement. This section expands on these calculations to determine the maximum range diagram, if the rotorcraft do not have to return to the base. This results in the payload range diagram as shown in Figure 9.1. The range mainly depends on the weight of the rotorcraft. Initially the payload and operational empty weight are considered, without fuel weight. This leads to a range of 0 km. Slowly the fuel is added until the maximum take-off weight is reached. The payload weight is then decreased in steps until only the fuel and empty weight remain. Note that this method does not take extra fuel tanks, or extra payload with less fuel, into account. This could be investigated in a later stage of the design.
Using the method described in Section 4.2.4 the required power to cruise at 1500 meter altitude is calculated, for every weight. The cruise is performed at a speed of 80 kts, as defined by the requirements in Chapter 2.
The mass flow of the fuel per hour is calculated using Equation (9.1), where the specific fuel consumption of the engine is 0.282 $kg/kWhr$ as described in Section 4.2.5. The required power as function of weight is determined using the method described in Section 4.2.4.

$$\dot{m}_{fuel} = SFC \cdot P_{req} \tag{9.1}$$

The endurance of the rotorcraft in hours can be expressed as the fuel weight divided by the fuel flow.

$$Endurance = \frac{W_{fuel}}{\dot{m}_{fuel}} \tag{9.2}$$

Consecutively the range of the rotorcraft for a given payload and fuel weight is found using Equation (9.3), where the cruise speed is equal to 80 kts. This relationship is displayed in Figure 9.1.

$$Range = Endurance \cdot V_{cruise} \tag{9.3}$$

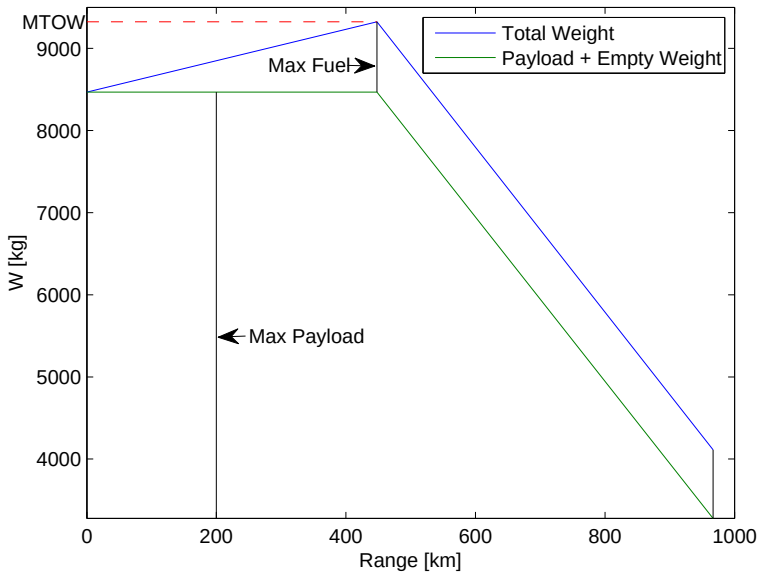

Figure 9.1: Payload range diagram

It can be concluded that the maximum range without payload is 967 km, while flying at maximum take-off weight results in a range of 448 km. This is further than the actual range required for the mission, but does not take the hovering stages into account.

9.2 Climb Performance

The climb performance of the rotorcraft is dependent on the required power, available power and weight of the rotorcraft(Equation (4.54). These are influenced by the amount of payload and the altitude. The rate of climb is plotted as a function of flight speed for sea level and cruise altitude in Figures 9.2 and 9.3. The power curves from Section 4.2.6 are used as input data.

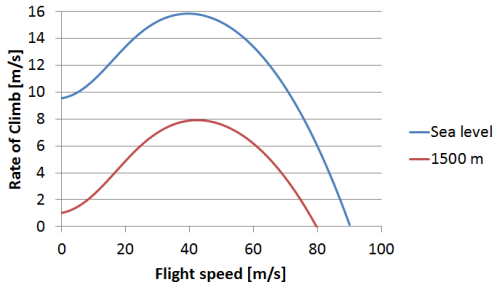

Figure 9.2: Climb performance of fully loaded rotorcraft

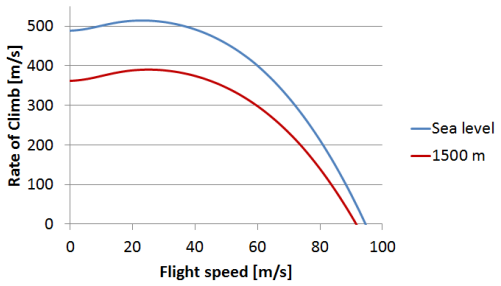

Figure 9.3: Climb performance of empty rotorcraft

The rate of climb shows the reverse trend when compared to the required power, since the available power remains constant with flight speed. From Figure 9.2 one can conclude that the maximum cruise speeds due to power constraints are 90 m/s and 82 m/s at respectively sea level and cruise altitude. These values are well above the maximum required flight speed of 100 kts (51.44 m/s). For the empty rotorcraft even higher flight speeds are possible of 91.5 m/s at cruise altitude and 95.5 m/s at sea level.
Another important performance parameter is the hover ceiling of the rotorcraft. This obtained by calculating the rate of climb in hover for different altitudes and checking where it becomes zero. Therefore the rate of climb in hover (no forward speed) versus the rate of climb is shown in Figure 9.4.

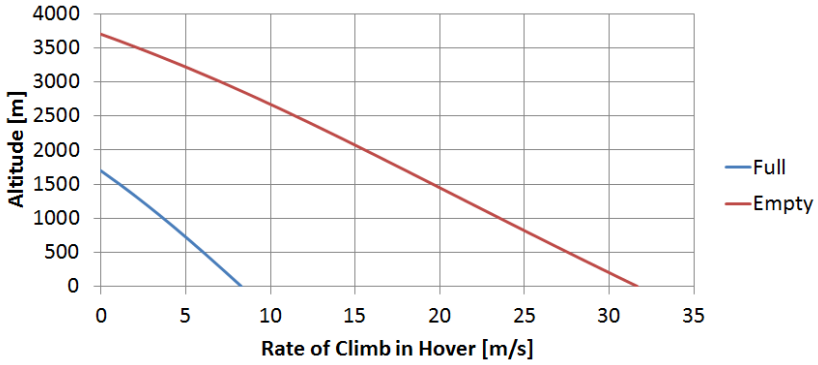

Figure 9.4: Altitude versus rate of climb

Two hover ceilings can be identified. For the fully loaded rotorcraft the hover ceiling is 1685 meter, while the ceiling of the empty rotorcraft is 3710 meter. The decrease in performance is contributed to two factors: firstly, the engines lose part of their power with increasing altitude as shown in Equation (4.53). Secondly, the air becomes less dense, which increases the required power, as described in Section 4.2.4.

9.3 Flight Envelope

The climb performance plots clearly indicate that the rotorcraft have a minimum and maximum flight speed for each altitude. This is used to specify the flight envelope in Figure 9.5.
Another constraint on the flight speed is the Mach number at the tip of the main rotor blades. This Mach number should never exceed the drag divergence number. The main rotor is critical in this case, since it has a higher tip speed than the horizontal tail rotors. The drag divergence Mach number of the SSC-H07 airfoil is 0.86 [30].
The actual experienced air speed at the tip of the blades is found using Equation (9.4), which consists of two factors: the tip speed of the rotor plus some incoming free stream velocity.

$$V_{total} = V_{tip} + V\cos(\alpha) \tag{9.4}$$

The angle of attack of the rotorcraft was determined to be 9.74 degrees in forward flight with payload in Section 5.4.4. The tip speed of the main rotor was determined to be 217.8 m/s in Section 4.2.1.

The Mach number is calculated using Equation (9.5)

$$M_{total} = \frac{V_{total}}{\sqrt{\gamma RT}} \tag{9.5}$$

Since the temperature varies with altitude, a dependency is seen in Figure 9.5. The temperature is found using the international standard atmosphere relations.
Finally the maximum forward speed is obtained by combining Equation (9.4) and (9.5).

$$V_{\max} = \frac{M_{drag}\sqrt{\gamma RT} - V_{tip}}{\cos(\alpha)} \tag{9.6}$$

Both the power constraints as well as the Mach divergences boundaries of the tip are plotted in Figure 9.5. The flight envelope of the design is limited in the following way: it should remain under the red border and to the left of the blue border. It can be concluded that the maximum flight speed is limited by the drag divergence at the tip of the main rotor blade for altitudes lower than 2000 meter. Higher up, the flight envelope is completely determined by the required and available power. The absolute ceiling with payload is 2750 meter at a flight speed of 44 m/s. The maximum speed at cruise altitude of 1500 m is 71.4 m/s, which complies with the requirement on maximum speed.

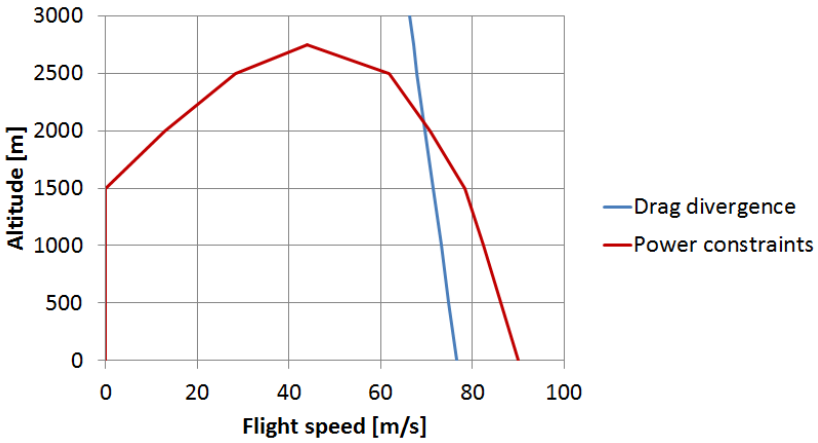

Figure 9.5: Flight envelope of fully loaded rotorcraft

10. Communication

The unmanned ducted fans require a steady stream of communication with the ground to enable safe operation. Furthermore, the twin-lift concept that LIFT^2 introduces, requires extra communication between the two rotorcraft. This chapter discusses the communication required for a safe mission completion. In Section 10.1, the general communication flow of the LIFT^2 system is discussed. Section 10.2 presents the corresponding data handling. Finally, the necessary software and hardware are discussed in Section 10.3.

10.1 Communication Flow

This section discusses the communication flow of LIFT^2 (Figure 10.1). As discussed before, the communication between the ground station and the rotorcraft, as well as the communication between the two rotorcraft in the system is important. Subsection 10.1.1 describes the link between the rotorcraft and the ground station. In Subsection 10.1.2 the communication between the two rotorcraft is discussed.

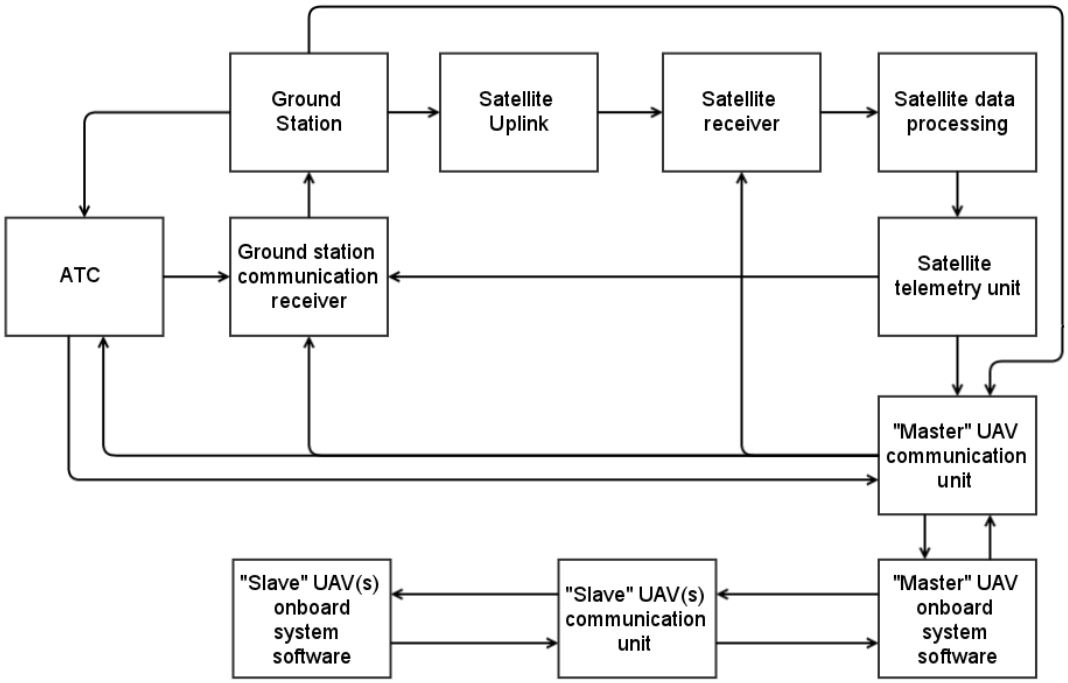

Figure 10.1: Communication flow diagram

10.1.1 Communication: Ground Station - Rotorcraft

Communication systems are composed of several elements. Figure 10.2 gives a one way (simplex) communication configuration. Figure 10.3 shows the elements of a two way (duplex) digital link. The encoder gives the data a code which is known by the receiver. The modulator modulates the signal (e.g. amplitude modulation (AM)) in order to transport it. The communication system between the ground control station and the rotorcraft consists of the subsequent types.

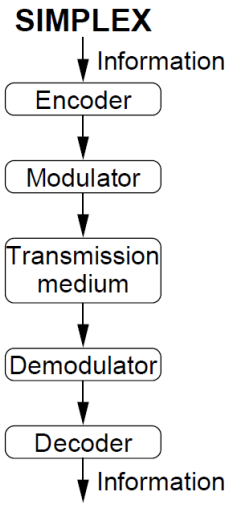

Figure 10.2: Simplex communication system [40]

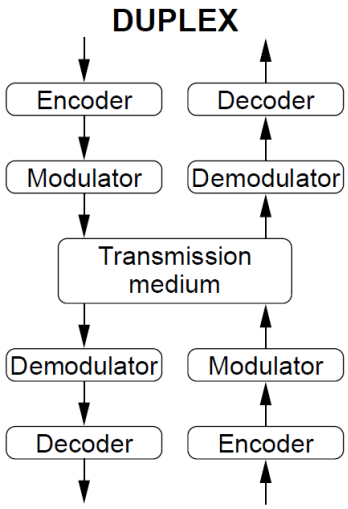

Figure 10.3: Duplex communication system [40]

Control Command and control (C2) data links are necessary when the ground crew takes over the controls from the autonomous vehicle. For this critical link a back-up is required in order to prevent loss of signal due to e.g. sudden interference of other signals. Widely spread frequencies for the original and back up signal are needed in order to have frequency diversity [35]. Most of the systems used here are duplex. The C2 link generally has a low bandwidth which is compatible with the very high frequency (vhf) and ultra high frequency (uhf) ranges for the line of sight communication and, low-bandwidth low earth orbit satellite constellations for beyond line of sight communication.

Health and Status The ground crew needs to monitor the status of the autonomous vehicle constantly. This is why there is a so called payload link which transmits the health and status of the on-board systems. In general this link is mission critical but not flight critical. The link requires a high-bandwidth connection because the data transmitted comes from e.g. video feeds [35].

Prevent Collision When the UAV operates within airspace used by other types of aerial vehicles, mid air collision is a possible risk. Every rotorcraft needs to have a transponder in order to identify itself and transmit data to avoid mid-air collisions. This data consist of information about the position of the vehicle and hence it supports airspace management [35]. When the airspace is shared with manned aircraft, communication with Air Traffic Control (ATC) is essential. There are two ways of communicating with ATC, the communication can either go from the ground station via the rotorcraft itself to the ATC or the ground control can have direct contact with ATC. The latter option has limitations with respect to terrain blockage and the Earth's curvature [35].

Antenna One of the most important hardware components of the communication system is the antenna. The antenna influences the performance and power supply of the system directly. The antenna integration must be done with care in order to optimise both aerodynamics and the antenna coverage. A very important parameter in the design of the communication system is the signal-to-noise ratio which needs to be large enough in order to receive the signal and retrieve the data from it. Another important aspect is the encryption of the signals. Hackers can try to take control of the rotorcraft or disturb the signals (jamming) which can lead to a crash. Low probability of detection and low probability of interception capabilities are therefore needed [35].

10.1.2 Communication between Rotorcraft

Besides the communication between the ground station and the rotorcraft, good communication between the two rotorcraft needs to be ensured. The UAV system will operate with the master-slave communication protocol. This is a communication model where one vehicle has the unidirectional control over all the other vehicles in the system. Here also the C-band will be used, as the distance between the rotorcraft will be small and hence the line of sight communication will always be possible [27]. The master will be programmed for the mission in autonomous operation mode, and will be directly controlled by the ground crew in other situations. In all case, the master will initiate the signals sent to the slave system.
The health and safety of the slave vehicle is safeguarded by the master rotorcraft. Also a passive link between the ground station and the slave vehicles is needed as a redundancy for the link between the master-slave configuration.

10.1.3 Methods of Communication

For both parts of the communication (i.e. ground station-R/C, R/C-R/C) two methods are available: line of sight communication and beyond line of sight communication. In this section both are explained briefly.

Line of Sight Communication

Line of sight communication is possible when the distance between the transmitter and receiver is close enough. The line of sight distance is dependant on the altitude of both the transmitter and receiver (see Figure 10.4) [35]. In order to keep track of the autonomous vehicle the ground control station needs to have the knowledge of the actual position of the rotorcraft and it needs to be able to know the future position of the vehicle in order to re-establish the link if it is lost. Furthermore mostly directional antennas are used since the pointing accuracy becomes more critical when the distance increases [35]. The C-band is used for line of sight communication because it performs well in adverse weather conditions [27].

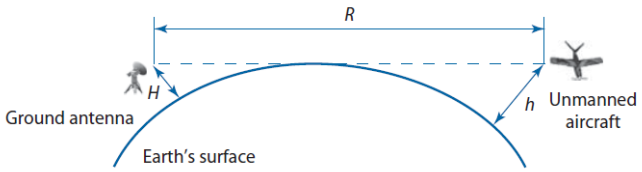

Figure 10.4: Line of sight distance [35]

Beyond Line of Sight Communication

Beyond line of sight communication is needed when line of sight communication is not possible due to obstacles or the curvature of the earth. Here, a third relay is necessary in order to transmit the signal. Usually satellites are used for this but airships or aircraft can be used as well. Figure 10.5 illustrates the beyond line of sight communication. The K_u-band (11.2 GHz-14.2 GHz) is usually used because it is less restricted in power [27]. High gain antennas are used and the high bandwidth satellites are geosynchronous (i.e. it stays on the same location above the equator).

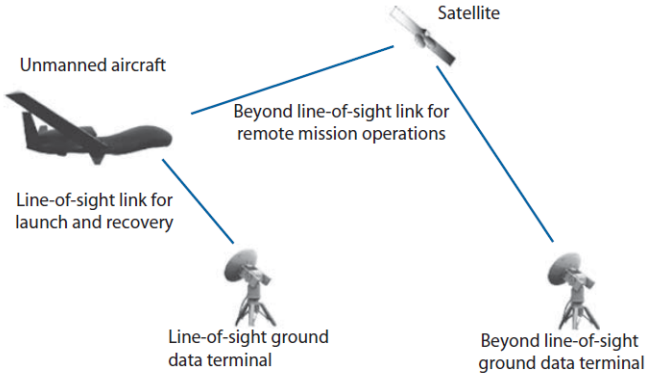

Figure 10.5: Beyond line of sight communication [35]

10.2 Data Handling

Being a system of autonomous unmanned vehicles, LIFT^2 will gather a lot of data during its mission. The system needs to be able to process this data in a fast and efficient manner. Each rotorcraft will posses a Central Processing Unit (CPU) which acts as the brain of the vehicle. This main CPU will need several watchdogs to detect and recover malfunctions. Furthermore every sub-part will have a watchdog. When data needs to be stored it is first stored on the local flash memory before transmitting it to the main memory of the rotorcraft. The main memory needs to be large enough to be able to store all the data and a backup is essential. Figure 10.6 shows the preliminary data handling flow diagram. The detailed design of this subsystem is outside the scope of this project.

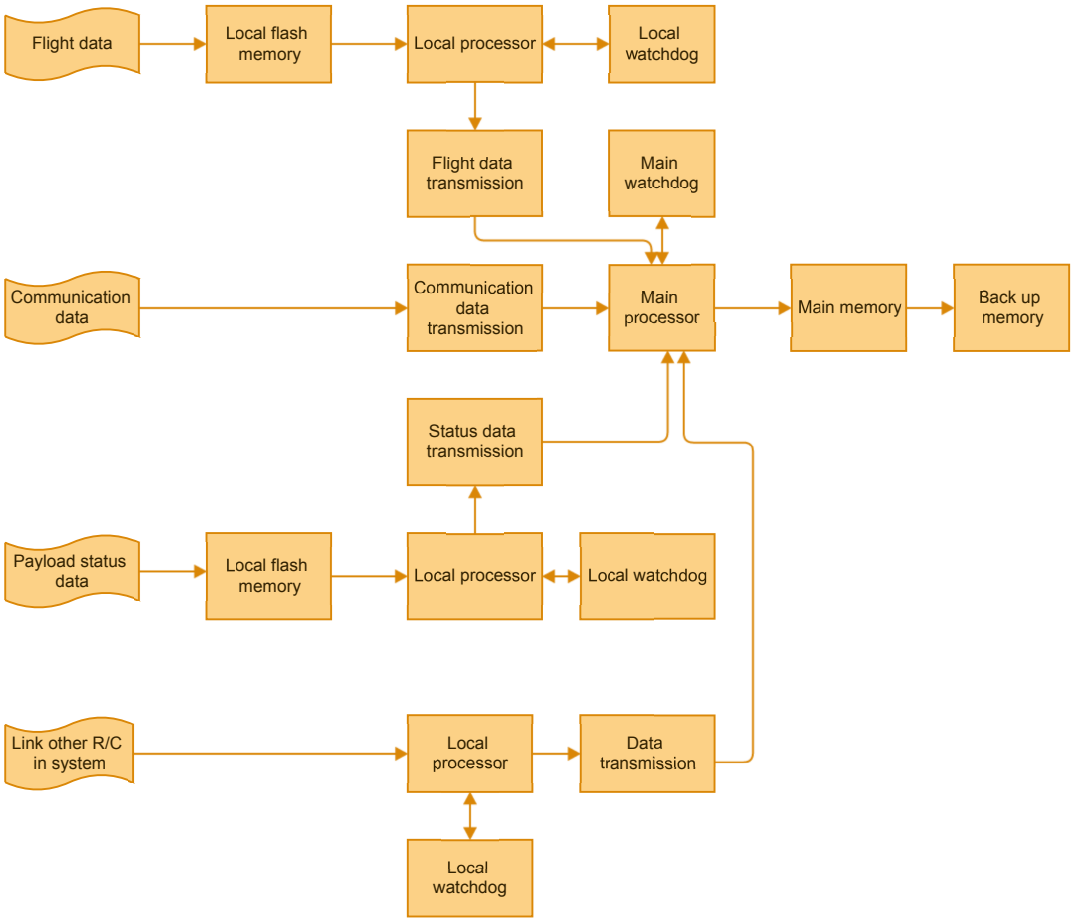

Figure 10.6: Data handling flow diagram

10.3 System Architecture

Now that an analysis of the communication flow is performed, the system architecture can be determined. The system architecture describes the general components and structures present in the system and can be decomposed in three levels. Firstly there is the complete UAV system which includes the ground station and other external components (e.g. satellites). Secondly there is the autonomous twin-lift system and lastly there is the individual rotorcraft.

In general the individual system can be subdivided into the flight critical system (VMS), which controls all the interfaces required for stable flight, and the mission critical system (MMS). The Mission Management System takes part in the general mission planning, which relates to the trajectory control. The system that controls the interrelation between the rotorcraft provides input for both VMS and MMS. The actual flight status of both rotorcraft effect the stability of the overall flight and is thus part of the flight critical systems, while the overall system status and data logging affect the mission critical system. The ground station normally only provides input for the Mission Management System, as the rotorcraft is supposed to fly autonomously. Only in case of manual override, the flight critical system is controlled by the ground station.
As explained in the previous section, the combined rotorcraft system applies a master-slave strategy. This protocol implements a single rotorcraft with all active autonomous mission management functions (i.e the master), while the other merely performs the instructions provided by the leader (i.e the slave). As a result both rotorcraft have an identical system architecture, however the mission management functions are set non active in the slave. Note that a critical part of the system is that both rotorcraft communicate individually with the control center. This is introduced as a fail safe mechanism, such that both systems are completely monitored in the ground station. Moreover this allows the control center to switch rolls of master and slave at all times. Figure 10.7 presents the global software diagram.

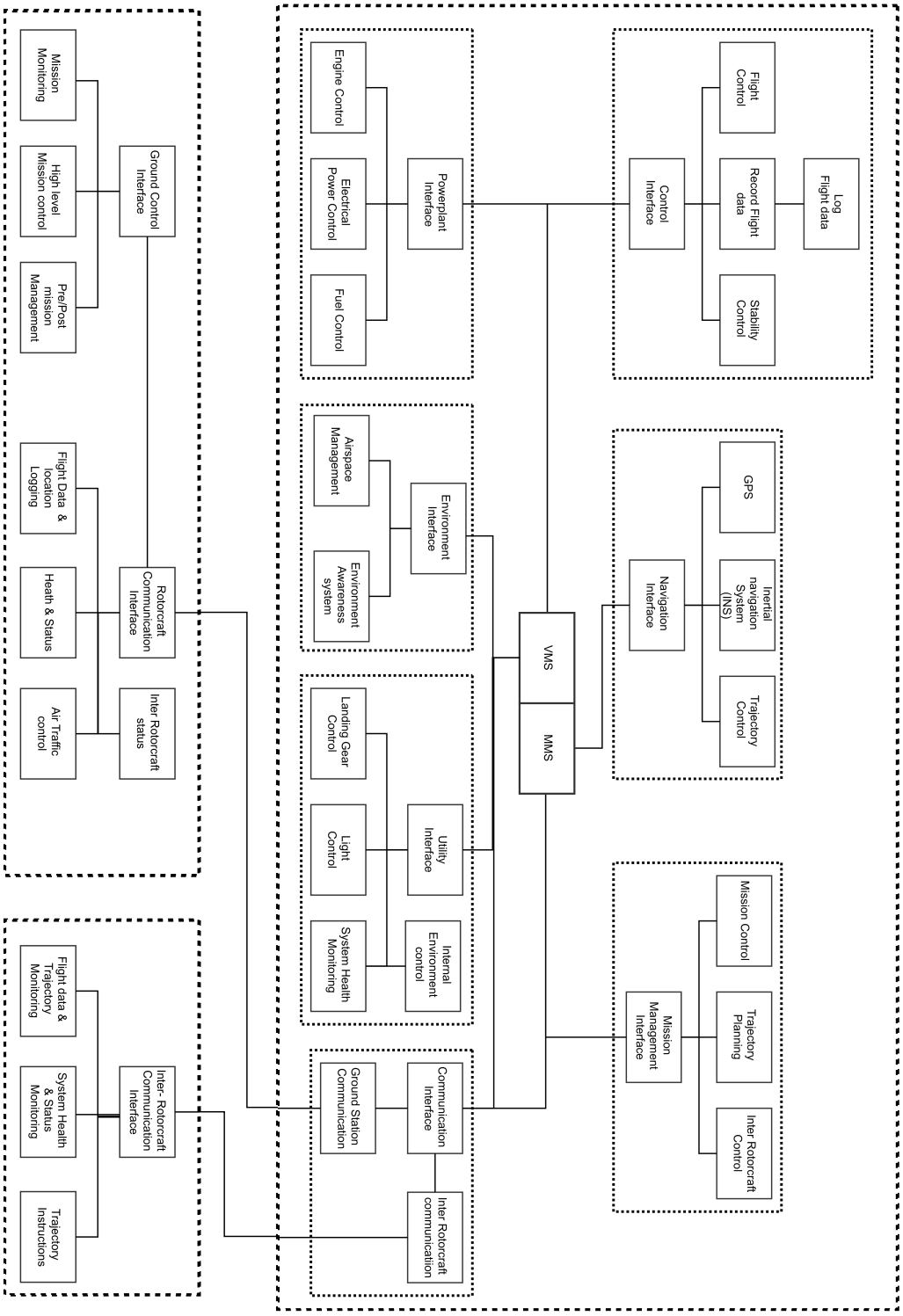

Figure 10.7: Software diagram

The hardware diagram in Figure 10.8 shows the required hardware components. The lift and control system consists of all four hubs and rotors. The power needed for the shaft and for changing the pitch of the blades is supplied by the engine. The engine also generates electricity that is stored in a battery. This battery supplies power to the wheels and the mechanism of the struts of the landing gear. The avionics consist of a communication antenna, GPS receiver, flight data recorder, video cameras, an air temperature sensor and passive detections sensors, all supplied by power from the battery. The GCT 20 QVGA+ Thermal Imaging Camera was chosen for its good capabilities and performance, it can be used in fog and in complete darkness to avoid collision [8]. The very compact size and lightweight structure make this camera very suitable for a UAV. Ultrasonic distance sensors were also considered but are not used as they are not reliable on high scale [59].

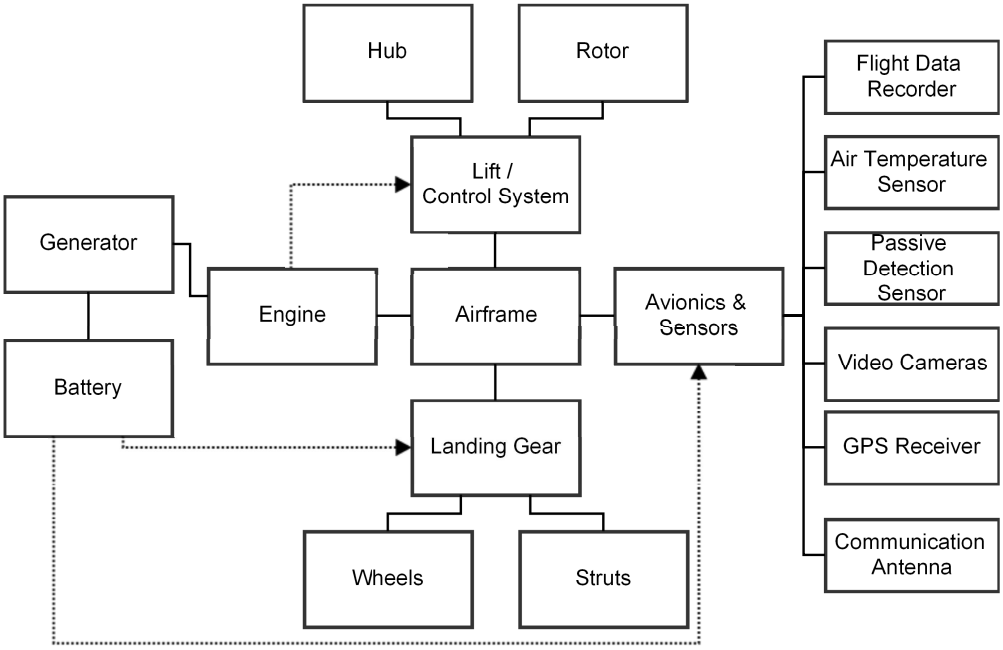

Figure 10.8: Hardware diagram

To supply the electrical power to the avionics and wheels, an electric circuit is needed as shown in Figure 10.9. Energy from the generator is stored in the battery. A programmed controller controls the electrical power to the right system.

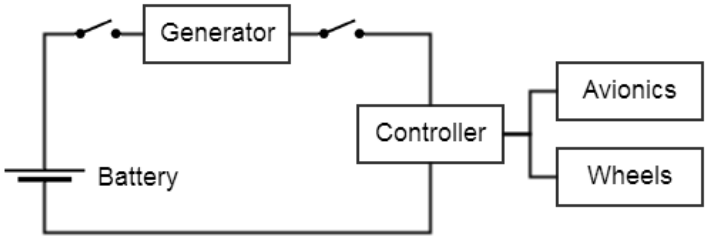

Figure 10.9: Electrical block diagram

11. Operations & Logistics

The operation and logistics aspect of the LIFT^2 system is shown in the flow diagram (Figure 11.1). Having chosen a ducted fan design, specific needs of this design are added in this report.
The dashed lines are used to indicate the location where a certain action takes place. One of those locations is the home base, where the UAV system is stored and maintained. The field base is set up at a location close to the disaster area where enough infrastructural support is available.
The dotted lines are paths that do not need to be followed but can be if the circumstances call for it. For example scheduled maintenance is performed after the return to the home base but only when there is a need for it and not after every return.
The hexagons indicate different elements involved in the operation. These are: UAV, ground station and an in-field support kit. The rectangles symbolise tasks that need to be performed to accomplish the mission. Rectangles with round corners are there to indicate the start and end of the mission.
A mission is initiated when the Red Cross makes the decision to deploy the mobile hospital. This is indicated in the flow diagram as the mission start. The equipment is then checked for damage, packed and deployed to the field base. After unpacking and checking the equipment for damage, the first drop-off can be flown. The mission is to deploy an entire hospital which consists of six containers to the disaster area. During one drop-off flight one container can be placed. After the UAVs return from the drop-off it is refuelled and checked for damage. Repairs are performed if needed with the aid of the in-field support kit. In case that this is not sufficient, additional materials will be requested from the home base and delivered. After all the containers are placed, the mission is ended and all equipment is packed and returned to the home base. At the home base the unpacking and damage checking is done. Scheduled maintenance is performed if needed and the in-field repair kit is restocked.

Requirements on the system arise from the transport of the rotorcraft and the system to the location of the mission. The payload (the portable hospitals) is transported close to the disaster area in standard size shipping containers. The UAV system has a ferry range of about 967 km, as calculated in Chapter 9 and could thus fly independently across this distance. However for deployment further away different means of transport are required. At this moment the only transport capable to bring the LIFT^2 across a large distance would be a ship with an available area of roughly two times 14.3 m by 22.3 m.
Another requirement that follows directly from the operations diagram, is a limit on the weight of the different parts. If repairs need to be performed in the field base, no heavy machinery is available. A common requirement is the two-man lift, meaning two people should be able to lift a part. The maximum part weight is then set to 150 lb (=68 kg) [35]. It is also an option to bring machinery in the field kit, so this is a trade-off that needs to be performed. Another possibility is to define certain repairs that can only be performed at the home base.
For maintenance in this case, three categories can be defined: scheduled maintenance, repair on demand and normal checks.
Scheduled maintenance is always performed at the home base. In predefined intervals certain tasks are performed.
Repair on demand should always be performed in the field base. If this is not possible it will have a heavy impact on the mission as a new UAV needs to be brought to the field base. This of course does not include repairs done during maintenance.
Regular checks are performed after transport for all parts of the system. For the UAV an additional pre-flight check before every take-off is done.

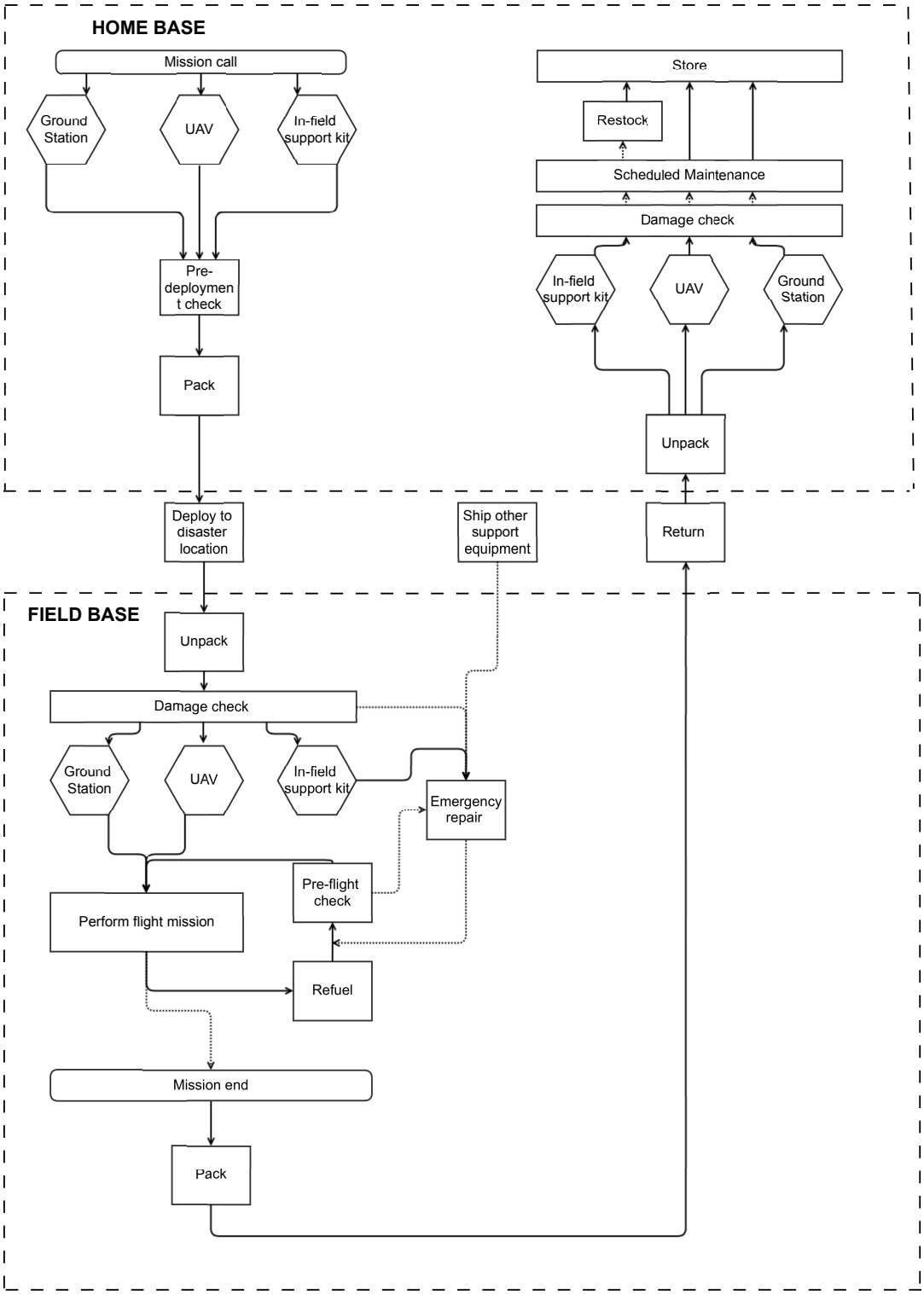

Figure 11.1: Operations and logistics flow diagram

12. Risk Analysis

This chapter involves a risk analysis of the proposed twin-lift system with ducted fan rotorcraft. Risk is a measure of uncertainty of attaining a requirement. In a project, risk can never be removed completely, but it can be made negligible. Therefore, the associated risk of a project is a very important criteria in the design process. In Section 12.1, the definition of risk is introduced. Afterwards, the risk map for the twin-lift system is presented in Section 12.2.

12.1 Risk definition

Risk has a big influence in all three sectors of the design project. Technical performance, schedule and cost are interconnected through risk. This interdependency is the reason why risk will never be removed completely. When very high technical goals are set to reduce the technical risk, the cost and schedule risk will be increased. Decreasing the risk of one of the sectors will result in an increased risk in the other sectors. A proper balance between the different disciplines needs to be found in order to make the risk acceptable.

Risk is defined as the product of the likelihood and the consequence of an event. Identification of potential risks is the first step in a proper risk assessment. Next, the likelihood and the consequence of a failure of these parts are assessed. Table 12.1 ranks the likelihood and consequence qualitatively and quantitatively by order of severance. In the next section a risk map is formed for the chosen design concept.

Table 12.1: Description and weighting of likelihood & consequence

Weight	Likelihood	Description
1	Proven flight design	The concept is used many times in various flight systems
2	Extrapolated from exisiting flight design	The concept has been used for some typical aerial vehicles
3	Based on existing non-flight engineering	The concept is used in non-aeronautical related systems
4	Working lab model	Labratory research has had small scale success on the concept
5	Feasible in theory	Theoretical theory shows that the concept should work

Weight	Consequence	Description
1	Neglible	Inconvenience or non-operational impact
2	Marginal	Degradation of secondary mission elements or small reduction of technical performance
3	Critical	Mission success is questionable or considerable reduction in performance
4	Catastrophic	Mission failure or significant non-achievement of performance

12.2 Risk map

Now that the method is defined, a risk map can be developed. A risk map is used to visualise the possible risk of a design. In the map, the consequence of an event is placed on the horizontal axis and the likelihood of that event on the vertical axis.
For the twin-lift system with two ducted fan rotorcraft, the following parts can be subjected to a risk:

1. Main rotor
2. Horizontal fenestrons
3. Vertical fenestron
4. Fuselage
5. Stability control system individual rotorcraft
6. Stability control system complete concept
7. Communication link
8. Data link
9. Cost

Since the ducted fan concept is a very innovative design, the development and operation brings along extra risks compared to conventional helicopters. The *main rotor* design is extrapolated from existing flight data so the probability of failure is limited. However, failure of the main rotor results in a catastrophic event.
The *vertical fenestron* is a concept that is already used on conventional helicopters, which decreases the probability of failure but the consequence of tail failure is again catastrophic, making yaw control impossible in case of a failure. The

horizontal fenestrons that are used to control pitch and roll motion have a higher probability of failure, since this it is a new concept to use the fenestrons horizontally. Failure of these fenestrons however still results in a catastrophic situation in which the separate rotorcraft become uncontrollable in pitch and roll direction.
One of the main advantages of the ducted fan concept in a twin-lift configuration is the encasing of its main rotor by the *fuselage*. Although the probability of fuselage failure is higher due to the infancy of the design, the results of failure will be less catastrophic. In case of a mid air collision, the encasing also prevents a catastrophic disaster since the blades of the two rotorcraft would not be able to collide.
The *stability control system* of both the individual rotorcraft and the entire system comes with higher probability of failure since it has not been a proven flight design. The rotorcraft and the system are inherently unstable so a failure of these systems would result in a catastrophic event.
As soon as the *communication and data link* between the two rotorcraft is lost, a catastrophic situation could occur. However, since this has already worked for existing flights, these links are less likely to fail.
Finally, the *cost* of the twin-lift system also comes with a certain risk. Although an unexpected raise in cost is not catastrophic, there is a critical consequence to an increase in cost. Eventually the system needs to be profitable, which is why the cost is not negligible. Since the concept is completely new, the cost are only extrapolated from existing flights and the probability that the cost increases is not eliminated completely.

The risk map of the design concept is presented in Table 12.2. A subsystem with a negligible consequence and a low probability results in a low risk, indicated in green in the table. Events with a high consequence and a high probability come with a high risk, placing the events in the corner indicated in red. In later design stages, a risk mitigation plan should be addressed to decrease the probability of occurrence and the consequences of failure. In this way, unacceptable risks should be eliminated. The ultimate goal of the risk mitigation is to get all subsystems to the lower left hand corner.

Table 12.2: Risk map

		Consequence			
		Negligible	**Marginal**	**Critical**	**Catastrophic**
Likelihood	**Feasible in theory**		Fuselage		
	Working laboratory model				
	Based on non-flight engineering				Horizontal fenestrons Control systems
	Extrapolated from existing flight			Cost	Main rotor Vertical fenestron Communication link Data link
	Proven flight design				

13. RAMS Analysis

The reliability, availability, maintainability and safety of the $LIFT^2$ is analysed in this chapter. Firstly in Section 13.1 the general fault tree is considered for events leading to a loss of the airframe. Secondly the redundancy philosophy which will be applied is elaborated in Section 13.2. Finally a basic prediction of the reliability and availability is made in Section 13.3.

13.1 Fault Tree Analysis

To analyse the failure possibilities during flight a fault tree is made, shown in Figure 13.1. This specific fault tree shows the general safety hazards which could occur during flight of a conventional rotorcraft. The tree is kept at a basic level to correspond to the simplicity of the current design stage. This section discusses the possible events leading to loss of the ducted fan rotorcraft during flight, and details possible discrepancies between the various configurations conceived in this project stage.

13.1.1 The Conventional Fault Tree

Figure 13.1 details the possible occurrence of critical events leading to the loss of the ducted fan rotorcraft during flight. Redundancy in the tree is kept at level two (meaning two duplicate systems or subparts), though this is just for indicative purposes as the actual level can vary. Events in the tree are triggered by the AND or OR gates of the previous level. The first level of failures is seen as catastrophic and any of them being triggered will result in loss of the rotorcraft, as indicated by the OR gate in the diagram. These events are indicated as F1 to F6, subdivided into subparts. Due to readability of the diagram only the first level events have been numbered along with the subparts of the first event as an example. The main events will now be discussed in the following list:

F1 **Power system failure:**

- F1.1 Engine failure: a single engine loss will not result in the immediate loss of the ducted fan rotorcraft. However the payload should be dropped as safe and soon as possible, such that the ducted fan rotorcraft can return to base safely or land with the payload. If both the port and starboard engine fail the ducted fan rotorcraft will not be capable to recover and this incident might result into a crash.
- F1.2 Fuel system failure: A critical failure will result in the engines shutting down and an eventual possible loss of the ducted fan rotorcraft. There are two main categories in the fuel system failure. Firstly faults arising in the fuel tank, such as leakage or rupture, which could result in fire or explosion. Secondly there could be issues with the fuel supply system (pumps, fuel lines, etc...) with the same possible consequences.
- F1.3 Electrical system failure: the electrical system is the lifeline of the electronic hardware and electric actuators on-board of the rotorcraft. With the ducted fan rotorcraft being completely unmanned a total loss of the electrical systems will result in catastrophic failure. Therefore the system has a redundancy included to avert this failure.
- F1.4 Other

F2 **Control system failure:**

- F2.1 Actuator failure: actuators are used throughout the ducted fan rotorcraft to deflect control surfaces (to change the blade pitch). The loss of one actuator will not be fatal, however the loss of the whole actuator system (electrical or hydraulic) would be.
- F2.2 Sensor failure: the data recorded by the flight sensors is vital to perform the mission, one sensor failing should not result in the loss of the ducted fan rotorcraft. Therefore, there is a redundancy in the sensor system. However, should this system fail, the ducted fan rotorcraft will be flying 'blind' with no data coming in to aid its control (e.g. AF447 crash [6]).
- F2.3 Other

F3 **Communication and data handling failure:**

- F3.1 Locator failure: if the location devices fail, the system will not be able to perform its mission. However, ground control can take over and continue or let the ducted fan rotorcraft return to base using visual guidance. This failure is only critical when it is combined with a failure of the communication system.
- F3.2 Communication system failure: the communication between the base and ducted fan rotorcraft can be interrupted by failures on both sides. If this happens the ducted fan rotorcraft can find a safe deployment zone for the payload and return to the base. This failure is critical only when it is combined with the locator

failure. If this happens the system will not be able to position itself and it will not be able to return to the base. A solution to this is the emergency protocol in which the ducted fan rotorcraft will immediately land in case of both failures.

F3.3 Data handling failure: should the ducted fan rotorcraft be unable to process the commands coming in from the base or the data it receives from the sensors, it will not be able to continue safe flight. This would have immediate consequences on the control of the ducted fan rotorcraft related to the severity of the failure. However a redundancy is projected in the on-board computers to counter the occurrence.

F3.4 Other

F4 **Main rotor failure:**

F4.1 Rotor blockage: would immediately result in loss of the ducted fan rotorcraft.

F4.2 Structural failure: structural failure of the main rotor would result in an immediate loss of the ducted fan rotorcraft. The main cause of these failures is fatigue [9] in one of the following elements: the blades, flapping hinges or the drive-train. The second cause is damage by striking or being struck by an external object. Although a strike of an external object with the ducted fan rotorcraft is less catastrophic than it would be with a normal helicopter since there is a duct around the main rotor, this could still result in a crash. Any structural failure that would stop the main rotor turning will result in a crash since the ducted fan rotorcraft is incapable of autorotation.

F4.3 Other

F5 **Tail rotor failure:**

F5.1 Roll rotor failure: the two horizontal tail rotors provide roll and pitching moment. If one should fail following a similar failure as described with the main rotor events roll and pitch control might be lost. This loss would result in a catastrophic event.

F5.2 Vertical rotor failure: the vertical tail rotor provides yaw control. Failure of this rotor would result in the whole rotorcraft starting to spin around its axis followed eventually by a crash.

F6 **Structural failure:**

F6.1 Fuselage failure: a failure related to the structural integrity could result in severe damage to vital systems of the ducted fan rotorcraft or even to complete disintegration of the structure. Obviously this would lead to quite dangerous or even catastrophic events.

F6.2 Landing gear failure: a failure of the landing gear combined with a hard landing could severely damage the ducted fan rotorcraft, possibly creating unrepairable damage.

F6.3 Other: the fuselage is a combination of many structural elements maintaining the rigidity of the ducted fan rotorcraft. If they would fail to keep up this task the ducted fan rotorcraft might sustain heavy damage.

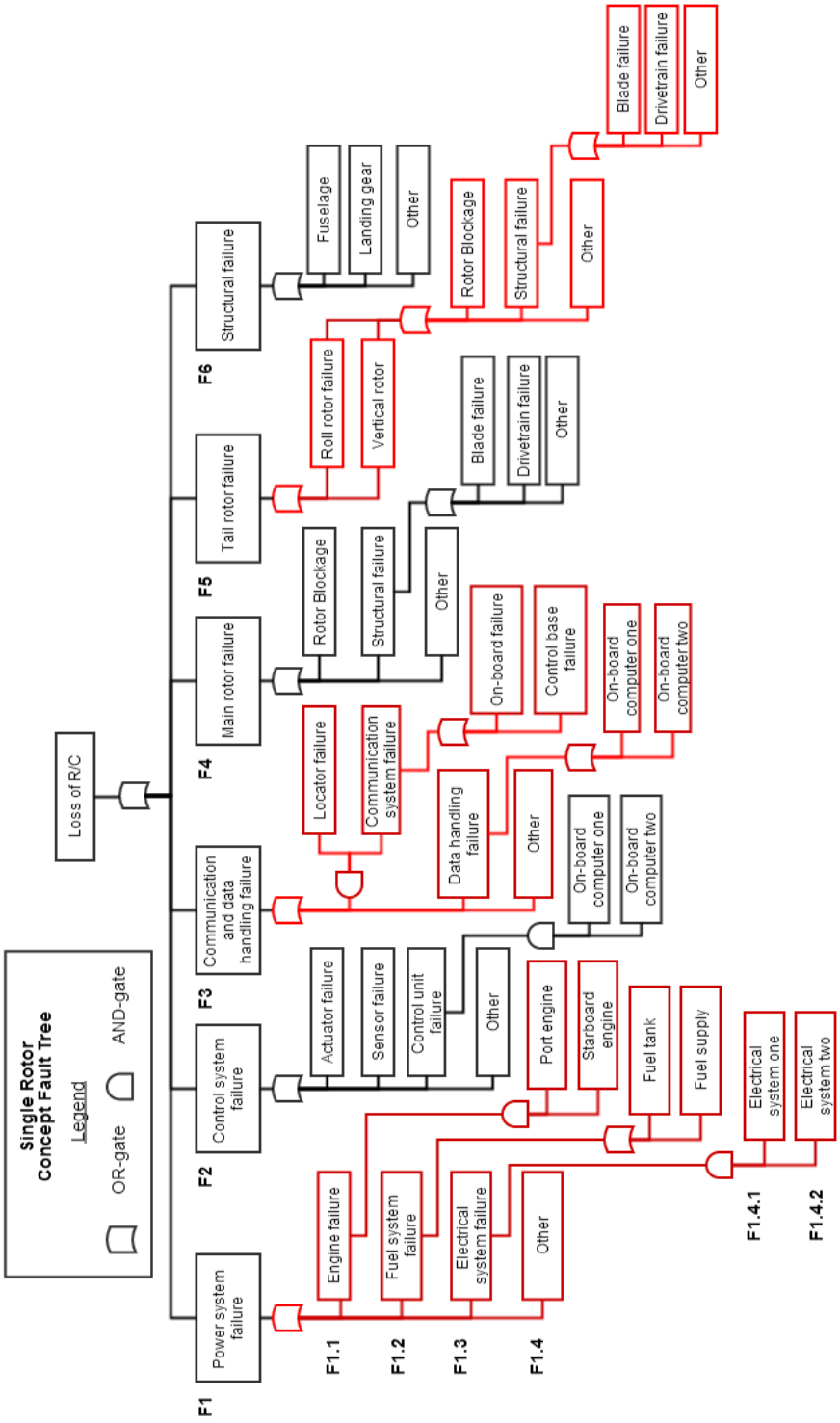

Figure 13.1: The general fault tree for a conventional rotorcraft during flight.

13.1.2 Applicability Twin-Lift Configuration

The fault tree in Figure 13.1 applies to a single ducted fan rotorcraft but can also apply to the LIFT^2 system taking into account some considerations. Firstly the communication of the master-slave protocol will be crucial for a good execution of the mission. For this the command & data handling systems will be extremely important in correspondence with the observation and communication systems. Secondly structural failure of the spreader bar, slings and container that leads

to a mission failure should be considered. Finally if one ducted fan rotorcraft fails the mission will be aborted. That is when the second rotorcraft manages to detach itself from the system instead of being dragged down with the other.

13.2 Redundancy Design Philosophy

In Section 13.1 the global redundancy level was assumed to be two to simplify the fault tree. However a redundancy of two can not be considered as safe. This section explains the redundancy philosophy which will be applied on the LIFT^2 rotorcraft. It is based on the work of Kenneth H. Eagle and Ajay S. Agarwala at Boeing Helicopters, published in the Annual Reliability and Maintainability Symposium proceedings of 1992 [17].

The redundancy philosophy, which will be applied is the technique called 'Brick Wall'. Boeing Helicopters use four design objectives to achieve helicopter flight safety, which will also be used in this design for flight critical electronics:

- When a component's flight safety is inherently critical (e.g. rotor blades, transmission), the component shall have a failure expectation of less than one failure in the life of the fleet.
- In all other cases, no single failure shall cause a catastrophic (flight safety) loss.
- The system must stay operative after any two failures.
- Whenever a subsequent failure could cause a loss of safety, a mission abort is required.

Since not every element of the flight control system is critical, the system is divided into two parts. Firstly the Automatic Flight Control System (AFCS), compromising the bulk of the hardware and containing all functions not affecting flight safety. Secondly the Primary Flight Control System (PFCS), which only contain those functions and components which are critical. The brick wall redundancy architecture is shown in Figure 13.2, providing a system with three leg redundancy. Each leg is capable of analysing itself and taking itself offline if its health is compromised. Within each leg there are two redundant PFCS units to compare the outputs. When they are different the whole leg is shut down. This results in a three on three redundancy for the whole system. However each PFCS unit requires six separate sources of input, while the AFCS units require only three. On the output side there are three separate signals.

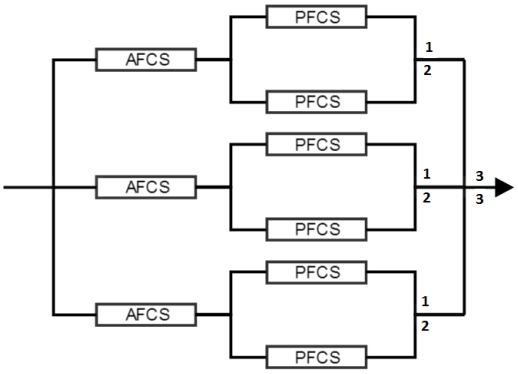

Figure 13.2: Brick wall redundancy architecture for the flight control system.

It is worth mentioning that the triple redundancy does not account for common-cause failure modes such as a lightning strike affecting all three legs. The advantages and disadvantages of the system are briefly discussed below:

- **Advantages:**
  - True triple redundancy is offered by the system in the sense that the mission does not have to be aborted in the case of a single failure.
  - Hidden failures do not influence the workings as each leg will be shut down individually if a discrepancy in the output of its two PFCS units is shown.
  - The numerical reliability of the system is considerably improved in comparison to a two out of three voting redundancy system.
  - The architecture is able to comply with the Boeing Helicopters safety design objectives, while the conventional designs (e.g. duplex redundancy, two out of three voters) cannot.
- **Disadvantages:**
  - Redundancies comprise a multiple of parts more than their single unit counterparts. This increases the maintenance rate of the system.

- The cost and weight of the design are higher than the two out of three voter, but cheaper than a system with quad AFCS and PFCS voters.
- It is as susceptible to common cause failures as other methods.
- It requires an increased amount of sensors feeding the PFCS with data.

13.3 Reliability and Availability Prediction

This section will give a prediction of the reliability and availability of the unmanned aerial system. It is chosen to give this prediction based on the UAV reliability study done by the United States Office of the Secretary of Defence in 2003 [62]. This study focusses on military drones such as the Predator. However it was still chosen to compare to this study as these systems consist of roughly the same categories of subsystems (e.g. the communication system will be similar).

13.3.1 Expected Reliability

The average sources of system failures for the U.S. military UAV fleet is given in Figure 13.3a. The projections seen in the diagram are based on 100,000 flight hours. Figure 13.3b shows the distribution of failures for the Israeli Defence Forces. These UAVs are mostly manufactured by Israeli Aircraft Industries (IAI). The data provided by IAI spans twenty five years of experience. From the data it can be seen that the propulsion and flight control subsystems account for the majority of the system failures. Having a cumulative share of 60% to 63% of all failures and the highest effect on reliability.

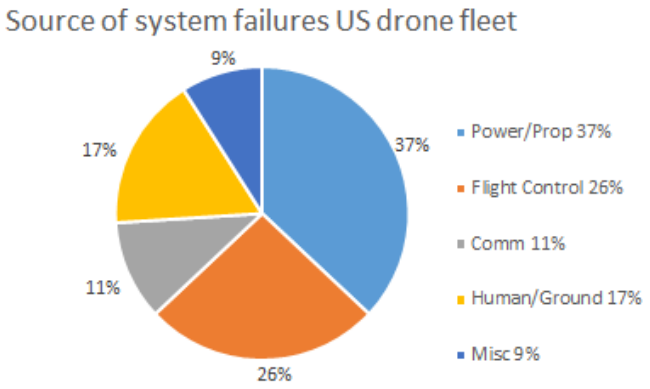

(a) US military UAV fleet

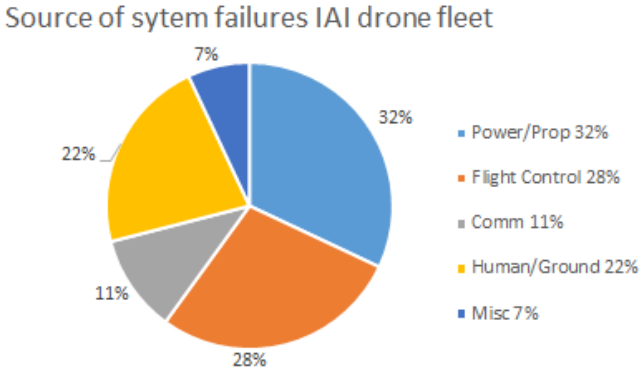

(b) IAI UAV fleet

Figure 13.3: Distribution of system failure sources based on 100,000 flight hours [62].

Reliability however is not constant throughout the lifetime of the vehicles, following the so called bathtub-curve. As the design is in its infancy, it will suffer from early reliability issues until the product matures. Nearing its end of life the reliability will start to decrease again. The increasing reliability of the U.S. fleet is shown in Figure 13.4. It is expected that the LIFT^2 rotorcraft will follow a similar process during its life starting at a reliability somewhere between 70% and 80%, since UAVs are still in a new area of research with the propulsion and communication subsystem being most critical.

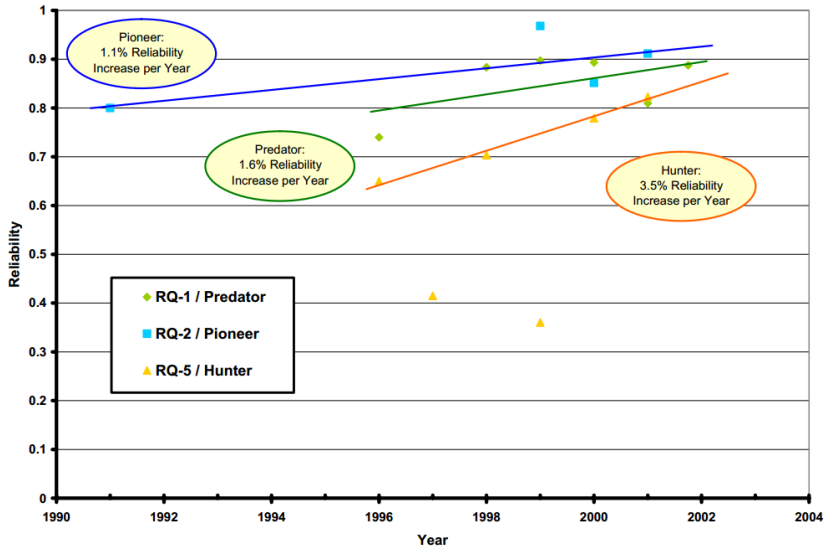

Figure 13.4: Reliability of the U.S. UAV fleet [62].

13.3.2 Expected Availability

Reliability is closely related to availability. Availability is the measure indicating the percentage of time a system is operational versus the scheduled time. Figure 13.5 shows the availability for the U.S. UAV systems. A similar conclusion as for reliability can be made: The availability will increase as the system matures. However there is a big discrepancy between the systems. Similar behaviour is expected from the LIFT^2 system, starting at an availability of at least 75% ending up eventually with at least 90%.

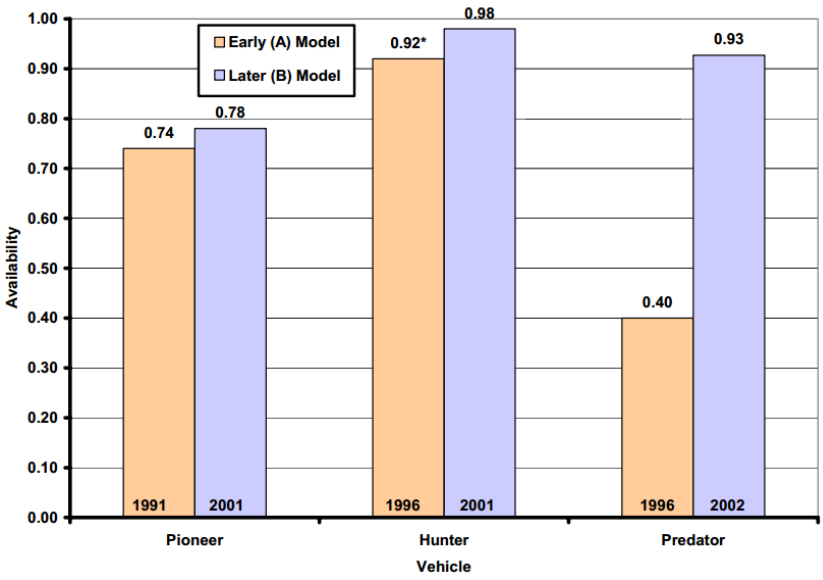

Figure 13.5: Availability for the U.S. UAV fleet [62].

13.3.3 Applicability to LIFT^2

A ducted fan has not been applied before on such scale other than test vehicles. It is expected therefore that there will be a considerable amount of infancy problems in this design, affecting reliability and availability. However, in short-term these problems will be resolved and the reliability of the system will increase.

13.3.4 Maintainability

To assure maintainability the design will need to take into account easy access for maintenance crew and use components which are relatively easy to come by. The first can be achieved by placing maintenance hatches near maintenance prone locations. The second objective can be accomplished by using common used components and off-the-shelve items such that a replacement part is easily found. The scheduled and unscheduled maintenance is bounded by the EASA CS 29.1529 Instructions for Continued airworthiness superseding the decisions of the ICAO convention ANNEX 8 'Airworthiness of

Aircraft'.[19]

The objective of a maintenance program is to ensure the inherent safety and reliability levels of the system, as well as restoring it when deterioration has occurred. At the same time, the goal is to accomplish these goals at minimum cost. This is done by using the Maintenance Review Board process (MRB) to create a maintenance program for scheduled and unscheduled maintenance of the system. The MRB process is shown in Figure 13.6. During the type certification the Maintenance Review Board process is started by creating a board consisting of authorities, manufacturers and customers. This board will come up with a maintenance program based on evaluation methods such as the MSG-3, which evaluates Maintenance Significant Items (MSI). In this case the MSI would for example be the software, airframe and propulsion subsystems.

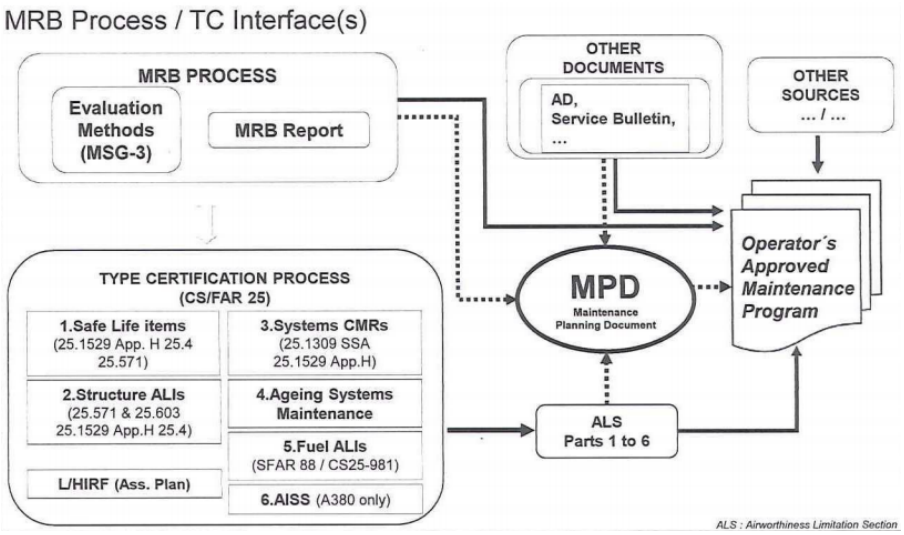

Figure 13.6: The Maintenance Review Board process used in the aviation industry to create a maintenance program [33].

14. Sustainability

Three types of sustainability can be defined: environmental, social and economic sustainability. Environmental sustainability is mainly determined by the emission of hazardous gasses into the atmosphere, which will be elaborated on in Section 14.1.2. The social sustainability comes from the effect the rotorcraft has on surrounding people. The main component of this sustainability is the noise, described in Section 14.2.1. The cost per mission is the main factor influencing the economic sustainability of the design. This is therefore elaborated on in Chapter 15.

14.1 Environmental Sustainability

The environmental sustainability of the design can be described as the amount of renewable resources used by the design, when it is in service. This involves the selection of a specific type of engine and fuel, which is elaborated on in Section 14.1.1. During the design process two T700-GE-701 engines were already selected. This section explains why they were the best option. Section 14.1.2 elaborates on the particles emitted during a full mission.

14.1.1 Renewable Resources

Renewable sources play an important factor in the design of aerial vehicles. A very good solution would be to create a fully electric vehicle. Engines exist to create the high power required by heavy rotorcraft, however, these engines are large and heavy and require an extreme amount of batteries. Furthermore, after flying the mission profile once, these batteries would need too much time to recharge before starting a new mission. Replaceable batteries could solve the latter, but the required space for the batteries is too high to realise.
Fuel cells are not a possibility either, since the power output is too small. Only very small helicopters have been flown on fuel cells, but they did require less than 10 kW of power [64]. Ammonia is another renewable source as it can be made from nitrogen, taken from the atmosphere, and hydrogen. This alternative fuel can be used in existing rotorcraft engines with minor modifications. Although the combustion of ammonia does not emit greenhouse gases, the production of ammonia does. Also, the fuel consumption is three times higher and is not safe for humans as the vapour is life threatening. Ammonia therefore will not be used [38]. UOP LLC, a Honeywell company, has developed a bio fuel which is a perfect alternative for the JP-8 jet fuel. Helicopters have already flown on the Bio-Synthetic Paraffinic Kerosene (Bio-SPK) without modifying the engines [52]. This renewable fuel would be an ideal solution for a helicopter. However, one full fuel tank would already require an area of $3m^2$ to grow plants. This means that too much space would be needed to call bio fuel a sustainable source of energy [57].
Since all these alternative options are not deemed to be feasible regular A-1 fuel will be used for this design.

14.1.2 Emission

The emission of the rotorcraft is expressed as the amount of several types of particles emitted into the atmosphere. To determine this, the statistical method described by Theo Rindlisbacher is used [72]. The emission in kg per mission segment is calculated using Equation (14.1), which uses the fuel weight per mission segment, which was calculated in Section 4.1.2 as input.

$$W_{particles} = 2W_{fuel}EI_{particle} \tag{14.1}$$

The factor two accounts for the fact that two rotorcraft are used to transport the payload. Four types of particles are investigated: nitrogen oxide (NO_x), hydrocarbons (HC), carbon monoxide (CO) and non-volatile particles (PM). The emission factor EI of each particle is calculated using Equation (14.2) until (14.5), where the required power per mission segment is determined in Section 4.2 and should be entered in horsepower. This required power has been divided by two since only one engine is considered. The second engine is taken into account by inputting the complete fuel weight into Equation (14.1).

$$EI_{NO_x} = 0.2113 \cdot P_{req}^{0.5677} \tag{14.2}$$

$$EI_{HC} = 3819 \cdot P_{req}^{-1.0801} \tag{14.3}$$

$$EI_{CO} = 5660 \cdot P_{req}^{-1.11} \tag{14.4}$$

$$EI_{PM} = -4.8 \cdot 10^{-8} P_{req}^2 + 2.3664 \cdot 10^{-4} P_{req} + 0.1056 \tag{14.5}$$

The resulting emission factors and emitted particle weights per mission segment are compiled in Table 14.1. The total fuel weight in this table does not include the 5% reserve fuel that was taken into account in Section 4.1.2.

Table 14.1: Particle emission of two rotorcraft

Segment	P_{req} [Hp]	EI_{NO_x} [g/kg]	EI_{HC} [g/kg]	EI_{CO} [g/kg]	EI_{PM} [g/kg]	W_{fuel} [kg]	WNO_x [g]	W_{HC} [g]	W_{CO} [g]	W_{PM} [g]
Hover 1	515	5.83	6.93	8.62	0.19	24.22	141	168	209	4.68
Cruise 1	1271	9.74	2.61	3.16	0.34	484.21	4716	1264	1531	166
Hover 2	1652	11.30	1.97	2.36	0.43	38.87	439	76.4	91.9	17
Hover 3	1652	11.30	1.97	2.36	0.43	77.73	879	153	184	33
Cruise 2	478	5.59	7.51	9.36	0.19	177.16	990	1330	1658	33
Hover 4	515	5.83	6.93	8.62	0.19	12.11	70.6	83.9	104	2.34
Total							7237	3074	3778	255

From this table it can be concluded that during the mission 7.237 kg of nitrogen oxide, 3.074 kg of hydrocarbons, 3.778 kg of carbon monoxide and 0.255 kg of non-volatile particles are emitted.

14.2 Social Sustainability

Social sustainability is obtained by creating a helicopter that is liveable and healthy for the people. The emission calculated in the previous section can therefore also be seen as part of the social sustainability. The most important factor in the social sustainability is the noise produced by the rotorcraft elaborated on the next section. Furthermore, the help the system will deliver to those in need, is explained as part of sustainability.

14.2.1 Noise

Noise is the main factor influencing the social sustainability of LIFT^2. Noise can be defined as sound, which is perceived as annoying to surrounding people. The noise produced by the rotorcraft can generally be divided in four sections: the rotational noise of the rotor blades, the rotor vortex noise and fan [53].

The rotational noise of the rotorcraft is mainly determined by the the speed of the rotors. In general, tip speeds higher than 750 ft/s are assumed to lead to unacceptable noise levels. Both the main rotor and all tail rotors stay within this tip speed boundary.

The vortex noise of the rotorcraft also depends on the speed of the blades and the area of the blades [53]. The tip speed was determined to be within acceptable bounds of 750 ft/s. The area of the blades can be expressed in terms of blade solidity. The blade solidity of the main rotor and the horizontal tail rotor of 0.118 and the vertical tail rotor of 0.5 is considerably higher than for conventional rotorcraft and tail rotors [65]. Therefore the vortex noise of this system is lower than that of conventional rotorcraft.

The fan noise is defined as the noise produced by the lifting part of the shroud. It is mainly determined by the mass flow moving through the duct. Generally this noise is low when compared to the rotational and vortex noise [53].

From this initial noise analysis the main conclusion to be drawn is that the concept stays within noise limits regarding to rotational and vortex noise. Furthermore, the use of ducts around the rotors reduces the noise perceived by the public. Since the rotorcraft are to be used in disaster areas, noise is not a driving requirement. It should, however, be further investigated during detailed design in the future.

14.2.2 Help In Disaster Areas

The main goal of LIFT^2 is to bring medical assistance to people. More lives will be saved when Hospitainer units can be transported fast to the disaster areas. This factor aids to the social sustainability of the system. The fact that the system will be operating in harsh environments will also lower the necessity of a quiet system. In disaster areas, those in need of help might not care too much about the produced noise as long as their medical attention arrives in time.

15. Cost Analysis

An aerial vehicle in general passes through four different phases during its life cycle: design, production, operation and disposal. Associated with each phase is a net cost value. LIFT^2 only produces revenue in the operational stage, while all the other stages require investments. In addition, cost of the different life cycle stages (i.e. the program cost) need to account for the pre acquisition cost.
This chapter starts with a general chapter on cost analysis in which standards are set and safety factors are defined for this cost analysis. In the subsequent sections each cost segment mentioned earlier is analysed in more detail. The chapter is then concluded with a prediction for the return of investments for LIFT^2. A tabular overview of all cost contributions can be found in Appendix D.

15.1 General

The cost analysis presented here generally follows the suggestion from Gundlach [35] but where deemed appropriate, some adaptations are made. As the reference suggests some cost estimation relations are based on dollars, hence the entire cost estimation is done in US dollars and afterwards converted to Euro. The estimation is based on the 2013 value of the currency as for the current year the average consumer price index is not available yet.
For a first estimation of the labour cost it is assumed that the entire work process from design to production is carried out in the Netherlands. In a later stage it might prove beneficial to outsource labour to other countries.

Labour cost (C) depends on the amount of labour (Hr) and the labour price (R) (Equation (15.1)).

$$C = Hr * R \tag{15.1}$$

The cost of labour today is higher than just the hourly pay of the worker. Medical insurance and paid vacation increase the actual cost for the employer. This is summarised in the fringe factor in Equation (15.2). In addition there are facility and administrative costs associated with having employees which is accounted for in the overhead factor. Accounting and other general cost will increase the effective labour cost as well.

$$R = R_{basic} * (1 + Fringe) * (1 + Overhead) * (1 + G\&A) \tag{15.2}$$

For materials the procurement cost are higher than just the material price. Again this is accounted for by a factor.

$$Cost_{procured} = Cost_{basic} * (1 + G\&A) \tag{15.3}$$

All those factors vary among companies and countries. For now it is assumed that all the work is performed in the Netherlands. The factors then are assumed to be $Fringe = 0.35$, $Overhead = 0.3$ and $General\&Accounting = 0.1$. The values are picked with engineering judgement after investigating the range.[35]
To simplify the cost analysis it is assumed that only two salary brackets exist, one for engineering and technicians. The average annual salary of an engineer in the Netherlands is estimated to be 106,000$ and for technicians it is estimated to be 39,000$ [78]. The amount of working days in a year is approximated to be 250 and the working hours per day to be 8. With this information the hourly basic labour rate is determined.
To the estimated working hours a so called raw labour reserve is applied. This accounts for unexpected events such as sick leave. This factor is set to π in accordance with the suggestion in Gundlach [35].
In addition to these factors, two other factors are applied to the overall cost: the realism factor and the management reserve. The realism factor is used to account for the unknowns in the project(e.g. human mistakes, defective materials). Gundlach suggests a realism factor in the range of 2-3[35]. For this case 2.5 is selected. The management reserve is used to account for factors that go beyond the scope of the project (e.g. sudden increase in material cost). It is applied to labour and materials and can be removed as soon as contracts have been made. In this case 1.2 is selected based on engineering judgement.

15.2 Pre-acquisition Cost

Before the actual design phase starts the design goals need to be determined. Generally the idea for a new project is either based on a need or a seed. A need is a market demand for a certain service or commodity, whereas a seed is a new discovery or advancement in science or technology. For this project both factors play a role although it is mainly based on seed. Hospitainer has a need to transport the hospital container but since this is already possible with existing heavy lift-helicopters it is not a general market need. The seed in this case can be defined as the recent improvements in autopilots and rotorcraft technology.

A market analysis gives insight into potential market niches, which the system under consideration could fill. It

aids in identifying possible stakeholders and their requirement on the system. Then a list of requirements can be made to constrain the design space. Performing the market analysis and identifying the requirements are two closely interlinked processes. The market analysis might discover requirements on the system or it can be used to confirm already existing requirements. For a more detailed market analysis please refer to Chapter 3.

If the idea is deemed profitable after this analysis the project enters the next stage. The details of the project are then either passed on to the corresponding in-house department or a request for proposal is issued to have subcontractors compete for possibility of carrying out the design. In the latter case all interested subcontractors have to make a proposal and a committee chooses the, in their opinion, best suited candidate.

All those steps have a significant amount of work and thus cost associated with it, which are accounted for as pre acquisition costs. Depending on the individual project these costs are shared among the different parties or taken up by a single one. The pre acquisition cost have been estimated to be 100 thousand US dollars for the contractor carrying out the design.

15.3 Design Cost

During the design phase, several components need to be designed: the aerial vehicle itself, payload, software, ground station, aircraft launch, recovery system and the support equipment. For this phase the main cost are related to the engineering labour cost.

After the first design is completed, tests need to be performed to validate the models utilised during the design. For LIFT^2, validation through test is of major importance as there is little experience with the ducted fan configuration presented here. Especially the flow simulation in CFD requires validation as these models are known to be error prone and the flow over the rotorcraft is expected to be rather complex. In addition to the test required for model validation certification test are required. The transition between validation and certification test is seamless. Again the testing required for certification is expected to be extensive due to the novelty of the design. Some test can serve both purposes at the same time. Testing cost originate from the manufacturing of prototypes, the rent of test facilities, the consumables during the test (e.g. fuel) and the labour of performing test and analysing the results.

Next to those rather obvious cost there are some more hidden cost. Documentation of the design process, financing, facilities and profit of subcontractors also add to the design cost. The total design cost for LIFT^2 has been estimated at 7.12 billion US dollars.

15.4 Production Cost

Production cost can be subdivided into production cost of the three major system components: for the aerial vehicle, the payload and the ground station. For each the production cost consists mainly of labour cost and material cost although facility and tooling cost also play a role.

A major factor that influences the production cost are the materials chosen. Besides the influence on the material procurement cost the material choice also has an influence on the tooling required, the process used and the required education of the craftsmen. The fuselage and landing gear are made of aluminium while the blades are made of composites. For the production cost the factor for composite has been used. As parts of the aerial vehicle are made of metal this is an overestimation which is meant to functions as a buffer. The rather novel design will lead to an accumulation of errors as the workmen are not used to this type of layout and thus is more error-prone. Resulting cost for correction and repair will equal out the overestimation of the production cost.

For one LIFT^2 system the production cost has been estimated to be 43.7 million dollars.

15.5 Operation Cost

During operations some of the costs are associated with labour, where a division is made between direct and indirect labour. Direct labour involves maintenance and operation, whereas indirect labour involves for example administration. Materials that also add up to the cost are obviously fuel, oil and lubricants but also parts replaced during maintenance. Beyond-line-of-sight communication adds cost too, as charges apply to satellite usage. The cost for deployment adds to the overall operation costs. Another cost that should be consider is replacement cost. If a rotorcraft is lost it needs to be replaced. A more detailed cost split up can be viewed in Appendix D.

For the operation cost it is assumed that no rotorcraft is lost. Gundlach [35] suggests to include a cost item related to the possible loss of a rotorcraft. Essentially the price for the replacement is then divided over all missions. That component is so high compared to the rest that it blurs the actual always occurring operation cost too much and was

thus excluded.

For one mission that includes the deployment and the placement of six containers for a hospital the total mission cost is estimated to be 269 thousand US dollar.

15.6 Disposal Cost

Compared to the other major cost items the disposal costs are assumed to be minor [35]. One might even argue that the disposal of the system has some revenue for the owner or at least be cost neutral.

The system disposal can be associated with revenue when it is sold to another user. For aircraft it is often the case that a passenger aircraft is reused as a freighter after some changes have been made to the interior of the aircraft. In the case of the ducted fan a possible scenario would be to sell the used system for short distance use after it is no longer used for the mission profile designed. That might be for example in the shipping industry for the placement and rearrangement of containers. Another different scenario is to split up the twin lift system and resell the two rotorcraft independently.

A cost neutral alternative for disposal is to donate the system for educational purpose to schools, universities or museums. Mostly that ends the flying life of the system and it is used for static display only.

If none of the above mentioned options is possible, the system should be recycled. Some parts can be sold for profit, material can be recycled and sold, but overall the net cost is expected to be negative, thus requiring investment from the owner.

For this system a neutral disposal cost is assumed as a conservative approach. Due to the novelty of the design it is expected there is interest in exhibiting a non flight model is high among museums and educational institutes.

15.7 Return of Investment

The return of investment is a measure for how profitable a project is. It is mathematically defined as

$$ROI = \frac{gain\,from\,investment - cost\,of\,investment}{cost\,of\,investment} \tag{15.4}$$

This analysis can be made either for the company designing and developing the system or the operator of the system. The first one is important to attract investors for LIFT^2, while the latter has an influence on how many units are sold. Only the return of investment for the system design project is presented in this report. To obtain a comparable and reproducible value for the return of investment a time period needs to be defined. In the first phase of the project investments are required and only in later stage there is a return with the sales of the system.

As an approximation, the cost of investment can be assumed to be equal to the sum of the design and the pre acquisition cost (Equation (15.5)).

$$cost\,of\,investment = preaquisition\,cost + design\,cost \tag{15.5}$$

The gain from the investment is set equal to the product of the difference between system sale and production price and the number of systems sold (Equation (15.6).

$$gain\,of\,investment = number\,of\,systems\,sold * (system\,sales\,price - system\,production\,price) \tag{15.6}$$

As the pre-acquisition, design and production cost have already been estimated, only the number of systems sold and the sales price need to be determined.
The price of the system needs to be determined with great care. A high sales price lowers the required number of systems sold to reach a break even point. At the same time a high price might encourage possible clients to buy a cheaper competitor product and therefore lower the number of systems sold.
A lower bound of the sales price is set by the system production cost. If they are not covered by the sales price each sale would be a loss for the company. The production price is 43.7 million and needs to be accounted for in the sales price. Figure 15.1 depicts the relationship between system sales price and number of systems that need to be sold in order to reach the break-even-point.

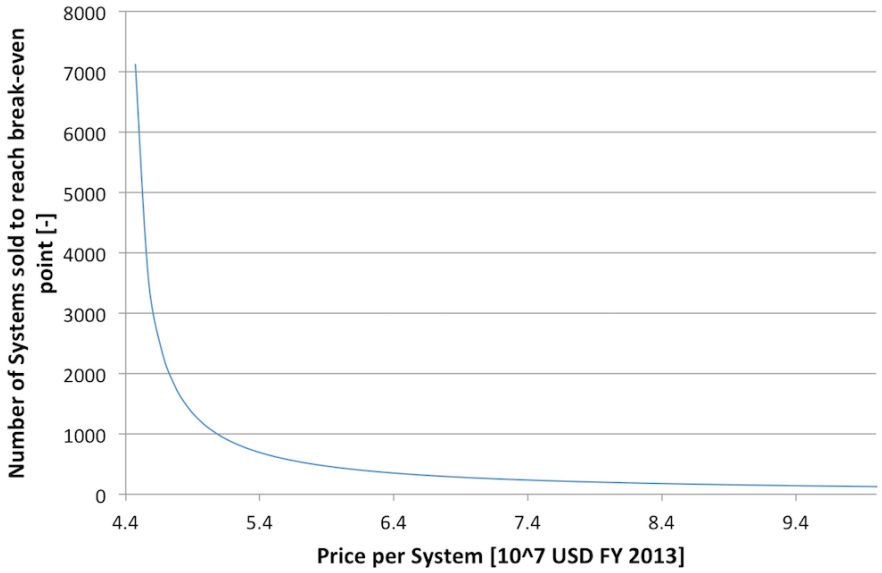

Figure 15.1: Number of LIFT^2 systems sold to reach break-even-point vs price per system

The graph shows asymptotic behaviour as expected. A price around 80 million seems a good trade-off between price and number of systems needed to be sold. Table 15.1 shows the values of graph 15.1 for some prices around the selected value.

Table 15.1: LIFT^2 sales required to reach break-even-point

LIFT^2 sale price [million $]	**70**	**80**	**90**
LIFT^2 systems sold to reach break-even-point [-]	271	197	154

So if the price is set at 80 million dollars about 200 systems need to be sold to reach the break-even point and start making profit. The price is comparable to the price of two Chinook helicopters (see Chapter 3). The required number of sales is deemed reasonable due to the flexibility of LIFT^2 and a sales price of 80 million per system is adopted.

It is assumed that the design phase of LIFT^2 lasts 20 years (from the start of the design to the first delivery). Furthermore, the cost per year is set to be constant for simplification purposes. In reality the money required per year will be dependent on the stage of the design. For example during the testing phase there will be a higher demand to pay for prototypes and testing facilities.

Furthermore the production capacity is set to 15 systems per year and it is assumed that all can be sold. It is assumed only full systems are sold, thus two rotorcraft with a ground station. Figure 15.2 depicts the return of investment dependent on the time span considered when the assumption explained before hold.

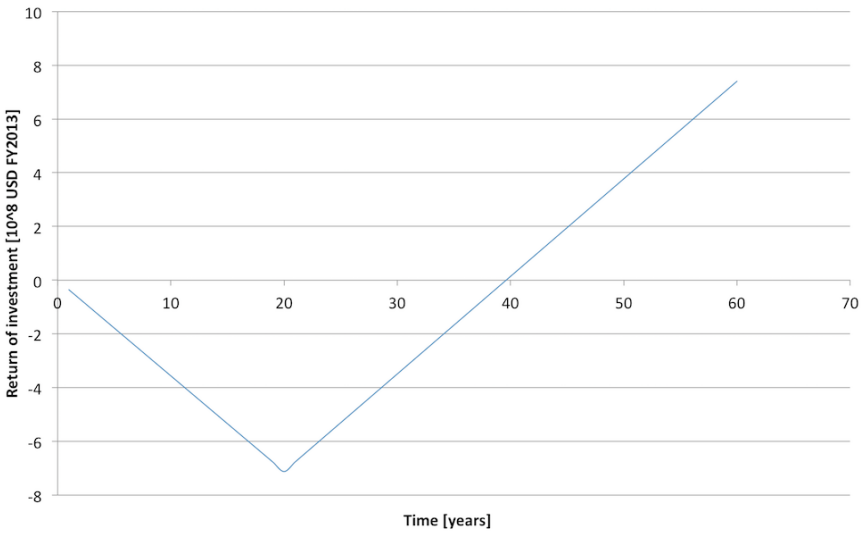

Figure 15.2: Return of investment dependent on the time range considered

The values presented are only first estimates. Some cost parameter might still change during the course of this project. As an example the design cost might increase due to some unforeseen technical problems (see also the risk analysis in Chapter 12). It can also be considered to outsource the production to a low labour cost country to lower the production cost. Then a trade-off between social factor, quality and cost is necessary.

Furthermore it can be considered to not only sell complete systems but also separate system parts. That could be a single rotorcraft but also for example the control structure established for a UAV twin-lift system. In addition maintenance and support will bring some additional revenues. Considering this it is likely that a break-even-point is reached sooner as indicated above. It also makes the return of investments an underestimation. In the next design phases, a revision of the cost analysis is suggested.

16. Product development

Now the preliminary design phase has been finished, it is important to know what could be improved and what has to be done in further design stages. This chapter describes the activities to be performed after the end of this DSE project. First Section 16.1 gives an overview of the tasks to be performed by means of a flow diagram. Section 16.2 allocates a time frame to these activities with the aid of a Gantt-chart. Finally, section 16.3 gives detailed recommendations on how to continue the design process.

16.1 Project Development

This section contains a block diagram (Figure 16.1) with activities that are to be performed after the end of this project. First of all, the design will have to be considered in more detail. Subsystems such as the fuselage, rotor, ground station, control system and container attachment are designed in depth. When the design is complete, small scale prototypes are developed for wind tunnel tests and CFD programs are used for optimisation. Although the testing block is after the detailed design, it also runs parallel with it. If small scale tests are successful, a real-size prototype has to be produced, tested and certified. Communication with interested companies also sets off after this stage. Before the line-production can start, materials have to be allocated, employees have to be hired, the machines have to be prepared and the entire production logistics has to be set up. When contracts have been sealed component production and assembly will commence and the product will be delivered to the customers. Finally, everything is documented and advertisement in different areas might be initiated.

16.2 Time Frame

The time frame for the post-design activity is presented in the Gantt chart shown Figure 16.2. The most time consuming activities are the detailed design of the stability and control system and the certification of the LIFT^2 system. As there is little to no experience with an autonomous twin-lift system, the development will require a large amount of time. Certification is a time consuming activity in any design. Even more so as an unmanned air vehicle of such a large size has never been designed or certified and no clear regulations are available.

16.3 Design Recommendations

As the design process is highly iterative and dynamic, it is not possible to optimise the conceptual design within the time constraints of this DSE project. This section gives recommendations on what should be done if the design of the $LIFT^2$ is taken to the next level.

Overall it is important to perform more iterations. In this report the process has been cut of after the first iteration. Especially for the initial sizing, the feedback from the various disciplines are prone to change the results considerably. Furthermore, sizing has been performed based on a modified method designed for conventional helicopter. Developing a method more tailored to specific design perks and challenges inherent to the ducted fan would greatly increase reliability of the first order estimations.

For all aerodynamic considerations a CFD model would greatly simplify the design process and increase the accuracy of the results. Creating a CFD model, is a challenge on itself. There is little to no experience with aerial vehicles like the one used in the $LIFT^2$, which makes validation of any computational approach nearly impossible. Therefore, wind tunnel test are required to validate CFD models and if necessary make the required adaptations. This is of high importance as in the end all other disciplines rely on the information on the aerodynamic forces as input for their sizing.

To increase the accuracy of the structural analysis, deflections and deformations should be accounted for and especially for the blade design. As for the rotor blades the nature of the stresses changes significantly it might be of use to consider changing ply directions over the span. For the fuselage design other load cases besides hover should be analysed to ensure structural integrity during all flight phases. Similarly, the improved sizing of undercarriage should account for horizontal forces that occur during non-vertical landing. Furthermore, a structural analysis needs to be performed for all parts of the aerial vehicle, which was not possible for this project due to time constraints.

Further into the design process lateral and longitudinal stability should be considered, both for a single rotorcraft and for the system. The state space representation of the system needs to be improved by critically reviewing all simplifications made. It might be necessary to consider the non-linear system. To improve the modelling of the inverted pendulum motion longitudinal and lateral stability of the system should be combined in one simulation tool.

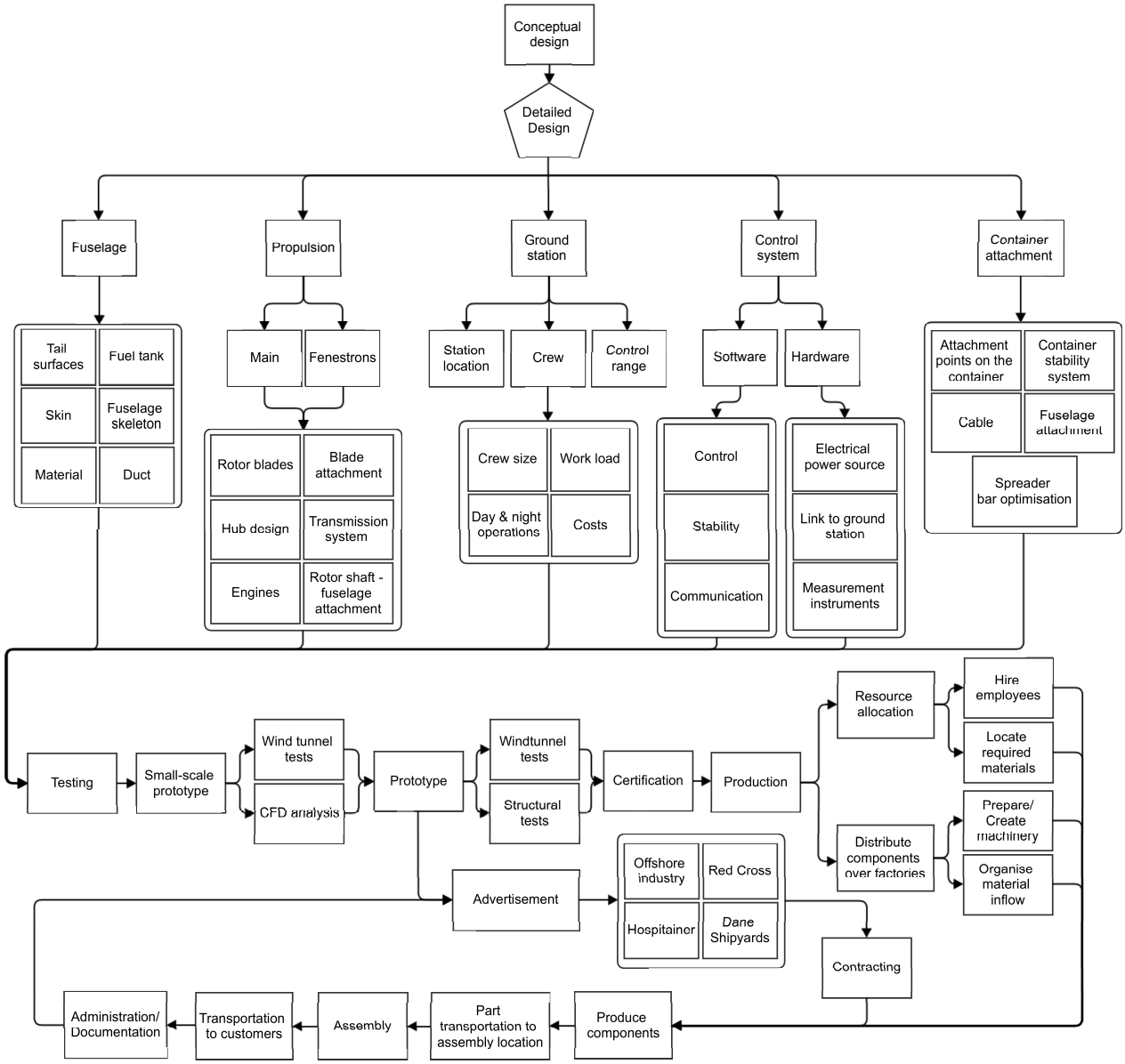

Figure 16.1: Project design & development logic block diagram

For certification and marketing purposes it is also required to perform a more detailed analysis of the noise emission of the ducted fans.

After the improved conceptual design, the detail design follows. All components down to every bolt will be sized and engineering drawings are required to show the arrangement of the parts. Only then the production of the first $LIFT^2$ can commence.

ID	Task Name	Duration	Start	Finish
1	Detailed design	1700 days	Fri 4-7-14	Thu 7-1-21
2	Testing	400 days	Fri 8-1-21	Thu 21-7-22
3	Small-scale prototype	2 days	Fri 22-7-22	Mon 25-7-22
4	Wind tunnel test	100 days	Tue 26-7-22	Mon 12-12-22
5	CFD Analysis	100 days	Tue 26-7-22	Mon 12-12-22
6	Prototype	5 days	Tue 13-12-22	Mon 19-12-22
7	Wind tunnel test	200 days	Tue 20-12-22	Mon 25-9-23
8	CFD Analysis	200 days	Tue 20-12-22	Mon 25-9-23
9	Advertisement	1200 days	Tue 13-12-22	Mon 19-7-27
10	Certification	1700 days	Tue 26-9-23	Mon 1-4-30
11	Resource Allocation	300 days	Tue 2-4-30	Mon 26-5-31
12	Distribute components	300 days	Tue 2-4-30	Mon 26-5-31
13	Hire employees	50 days	Tue 27-5-31	Mon 4-8-31
14	Locate required materials	50 days	Tue 27-5-31	Mon 4-8-31
15	Prepare/create	50 days	Tue 27-5-31	Mon 4-8-31
16	Organise material inflow	50 days	Tue 27-5-31	Mon 4-8-31
17	Contracting	1000 days	Tue 20-7-27	Mon 19-5-31
18	Production	600 days	Tue 5-8-31	Mon 21-11-33
19	Part transportation to	20 days	Tue 22-11-33	Mon 19-12-33
20	Assembly	100 days	Tue 20-12-33	Mon 8-5-34
21	Transportation to	50 days	Tue 9-5-34	Mon 17-7-34
22	Wrap up	100 days	Tue 18-7-34	Mon 4-12-34

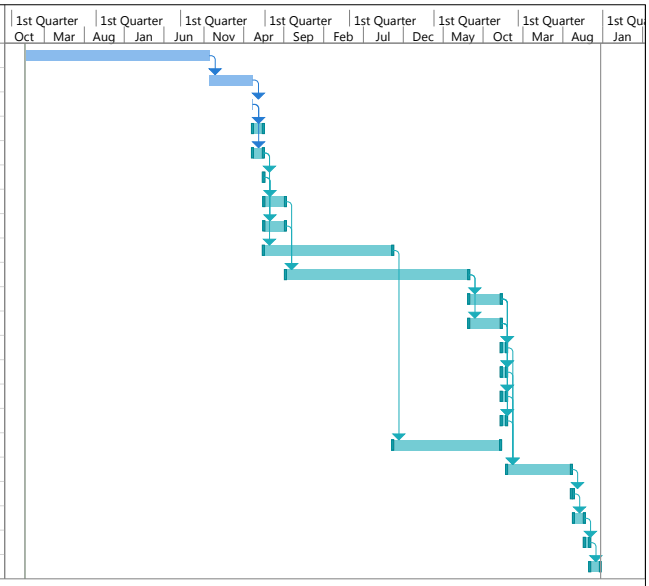

Project: Gantt chart
Date: Sun 22-6-14

Task
Split
Milestone
Summary
Project Summary
Inactive Task
Inactive Milestone
Inactive Summary
Manual Task
Duration-only
Manual Summary Rollup
Manual Summary
Start-only
Finish-only
External Tasks
External Milestone
Deadline
Progress
Manual Progress

Page 1

Figure 16.2: Gantt chart of all post-design activities

17. Conclusion

In this report the design of a twin-lift rotorcraft system with two ducted fans has been presented. The result is the LIFT^2 system which complies with all stakeholder requirements. Nevertheless, designing is a continuous optimization process and some recommendations on how to improve the system during the next design steps are given in Chapter 16. Next to the system sizing also marketing aspects such as market demand and cost have been analysed.

Besides the use for the mission defined by Hospitainer, a future market for LIFT^2 could lie in the off-shore industry which currently experiences a growing demand. In general the twin-lift configuration can fulfil a wide range of different missions, which makes it a versatile tool to be used in the growing rotorcraft market.

Table 17.1 gives a short overview of the most important requirements and check marks are put if they have been met.

Table 17.1: Compliance Matrix

	Stakeholder Requirements	**System Compliance**
Configuration [-]	twin-lift technology	✓
Operation mode [-]	autonomously	✓
Cruise velocity [kts]	80	✓
Maximum speed [kts]	100	✓
Range [km]	200 with payload + 200 without payload	✓
Hover time [min]	30	✓
Mission duration	six per day	✓

As an input for the initial sizing the mission profile and the stakeholder requirements as defined in the baseline report have been revised and used [26]. With Prouty's method revised for ducted fan design the maximum take-off weight of one rotorcraft has been estimated to be 9324 kg with an operational empty weight of 3258 kg, a mission fuel weight of 855kg and a total payload weight of 5211 kg. The power is given by two T700-GE-701 engines which provide a total power installed of 2531 kW at sea level. During one mission with this engine choice 7.237 kg of nitrogen oxide, 3.074 kg of hydrocarbons, 3.778 kg of carbon monoxide and 0.255 kg of non-volatile particles are emitted.

The fuselage size scales with the main rotor radius which are 14.91 m and 6.61 m respectively. For control three tail rotors are chosen, two horizontal ones to provide pitch and roll control and one vertical fenestron to provide anti-torque and yaw control. While the width of the fuselage is determined by the main rotor diameter, the length is set by arms of the tail rotors and is 23.2 m. The height of the fuselage of 1 m is determined by the required value needed for storage and the duct length of the main rotor.

Momentum theory and blade element theory have been utilised to determine the optimum design for the rotor. The radius of the main rotor is 6.61 m with a hub radius of 1.32 m. The Sikorsky SSC-A07 airfoil is utilised for the blades, which have a constant chord of 0.5 m and a polynomial twist distribution. Tail surfaces are designed to unload the tail rotors in forward flight. While the horizontal tail surfaces are capable of providing 50% of the needed control thrust in forward flight, the vertical tail fin has been designed to only provide 25% of the required anti-torque in order to keep its size within acceptable boundaries. Analysis based on actuator disk theory in combinations with a low autorotation index have proven that the ducted fans designed cannot perform a controlled landing in autorotation.

For the main rotor a bearing-less hub has been selected based on qualitative analysis. The rotor blades have been modelled as an equivalent closed-section beam and a stress analysis then yielded M55UD (i.e. a carbon fibre composite) as most appropriate material. The root thickness has been determined to be 0.02 m, which decreases towards the tips. The stresses on the circular fuselage have been calculated by dividing it into equivalent straight beams, which are under an angle with respect to each other. Cost and weight considerations then favoured aluminium as material for the fuselage. The external payload is attached to the fuselage at four points via bolts. The landing gear consists of retractable struts with wheels. They are made of aluminium with a diameter of 0.145 m.

Stability analyses have been performed for the longitudinal stability of a single rotorcraft as well as for the entire LIFT^2 with payload. A single ducted fan is statically stable which has been proven by determining the moment coefficient gradient. The linearised equation of motion show that uncontrolled a single ducted fan is inherently unstable which has been solved by applying a PID-controller.
For the entire LIFT^2 the equations of motion are determined by the Lagrange method. Solving the linearised system for the LIFT^2 yields the conclusion that the system is unstable. In contrast to the case of the single rotor the problem can not be solved with a PID-controller but requires more powerful control algorithms.

The maximum range of one rotorcraft without payload is 967 km and its maximum speed at cruise altitude is 71.9 m/s. It's hover ceiling is 3710 m which reduces to 1685 m when the payload is attached. The absolute ceiling for the loaded case has been determined to be 2750 m.

Being an unmanned system the communication between ground station and aerial vehicles is of uttermost importance for the LIFT^2. For line-of-sight communication the C-band is used, while beyond line-of-sight communication is achieved via satellite relay on the K_u-band. The rotorcraft work in a master-slave configuration, meaning that the ground station has a command link with the master, which then passes the required commands to the slave. Connection between slave and ground station serves only as a back-up for emergency situations.

During design and operation the two major risk factors for the LIFT^2 system have been identified as the horizontal fenestrons and the control system. Both are working theory models but have not been proven in flight and their failure would be catastrophic. That being said innovation is always connected to risk and it has been a concious decision to accept this.

The total design cost for LIFT^2 have been estimated at 7.1 billion US dollars. With a sales price of 80 million US dollar for LIFT^2 and production cost of 43.7 million revenues are expected about 40 years after the project start.

Bibliography

[1] J. Sparrow A. Wynter. Climate change creating new complex emergencies, 2007.

[2] Aeroweb. General electric t700-ge-701. http://www.bga-aeroweb.com/Engines/T700-GE-701.html, June 2014.

[3] airfoiltools.com. Airfoil tools.

[4] John David Anderson Jr. *Fundamentals of aerodynamics*. Tata McGraw-Hill Education, 1985.

[5] Statoil aviation. Jet a-1 product information. http://www.statoilaviation.com/en_EN/pg1332347009500/ar1334072083204/statoilAviation/fuel_jeta1.html, 2014.

[6] BEA. Final report: flight af 447 rio de janeiro - paris. Technical report, Bureau d'Enquetes et d'Analyses pour la securite de l'aviation civile, 2012.

[7] Boeing. Boeing a160 hummingbird. http://www.boeing.com/boeing/bds/phantom_works/hummingbird.page.

[8] businesswire.com. Line thermal imaging low light marine cameras.

[9] CAA. Caa paper 2003/1 helicopter tail rotor failures. Technical report, Civil Aviation Authority, 2003.

[10] ACP Composites. Mechanical properties of carbon fiber composite materials, fiber/epoxy resin (120^o cure), 2009.

[11] H.C. Curtiss. Studies of the dynamics of the twin-lift system. Technical report, Princeton University, 1987.

[12] Taylor Cox David Gibbings. Undercarriages of helicopters. http://www.helis.com/howflies/skids.php.

[13] A.J. Clark School of Engineering Dr. Ibrahim A. Assakkaf. Effective length of column buckling at different conditions. http://www.assakkaf.com/courses/enes220/lectures/lecture27.pdf.

[14] S.W Dr.Beckwith. Designing with composites: Suggested "best practices" rules.

[15] R. Dwight. *AE2220-I Applied Numerical Analysis Reader*. Delft University of Technology, Faculty of Aerospace Engineering, January 2013.

[16] Kyrilian Dyer. Aerodynamic study of a small, ducted vtol aerial vehicle. Technical report, S..B. Mechanical Engineering, MIT, 2002.

[17] Kenneth H. Eagle. Redundancy design philosophy for catastrophic loss protection. *Annual Reliability and Maintainability Symposium*, 1992.

[18] EASA. Certification specifications for large aeroplanes cs-25, September 2007.

[19] EASA. Certification specifications for large rotorcraft cs-29, December 2012.

[20] Dr.-Ing. B. Eck. *Ventilatoren*. Springer Verlag, 1952.

[21] eesa. Young's moduli of different materials in aerospace industry. http://www.spaceflight.esa.int/impress/text/education/Mechanical$%$20Properties/Question_Mechanical_Properties_12.html.

[22] D-STAR Engineering. Reduced disk loading offers greater lift capacity, 2008.

[23] F. Gonzalo et al. Java simulation of embedded control systems., September 2010.

[24] J. Banas et al. Gt athena. Technical report, Georgia Institute of Technology, 2008.

[25] Jon Grossman et al. *Vertical Envelopment and the Future Transport Rotorcraft*. Arroyo center RAND, 2003.

[26] M.J. Beuker et al. Dse - unmanned multi-lift rotorcraft for aid in disasters. Technical report, Technological University Delft, 2014.

[27] M.J. Beuker et al. Dse - unmanned multi-lift rotorcraft for aid in disasters. Technical report, Technological University Delft, 2014.

[28] W.G. Bousman et al. Design considerations for bearingless rotor hubs. Technical report, U.S. Army Aeromechanics Laboratory, 1989.

[29] A. Filippone. *Flight Performance of Fixed and Rotary Wing Aircraft*. Elsevier Ltd., edition 1 edition, 2006.

[30] Robert J. Flemming. An experimental evaluation of advanced rotorcraft airfoils in the nasa ames eleven-foot transonic wind tunnel. Nasa contract report 166587, September 1984.

[31] E.A. Fradenburgh. *A Simple Autorotational Flare Index*. American Helicopter Society, 1984.

[32] Peretz P. Friedmann. Rotary-wing aeroelasticity: Current status and future trends. *AIAA Journal*, 42, 2004.

[33] Carlos Lopez De La Osa Garcia. Scheduled maintenance development, based on airbus' experience, 2013.

[34] F. Marc de Piolenc G.E. Wright Jr. Ducted fan design, 2000-2001.

[35] Jay Gundlach. *Designing Unmanned Aircraft Systems*. American Institute of Aeronautics and Astronautics, 2012.

[36] Doug A. Hodgons. Undercarriage of helicopters patent. `http://goo.gl/iHrdDC`.

[37] S. F. Hoerner. *Fluid Dynamic Drag*. Sighard F. Hoerner, 1965.

[38] Don Hofstrand. Ammonia as a transportation fuel. `http://www.agmrc.org/renewable_energy/renewable_energy/ammonia-as-a-transportation-fuel/`, May 2009.

[39] R.W. Hovey. *Ducted Fans for Light Aircraft: Analysis, Design, and Construction*. Unknown, 1982.

[40] David C. Hutchings. Communication systems 3 (eng3014), 2013.

[41] Inc. Igor I. Sikorsky Historical Archives. Sikorsky s-64 flight parameters and dimensions. `http://www.sikorskyarchives.com/index.php`.

[42] D. Guha-Sapir J. Leaning. Natural disasters, armed conflict, and public health. *The New England Journal of Medicine*, 2013.

[43] IHS Jane's. Boeing ulb little bird. `https://janes.ihs.com/CustomPages/Janes/DisplayPage.aspx?DocType=Reference&ItemId=++++1345273&Pubabbrev=JAWA`.

[44] IHS Jane's. Kaman k-1200 k-max. `https://janes.ihs.com/CustomPages/Janes/DisplayPage.aspx?DocType=Reference&ItemId=+++1343334`.

[45] IHS Jane's. Northrop grumman mq-8b fire scout uav. `https://janes.ihs.com/CustomPages/Janes/DisplayPage.aspx?DocType=Reference&ItemId=++++1355940&Pubabbrev=JFS_`.

[46] IHS Jane's. Sikorsky ch-53e flight parameters and dimensions. `https://janes.ihs.com/CustomPages/Janes/DisplayPage.aspx?DocType=Reference&ItemId=+++1344820`.

[47] IHS Jane's. Ec 725. `https://janes.ihs.com/CustomPages/Janes/DisplayPage.aspx?DocType=Reference&ItemId=++++1342881#`, October 2012.

[48] IHS Jane's. Chinook flight parameters and dimensions. `https://janes.ihs.com/CustomPages/Janes/DisplayPage.aspx?DocType=Reference&ItemId=+++1343229`, October 2013.

[49] IHS Jane's. Mil mi 46 flight parameters and dimensions. `https://janes.ihs.com/CustomPages/Janes/DisplayPage.aspx?DocType=Reference&ItemId=+++1345184`, October 2013.

[50] Diaz J.H. The influence of global warming on natural disasters and their public health outcomes. Technical report, School of Public Health, Lousiana State University, 2007.

[51] Christos Kassapoglou. *Design and Analysis of Composite Structures: With Applications to Aerospace Structures*. John Wiley & Sons, 2013.

[52] Hal KLopper. First biofuel-powered military helicopter takes flight. `http://www.boeing.com/Features/2010/09/bds_feat_rnlaf_09_07_10.html`, September 2010.

[53] J. Marte & D. Kurtz. A review of aerodynamic noise from propellers, rotors, and lift fans. Technical report, California Institute of Technology, 1970.

[54] A. Leboulanger. Global civil and military helicopter market, helicopter manufacturers to stand the test of financial volatility. Technical report, Frost & Sullivan, 2012.

[55] J. G. Leishman. *Principles of Helicopter Aerodynamics*. Cambridge University Press 2006, 2000.

[56] T.H.G Megson. *Aircraft Structures for Engineering Students*. Elsevier Aerospace Engineering Series, 2007.

[57] Tom Murphy. The biofuel grind. `http://physics.ucsd.edu/do-the-math/2011/11/the-biofuel-grind/`, November 2011.

[58] L.M. Myers. Aerodynamic experiments on a ducted fan in hover and edgewise flight. Master's thesis, Pennsylvania State University, 2009.

[59] S.Montenegro N.Gageik, T.Müller. Obstacle detection and collision avoidance using ultrasonic distance sensors for an autonomous quadrocopter. Technical report, University of Würzburg, Faculty of Aerospace Information Technology, September 2012.

[60] Norman S. Nise. *Control Systems Engineering*. John Wiley & Sons, Inc., fourth edition, 2004.

[61] Norman S. Nise. *Control Systems Engineering*. John Wiley & Sons, Inc., sixth edition, 2011.

[62] Office of the Secretary of Defence. Unmanned aerial vehicle reliability study. Technical report, Department of Defence, 2003.

[63] US Department of Transportation. Helicopter flying handbook, 2012.

[64] Jason Paur. First fuel cell helicopter completes successful flight. `http://www.wired.com/2009/11/first-hydrogen-fuel-cell-helicopter-makes-successful-flight/`, November 2009.

[65] M. Pavel. Guidelines for a first dimensioning of helicopter rotor, 2012.

[66] M.D. Pavel. Advanced dynamics ae4315, 2013.

[67] J.L. Pereira. *Hover and Wind-Tunnel Testing of Shrouded Rotors for Improved Micro Air Vehicle Design*. PhD thesis, University of Maryland, 2008.

[68] JVR Prasad, Manoj Mittal, and Daniel P Schrage. Control of a twin lift helicopter system using nonlinear state feedback. *J. AM. HELICOPTER SOC.*, 36(4):57–65, 1991.

[69] Raymond W Prouty. *Helicopter performance, stability, and control*. Krieger pub co, 1995.

[70] Omri Rand and Vladimir Khromov. Helicopter sizing by statistics. *Journal of the American Helicopter Society*, 49(3), 2004.

[71] D.P. Raymer. *Aircraft Design: A Conceptual Approach*. AIAA, 1999.

[72] Theo Rindlisbacher. Guidance on the determination of helicopter emissions. Technical report, Swiss confederation, 2009.

[73] R. Schindler and E. Pfisterer. Impacts of rotor hub design criteria on the operational capabilities of rotorcraft systems, 1987.

[74] Jeff Scott. Drag of cylinders & cones. `http://www.aerospaceweb.org/question/aerodynamics/q0231.shtml`.

[75] W. Würz Th. Lutz and S. Wagner. Numerical optimization and wind-tunnel testing of low reynolds-number airfoils. Technical report, University of Stuttgart, 2001.

[76] Trefis. Utc's sikorsky helicopter business is poised for long term growth despite weak u.s. military spending. *Forbes*, 2014.

[77] unknown. Gas turbine engines. Aviation Week & Space Technology, January 2005.

[78] unkown. Process control engineer salary.

[79] Th. van Holten and J.A. Melkert. Helicopter performance, stability and control, 2012.

[80] C. N. Keys W. Z. Stepniewski. *Rotary-wing Aerodynamics*. Dover Publications, 1984.

[81] R. J. Weir. Ducted propeller design and analysis, October 1987.

[82] Agusta Westland. Agusta westland project zero.
`http://www.agustawestland.com/node/6902`.

[83] David G. Rethwisch William D. Callister. *Materials Science and Engineering*. Wiley, 2011.

[84] C. Willis. Helicopter values online. *VIEWPoint Issue 41*, 2013.

[85] J.E. Young. Helicopter vertical stabilizer design considerations. Master's thesis, Naval Postgraduate School Monterey, June 1983.

A. Simulation Download Manual

- Go to `http://www.oracle.com/technetwork/java/javase/downloads/jdk8-downloads-2133151.html`
- Check the 'Accept License Agreement' box and click on the download for the correct operating system (Figure A.1).

Java SE Development Kit 8u5

You must accept the Oracle Binary Code License Agreement for Java SE to download this software.

Accept License Agreement Decline License Agreement

Product / File Description	File Size	Download
Linux x86	133.58 MB	jdk-8u5-linux-i586.rpm
Linux x86	152.5 MB	jdk-8u5-linux-i586.tar.gz
Linux x64	133.87 MB	jdk-8u5-linux-x64.rpm
Linux x64	151.64 MB	jdk-8u5-linux-x64.tar.gz
Mac OS X x64	207.79 MB	jdk-8u5-macosx-x64.dmg
Solaris SPARC 64-bit (SVR4 package)	135.68 MB	jdk-8u5-solaris-sparcv9.tar.Z
Solaris SPARC 64-bit	95.54 MB	jdk-8u5-solaris-sparcv9.tar.gz
Solaris x64 (SVR4 package)	135.9 MB	jdk-8u5-solaris-x64.tar.Z
Solaris x64	93.19 MB	jdk-8u5-solaris-x64.tar.gz
Windows x86	151.71 MB	jdk-8u5-windows-i586.exe
Windows x64	155.18 MB	jdk-8u5-windows-x64.exe

Figure A.1: JDK download

- Run the installation file and follow the steps.
- When the installation is finished, go to `http://www.eclipse.org/downloads/`
- Choose the the correct operating system (Figure A.2) and click on the download link.

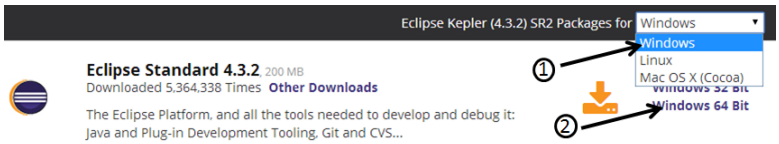

Figure A.2: Eclipse download

- Click on
- When downloading is finished, unpack eclipse-standard-kepler-SR2-win32-x86_64.zip
- Open eclipse and doubleclick eclipse.exe
- Click Browse..., choose the folder Java Simulation as workspace and click two times OK.
- When Eclipse has loaded, close the Welcome Screen.
- Select LIFT2Simulation and click
- Click on the simulation screen to activate the controls.

B. Simulation Runge-Kutta Method

Listing B.1: "StateSpace.java"

```
// Get rates for a certain state
public double[] getRate (double[] state, double[] input) {
        rate [0] = Xu*state[0] + Xw*state[1] + Xq*state[2] + Xthetaf*state[3]
                + XCT1*input[0] + XCT2*input[1] + XCT3*input[2];
        rate [1] = Zu*state[0] + Zw*state[1] + Zq*state[2] + Zthetaf*state[3]
                + ZCT1*input[0] + ZCT2*input[1] + ZCT3*input[2];
        rate [2] = Mu*state[0] + Mw*state[1] + Mq*state[2] + Mthetaf*state[3]
                + MCT1*input[0] + MCT2*input[1] + MCT3*input[2];
        rate [3] =  0*state[0] +  0*state[1] +  1*state[2] +       0*state[3]
                +    0*input[0] +    0*input[1] +    0*input[2];
        return rate;
}

// Step the process for an increment of time
public double[] step (double dt, double[] state) {
        rates1 = getRate (state, input1);
        for (int i = 0; i <numEqn; i++)
                k1[i]= state[i]+ dt * rates1[i]/2.0;
        rates2 = getRate (k1, input1);
        for (int i = 0; i <numEqn; i++)
                k2[i]= state[i]+ dt * rates2[i]/2.0;
        rates3 = getRate (k2, input1);
        for (int i = 0; i <numEqn; i++)
                k3[i]= state[i]+ dt * rates3[i];
        rates4 = getRate (k3, input1);
        for (int i = 0; i <numEqn; i++)
                state[i] = state[i]
                + dt * (rates1[i]+2*rates2[i]+2*rates3[i]+rates4[i])/6.0;
        return state;
}
```

C. SolidWorks Verification

This appendix describes the verfication procedure of SoldidWorks' flow simulation program (SolidWorks 2014). In order to verify that the results are accurate enough, two simple models are analysed for their drag coefficients, namely a sphere and a disk. The sphere is a standard model, often used in drag analysis and the disk is the most representative geometry representing the fuselage.

C.1 Setup

The drag coefficient of both shapes are dependent on the Reynolds number (Re) of the flow, which is in turn dependent on flow properties and model geometry. The Reynolds number is described as in Equation (C.1).

$$\mathrm{Re} = \frac{\rho V l}{\mu} \tag{C.1}$$

In which:

- Re is the reynolds number [-]
- ρ is the air density [kg/m^3]
- V is the airspeed [m/s]
- l is the reference length of the geometry [m]
- μ is the dynamic viscosity [kg/(s·m)]

The drag coefficient of a sphere and a disk as function of the Reynolds number is shown as an experimental relation in Figure C.1 [74]. After performing the Computational Fluid Dynamics (CFD) analysis on both geometries, this graph is used verify the obtained drag coefficients

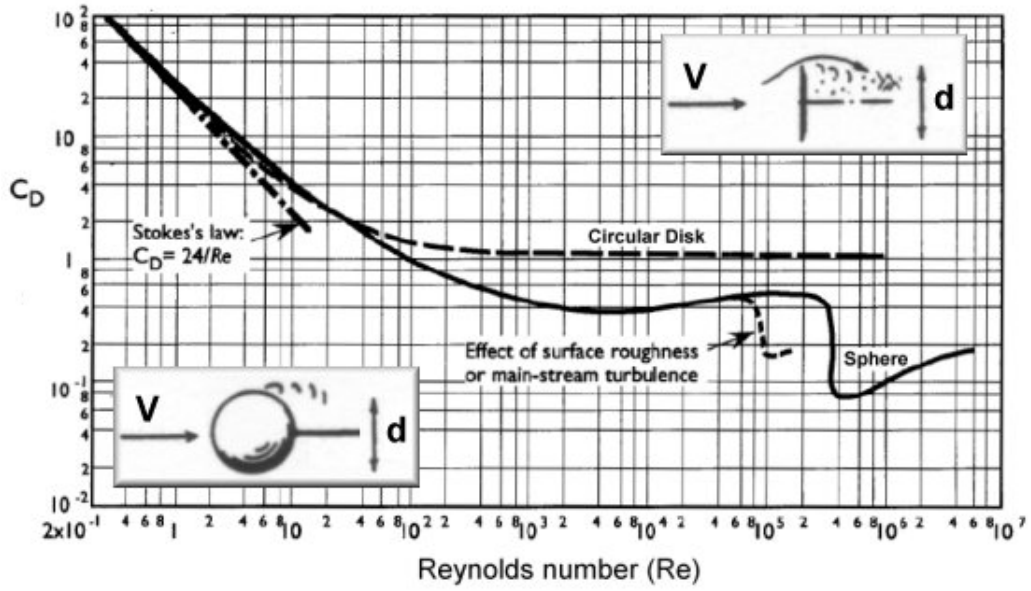

Figure C.1: Drag coefficient of a sphere and disk as a function of Reynolds number [74]

Both the sphere and the disk have a diameter of 50 mm, which is the value used for the reference length l. Furthermore the disk has a 10 mm thickness. The atmospheric properties are set at SolidWork's default values, i.e. $\rho = 1kg/m^3$, T = 292.2 K, P =101325 Pa. The dynamic viscosity is mainly dependent on temperature and in this case $\mu = 1.83 \cdot 10^-5$. Both models are analysed for two different Reynolds numbers, by varying the velocity of the free stream, namely V=0.003 m/s and V=0.3 m/s. Evaluating Equation (C.1) for these velocities yields:

$$\mathrm{Re} = \frac{1 \cdot 0.003 \cdot 50 \cdot 10^{-3}}{1.83 \cdot 10^{-5}} = 8.21 \tag{C.2}$$

$$\mathrm{Re} = \frac{1 \cdot 0.3 \cdot 50 \cdot 10^{-3}}{1.83 \cdot 10^{-5}} = 821.02 \tag{C.3}$$

Other inputs in the SolidWorks' flow analysis wizard:

- SI Units
- Analysis type: external
- Fluids: air
- Flow type: laminar and turbulent
- Default wall thermal condition: Adiabatic wall
- Wall roughness = 0 micrometer
- Result resolution: 3

C.2 Results

Among various results that the flow analysis gives, only one is important in this case: the resultant force on the object (denoted by GG Force 1 in SolidWorks). This total force equals the drag and the corresponding drag coefficient is calculated by:

$$C_D = \frac{D}{\frac{1}{2}\rho V^2 S} \tag{C.4}$$

The flow over the disk and sphere is illustrated in Figures C.2a and C.2b. Furthermore, the CFD results are compared with the experimental values in Table C.1.

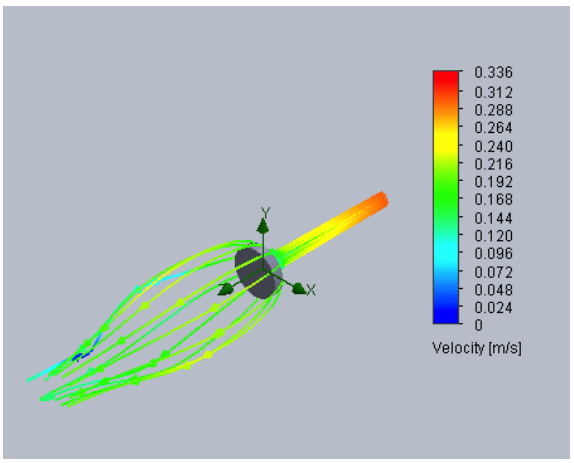

(a) Velocity flowlines over a disk V=0.3 m/s

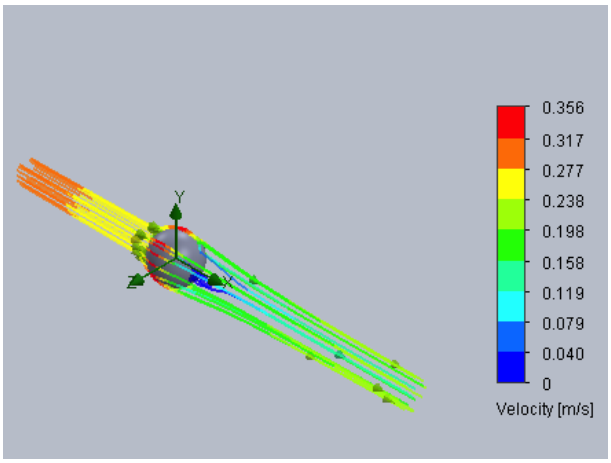

(b) Velocity flowlines over a sphere V=0.3 m/s

Table C.1: Drag coefficient comparison of a disk and sphere at different Reynolds numbers calculated by CFD and measured during experiments

	Re [-]	CD (CFD) [-]	CD (Experimental) [-]	Deviation [%]
Sphere	8.21	4,74	4,9	3,21
	821	0,42	0,45	7,42
Disk	8.21	5,18	5,0	3,65
	821	1,22	1,2	2,03

Table C.1 shows deviations of drag coefficients within 5%, except for the sphere at a Reynolds number of 821. Since the deviations remain within 10%, for design purposes in this stage, the tool is considered verified.

D. Cost Analysis

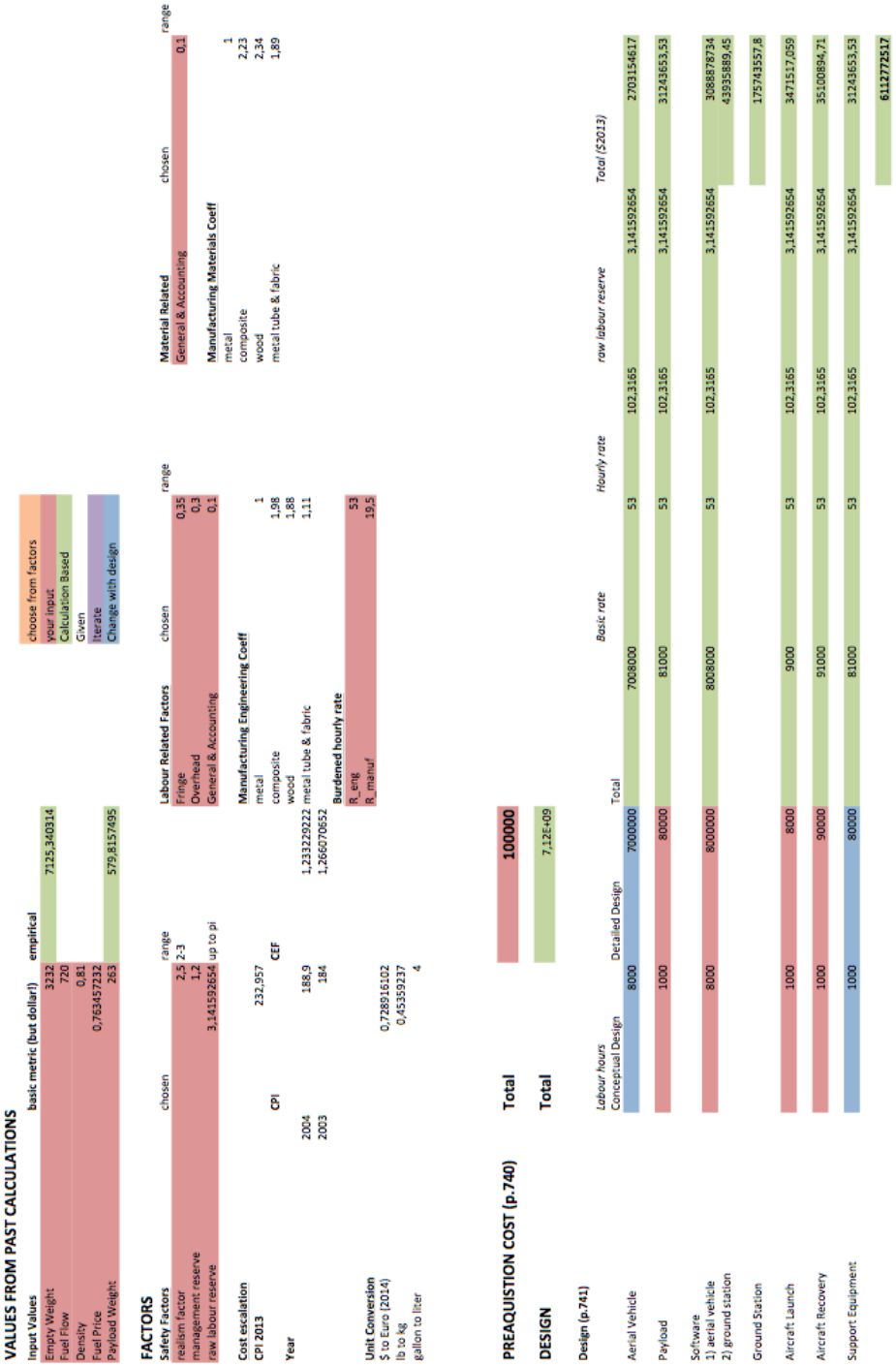

VALUES FROM PAST CALCULATIONS

Input Values	basic metric (but dollar!)	empirical	
Empty Weight	3232	7125,340314	
Fuel Flow	720		
Density	0,81		
Fuel Price	0,763457232		
Payload Weight	263	579,8157495	

	choose from factors
	your input
	Calculation Based
	Given
	Iterate
	Change with design

FACTORS

Safety Factors	chosen	range
realism factor	2,5	2-3
management reserve	1,2	
raw labour reserve	3,141592654	up to pi

Cost escalation		
CPI 2013	232,957	
	CPI	CEF
Year	2004	188,9
	2003	184

Unit Conversion	
$ to Euro (2014)	0,728916102
lb to kg	0,45359237
gallon to liter	4

Labour Related Factors	chosen	range
Fringe	0,35	0,35
Overhead	0,3	0,3
General & Accounting	0,1	0,1

Manufacturing Engineering Coeff	
metal	1
composite	1,98
wood	1,88
metal tube & fabric	1,11

Burdened hourly rate	
R_eng	53
R_manuf	19,5

Material Related	chosen	range
General & Accounting	0,1	0,1

Manufacturing Materials Coeff	
metal	1
composite	2,23
wood	2,34
metal tube & fabric	1,89

PREAQUISTION COST (p.740) Total 100000

DESIGN Total 7,12E+09

Design (p.741)	Labour hours Conceptual Design	Detailed Design	Total	Basic rate	Hourly rate	raw labour reserve	Total ($2013)
Aerial Vehicle	8000	7000000		7008000	53	102,3165	3,141592654	2703154617
Payload	1000	80000		81000	53	102,3165	3,141592654	31243653,53
Software							
1) aerial vehicle	8000	8000000		8008000	53	102,3165	3,141592654	3088878734
2) ground station								43935889,45
Ground Station								1757435578
Aircraft Launch	1000	8000		9000	53	102,3165	3,141592654	34715170,59
Aircraft Recovery	1000	90000		91000	53	102,3165	3,141592654	35100894,71
Support Equipment	1000	80000		81000	53	102,3165	3,141592654	31243653,53
								6112772517

Figure D.1: Cost table (part1)

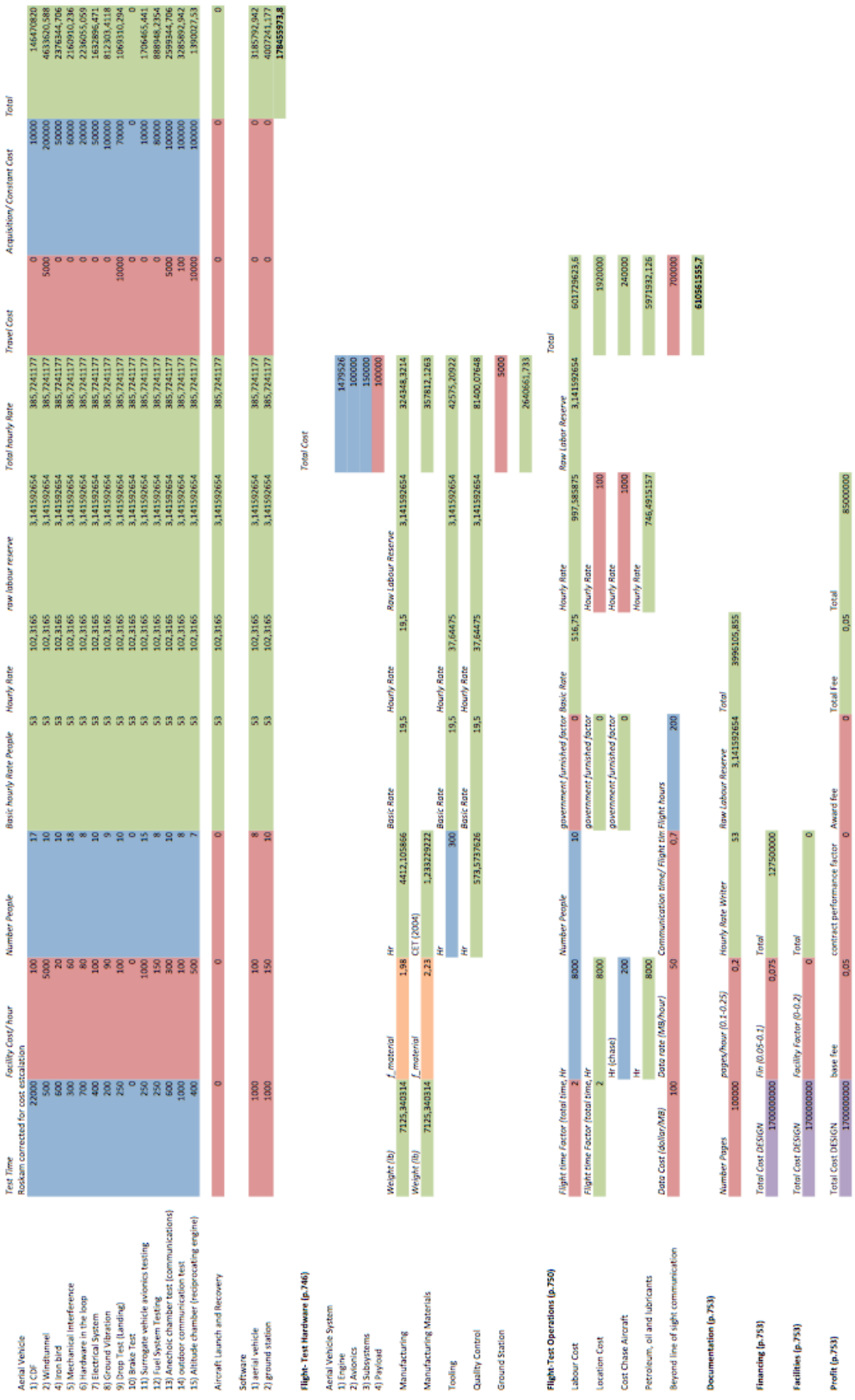

Figure D.2: Cost table (part2)

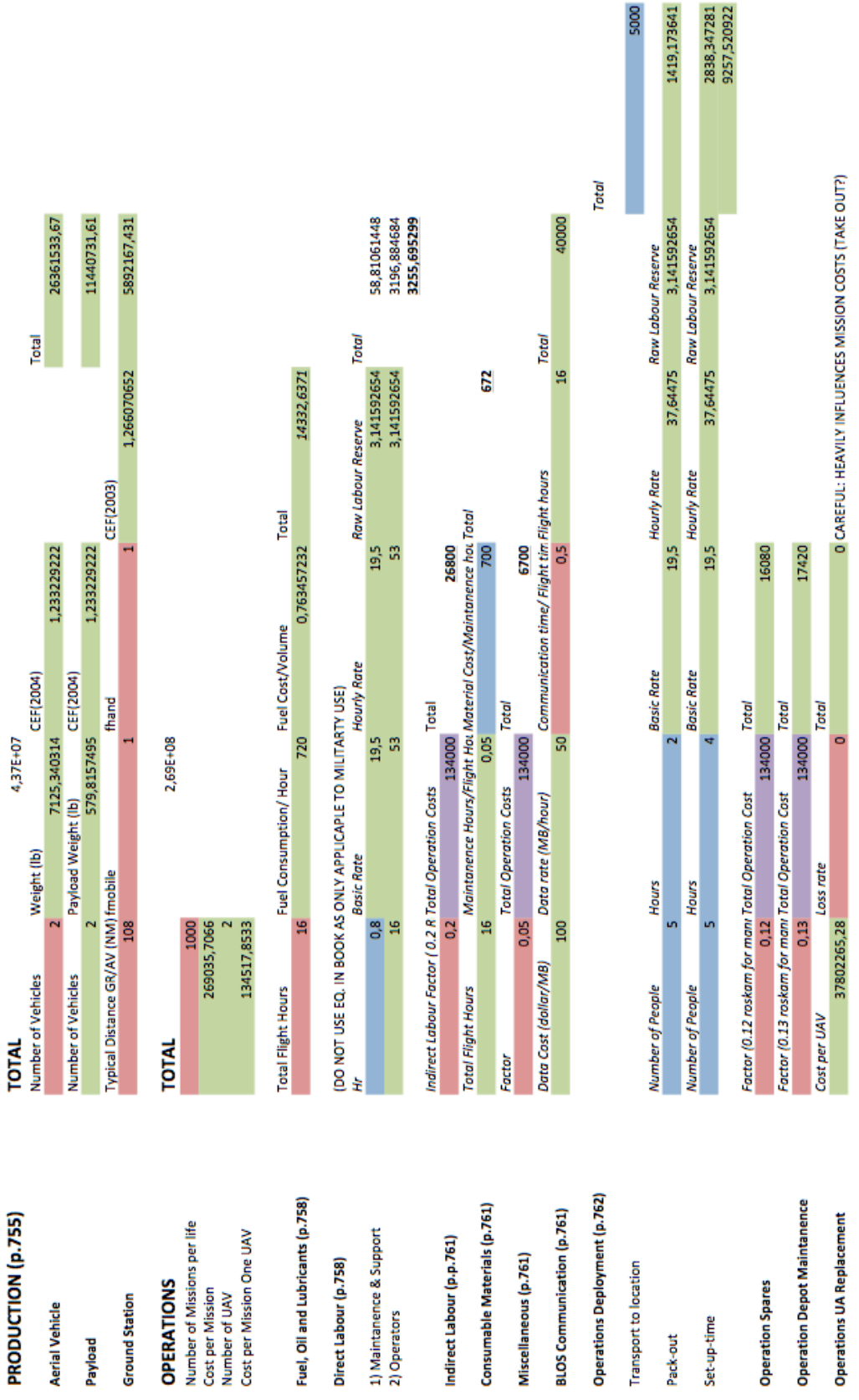

Figure D.3: Cost table (part3)

E. Project Plan

The project plan describes the organisational structure of the DSE group 11 in the final phase. For a detailed schedule of this phase please refer to the mid-term report [27]. In contrast to previous reports the planning of the next step is not discussed in the project plan but in a separate chapter (see Chapter 16 as it is more extensive.

Section E.1 defines the project and describes the setting of this report within the project. Consecutively the roles and responsibilities of each group member are specified by an organogram and a technical function division in Section E.2.

E.1 Project Definition

The project originates from the request of the Hospitainer company together with the Netherlands Red Cross for designing an aerial vehicle capable of transporting Hospitainter containers to disaster areas. The TU Delft Aerospace department was inspired by this request to explore the possibility of a multi-lift unmanned aerial vehicle system capable of transporting such loads. A problem objective statement (POS) has been set up, in order to clearly define the problem that is to be solved during the project. For this project the objective is defined as follows:

> *The project, executed by 10 students in 11 weeks, will prove the possibility of using an autonomous system of multiple unmanned aerial vehicles to transport a payload.*

The project will consist of the following phases with their corresponding milestones as product:

	Description	**Milestone**
Phase 1	Project planning	Project plan
Phase 2	Mission analysis & Requirement definition	Baseline report
Phase 3	Design concept analysis	Mid-term report
Phase 4	Detailed concept	Final report
Phase 5	Design presentation	Symposium presentation

A detailed description of the workflow and the phases of the project can be found in the Baseline Report [26]. With this report, phase 4 is concluded and a conceptual design is presented.

E.2 Roles & Responsibilities

The organogram gives the organisational function of every group member in the DSE project. Figure E.1 shows the organogram for the DSE project. The project manager is the central point of contact in the group. She makes sure the group meetings are held in a structured way and keeps track of every member's opinion. In addition the project manager keeps a clear overview of the tasks that the team has done and the tasks that have to be send to quality control. The project manager assistant helps the project manager with assigning the tasks and keeping track of the project progress. The secretary takes note of the important elements during meetings, both with the tutor as with the group itself. The notes are documented for later reference. The quality control is done by three people. The overall quality control is checked by the quality control manager. One person is in charge of the editing of the report and another one is in control of the quality of the content.

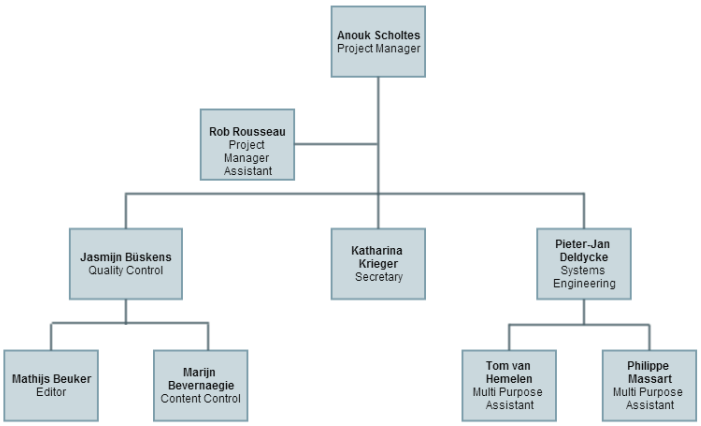

Figure E.1: Project organogram

Besides the organisational role each group member has a technical expertise.The project team was split into four groups, as shown in Figure E.2. Due to uneven workload among the specialities (a large part of the power and performance calculations have already been performed for the mid-term review) some group members worked on two areas.

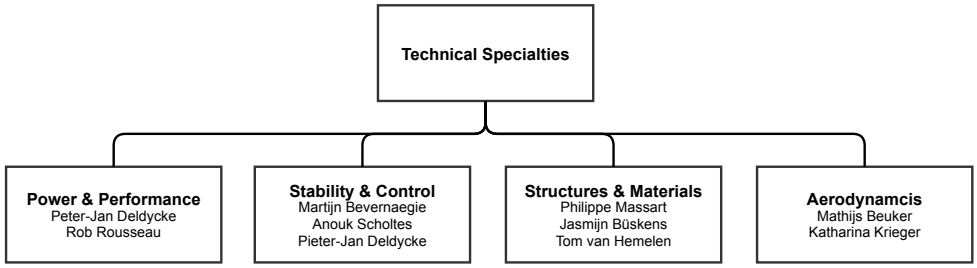

Figure E.2: Group division during the final review

F. Equations of Motion

The non-linear equations of motions are listed below:

$$m_h\ddot{a}_1 - F_3 - F_5 - F_1 + m_l\ddot{a}_1 + \frac{m_s\ddot{a}_1}{2} - l_1 m_l \sin(\alpha_1)\,\dot{\alpha}_1^2 - l_3 m_l \sin(\alpha_3)\,\dot{\alpha}_3^2 - \frac{l_1 m_s \sin(\alpha_1)\,\dot{\alpha}_1^2}{2} + l_1 m_l \cos(\alpha_1)\,\ddot{\alpha}_1 + l_3 m_l \cos(\alpha_3)\,\ddot{\alpha}_3 + \frac{l_1 m_s \cos(\alpha_1)\,\ddot{\alpha}_1}{2} = 0 \tag{F.1}$$

$$m_h\ddot{a}_2 - F_4 - F_5 - F_2 + \frac{m_s\ddot{a}_2}{2} + \frac{l_2 m_s \sin(\alpha_2)\,\dot{\alpha}_2^2}{2} - \frac{l_2 m_s \cos(\alpha_2)\,\ddot{\alpha}_2}{2} = 0 \tag{F.2}$$

$$F_6 + F_8 + F_{10} + gm_h + gm_l + \frac{gm_s}{2} + m_h\ddot{b}_1 + m_l\ddot{b}_1 + \frac{m_s\ddot{b}_1}{2} - l_1 m_l \cos(\alpha_1)\,\dot{\alpha}_1^2 - l_3 m_l \cos(\alpha_3)\,\dot{\alpha}_3^2 - \frac{l_1 m_s \cos(\alpha_1)\,\dot{\alpha}_1^2}{2} - l_1 m_l \sin(\alpha_1)\,\ddot{\alpha}_1 - l_3 m_l \sin(\alpha_3)\,\ddot{\alpha}_3 - \frac{l_1 m_s \sin(\alpha_1)\,\ddot{\alpha}_1}{2} = 0 \tag{F.3}$$

$$F_7 + F_9 + F_{10} + gm_h + \frac{gm_s}{2} + m_h\ddot{b}_2 + \frac{m_s\ddot{b}_2}{2} - \frac{l_2 m_s \cos(\alpha_2)\,\dot{\alpha}_2^2}{2} - \frac{l_2 m_s \sin(\alpha_2)\,\ddot{\alpha}_2}{2} = 0 \tag{F.4}$$

$$\alpha_1 k_1 - F_3 l_1 \cos(\alpha_1) - F_5 l_1 \cos(\alpha_1) + {l_1}^2 m_l\ddot{\alpha}_1 + \frac{{l_1}^2 m_s\ddot{\alpha}_1}{2} - g l_1 m_l \sin(\alpha_1) - \frac{g l_1 m_s \sin(\alpha_1)}{2} + l_1 m_l \cos(\alpha_1)\,\ddot{a}_1 + \frac{l_1 m_s \cos(\alpha_1)\,\ddot{a}_1}{2} - l_1 m_l \sin(\alpha_1)\,\ddot{b}_1 - \frac{l_1 m_s \sin(\alpha_1)\,\ddot{b}_1}{2} - l_1 m_l \cos(\alpha_1)\,\dot{\alpha}_1\dot{b}_1 - \frac{l_1 m_s \cos(\alpha_1)\,\dot{\alpha}_1\dot{b}_1}{2} - l_1 m_l \sin(\alpha_1)\,\dot{\alpha}_1\dot{a}_1 - \frac{l_1 m_s \sin(\alpha_1)\,\dot{\alpha}_1\dot{a}_1}{2} + l_1 l_3 m_l \cos(\alpha_1 - \alpha_3)\,\ddot{\alpha}_3 - l_1 l_3 m_l \sin(\alpha_1 - \alpha_3)\,(\dot{\alpha}_1 - \dot{\alpha}_3)\,\dot{\alpha}_3 = 0 \tag{F.5}$$

$$\alpha_2 k_2 + F_4 l_2 \cos(\alpha_2) + F_5 l_2 \cos(\alpha_2) + \frac{{l_2}^2 m_s\ddot{\alpha}_2}{2} - \frac{g l_2 m_s \sin(\alpha_2)}{2} - \frac{l_2 m_s \cos(\alpha_2)\,\ddot{a}_2}{2} - \frac{l_2 m_s \sin(\alpha_2)\,\ddot{b}_2}{2} - \frac{l_2 m_s \cos(\alpha_2)\,\dot{\alpha}_2\dot{b}_2}{2} + \frac{l_2 m_s \sin(\alpha_2)\,\dot{a}_2\dot{\alpha}_2}{2} = 0 \tag{F.6}$$

$$\alpha_3 k_3 - F_5 l_3 \cos(\alpha_3) + {l_3}^2 m_l\ddot{\alpha}_3 - g l_3 m_l \sin(\alpha_3) + l_3 m_l \cos(\alpha_3)\,\ddot{a}_1 - l_3 m_l \sin(\alpha_3)\,\ddot{b}_1 - l_3 m_l \cos(\alpha_3)\,\dot{\alpha}_3\dot{b}_1 - l_3 m_l \sin(\alpha_3)\,\dot{a}_1\dot{\alpha}_3 + l_1 l_3 m_l \cos(\alpha_1 - \alpha_3)\,\ddot{\alpha}_1 - l_1 l_3 m_l \sin(\alpha_1 - \alpha_3)\,(\dot{\alpha}_1 - \dot{\alpha}_3)\,\dot{\alpha}_1 = 0 \tag{F.7}$$

$$\alpha_4 k_4 + F_5 l_4 \cos(\alpha_4) = 0 \tag{F.8}$$

The linearised equations are shown in the state space system in Figure F.1.

$$
\begin{pmatrix}
1 & 0 & 0 & 0 & 0 & 0 & 0 & 0 & 0 & 0 & 0 & 0 & 0 & 0 \\
0 & 1 & 0 & 0 & 0 & 0 & 0 & 0 & 0 & 0 & 0 & 0 & 0 & 0 \\
0 & 0 & 1 & 0 & 0 & 0 & 0 & 0 & 0 & 0 & 0 & 0 & 0 & 0 \\
0 & 0 & 0 & 1 & 0 & 0 & 0 & 0 & 0 & 0 & 0 & 0 & 0 & 0 \\
0 & 0 & 0 & 0 & 1 & 0 & 0 & 0 & 0 & 0 & 0 & 0 & 0 & 0 \\
0 & 0 & 0 & 0 & 0 & 1 & 0 & 0 & 0 & 0 & 0 & 0 & 0 & 0 \\
0 & 0 & 0 & 0 & 0 & 0 & 1 & 0 & 0 & 0 & \frac{l_1 m_l + l_1 m_s}{m_h + m_l + \frac{m_s}{2}} & 0 & \frac{l_3 m_l}{m_h + m_l + \frac{m_s}{2}} & 0 \\
0 & 0 & 0 & 0 & 0 & 0 & 0 & 1 & 0 & 0 & 0 & -\frac{l_2 m_s}{2\left(m_h + \frac{m_s}{2}\right)} & 0 & 0 \\
0 & 0 & 0 & 0 & 0 & 0 & 0 & 0 & 1 & 0 & -\frac{\left(\alpha_{10} l_1 m_l + \frac{\alpha_{10} l_1 m_s}{2}\right)}{\left(m_h + m_l + \frac{m_s}{2}\right)} & 0 & -\frac{\alpha_{30} l_3 m_l}{\left(m_h + m_l + \frac{m_s}{2}\right)} & 0 \\
0 & 0 & 0 & 0 & 0 & 0 & 0 & 0 & 0 & 1 & 0 & -\frac{\alpha_{20} l_2 m_s}{2\left(m_h + \frac{m_s}{2}\right)} & 0 & 0 \\
0 & 0 & 0 & 0 & 0 & 0 & 0 & \frac{l_1 m_l + \frac{l_1 m_s}{2}}{{l_1}^2 m_l + \frac{{l_1}^2 m_s}{2}} & 0 & -\frac{\left(\alpha_{10} l_1 m_l + \frac{\alpha_{10} l_1 m_s}{2}\right)}{\left({l_1}^2 m_l + \frac{{l_1}^2 m_s}{2}\right)} & 0 & 1 & 0 & \frac{l_1 l_3 m_l}{{l_1}^2 m_l + \frac{{l_1}^2 m_s}{2}} & 0 \\
0 & 0 & 0 & 0 & 0 & 0 & 0 & 0 & -\frac{1}{l_2} & 0 & 0 & 0 & 1 & 0 \\
0 & 0 & 0 & 0 & 0 & 0 & 0 & \frac{1}{l_3} & 0 & -\frac{\alpha_{30}}{l_3} & 0 & \frac{l_1}{l_3} & 0 & 1
\end{pmatrix}
\begin{pmatrix}
\dot{a}_1 \\ \dot{a}_2 \\ \dot{b}_1 \\ \dot{b}_2 \\ \dot{\alpha}_1 \\ \dot{\alpha}_2 \\ \dot{\alpha}_3 \\ \dot{a}_{11} \\ \dot{a}_{21} \\ \dot{b}_{11} \\ \dot{b}_{21} \\ \dot{\alpha}_{11} \\ \dot{\alpha}_{21} \\ \dot{\alpha}_{31}
\end{pmatrix} =
$$

$$
\begin{pmatrix}
0 & 0 & 0 & 0 & 0 & 0 & 0 & 1 & 0 & 0 & 0 & 0 & 0 & 0 \\
0 & 0 & 0 & 0 & 0 & 0 & 0 & 0 & 1 & 0 & 0 & 0 & 0 & 0 \\
0 & 0 & 0 & 0 & 0 & 0 & 0 & 0 & 0 & 1 & 0 & 0 & 0 & 0 \\
0 & 0 & 0 & 0 & 0 & 0 & 0 & 0 & 0 & 0 & 1 & 0 & 0 & 0 \\
0 & 0 & 0 & 0 & 0 & 0 & 0 & 0 & 0 & 0 & 0 & 1 & 0 & 0 \\
0 & 0 & 0 & 0 & 0 & 0 & 0 & 0 & 0 & 0 & 0 & 0 & 1 & 0 \\
0 & 0 & 0 & 0 & 0 & 0 & 0 & 0 & 0 & 0 & 0 & 0 & 0 & 1 \\
0 & 0 & 0 & 0 & \frac{{\alpha_{110}}^2 l_1 m_l + \frac{{\alpha_{110}}^2 l_1 m_s}{2}}{m_h + m_l + \frac{m_s}{2}} & 0 & \frac{{\alpha_{310}}^2 l_3 m_l}{m_h + m_l + \frac{m_s}{2}} & 0 & 0 & 0 & 0 & \frac{2\,\alpha_{10}\,\alpha_{110}\,l_1\,m_l + \alpha_{10}\,\alpha_{110}\,l_1\,m_s}{m_h + m_l + \frac{m_s}{2}} & 0 & \frac{2\,\alpha_{30}\,\alpha_{310}\,l_3\,m_l}{m_h + m_l + \frac{m_s}{2}} \\
0 & 0 & 0 & 0 & 0 & -\frac{{\alpha_{210}}^2 l_2 m_s}{2\left(m_h + \frac{m_s}{2}\right)} & 0 & 0 & 0 & 0 & 0 & -\frac{\alpha_{20}\,\alpha_{210}\,l_2\,m_s}{\left(m_h + \frac{m_s}{2}\right)} & 0 \\
0 & 0 & 0 & 0 & 0 & 0 & 0 & 0 & 0 & 0 & \frac{2\,\alpha_{110}\,l_1\,m_l + \alpha_{110}\,l_1\,m_s}{m_h + m_l + \frac{m_s}{2}} & 0 & \frac{2\,\alpha_{310}\,l_3\,m_l}{m_h + m_l + \frac{m_s}{2}} \\
0 & 0 & 0 & 0 & 0 & 0 & 0 & 0 & 0 & 0 & 0 & \frac{\alpha_{210}\,l_2\,m_s}{m_h + \frac{m_s}{2}} & 0 \\
0 & 0 & 0 & 0 & \frac{-{\alpha_{310}}^2 - k_1 + g\,l_1\,m_l + \frac{g\,l_1\,m_s}{2} + \alpha_{110}\,a_{110}\,l_1\,m_l + \frac{\alpha_{110}\,a_{110}\,l_1\,m_s}{2}}{{l_1}^2\,m_l + \frac{{l_1}^2\,m_s}{2}} & 0 & \frac{{\alpha_{310}}^2}{{l_1}^2\,m_l + \frac{{l_1}^2\,m_s}{2}} & \frac{\alpha_{10}\,\alpha_{110}\,l_1\,m_l + \frac{\alpha_{10}\,\alpha_{110}\,l_1\,m_s}{2}}{{l_1}^2\,m_l + \frac{{l_1}^2\,m_s}{2}} & 0 & \frac{\alpha_{110}\,l_1\,m_l + \frac{\alpha_{110}\,l_1\,m_s}{2}}{{l_1}^2\,m_l + \frac{{l_1}^2\,m_s}{2}} & 0 & \frac{b_{110}\,l_1\,m_l + \frac{b_{110}\,l_1\,m_s}{2} + l_1\,l_3\,m_l + \alpha_{10}\,a_{110}\,l_1\,m_l + \frac{\alpha_{10}\,a_{110}\,l_1\,m_s}{2}}{{l_1}^2\,m_l + \frac{{l_1}^2\,m_s}{2}} & 0 & -\frac{2\,\alpha_{310}\,(\alpha_{10} - \alpha_{30})}{\left({l_1}^2\,m_l + \frac{{l_1}^2\,m_s}{2}\right)} \\
0 & 0 & 0 & 0 & 0 & \frac{2\left(\frac{g\,l_2\,m_s}{2} - \frac{\alpha_{210}\,a_{210}\,l_2\,m_s}{2}\right)}{{l_2}^2\,m_s} & 0 & 0 & -\frac{\alpha_{20}\,\alpha_{210}}{l_2} & 0 & \frac{\alpha_{210}}{l_2} & 0 & \frac{2\left(\frac{b_{210}\,l_2\,m_s}{2} - \frac{\alpha_{20}\,a_{210}\,l_2\,m_s}{2}\right)}{{l_2}^2\,m_s} & 0 \\
0 & 0 & 0 & 0 & \frac{\alpha_{110}\,l_1\,(\alpha_{110} - \alpha_{310})}{l_3} & 0 & -\frac{(k_3 - g\,l_3\,m_l - \alpha_{310}\,a_{110}\,l_3\,m_l + \alpha_{110}\,l_1\,l_3\,m_l\,(\alpha_{110} - \alpha_{310}))}{{l_3}^2\,m_l} & \frac{\alpha_{30}\,\alpha_{310}}{l_3} & 0 & \frac{\alpha_{310}}{l_3} & 0 & \frac{l_1\,l_3\,m_l\,(\alpha_{10} - \alpha_{30})\,(\alpha_{110} - \alpha_{310}) + \alpha_{110}\,l_1\,l_3\,m_l\,(\alpha_{10} - \alpha_{30})}{{l_3}^2\,m_l} & 0 & \frac{b_{110}\,l_3\,m_l + \alpha_{30}\,a_{110}\,l_3\,m_l - \alpha_{110}\,l_1\,l_3\,m_l\,(\alpha_{10} - \alpha_{30})}{{l_3}^2\,m_l}
\end{pmatrix}
\begin{pmatrix}
a_1 \\ a_2 \\ b_1 \\ b_2 \\ \alpha_1 \\ \alpha_2 \\ \alpha_3 \\ a_{11} \\ a_{21} \\ b_{11} \\ b_{21} \\ \alpha_{11} \\ \alpha_{21} \\ \alpha_{31}
\end{pmatrix} +
$$

$$
\begin{pmatrix}
0 & 0 & 0 & 0 & 0 & 0 & 0 & 0 & 0 & 0 \\
0 & 0 & 0 & 0 & 0 & 0 & 0 & 0 & 0 & 0 \\
0 & 0 & 0 & 0 & 0 & 0 & 0 & 0 & 0 & 0 \\
0 & 0 & 0 & 0 & 0 & 0 & 0 & 0 & 0 & 0 \\
0 & 0 & 0 & 0 & 0 & 0 & 0 & 0 & 0 & 0 \\
0 & 0 & 0 & 0 & 0 & 0 & 0 & 0 & 0 & 0 \\
0 & 0 & 0 & 0 & 0 & 0 & 0 & 0 & 0 & 0 \\
\frac{1}{m_h + m_l + \frac{m_s}{2}} & 0 & \frac{1}{m_h + m_l + \frac{m_s}{2}} & 0 & \frac{1}{m_h + m_l + \frac{m_s}{2}} & 0 & 0 & 0 & 0 & 0 \\
0 & \frac{1}{m_h + \frac{m_s}{2}} & 0 & \frac{1}{m_h + \frac{m_s}{2}} & \frac{1}{m_h + \frac{m_s}{2}} & 0 & 0 & 0 & 0 & 0 \\
0 & 0 & 0 & 0 & 0 & -\frac{1}{\left(m_h + m_l + \frac{m_s}{2}\right)} & 0 & -\frac{1}{\left(m_h + m_l + \frac{m_s}{2}\right)} & 0 & -\frac{1}{\left(m_h + m_l + \frac{m_s}{2}\right)} \\
0 & 0 & 0 & 0 & 0 & 0 & -\frac{1}{\left(m_h + \frac{m_s}{2}\right)} & 0 & -\frac{1}{\left(m_h + \frac{m_s}{2}\right)} & -\frac{1}{\left(m_h + \frac{m_s}{2}\right)} \\
0 & 0 & \frac{l_1}{{l_1}^2 m_l + \frac{{l_1}^2 m_s}{2}} & 0 & \frac{l_1}{{l_1}^2 m_l + \frac{{l_1}^2 m_s}{2}} & 0 & 0 & 0 & 0 & 0 \\
0 & 0 & 0 & -\frac{2}{l_2 m_s} & -\frac{2}{l_2 m_s} & 0 & 0 & 0 & 0 & 0 \\
0 & 0 & 0 & 0 & \frac{1}{l_3 m_l} & 0 & 0 & 0 & 0 & 0
\end{pmatrix}
\begin{pmatrix}
F_1 \\ F_2 \\ F_3 \\ F_4 \\ F_5 \\ F_6 \\ F_7 \\ F_8 \\ F_9 \\ F_{10}
\end{pmatrix}
$$

Figure F.1: State Space System